

MILLIMETER-WAVE GENERATION VIA PLASMA THREE-WAVE MIXING

AIR FORCE OFFICE OF SCIENTIFIC INFORMATION (AFOSI)
 MONITORING AND INTELLIGENCE
 1700 AIR FORCE DRIVE
 RANDOLPH AFB TEXAS 78150
 (512) 336-1200
 AFOSI 170-12
 1700 AIR FORCE DRIVE
 RANDOLPH AFB TEXAS 78150
 (512) 336-1200
 AFOSI 170-12
 1700 AIR FORCE DRIVE
 RANDOLPH AFB TEXAS 78150
 (512) 336-1200
 AFOSI 170-12

Approved for publication and distribution under E.O. 11652

SDTIC
ELECTE
MAY 30, 1990
B

UNCLASSIFIED

SECURITY CLASSIFICATION OF THIS PAGE

REPORT DOCUMENTATION PAGE

Form Approved
OMB No. 0704-0188

1a. REPORT SECURITY CLASSIFICATION Unclassified			1b. RESTRICTIVE MARKINGS		
2a. SECURITY CLASSIFICATION AUTHORITY			3. DISTRIBUTION / AVAILABILITY OF REPORT Approved for public release; distribution unlimited.		
2b. DECLASSIFICATION / DOWNGRADING SCHEDULE			4. PERFORMING ORGANIZATION REPORT NUMBER(S)		
5. MONITORING ORGANIZATION REPORT NUMBER(S) AFOSR-TR. 90-0526			6a. NAME OF PERFORMING ORGANIZATION Hughes Research Laboratories		
6b. OFFICE SYMBOL (If applicable)			7a. NAME OF MONITORING ORGANIZATION Air Force Office of Scientific Research/NP		
6c. ADDRESS (City, State, and ZIP Code) 3011 Malibu Canyon Road Malibu, CA 90245 (213) 317-5000			7b. ADDRESS (City, State, and ZIP Code) Bolling Air Force Base, Bldg. 410 Washington, D.C. 20332-6448		
8a. NAME OF FUNDING / SPONSORING ORGANIZATION Air Force Office of Scientific Research/NP			8b. OFFICE SYMBOL (If applicable) NYF		
9. PROCUREMENT INSTRUMENT IDENTIFICATION NUMBER F49620-85-C-0059			10. SOURCE OF FUNDING NUMBERS		
8c. ADDRESS (City, State, and ZIP Code) Bolling Air Force Base, Bldg. 410 Washington, D.C. 20332-6448			PROGRAM ELEMENT NO. 61102F	PROJECT NO. 2301	TASK NO. A 8
11. TITLE (Include Security Classification) MILLIMETER-WAVE GENERATION VIA PLASMA THREE-WAVE MIXING (U)			WORK UNIT ACCESSION NO.		
12. PERSONAL AUTHOR(S) Schumacher, R.W., Santoru, J., and Goebel, D.M.					
13a. TYPE OF REPORT Final		13b. TIME COVERED FROM 85/4/1 TO 90/1/31		14. DATE OF REPORT (Year, Month, Day) 1990 February	
15. PAGE COUNT 292					
16. SUPPLEMENTARY NOTATION					
17. COSATI CODES			18. SUBJECT TERMS (Continue on reverse if necessary and identify by block number)		
FIELD	GROUP	SUB-GROUP			
19. ABSTRACT (Continue on reverse if necessary and identify by block number)					
<p>Plasma three-wave mixing is a collective phenomena whereby electron-beam-driven electron plasma waves (EPWs) are nonlinearly coupled to an electromagnetic (EM) radiation field. The Hughes objective is to investigate the basic physics of three-wave mixing in the millimeter-wave regime and to establish the scaling of millimeter-wave characteristics with beam and plasma parameters. Our approach is to employ two counterinjected electron beams in a plasma-loaded circular waveguide to drive counterpropagating EPWs. The nonlinear coupling of these waves generates an EM waveguide mode which oscillates at twice the plasma frequency and is coupled out into rectangular waveguides. Independent control of the waveguide plasma, beam voltage, and beam current is exercised to allow a careful parametric investigation of beam transport, EPW dynamics and three-wave mixing physics.</p> <p>The beam-plasma experiment, which employs a wire-anode discharge to generate high-density ($<10^{13} \text{ cm}^{-3}$) plasma in a 3.8-cm-diameter waveguide, has been used to generate radiation at frequencies from 7 to 60 GHz. Two cold-cathode, secondary-emission electron guns ($\leq 90 \text{ kV}$, and $\leq 6.5 \text{ A}$) are used to excite the EPWs. Output</p>					
20. DISTRIBUTION / AVAILABILITY OF ABSTRACT <input checked="" type="checkbox"/> UNCLASSIFIED / UNLIMITED <input checked="" type="checkbox"/> SAME AS RPT. <input checked="" type="checkbox"/> DTIC USERS			21. ABSTRACT SECURITY CLASSIFICATION Unclassified		
22a. NAME OF RESPONSIBLE INDIVIDUAL DR Robert Walker			22b. TELEPHONE (Include Area Code) 202/767-5511		22c. OFFICE SYMBOL NYF

19 (Continued)

radiation is observed only when both beams are injected, and the total beam current exceeds a threshold value of 3 A. The threshold is related to the self-magnetic pinch of each beam which increases the beam density and growth rate of the EPWs. Above the threshold current, the millimeter-wave power scales nonlinearly with beam current up to peak values of 8 kW, which represents a peak beam-power conversion efficiency of 4% and a conversion efficiency of about 0.4% when averaged over the envelope of the amplitude-modulated millimeter-wave pulse. The millimeter-wave frequency scales as the square-root of the discharge current and equals twice the plasma frequency of the waveguide plasma. Radiation is coherent, but amplitude modulated at frequencies $< \omega_{pe}$, which scale as $M_i^{1/2}$. The optimum beam voltage increases with frequency/plasma density, and the radiation amplitude is very sensitive to relative beam positions.

We investigated the radiation characteristics using 15-cm-long and 1.9-cm-long waveguide cavities. The radiation modulation has a low-frequency (10 to 40 MHz) component which is controlled by the ion dynamics, and a high-frequency (~350 MHz) component. The low-frequency modulation depends on the beam current density and the background plasma density whereas the high-frequency modulation is largely independent of the experimentally controlled parameters. The 1.9-cm cavity imposes a longitudinal boundary condition on the beam-excited EPWs that results in normal modes in the voltage-tuning pattern; this is not observed using the 15-cm-cavity. Experiments using low helium gas pressure confirmed that collisions are a controlling factor in the saturation of the three-wave mixing process. We upgraded the experimental apparatus by adapting Hollow-Cathode-Plasma (HCP) electron guns to the three-wave-mixing experiment. The HCP E-guns can inject current densities up to 20 A/cm² at 30 kV. Using these E-guns, we found the beam-current threshold for single-beam radiation emission to be 9.2 A. Agreement between experimental results and theoretical predictions by N.A. Krall and M. Rosenberg of Krall Associates has been obtained.

TABLE OF CONTENTS

SECTION		PAGE
1	INTRODUCTION.....	1
2	APPROACH.....	4
	2.1 Theory.....	4
	2.1.1 Excitation of Electron Plasma Waves.....	4
	2.1.2 Coupling of Electron Plasma Waves to the Radiation Field.....	6
	2.2 Experimental Configuration.....	10
3	RESEARCH ACCOMPLISHMENTS.....	19
	3.1 Preliminary Beam-Plasma Experiments.....	19
	3.2 Hardware Optimization.....	31
	3.3 Beam Dynamics.....	35
	3.4 Scaling Experiments with Low Beam Current.....	41
	3.4.1 Frequency Scaling.....	49
	3.4.2 Amplitude-Modulation Scaling and Coherence.....	58
	3.4.3 Beam-Voltage Scaling.....	63
	3.4.4 Beam-Current Scaling.....	70
	3.4.5 Beam Positioning.....	73
	3.5 Radiation Modulation Characteristics in 15-cm-Long Cavity.....	73
	3.5.1 Scaling with Waveguide Plasma Density.....	77
	3.5.2 Scaling with Beam Current.....	80
	3.5.3 Correlation with an Electrostatic Probe.....	80

TABLE OF CONTENTS (Continued)

SECTION	PAGE
3.6 Radiation Modulation Characteristics in 1.9-cm-long Cavity.....	82
3.6.1 Theoretical Discussion of Cavity Modes.....	85
3.6.2 Power Scaling with Beam Voltage.....	88
3.6.3 Modulation Envelope and Fourier Transform.....	88
3.7 Radiation Power Scaling at Low Gas Pressure.....	91
3.7.1 Beam Current Scaling With Pressure...	95
3.7.2 Beam Voltage Tuning.....	95
3.7.3 Saturation of Output Power at Low Gas Pressure.....	99
3.8 Attempts to Increase Beam Current from Plasma-Anode Electron Guns.....	99
3.8.1 Reduce Beam HV Gap Spacing in 1.9-cm-long System.....	99
3.8.2 Increase Beam Mask Diameter.....	103
3.9 Hollow-Cathode-Plasma Electron Guns.....	103
3.10 Scaling Experiments with High Beam Current.....	112
3.11 Temporal Evolution of Radiation Spectrum.....	115
3.12 Radiation Produced by Interaction of Single Electron Beam with Background Plasma.....	122
3.13 Orbitron Experiments at the University of Tennessee.....	127
4 INTERACTIONS.....	115

TABLE OF CONTENTS (Continued)

SECTION		PAGE
5	PUBLICATIONS AND PATENTS.....	149
6	RESEARCH PERSONNEL.....	150
	REFERENCES.....	151

APPENDICES

A	ELECTROMAGNETIC-WAVE GENERATION IN A COUNTERSTREAMING-BEAM-PLASMA SYSTEM.....	A-1
B	ELECTROMAGNETIC-WAVE GENERATION THROUGH PLASMA THREE-WAVE MIXING.....	B-1
C	PLASMA-ANODE ELECTRON GUN.....	C-1



Accession For	
NTIS GRA&I	<input checked="" type="checkbox"/>
DTIC TAB	<input type="checkbox"/>
Unannounced	<input type="checkbox"/>
Justification	
By	
Distribution/	
Availability Codes	
Dist	Avail and/or Special
A-1	

LIST OF ILLUSTRATIONS

FIGURE		PAGE
1	Beam-Plasma-Waveguide System.....	8
2	Dispersion Relations for Plasma Three-Wave Mixing.....	11
3	Experimental Beam-Plasma Apparatus.....	14
4	Schematic of Plasma-Discharge and Electron- Beam Pulsed-Power Circuits.....	17
5	Millimeter-Wave Diagnostics and Power Measurement System.....	18
6	Preliminary Experimental Apparatus and Axial Plasma-Density Profile in Waveguide.....	21
7	Plasma Three-Wave-Mixing Experiment.....	22
8	Plasma-Loaded-Waveguide Section.....	23
9	Photograph of the Wire-Anode Plasma Discharge.....	24
10	Plasma-Discharge and E-beam Waveforms.....	25
11	Sample Langmuir-Probe Trace.....	26
12	Millimeter-Wave Diagnostics.....	28
13	Electron-Beam and Plasma Profiles Measured Across the Diameter of the Waveguide in the Output-Coupling Section.....	29
14	X-ray Film Exposure of 90-kV Electron Beam.....	30
15	Background Radiation at 20 GHz is Enhanced by more than 10 dB only when Both E-beams are Injected into the Plasma-Loaded Waveguide.....	32
16	Background Radiation at 35 GHz is Enhanced by 5 dB only when both E-beams are Injected into the Plasma-Loaded Waveguide.....	33
17	Photograph of the Optimized Three-Wave-Mixing Experiment.....	34

LIST OF ILLUSTRATIONS (Continued)

FIGURE		PAGE
18	Langmuir-Probe Configuration.....	36
19	Axial Plasma-Density Profiles.....	37
20	Radial Plasma and Electron-Beam Profiles Measured Across the Diameter of the Circular Waveguide at Two Axial Positions which Correspond to the Output Waveguide Locations.....	38
21	Bennett Pinch.....	40
22	Radial Beam Profile at $z = 15$ cm, $n_e = 2 \times 10^{11} \text{ cm}^{-3}$	42
23	Radial Beam Profile at $z = 15$ cm, $n_e = 5 \times 10^{12} \text{ cm}^{-3}$	43
24	Temporal Beam-Profile Evolution at Low Current.....	44
25	Radiation at 60 GHz is Generated by the Beam-Plasma System when Counterstreaming Beams are Injected into the Plasma-Loaded Waveguide.....	45
26	Simultaneous Injection of both Beams is Required to Generate mm-wave Radiation.....	46
27	Output Radiation Shifts to Low Frequency when both Beams are Injected without the High-Density Waveguide Discharge.....	47
28	Radiation at 50 GHz is Observed only when the Two Beam Pulses Overlap in Time.....	48
29	Frequency Scaling with Waveguide Discharge Current is Determined by Observing the mm-wave Output with an Array of Waveguide High-pass and Bandpass Filters.....	50
30	Frequency Scaling with Discharge Current up to 60 GHz and 800 A.....	51
31	Plasma-Density Scaling with Waveguide Discharge Current.....	53

LIST OF ILLUSTRATIONS (Continued)

FIGURE		PAGE
32	Wire-Anode Discharge-Voltage Scaling with Discharge Current.....	54
33	Output mm-wave Frequency Scales as $2\nu_p$	55
34	Frequency Scaling with Discharge Current Over a Lower Current Range and at Slightly Lower Gas Pressures.....	56
35	Output Frequency also Scales as $2\nu_p$ at Lower Plasma Density.....	57
36	Radiation Frequency Scales as $I_0^{1/2}$	59
37	Output mm-wave Radiation is Strongly Modulated on a Time Scale which is Near the Ion-Plasma Frequency.....	60
38	Millimeter Wave Modulation Frequency Decreases with Ion Mass.....	61
39	Millimeter-Wave Pulse-width and Inter- pulse-Period Scale as $M_i^{1/2}$	62
40	Phase-Coherence Measurement System.....	64
41	Beam-Voltage Tuning for $V_b^{1/2} = 19.5$ kV.....	66
42	Beam-Voltage Tuning for $V_b^{1/2} = 30$ kV.....	67
43	Millimeter-Wave Power Scaling with Beam Voltage.....	68
44	Millimeter-Wave Power Scaling with Beam Voltage at 60 GHz.....	69
45	Radiation Power is Optimized for Beam Voltage which Overlaps Regions of Intense Plasma Waves.....	71
46	Millimeter-Wave Power Scales Nonlinearly with Beam Current.....	72
47	Millimeter-Wave Power Scaling Curves for He, H ₂ and Ne.....	74

LIST OF ILLUSTRATIONS (Continued)

FIGURE		PAGE
48	Beam-steering Coils.....	75
49	Beam Steering Optimizes Output Radiation.....	76
50	The Modulation of Ka-Band Radiation is Dependent on the Waveguide Discharge Current.....	78
51	The Ka-Band Radiation is Strongly Modulated For a Waveguide Discharge Current of 500 A.....	79
52	Ka-Band Modulation IPP Depends on the Beam Current.....	81
53	Electrostatic Fluctuations Have the Same Frequency Components as the Output Radiation....	83
54	Electrostatic Fluctuations are Compared With the Disk Probe Signal Using a Faster Oscilloscope Time Scale.....	83
55	When Only One Beam is Injected Into the Waveguide Cavity, the Radiation and Disk Probe Signals Drop to Zero and the Probe Signal is Significantly Reduced.....	84
56	The Allowed EPW Modes are Determined by the Quantization Condition and the Dispersion Relation.....	86
57	Radiation Power Scaling With Beam Voltage for 1.9-cm-Long Waveguide Cavity Reveals the EPW Mode Structure Specified By the Cavity Longitudinal Boundary Conditions.....	89
58	Radiation Bursts are Modulated at Two Different Frequencies in the 1.9-cm-Long Waveguide Cavity.....	90
59	Peak Number 1 From Figure 58 Clearly Shows the High- and Low-Frequency modulation Components.....	92
60	Peak Number 2 from Figure 58.....	92

LIST OF ILLUSTRATIONS (Continued)

FIGURE		PAGE
61	Two Modulation Frequency Bands Are Evident in the Power Spectrum Calculated From Data Shown in Figure 58.....	93
62	Display of the Radiation Power Spectrum Using a Linear Scale.....	93
63	Display of High-Frequency Modulation Components Using an Expanded Scale.....	94
64	The Beam Current is Maximum at Low Helium Gas Pressure.....	96
65	Beam Current Scaling with Beam Discharge Current at Low Helium Gas Pressure.....	97
66	The Radiation Power Scaling With Beam Voltage Shows That the Power is Maximized for 20 kV.....	98
67	The Radiation Power Begins to Saturate at High Beam Current When Low Helium Gas Pressure is Used.....	100
68	The Electron Beam Current is Increased When the Gap Spacing is Reduced in the 1.9-cm-Long Waveguide System.....	102
69	Reducing the Gap Spacing Reduces the Beam Current in the 15-cm-Long System.....	102
70	The Emitted Beam Current Increases When the Beam Mask Diameter is Increased.....	104
71	The Radiation Power Scaling With Beam Current Indicates That Some Of the Beam Current Intercepts the Cavity Entrance Aperture and is Not Injected Into The Waveguide Cavity.....	104
72	Hollow-Cathode-Plasma Electron-Gun Configuration.....	106
73	Three-Wave Mixing Experiment Driven by Hollow-Cathode-Plasma Electron Guns.....	108

LIST OF ILLUSTRATIONS (Continued)

FIGURE		PAGE
74	HCP E-Gun Mechanical Assembly Drawing.....	109
75	HCP E-Gun Modulator and HV Circuit.....	110
76	HCP E-Gun Hollow-Cathode Discharge and Beam Current Waveforms.....	111
77	HCP E-Gun Beam Current Scaling with Hollow- Cathode Discharge Current.....	113
78	Radiation Power Scaling with Total Beam Current.....	114
79	Radiation Power Scaling with Total Beam Current at Reduced Helium-Gas Pressure.....	116
80	Radiation Power at 21 GHz Measured Using Tuned Receiver.....	118
81	Temporal Evolution of ω_p and $2\omega_p$ Spectral Components with $I_B = 6$ A.....	119
82	Temporal Evolution of ω_p and $2\omega_p$ Spectral Components with $I_B = 9.2$ A.....	120
83	Temporal Evolution of ω_p and $2\omega_p$ Spectral Components with $I_B = 6$ A and $I_D = 300$ A.....	121
84	Radiation Spectrum Measured Using Tuned Receiver with 60-A Discharge Current, 6-A Total Beam Current, 28-kV Beam Voltage, and 26 mTorr Helium-Gas Pressure.....	123
85	Radiation Spectrum with 60-A Discharge Current, 9.2-A Total Beam Current, 28-kV Beam Voltage, and 26-mTorr Helium-Gas pressure.....	124
86	Radiation Spectrum with 300-A Discharge Current, 6-A Total Beam Current, 28-kV Beam Voltage, and 25-mTorr Helium-Gas Pressure.....	125
87	Intense Electron Beam Can Produce Backscattered EPWs.....	126
88	Radiation Power Scaling with Single-Beam Current.....	128

LIST OF ILLUSTRATIONS (Continued)

FIGURE		PAGE
89	UT Orbitron Configuration and Drive Circuit.....	129
90	Theoretical Orbitron-Frequency Scaling with Wire Voltage.....	131
91	Vacuum-Orbitron Experiment.....	132
92	Low-Frequency (≤ 2 GHz) Emission from Vacuum Orbitron.....	133
93	Orbitron Discharge Voltage and Current During the Discharge Pulse.....	135
94	Orbitron Emission Frequency Increases with Time in each Discharge Pulse even Though the Wire Voltage is Decreasing.....	136
95	Highest Frequency Observed in 110 GHz.....	137
96	InSb Detector Records 110-GHz Signal through Two Filters.....	139
97	Orbitron Frequency Scales as the Square-Root of the Discharge Current as Predicted by Plasma-Three-Wave-Mixing Theory.....	140
98	Frequency Scaling with Current and Ion Mass Using a 7.3-cm-Diameter Orbitron at Hughes Research Laboratories.....	142
99	Frequency Scaling with Masked Cathode.....	144

SECTION 1

INTRODUCTION

This final report describes Hughes Research Laboratories' (HRL) investigation of millimeter-wave generation via plasma three-wave mixing. Specifically, we examined the plasma-physics issues relating to the generation of millimeter waves via the nonlinear interaction of two electron-beam-driven electrostatic plasma waves. The program supported an experimental effort to investigate the scaling of millimeter-wave power, frequency, and modulation with electron-beam and plasma parameters. We also compared experimental results with theoretical studies performed by M. Rosenberg and N.A. Krall of Krall Associates (Del Mar, CA).

Our approach to this investigation is to employ two counterinjected electron beams in a plasma-loaded waveguide to drive counterstreaming electron plasma waves (EPWs). The nonlinear coupling of these waves generates an electromagnetic waveguide mode that oscillates at twice the plasma frequency. Independent control of waveguide plasma density, gas species, beam voltage, and beam current allows a careful parametric study of three-wave-mixing physics. Although there have been earlier experimental studies of radiation generation in a plasma at twice the plasma frequency,¹⁻⁴ our program is the first to use high-power (≤ 90 kV, ≤ 6.5 A) beams in a high-density, plasma-filled waveguide to generate substantial radiation power levels (≤ 8 kW) at millimeter-wave frequencies.

Under this program we achieved significant understanding and made dramatic experimental demonstrations of the basic physics of plasma three-wave mixing. The following items summarize our accomplishments and experimental results.

- Significant millimeter-wave radiation is observed only when beams counterstream ($I_b \leq 9.2$ A) and only when each beam current is adjusted above a threshold of about 1.5 A.
- Frequency equals twice the plasma frequency, and scales as $I_d^{1/2}$ up to 60 GHz.
- Peak radiation power was ≤ 8 kW with peak efficiency $\leq 4\%$.
- Radiation power and efficiency increase nonlinearly with beam current.
- Power increases with ion mass.
- Radiation is coherent, but is amplitude modulated at frequencies $< \omega_{pi}$.
- Modulation frequency (~ 40 MHz) scales as $M_i^{1/2}$.
- Beam-voltage tuning ($V_B^L = V_B^H$) is required only at low current (corresponds to weak-turbulence regime).
- Optimum beam voltage increases with frequency (plasma density). The optimum beam voltage is 30 kV at 30 GHz and 43 kV at 60 GHz for 15-cm-long plasma.
- Beam steering via quadrupole fields optimizes power.
- Bennett pinch dominates beam dynamics and power scaling.
- Radiation modulation depends on waveguide plasma density and beam current, and correlates with electrostatic probe measurements.
- Experiments performed using a 1.9-cm-long beam-interaction cavity demonstrate that the cavity boundary conditions determine the allowed electron-plasma-wave modes.
- Radiation power nearly saturates at high beam current when low background gas pressure is used.
- Maximum total beam current increased to 200 A using Hollow-Cathode-Plasma (HCP) electron guns. The HCP E-gun concept was originally developed under Hughes Aircraft Company IR&D.

- Identified radiation output at ω_p and $2\omega_p$ when high beam currents are employed.
- Plasma produced via beam impact ionization of background helium gas shifts radiation frequency from Ka- to V-band when total beam current raised beyond 10 A.

We also used one high-current HCP E-gun to investigate radiation generation via the interaction of a single electron beam with a background plasma. With one beam we found:

- Single-beam radiation emission threshold is ~ 9 A.
- Saturation of single-beam radiation emission not observed up to 15 A, where radiation frequency increases above Ka-band.

In the following sections we will review our significant technical accomplishments in understanding and demonstrating the basic physics of millimeter-wave generation via plasma three-wave mixing. In Section 2 we present a simple plasma three-wave mixing theoretical model. This is followed by a discussion of the experimental configuration. In Section 3 we present our detailed experimental results, including radiation power, frequency, and modulation scaling with beam current, plasma density, and waveguide cavity length. Drafts of three papers which are being prepared for publication are enclosed in Appendices A, B, and C.

SECTION 2

APPROACH

In this section we present our simple theoretical model describing the plasma three-wave mixing process. We conclude with a description of the experimental apparatus which utilizes the three-wave mixing process to generate electromagnetic radiation.

2.1 THEORY

Plasma three-wave mixing is based on the beam-plasma-interaction problem^{5,6} that has been explored in numerous publications for almost 40 years. Beam-plasma phenomena for radiation generation is attractive because of the ease with which intense, high-frequency electron-plasma waves (EPWs) can be excited when a high-power electron beam is injected into a dense plasma. However, the problem of efficiently coupling the power in the electrostatic waves to a radiation field has hindered⁷ all previous attempts to use plasmas in millimeter-wave sources or amplifiers. In the following theoretical discussion, we will summarize the basic physics of beam-driven EPWs and present a simple kinematic model for the nonlinear coupling of two EPWs to the radiation field in a plasma-filled waveguide.

2.1.1 Excitation of EPWs

We begin the discussion by restricting the treatment to a weak, cold beam with density n_b and velocity v_b . By "weak" beam we mean that the ratio of beam density to plasma electron density,

$$\frac{n_b}{n_e} \equiv \epsilon \quad , \quad (1)$$

is small compared with unity ($\epsilon \ll 1$); by "cold beam" we mean that the beam temperature is much less than the beam energy.

Under these conditions, linear hydrodynamic theory^{5,6,8,9} (electron-beam flow through an electron fluid that is stationary in the lab frame with a fixed ion background) shows that the beam will excite EPWs with phase velocity

$$\frac{\omega_e}{k_e} \approx v_b, \quad (2)$$

and, with the well-known Bohm-Gross dispersion,

$$\omega_e^2 = \omega_p^2 + 3k_e^2 v_{th}^2 \approx \omega_p^2, \quad (3)$$

where ω_e and k_e are the EPW frequency and wave number, v_{th} is the plasma-electron thermal speed, and ω_p is the plasma frequency given by

$$\omega_p = \left(\frac{4\pi n_e e^2}{m_e} \right)^{1/2}. \quad (4)$$

Because v_{th} is much less than v_b , the second term in Eq. (3) is much less than ω_p^2 , so we have $\omega_e \approx \omega_p$. The waves will grow along the beam trajectory with temporal growth rate,

$$\Gamma_t = \frac{3^{1/2}}{2^{4/3}} \epsilon^{1/3} \omega_e, \quad (5)$$

and spatial growth rate,¹⁰

$$\Gamma_z = \frac{3^{1/6}}{2^{4/3}} \epsilon^{1/3} \left(\frac{v_b}{v_{th}} \right)^{2/3} k_e. \quad (6)$$

The linewidth of the excited waves expressed in terms of wave number spread is also related to beam strength ϵ according to

$$\frac{\Delta k_e}{k_e} \sim \frac{3}{2^{5/6}} \epsilon^{1/3} \quad (7)$$

Nonlinear theory^{8,9} shows that the EPW gains energy from the beam until it saturates by trapping beam electrons and broadening the beam-velocity distribution function. The saturated energy density in the EPW is given by

$$W = \frac{\langle E^2 \rangle}{4\pi} = \frac{n_b m_e v_b^2}{2} \left(\frac{\epsilon}{2} \right)^{1/3} \quad (8)$$

Because the factor $n_b m_e v_b^2 / 2$ is just the energy density in the electron beam, Eq. (8) shows that the fraction of beam energy coupled to EPW energy is $\sim (\epsilon/2)^{1/3}$. Note that for $n_b/n_e = 4\%$, up to 27% of the beam energy can be transferred to the EPWs.

The ratio $W/n_e T_e$ (where $n_e T_e$ is the plasma energy density) quantifies the strength of the beam-plasma interaction. For $W/n_e T_e$ greater than a few percent, the electric fields in the EPW begin to modify the plasma through ponderomotive-force effects. In this regime the EPWs and the plasma become strongly coupled and the beam-plasma system is said to be in the strong turbulence regime. In the opposite limit, where W is so small that

$$W/n_e T_e < (k_e \lambda_D)^2, \quad (9)$$

where λ_D is the electron Debye length [$\lambda_D = (kT_e/4\pi n_e e^2)^{1/2}$], the beam-plasma system is said to be weakly turbulent.

2.1.2 Coupling of the EPWs to the Radiation Field

The oscillating field of the EPW contains the power that we wish to extract from the electron beam, but the power is trapped

in the plasma as an electrostatic wave and must be coupled out in some manner as an electromagnetic mode. The Hughes solution to the coupling problem is to use two counterstreaming electron beams to excite two counterstreaming EPWs, as shown in Figure 1. These two waves are then nonlinearly coupled to a TM electromagnetic waveguide mode via plasma three-wave mixing. In this process, the electric field of one wave induces a velocity increment δv_e in the electron density fluctuations δn_e present in the second wave, thereby generating a nonlinear source current that is expressed as

$$J = e\delta n_e \delta v_e \quad (10)$$

This source current is nonlinear because it is a product of two first-order fluctuations of the two linear, primary waves.

The plasma three-wave-mixing process can be described quantitatively by using the dispersion relation for the plasma-loaded-waveguide mode and the energy and momentum conservation relations for three-wave mixing:

$$[\text{dispersion}] \quad \omega_o^2 = \omega_p^2 + \omega_c^2 + k_o^2 c^2 \quad (11)$$

$$[\text{energy conservation}] \quad \omega_o = \omega_{p1} + \omega_{p2} = 2\omega_p \quad (12)$$

$$[\text{momentum conservation}] \quad \vec{k}_{e1} + \vec{k}_{e2} = \vec{k}_o \quad (13)$$

In these relations ω_o is the electromagnetic-waveguide-mode frequency; ω_{p1} and ω_{p2} are the EPW angular frequencies; ω_c is the waveguide-cutoff frequency in vacuum; k_{e1} and k_{e2} are the EPW wave numbers; and k_o is the electromagnetic wave number. Dispersion for each beam-mode plasma wave is described by Eq. (2). As a consequence of wave-energy conservation [Eq. (12)], the current J [of Eq. (10)] oscillates at twice the

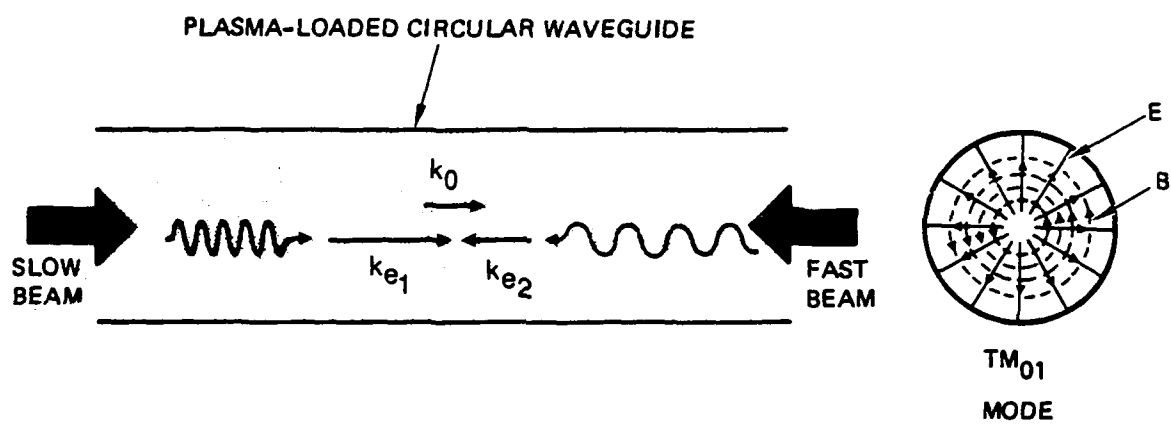


Figure 1. Beam-plasma-waveguide system.

EPW frequency. The oscillating axial current then couples to a TM electromagnetic waveguide mode at $2\nu_p$.

The beam speeds, and thus the phase velocities of the EPWs, are always smaller than the phase velocity ($\geq c$) of the electromagnetic wave. Consequently, k_{e1} and k_{e2} will be larger than k_o . To satisfy Eq. (13) with collinear, but oppositely directed EPWs, the two electron-beam speeds must therefore be unequal for finite k_o . Cutoff waveguide modes with $k_o=0$ will be excited for equal beam speeds. The beam-speed difference can be expressed in terms of the plasma-waveguide parameters by solving Eqs. (2), (3), (11), (12), and (13) simultaneously. Inserting Eq. (12) into (11) and solving for k_o , we obtain the waveguide-mode wave number:

$$k_o = \frac{\left(3\omega_p^2 - \omega_c^2\right)^{1/2}}{c} \quad (14)$$

This equation shows that ω_p must be greater than or equal to $3^{-1/2} \omega_c$ in order to couple to a waveguide mode. Inserting Eqs. (2) and (3) into (13) and equating the result to (14), we obtain the desired equation that relates the beam speeds to the plasma-waveguide parameters:

$$v_{b2} - v_{b1} = \frac{\left(3 - \omega_c^2/\omega_p^2\right)^{1/2} v_{b2} v_{b1}}{c} \quad (15)$$

In this equation, v_{b1} is the speed of the slow beam from the low-voltage gun and v_{b2} is the speed of the fast beam from the high-voltage gun. Note that this tuning condition is applicable only to weak beams ($n_b/n_e < 10^{-4}$). In the strong-beam case (strong-turbulence regime), a broad spectrum of EPW wave numbers can be generated, and the velocity requirements in Eq. (15) can be relaxed. Note also that for high-order TM modes with large

$\omega_c \sim 3^{1/2} \omega_p$, Eq. (13) requires that the two beam speeds be closely matched.

The dispersion relations described by Eqs. (2), (3), (11), (12), and (13) are plotted in Figure 2. The plot shows how two oppositely directed EPWs with different phase velocities (ω_p/k_{e1} and ω_p/k_{e2}) are coupled to a third space-charge wave with dispersion

$$\omega = \frac{2\omega_p}{k_{e1} - k_{e2}} k \quad (16)$$

A plasma-loaded-waveguide mode is excited at the intersection of this coupled space-charge wave with the electromagnetic dispersion curve.

As an example of a solution to Eq. (15), consider an experiment with a 3.81-cm-diameter waveguide operating in V-band at $\nu_0 = 50$ GHz. The plasma frequency ν_p will be 25 GHz, so Eq. (4) indicates that the waveguide plasma density must be $7.8 \times 10^{12} \text{ cm}^{-3}$. The cutoff frequency ν_c of the TM_{01} mode in the waveguide in vacuum is 6 GHz. If the energy of the fast electron beam is chosen at 60 kV, then the slow-beam energy must be 18 kV in order to satisfy Eq. (15). However, if a higher-order TM_{nm} mode is excited with $\nu_c \sim 43$ GHz, Eq. (15) requires that the beam energies be equal.

2.2 EXPERIMENTAL CONFIGURATION

Millimeter-wave generation via plasma three-wave mixing is being investigated using the beam-plasma-waveguide system shown in Figure 1. Two electron beams are counterinjected into a plasma-loaded circular waveguide, where they generate EPWs. The counterstreaming EPWs nonlinearly couple via the three-wave-mixing mechanism to generate a TM waveguide mode, which then propagates down the guide in the direction of the slower beam

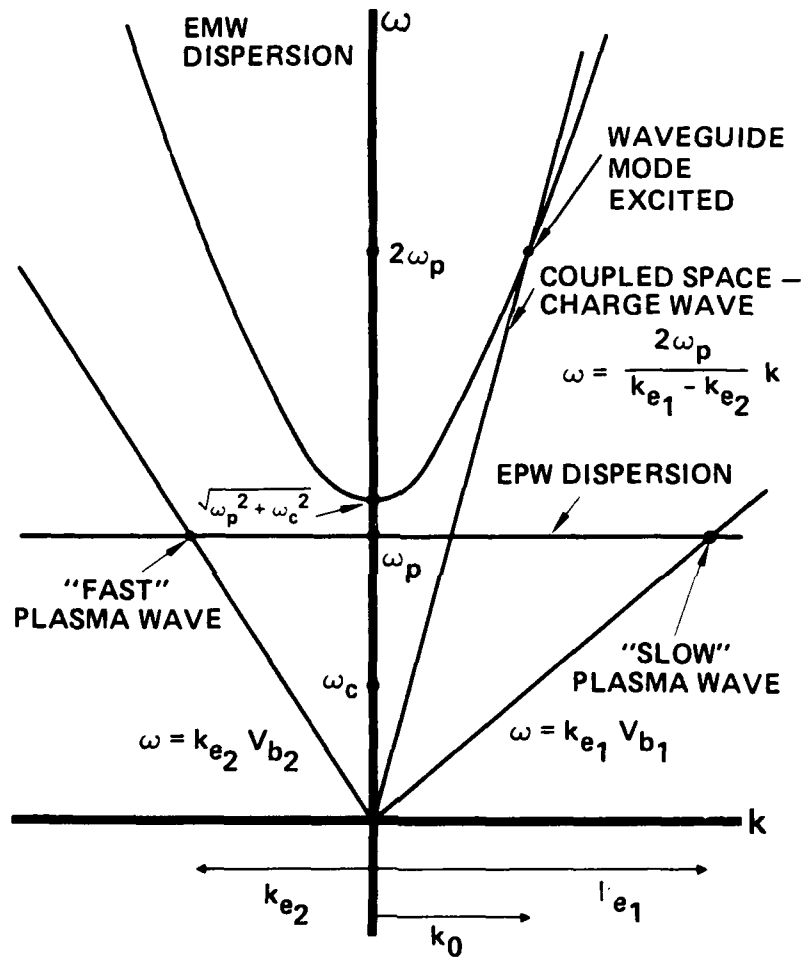


Figure 2. Dispersion relations for plasma three-wave mixing.

(as a consequence of momentum conservation). Consistent with energy conservation, the radiation frequency is centered at twice the plasma frequency. The plasma and beam parameters are listed in Table 1.

Figure 3 is a diagram of the experimental apparatus assembled for our investigation. High-density plasma ($\leq 1 \times 10^{13} \text{ cm}^{-3}$) is generated by a multiwire, wire-anode discharge¹¹⁻¹³ in the annular space surrounding a 3.8-cm-diameter perforated waveguide at helium-gas pressure in the 10- to 65-mTorr range. The microperforations allow both ionizing discharge electrons and background plasma to penetrate the waveguide, thus loading it with a high-density, quiescent plasma. The perforations are large compared with a Debye length, but small compared with the electromagnetic wavelength; therefore, radiation remains trapped in the guide while plasma can pass through freely. Both ends of the circular waveguide are terminated by highly transparent grids (80%). Radiation is coupled out of this waveguide-cavity configuration through rectangular waveguides that are oriented to align the electric-field vector of the TE_{10} (rectangular-waveguide) mode with the axial electric field of a TM mode in the circular waveguide.

Secondary-emission electron guns^{14,15} are used to generate the electron beams. As shown in Figure 3, each gun employs a separate wire-anode discharge in the region between the waveguide and the electron-gun cathode. The plasma in this discharge is partially confined between the waveguide-terminating grid on one side and a similar grid on the opposite side near the cathode. This latter grid also serves as the anode for the electron gun. A fraction of the ions produced in this plasma are extracted through the anode grid and are accelerated to the cathode (which is continuously held at negative high voltage) where they bombard the molybdenum electrode surface and produce secondary electrons. These electrons are accelerated back through the cathode-anode gap,

TABLE 3. Experiment Parameters.

- GAS : $H_2, He, Ne, Ar, Kr, \text{ or } Xe$ at 1 TO 65 mtorr
typically He at 24 mtorr
- PLASMA : $n_e = 2 \times 10^{11} \text{ cm}^{-3}$ to 10^{13} cm^{-3}
 $T_e \approx 5 \text{ eV}$
- BEAMS : $V_B \leq 90 \text{ kV}$, typically 20-50 kV
 $I_B \leq 3.5 \text{ A}$ (using cold-cathode electron guns,
and $I_B \leq 100 \text{ A}$ with Hollow-Cathode-
Plasma electron guns)
 $T_B \geq 15 \text{ eV}$
 $J_B \leq 4 \text{ A/cm}^2$
 $n_B \leq 6 \times 10^9 \text{ cm}^{-3}$, $0.03\% \leq n_B/n_e \leq 3\%$
- WAVEGUIDE : 3.8-cm diameter
46-cm, 15-cm, 1.9-cm long
- RADIATION : 7-60 GHz, peak power $\leq 8 \text{ kW}$

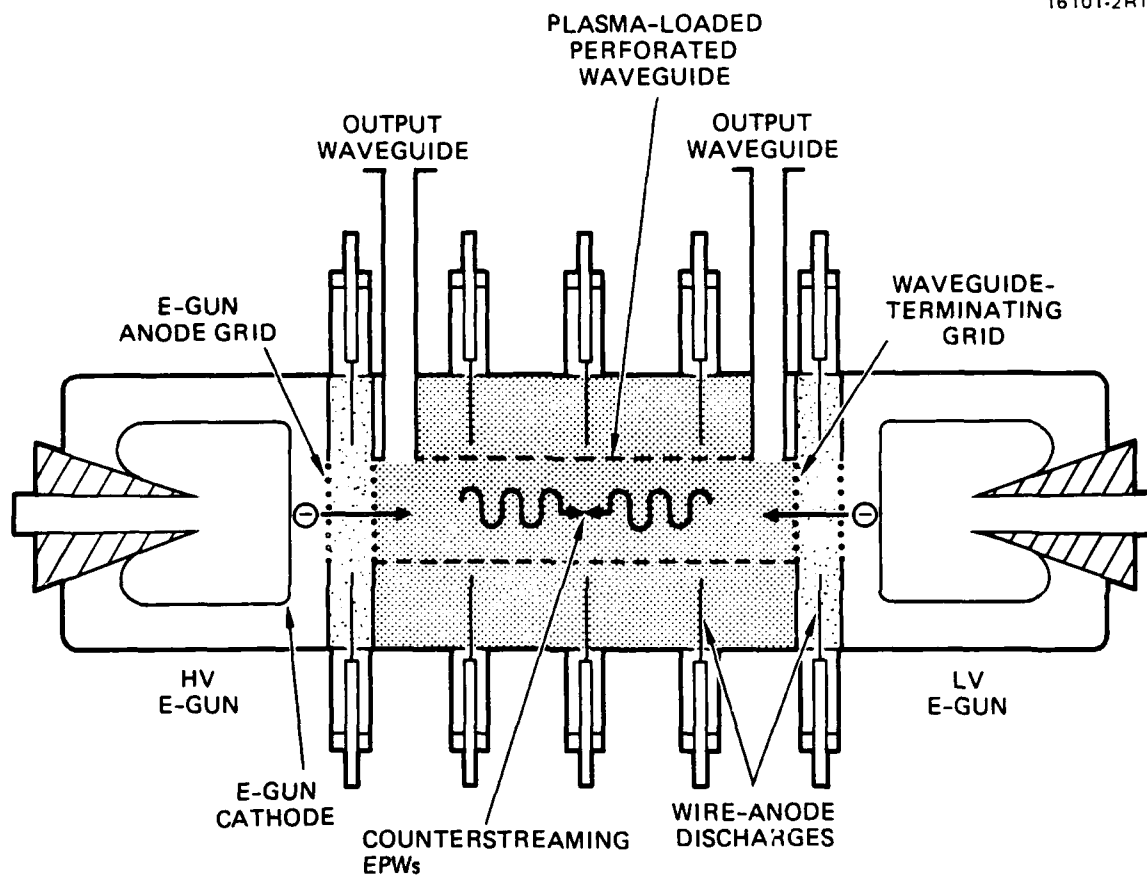


Figure 3. Experimental beam-plasma apparatus.

forming a high-energy beam. The beam then passes through the anode grid and the waveguide-terminating grid and is injected into the waveguide with low ($\sim 36\%$) loss to the grid structures. The beam then propagates through the plasma-filled waveguide where ion charge in the plasma neutralizes the electron space charge in the beam. This "ion-focusing" effect allows the beams to propagate without having to use magnetic-focusing fields.

The utility of the secondary-emission gun is based on the high secondary-emission yield γ_0 , which is obtained when high-energy ions strike gas-covered cathode-electrode materials. For example, γ_0 varies from 5 to 15 when helium ions in the 35- to 150-kV range strike a molybdenum cathode in the presence of 20 mTorr of helium gas.¹⁶

The electron-beam current is controlled at low voltage by modulating the (≤ 1 -kV) wire-anode discharge at the ground-potential environment of the anode electrode. Because the plasma is confined within the gridded-anode structure (plasma electrons are unable to overcome the ~ 1 -kV discharge-cathode drop to penetrate the gridded structure for ion current densities up to some limit), plasma closure of the high-voltage gap cannot occur and long-pulse ($\gg 1 \mu\text{s}$) operation is achieved. Modulation of the plasma source modulates the ion flux incident upon the cathode, which in turn controls the beam current. A mono-energetic beam is obtained throughout the beam pulse because the electron-beam is switched ON and OFF by the plasma source and not by the high-voltage supply for the cathode. Low-energy electrons produced from the rise and fall of the cathode voltage in conventional pulsed beams are not present. All this is accomplished without heater power and without high-vacuum-environment requirements, because the metallic cathode used in the secondary-emission gun cannot be poisoned.

The experiment is typically operated with 10- to 25- μs -wide flat-top pulses at a pulse-repetition frequency of 1 Hz. Circuits used to generate the plasma-discharge and beam pulses

are shown in Figure 4. A 25- μ s pulse-forming network (PFN) is employed to drive current pulses up to 800 A in the main waveguide-plasma-discharge section. A higher-impedance 18- μ s PFN drives the wire-anode discharge in the low-voltage electron gun (LV E-gun). GL-7703 ignitrons are used as closing switches to discharge both PFNs. The wire-anode discharge in the high-voltage (HV) E-gun is modulated by a circuit consisting of a capacitor and a XTRON-3 CROSSATRON^R Modulator Switch (CMS).^{17,18} The Hughes CMS is an advanced thyatron-like device that both closes and opens under grid control, so square-wave pulses can be obtained in hard-tube-modulator fashion without having to use a fixed-pulse-length PFN. The E-gun wire-anode current pulses are typically 10 to 100 A. Finally, capacitors are used to continuously maintain high voltage on the E-gun cathodes through 1-k Ω current-limiting resistors. The HV E-gun is designed to operate up to 120 kV, and the LV E-gun up to 50 kV.

Each of the five circuits shown in Figure 4 is instrumented with high-voltage probes and Pearson current transformers (CT). These diagnostics, as well as the Langmuir probes, are interfaced to an 11-channel IBM-PC/AT-based data-acquisition system and oscilloscope array, which are housed within an RFI-screen room. The output waveguides are also fed into the screen room where the radiation is analyzed by a network of millimeter-wave detectors, filters, attenuators, and mixers. Figure 5 is a schematic drawing of the millimeter-wave detection system. Cold tests of the cylindrical waveguide cavity show that about 1% of the Ka-band radiation generated within the waveguide is coupled into the output X-band waveguides. The bandwidth of the storage oscilloscopes is 100 MHz and the maximum sampling rate of the analog-to-digital converters in the computer is 1 Gigasample/second.

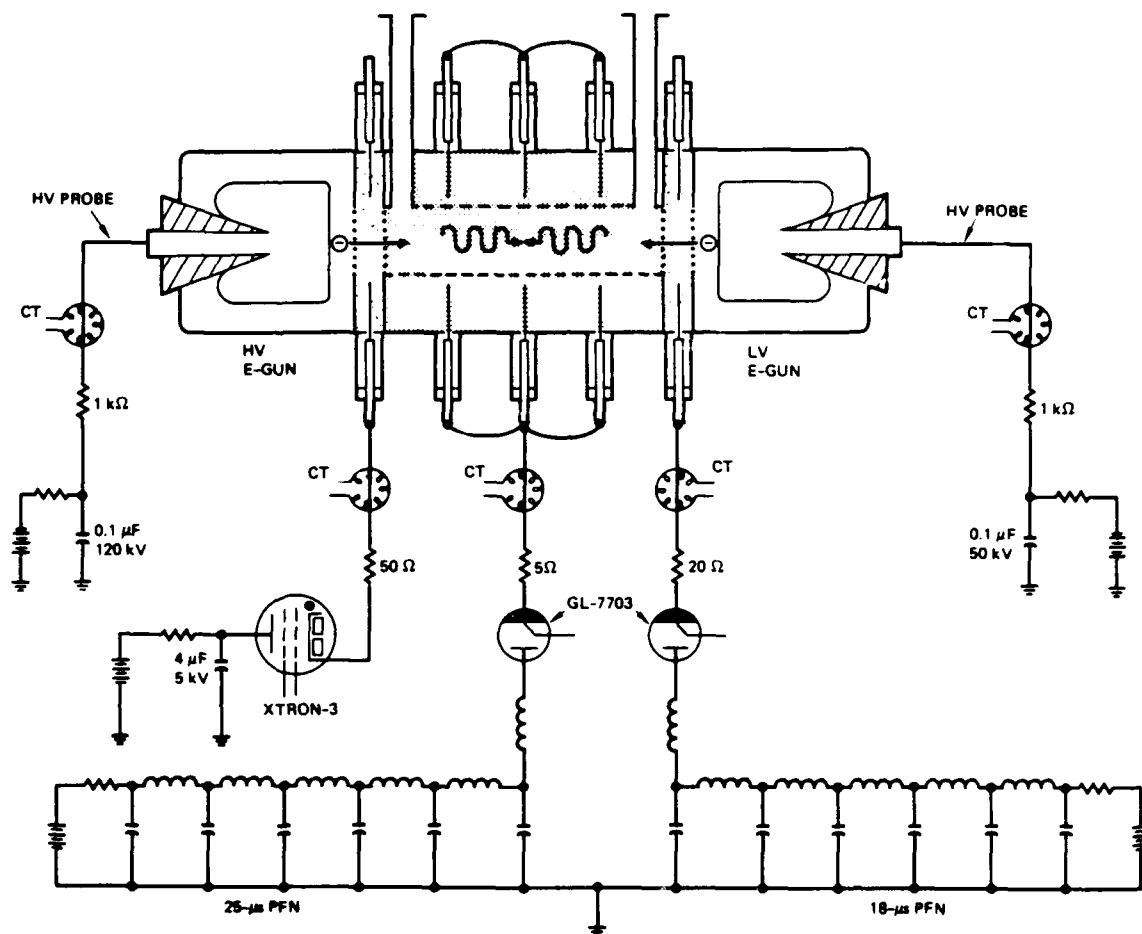


Figure 4. Schematic of plasma-discharge and electron-beam pulsed-power circuits.

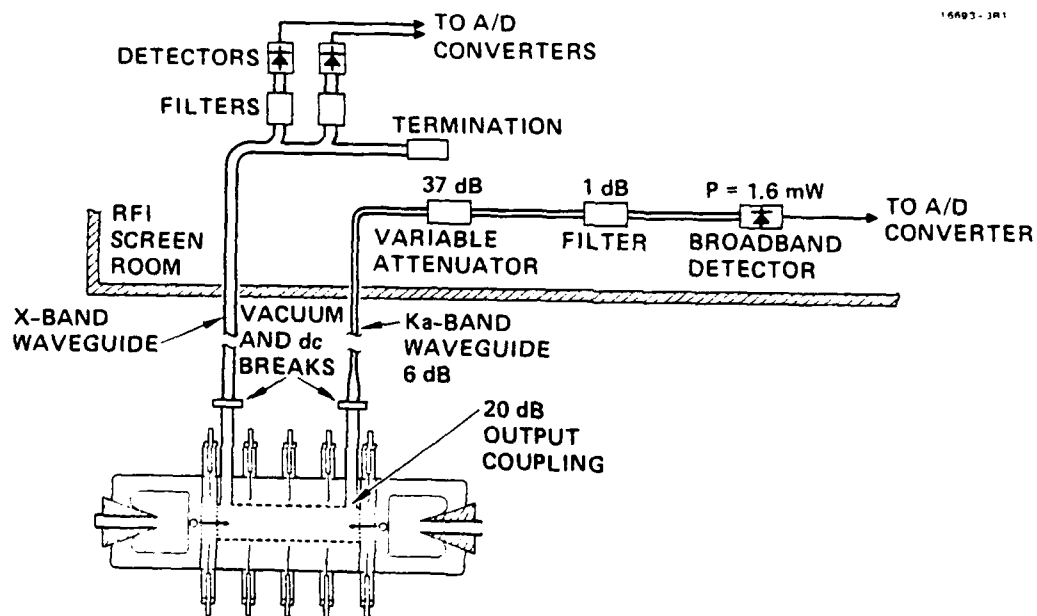


Figure 5. Millimeter-wave diagnostics and power measurement system.

SECTION 3

RESEARCH ACCOMPLISHMENTS

In the following section we review our significant technical accomplishments in understanding and demonstrating the basic physics of millimeter-wave generation via plasma three-wave mixing. We begin our review with a description of the preliminary beam-plasma experiments and our hardware optimization. We continue with electron-beam dynamics, and radiation scaling results using low (≤ 7 A) total beam currents and both high and low background-gas pressure. At 7 A of total beam current in a helium plasma, we measured peak power levels of 8 kW at 31 GHz. This corresponds to a peak beam-to-radiation conversion efficiency of 4%, and a conversion efficiency of about 0.4% when averaged over the amplitude-modulated radiation envelope. We then describe experiments investigating radiation modulation dependence on beam and waveguide plasma parameters, and observations of cavity modes in a short 1.9-cm-long waveguide cavity. We also describe attempts to increase the beam current to drive three-wave mixing to saturation, culminating in the adaptation of Hollow-Cathode-Plasma (HCP) E-guns to the three-wave-mixing experiment. Using the high current HCP E-guns we recorded detailed radiation spectra and we separately identified the ω_p and $2\omega_p$ radiation components. We also found that a single beam will drive the three-wave mixing process provided the beam current exceeds a threshold value of 9.2 A. Finally, we describe Orbitron experiments performed at HRL and at the University of Tennessee. In these experiments we found that Orbitron emission is actually generated by plasma three-wave mixing.

3.1 PRELIMINARY BEAM-PLASMA EXPERIMENTS

We constructed a preliminary beam-plasma-interaction system to test our initial ideas on a configuration that would allow us

to inject high-power, well-collimated E-beams into a uniform, plasma-loaded waveguide over broad ranges of plasma densities, beam currents, and beam voltages. As discussed below, the initial experiments revealed a number of hardware shortcomings, including over-focused E-beams, generation of background radiation from the plasma discharge, and an excessively long waveguide. The E-guns were modified to obtain collimated beams; the plasma-loaded waveguide was shortened; and the background radiation was eliminated by using larger-diameter anode wires which significantly reduced the discharge voltage and thus the free energy available to drive the background modes. We used the optimized experimental configuration to measure the scaling of millimeter-wave frequency and power with beam and plasma parameters.

The beam-plasma system was initially configured (as shown in Figure 6) with 46-cm-long waveguide and curved-cathode E-guns. This particular Pierce-shaped¹⁹ E-gun design (which does not require the beam to pass through an anode grid) is known as the Plasma-Anode E-Gun (PAG).²⁰ A photograph of the experiment is shown in Figure 7, with high-voltage cables leading to the E-guns on each end. Figure 8 is a photograph of the plasma-loaded-waveguide section with an array of twenty-four 10-kV bushings that feed the anode wires. Finally, Figure 9 is a photograph of the wire-anode discharge in the waveguide section. The 24 wires glow yellow-hot as a result of high-energy (~ 2.5 kV) discharge-electron collection.

Waveguide plasma densities up to $5 \times 10^{12} \text{ cm}^{-3}$ were generated using the 25- μs pulse-forming network (PFN) (shown in Figure 4), charged to ≤ 5 kV. An oscilloscope photograph of the discharge-current pulse is shown in Figure 10(a). The plasma is quiet (density fluctuations $\leq 5\%$) and relatively uniform over the 46-cm length of the waveguide [Figure 6(b)]. Plasma measurements were made with voltage-swept Langmuir probes. A sample Langmuir-probe trace is shown in Figure 11, which indicates a plasma

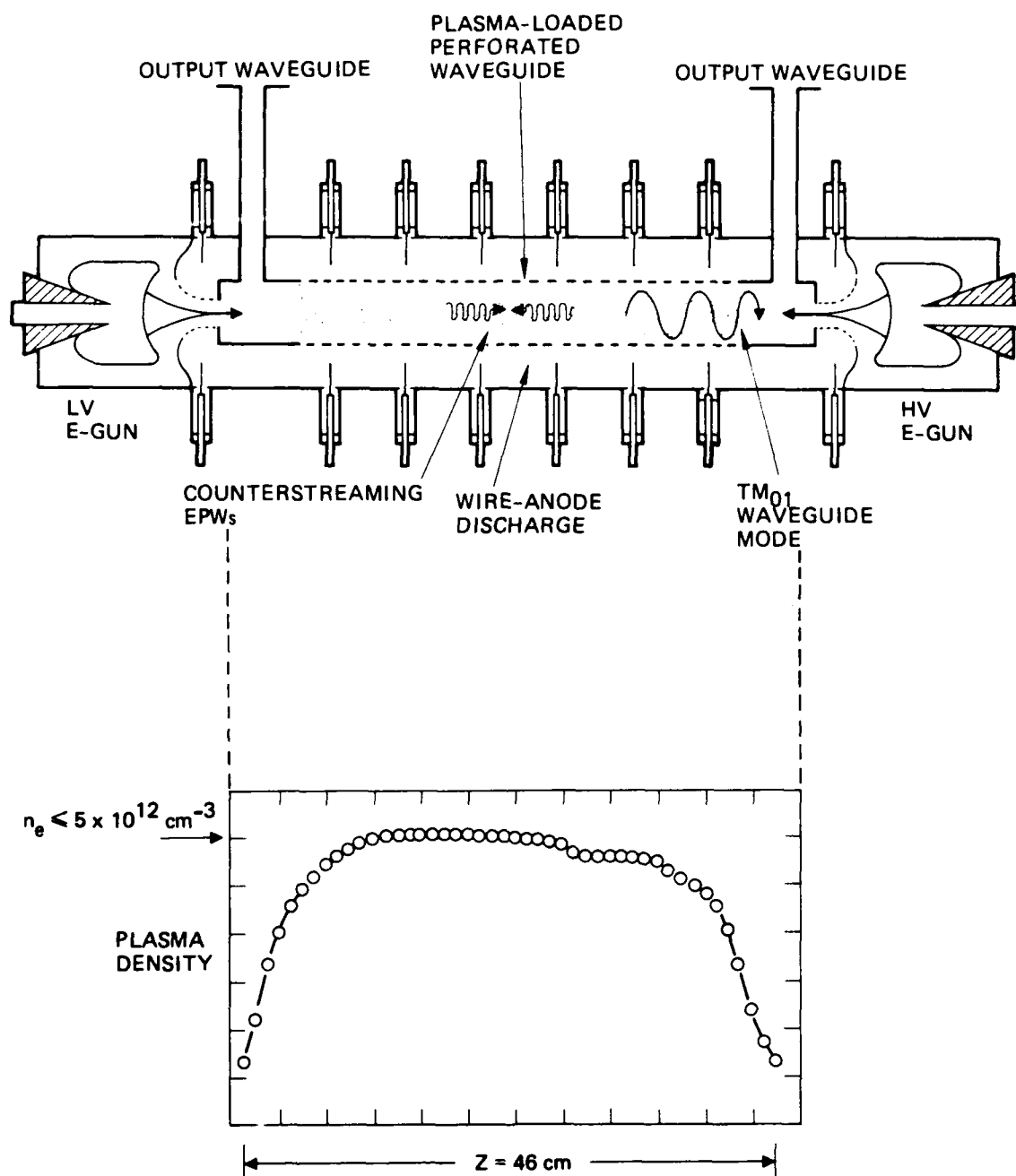


Figure 6. Preliminary experimental apparatus and axial plasma-density profile in waveguide.

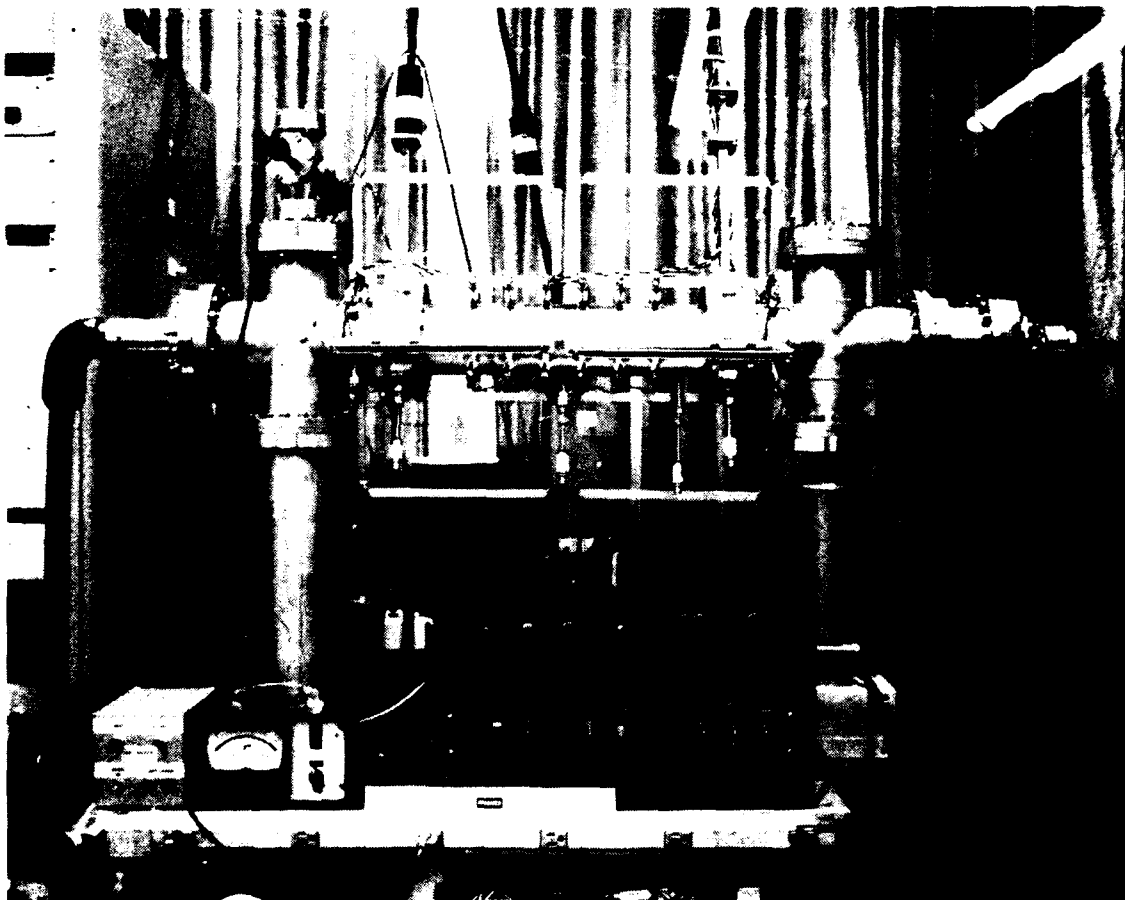


Figure 7. Plasma three-wave-mixing experiment with 46-cm-long cylindrical waveguide.

MC 16690

15612-2

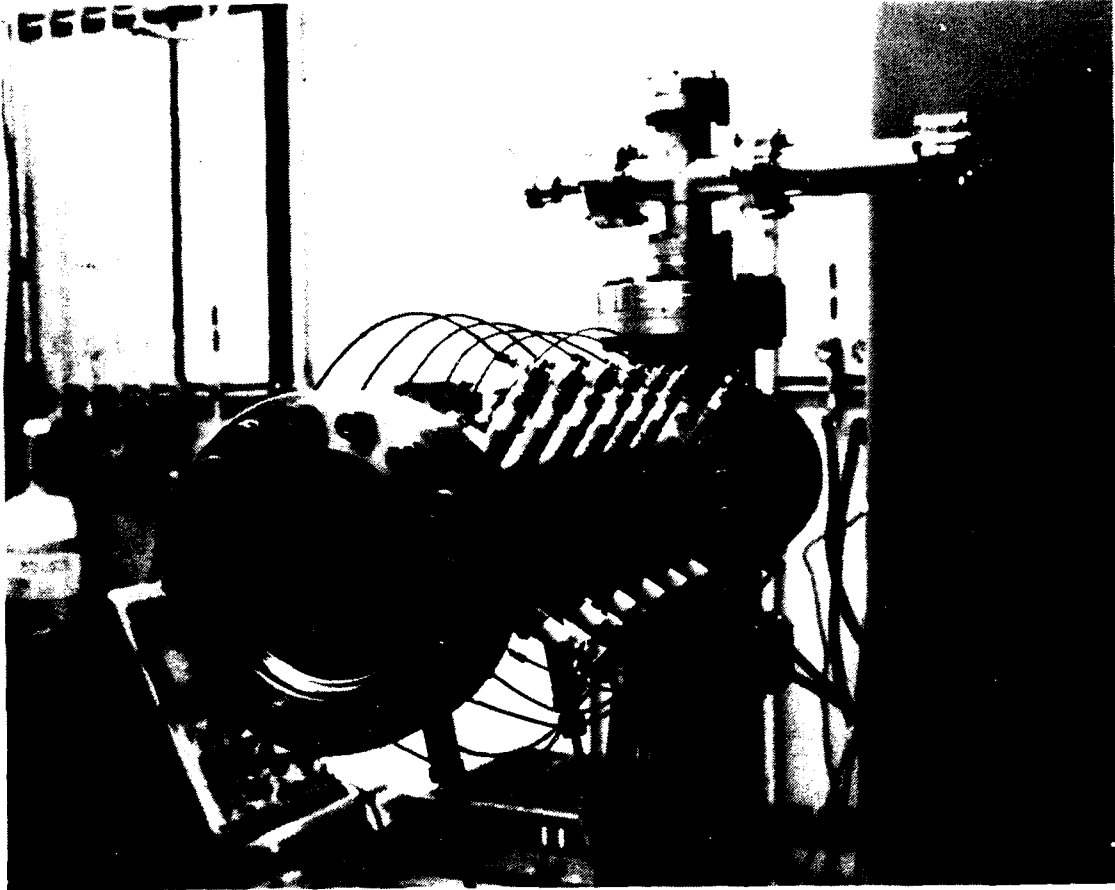


Figure 8. Plasma-loaded-waveguide section.



Figure 9. Photograph of the wire-anode plasma discharge.

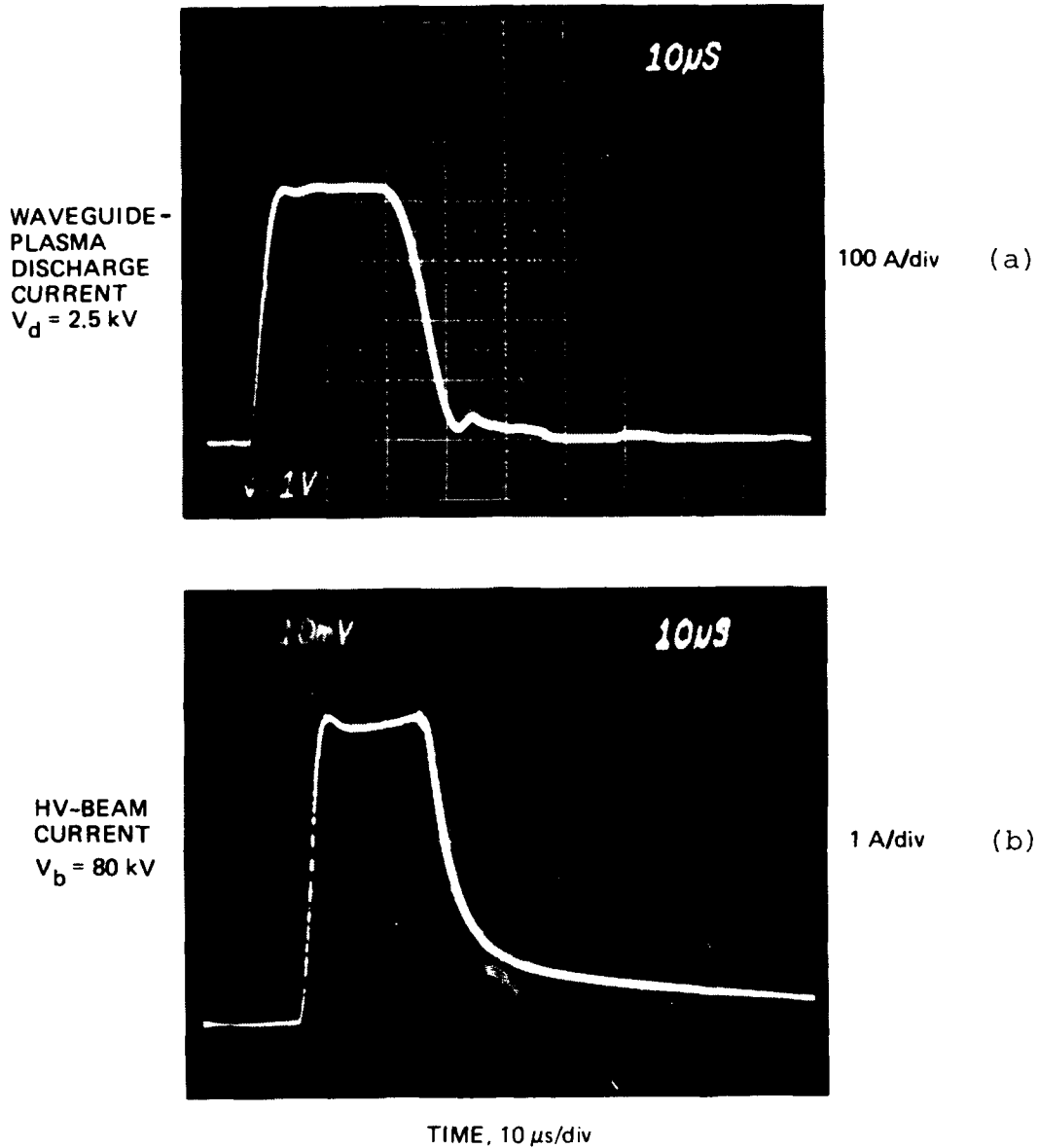
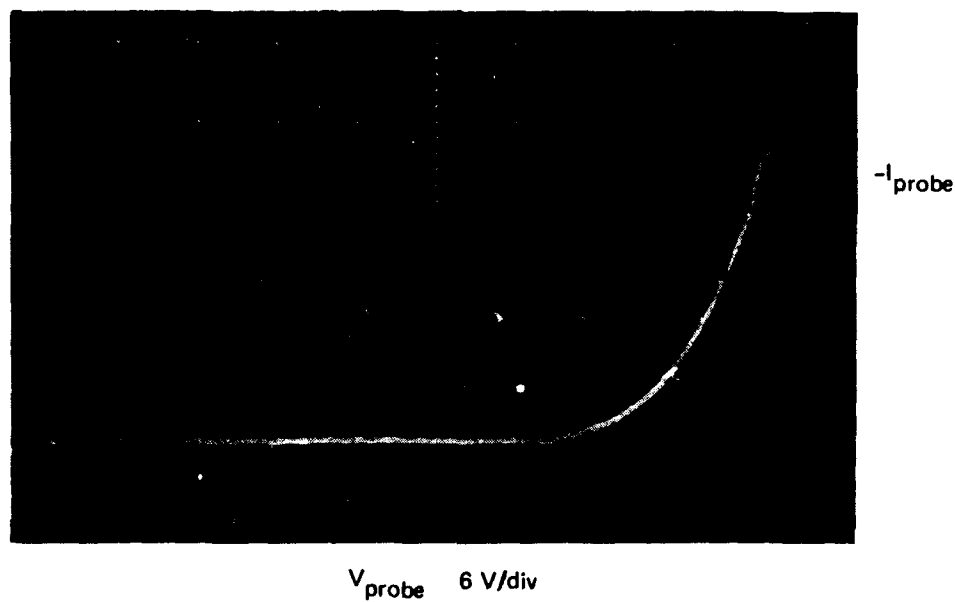


Figure 10. Plasma-discharge and E-beam waveforms. The waveguide-plasma discharge-current pulse is shown in (a) and the high-voltage beam-current pulse at 80-kV beam voltage is shown in (b).

15612-7



$$n_e \approx 1.2 \times 10^{12} \text{ cm}^{-3}$$

$$T_e \approx 5 \text{ eV}$$

$$V_p \approx 55 \text{ V}$$

Figure 11. Sample Langmuir-probe trace.

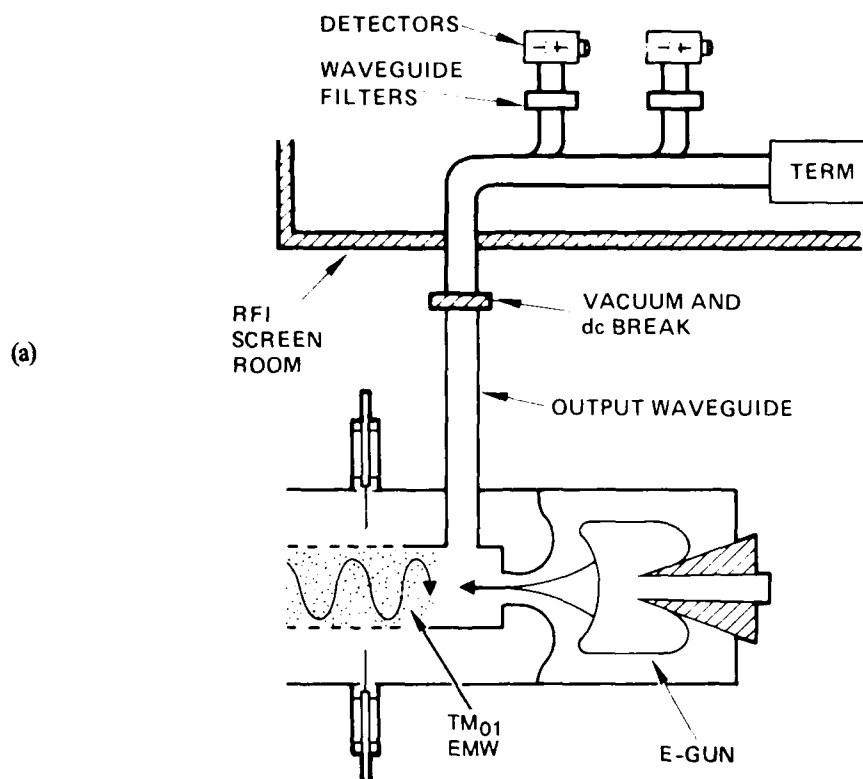
density of $1.2 \times 10^{12} \text{ cm}^{-3}$, an electron temperature of 5 eV, and a plasma potential (relative to the waveguide) of 55 V.

The radially directed wire-anode-discharge current inside the waveguide was also observed to drive low-power ($\leq 1 \text{ W}$) waveguide modes via three-wave mixing without the injection of axially directed beams. The diagnostic system for detecting this radiation is shown in Figure 12(a), and a sample output waveform of 35-GHz radiation is shown in Figure 12(b). We observed the coupling of this background millimeter-wave signal into the output rectangular waveguide at frequencies up to 40 GHz. Great care was taken (e.g., use of an RFI screen room, and employing a dc break in the waveguide to avoid ground-loop-current signals) to ensure that true electromagnetic signals were observed, rather than electrostatic or inductive noise from the plasma discharge and the pulsed-power circuits.

Two PAG guns were constructed and tested on the experiment. The higher-voltage gun was designed to operate at 120 kV, and it has demonstrated 6.5 A at 92 kV. The Hughes-patented CROSSATRON switch was employed to modulate the wire-anode section of the gun. This technique allowed the generation of 20- μs -long, square-wave pulses at 80 kV and 5 A, as shown in Figure 10(b). The beam-current pulse is delayed about 10 μs relative to the waveguide-plasma pulse. The low-voltage, PAG gun was operated at 35 kV and 3 A.

Preliminary tests of beam transport showed that both beams were over-focused and suffered from a large divergence angle ($\sim 10^\circ$) in the waveguide. Figure 13 plots the beam (and plasma-density) profile near the output-coupling section just downstream from the HV E-gun. At this axial position, the beam was already spread beyond the diameter of the E-gun output aperture. Figure 14 shows an x-ray film exposure taken at one end of the waveguide section when a 90-kV beam was injected into the opposite end. The exposure suggests that the beam had

mm-WAVE DIAGNOSTICS



OUTPUT WAVEFORM

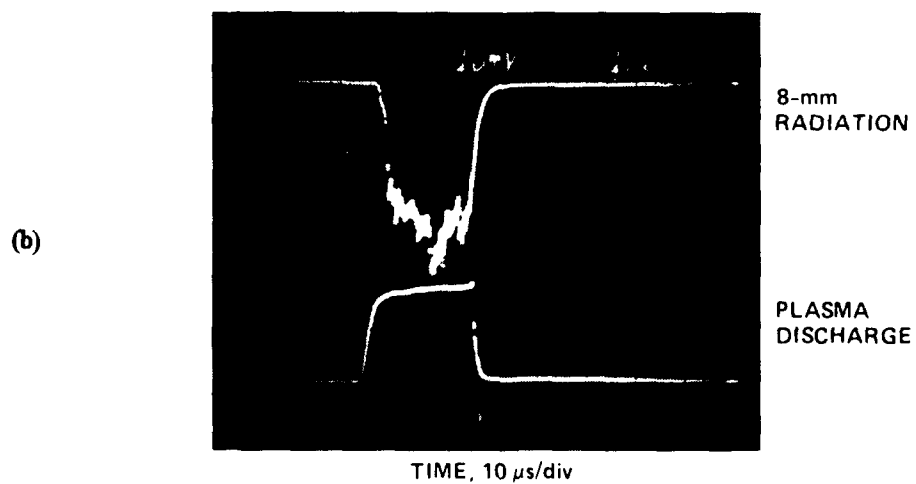


Figure 12. Millimeter-wave diagnostics. (a) Diagnostic circuit. (b) Sample output waveform at 35 GHz.

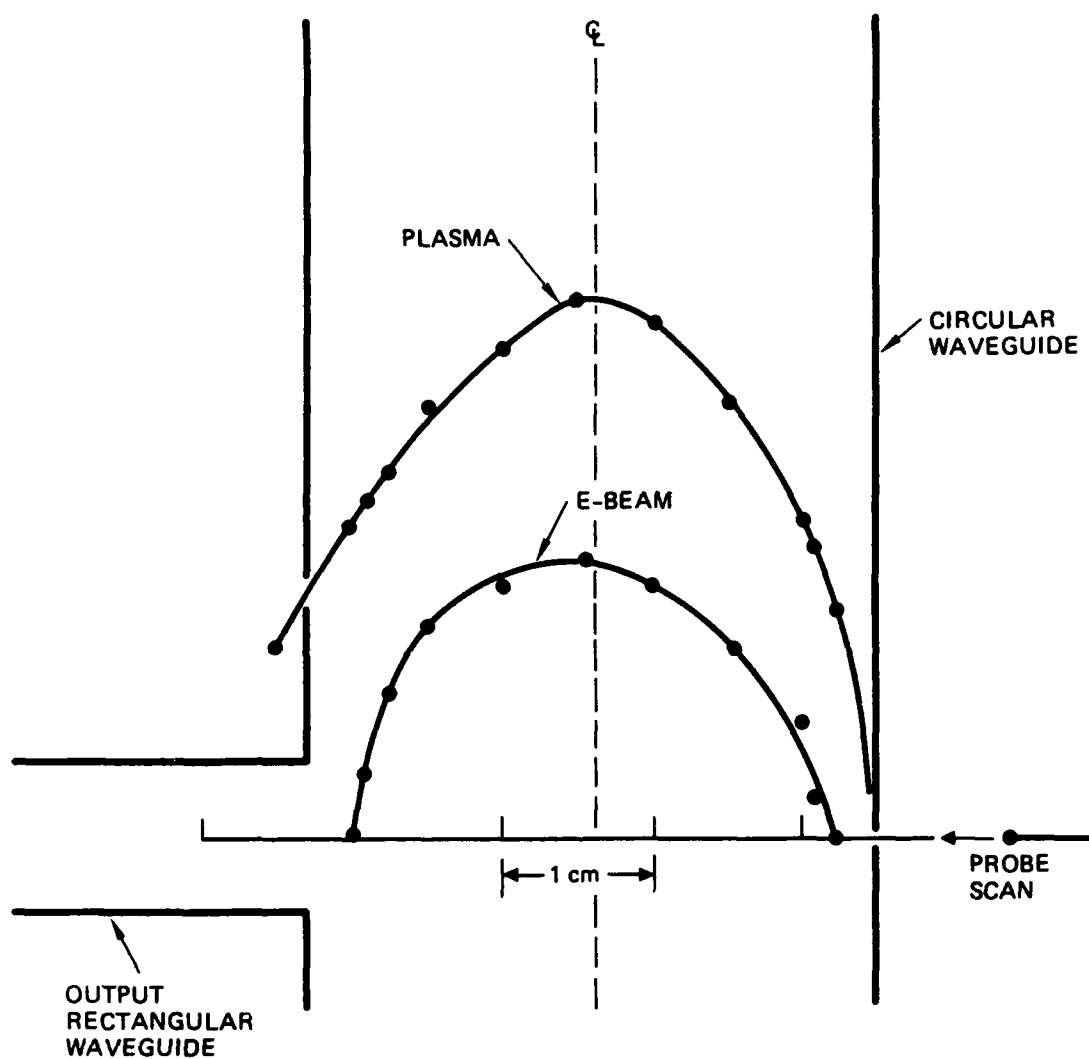


Figure 13. Electron-beam and plasma profiles measured across the diameter of the waveguide in the output-coupling section.

X-RAY FILM EXPOSURE

15612-8

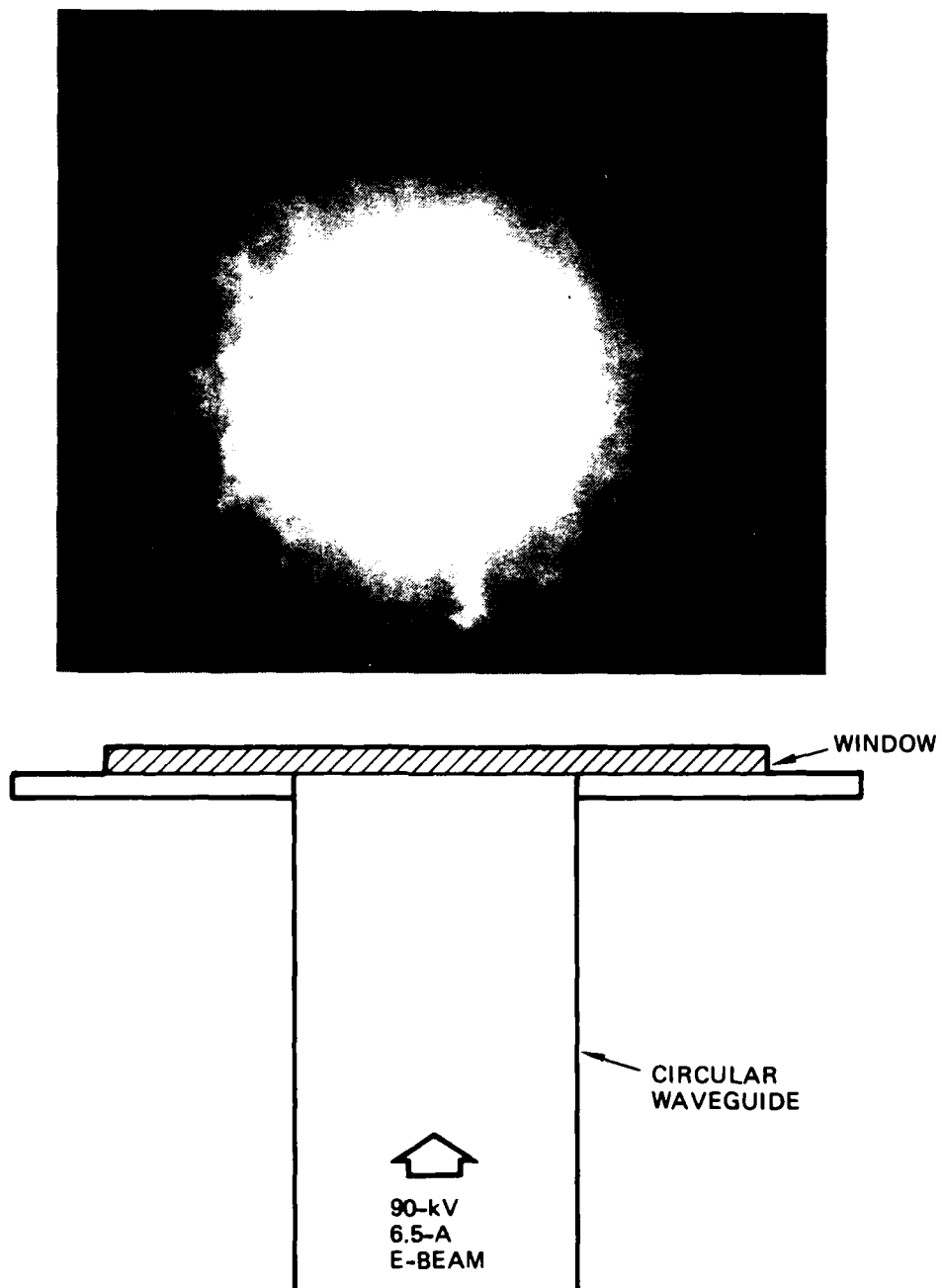


Figure 14. X-ray film exposure of 90-kV electron beam.

expanded to the full diameter of the waveguide, thus intercepting the wall of the guide. These observations indicated that the E-gun geometry had to be modified to avoid this over-focused condition.

Despite the large E-beam divergence angle, we were able to observe an enhancement of the background radiation when the beams were injected by shortening the length of the waveguide to allow the beams to overlap before they were intercepted by the waveguide wall. As shown in the sequence of oscilloscope waveforms in Figure 15, the background radiation was enhanced by more than 10 dB at 20 GHz only when the beams were injected simultaneously. A similar enhancement at 35 GHz is demonstrated in Figure 16.

3.2 HARDWARE OPTIMIZATION

After analyzing the results from our preliminary experiments, we modified the beam-plasma-waveguide system. The aims of the hardware optimization were (1) to shorten the length of the central target-plasma region to optimize the interaction between the EPWs generated by each beam; (2) to reduce the background radiation produced by the discharge electrons during the generation of the target plasma; and (3) to reduce the E-beam radial divergence as the beam propagates through the target plasma. The optimized configuration is shown schematically in Figure 3 and by a photograph in Figure 17. The target-plasma region is now 15.2 cm long, and is contained within a perforated, cylindrical waveguide with a diameter of 3.81 cm. The number of anode wires has been reduced from 24 to 12 and the wire diameter has been increased from 0.25 mm to 0.46 mm. This modification lowers the wire-anode discharge voltage from 2.5 kV to ≤ 1 kV and (as shown later) reduces the background radiation to below the threshold of our detectors. The electron-emitting surfaces on the E-guns are now flat rather

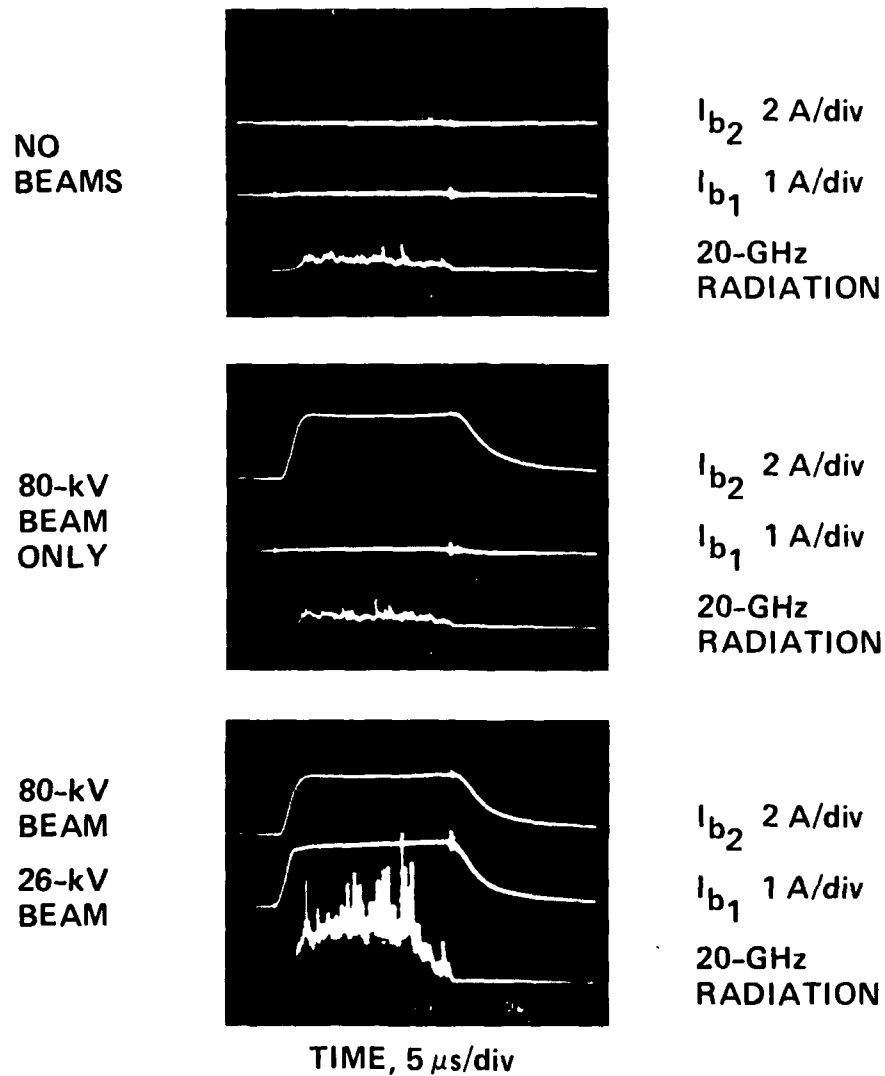


Figure 15. Background radiation at 20 GHz is enhanced by more than 10 dB only when both E-beams are injected into the plasma-loaded waveguide.

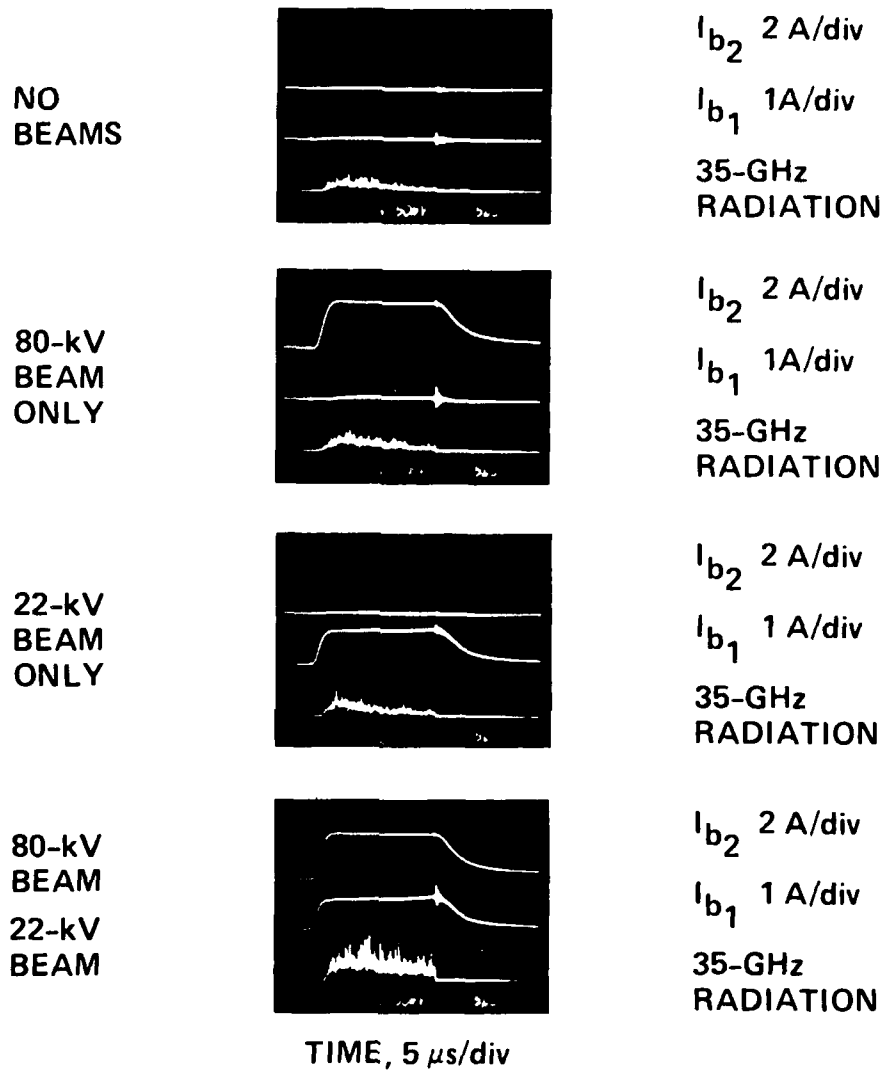


Figure 16. Background radiation at 35 GHz is enhanced by 5 dB only when both E-beams are injected into the plasma-loaded waveguide.

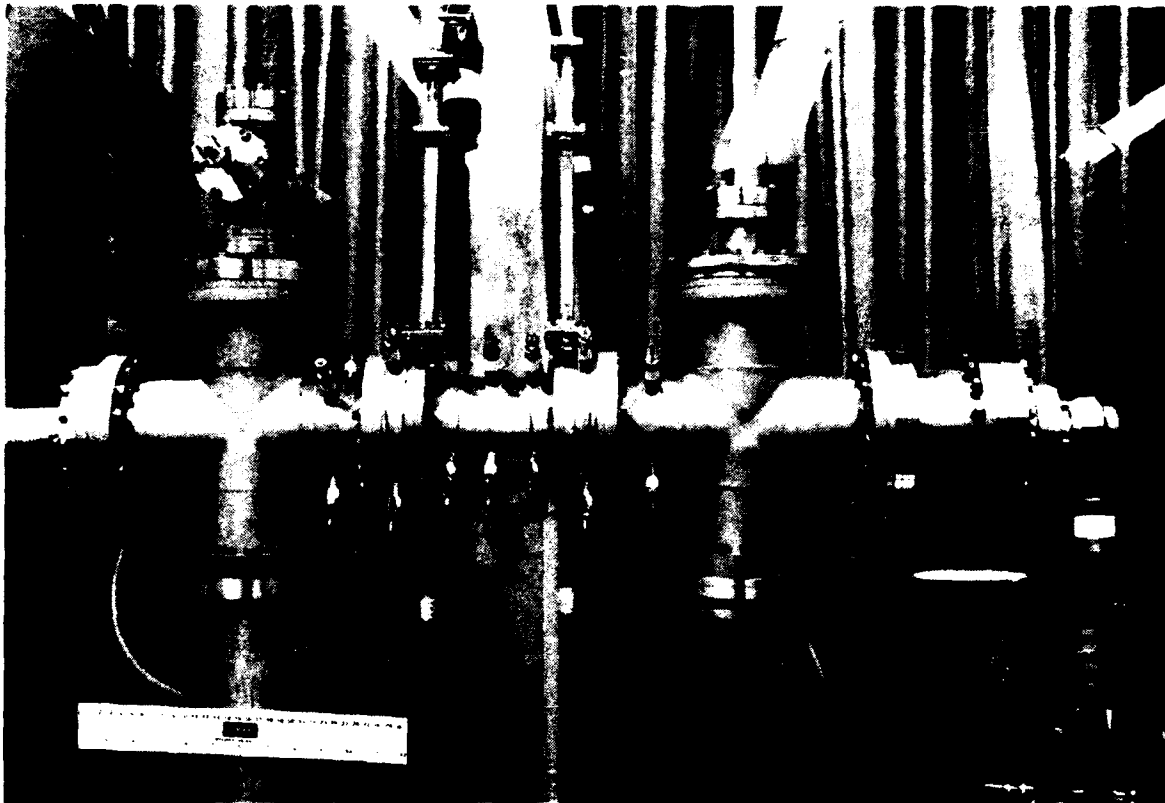


Figure 17. Photograph of the optimized three-wave-mixing experiment. The CROSSATRON Modulator Switch which is used to modulate one E-beam is shown in the lower right-hand corner.

than curved, and a planar E-gun geometry is now equipped with flat, beam-penetrating, high-transparency (80%) anode grids.

Langmuir probes are employed once again to determine the plasma parameters in the plasma-loaded waveguide. Two radial probes and one axial probe are used, as shown in Figure 18. Each probe consists of a 1-mm-diameter tantalum disk, which has a negligible perturbation effect on the discharge. The radial probes, which are attached to the experiment permanently, are also used to measure the E-beam profiles. One E-gun is removed and the axial probe is installed temporarily in order to measure the axial plasma profile. The observed profile is shown in Figure 19 under conditions where the center anode wires either are disconnected from the power supply or are driven through 47- Ω resistors. When the center wires are allowed to collect discharge current, the profile is more strongly peaked near the midplane. When the center wires are disconnected so that all the current is collected by the eight end-wires, the profile is significantly more uniform. Plasma from each E-gun wire-anode discharge also contributes to profile uniformity near the ends of the waveguide.

3.3 BEAM DYNAMICS

The radial plasma-density and E-beam profiles measured in the output-coupling sections are shown in Figure 20. The plasma profile is nearly identical to that which was measured in the preliminary experiments. However, the E-beam (50 kV, 5 A) profile now reveals a well-collimated beam that actually converges rather than diverges as the beam propagates through the plasma-loaded waveguide. At the beam-injection end of the waveguide (near the first output rectangular waveguide), the beam-current profile rises sharply on the edges and falls toward the axis. This profile is related to the ion density profile in the wire-anode-discharge section of the E-gun. The density is

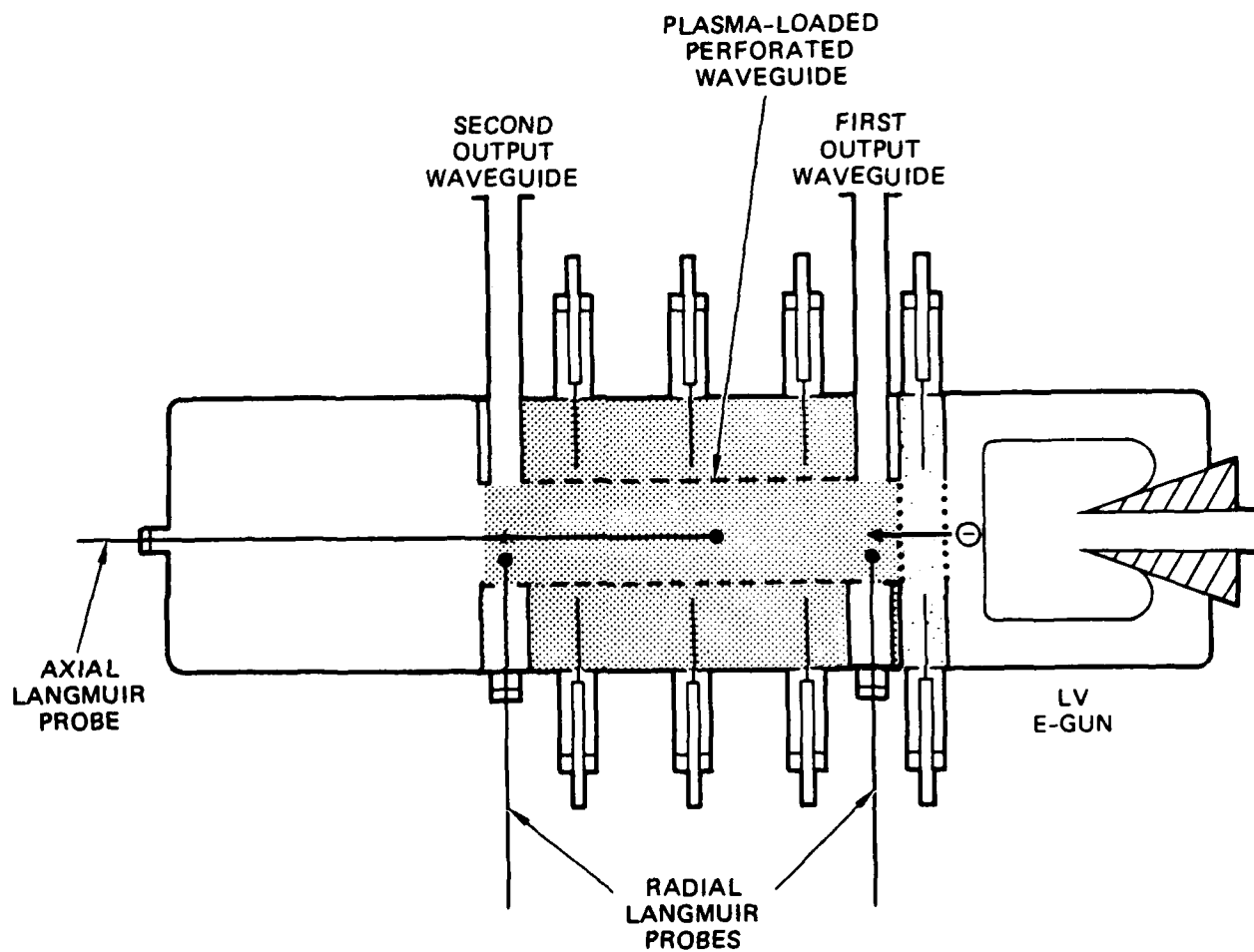


Figure 18. Langmuir-probe configuration.

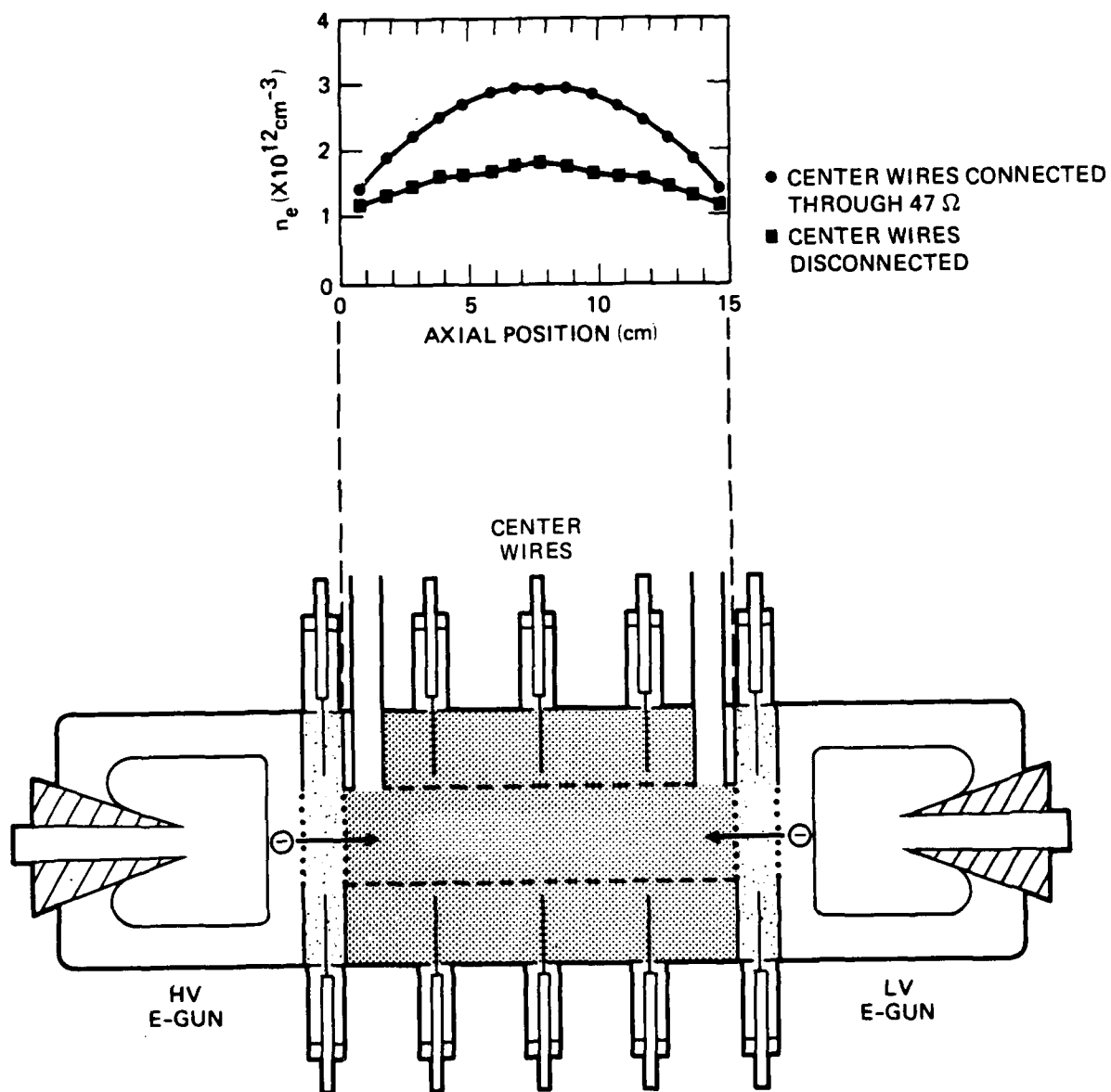


Figure 19. Axial plasma-density profiles.

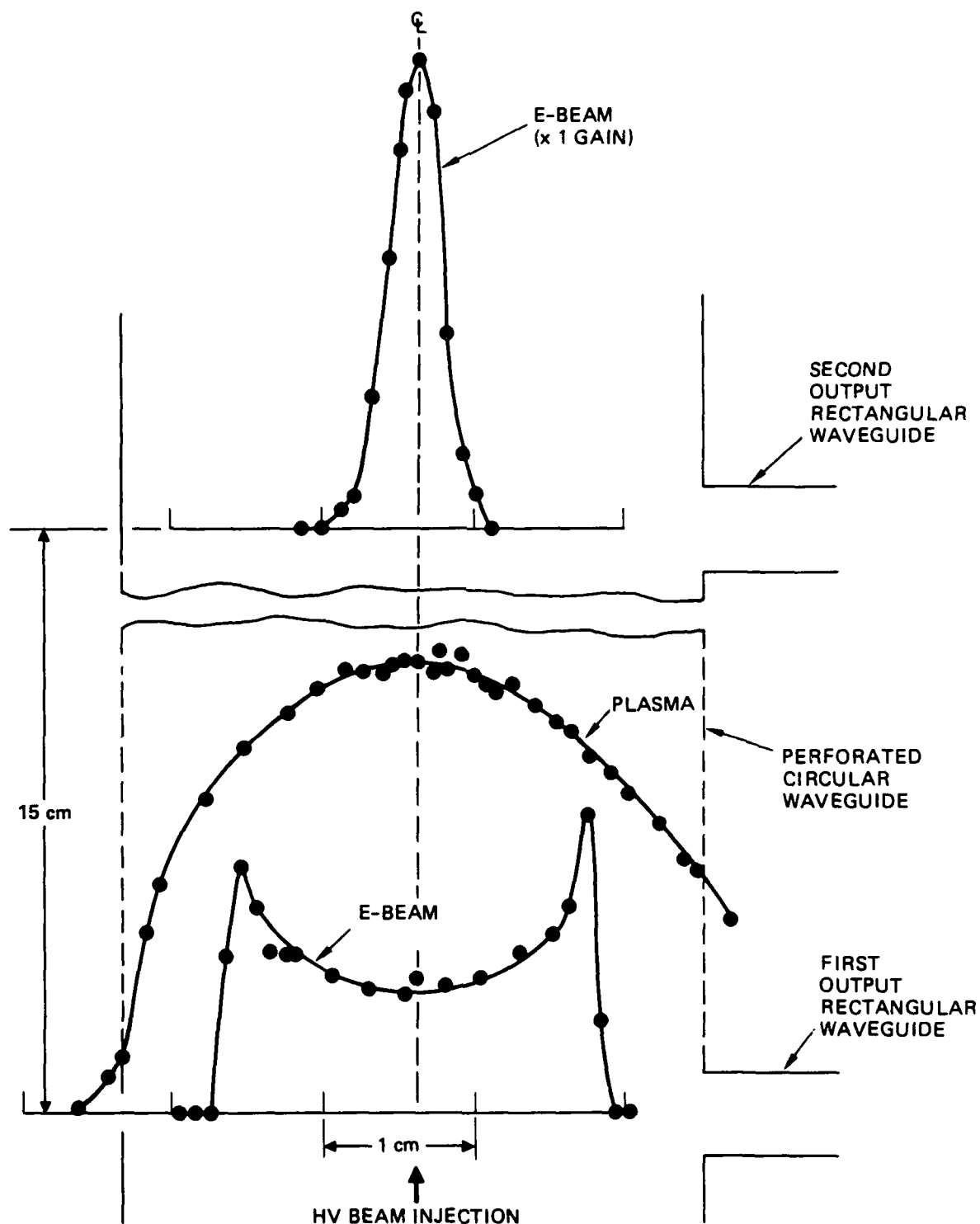


Figure 20. Radial plasma and electron-beam profiles measured across the diameter of the cylindrical waveguide at two axial positions which correspond to the output waveguide locations.

higher on the edge near the wires and lower near the axis. The 3.18-cm-diameter anode grid defines the beam diameter within the 3.81-cm-diameter waveguide.

At the opposite end of the waveguide (near the second output rectangular waveguide), as shown in Figure 20, the beam has actually converged after passing through the waveguide plasma. The full width at half maximum has decreased from 2.7 to 0.45 cm, and the beam current density on axis has increased by a factor of ~ 8 despite beam attenuation by the plasma.

This radial beam contraction is caused by the self-magnetic field of the electron beam. As shown in Figure 21, the beam generates a poloidal magnetic field, which can constrict the beam radius if the magnetic-field pressure exceeds the (transverse) beam thermal pressure. This process, which was suggested to us by Krall and Rosenberg, is known as the Bennett pinch effect.²¹ Quantitatively, the pinch condition may be expressed as:

$$\frac{B_p^2}{8\pi} \geq n_b T_b \quad , \quad (17)$$

where B_p is the poloidal magnetic field, and T_b is the perpendicular beam temperature. The threshold current at which the pinch occurs can be expressed as:

$$I_b^2 \geq 3.2 \times 10^{-10} n_b A_b T_b \quad , \quad (18)$$

where A_b is the cross-sectional beam area. Using a beam density of $3 \times 10^9 \text{ cm}^{-3}$ and $T_b = 10 \text{ eV}$ we predict a threshold current of 1.5 A, which is consistent with our measurements as discussed below.

The beam is predicted to evolve into the Bennett profile,

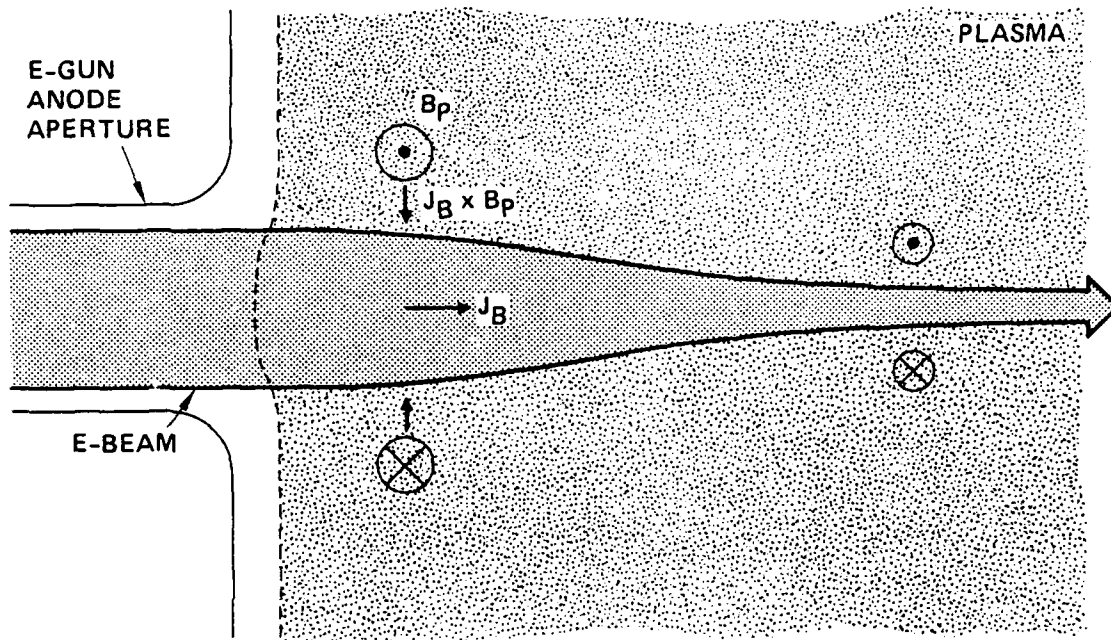


Figure 21. Bennett pinch.

$$I_b(r) = \frac{I_{b0}}{\left[1 + (r/a)^2\right]^2}, \quad (19)$$

where r is the radial position relative to the center of the beam, $a = (2\sqrt{2} \lambda_0/\beta) \times [T_b / (T_b - T_e)]^{1/2} \equiv$ Bennett radius, and $\beta = v/c$. A comparison of several measured radial beam profiles with the theoretically predicted Bennett profile is shown in Figures 22 and 23. In each case, we assume $T_b = 10$ eV. There is good agreement between experiment and Bennett-pinch theory. If the beam current is adjusted to a value which is slightly below the Bennett-pinch threshold, we observe a temporal collapse in the radial beam profile, as shown in Figure 24. In this case, the initially broad, inverted profile evolves toward the pinched-beam condition over a period of 15 μ s.

3.4 SCALING EXPERIMENTS WITH LOW BEAM CURRENT

Three-wave-mixing scaling experiments were performed using the optimized beam-plasma configuration. The relevant plasma and beam parameters are listed in Table 1. Millimeter-wave generation was unambiguously observed from counterstreaming beams, without the presence of background radiation from the discharge plasma. Employing the same detection techniques as those shown in Figure 5, we observed radiation at frequencies up to 60 GHz when the plasma discharge current was raised to 800 A. As shown in Figure 25, 60-GHz radiation is observed over a 13- μ s period within the envelope of the E-beam pulses, which overlap the plasma-discharge pulse. Note that no background radiation is observed from the plasma discharge before the beams are injected.

Figures 26, 27, and 28 demonstrate that a high-density discharge, as well as simultaneous injection of both beams, is required to generate the high-frequency millimeter-wave

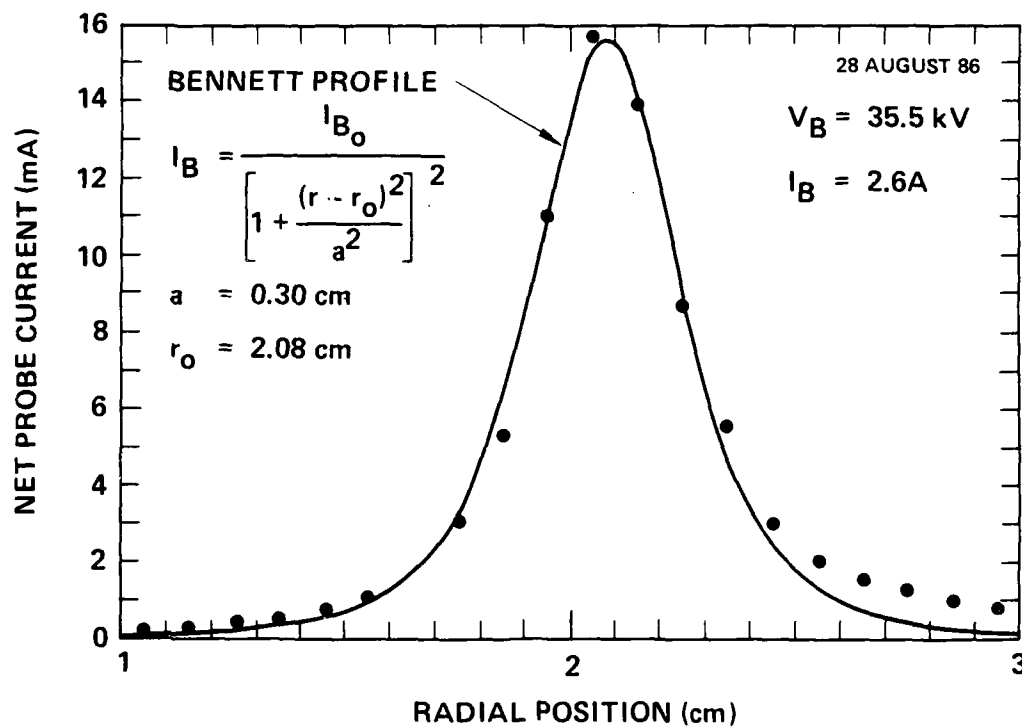


Figure 22. Radial beam profile at $z = 15 \text{ cm}$ and $n_e = 2 \times 10^{11} \text{ cm}^{-3}$.

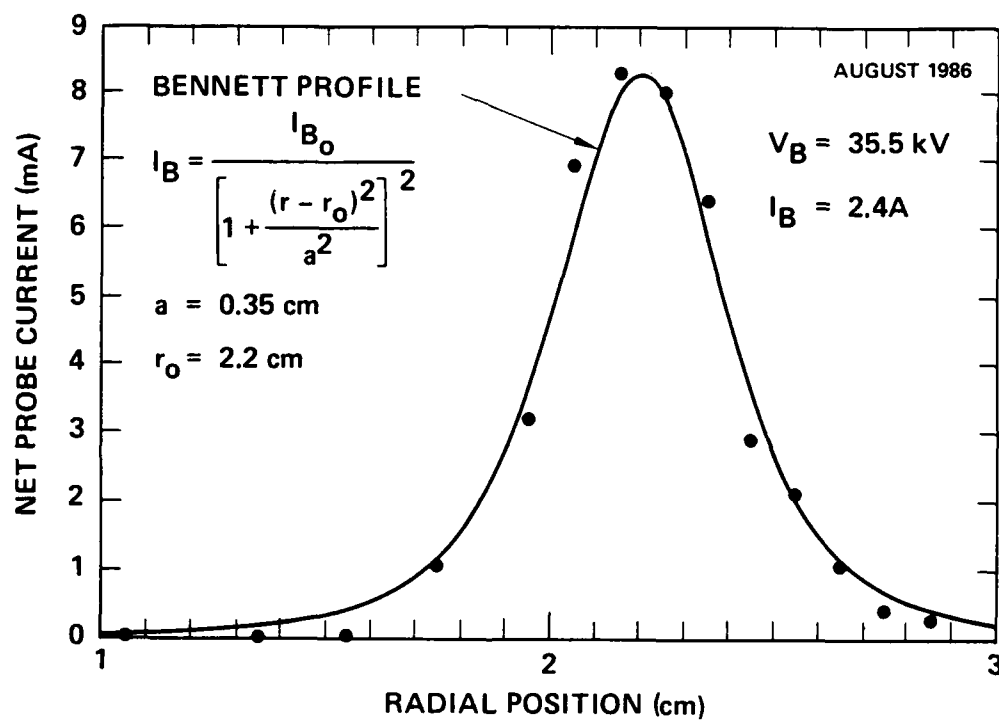


Figure 23. Radial beam profile at $z = 15 \text{ cm}$ and $n_e = 5 \times 10^{12} \text{ cm}^{-3}$.

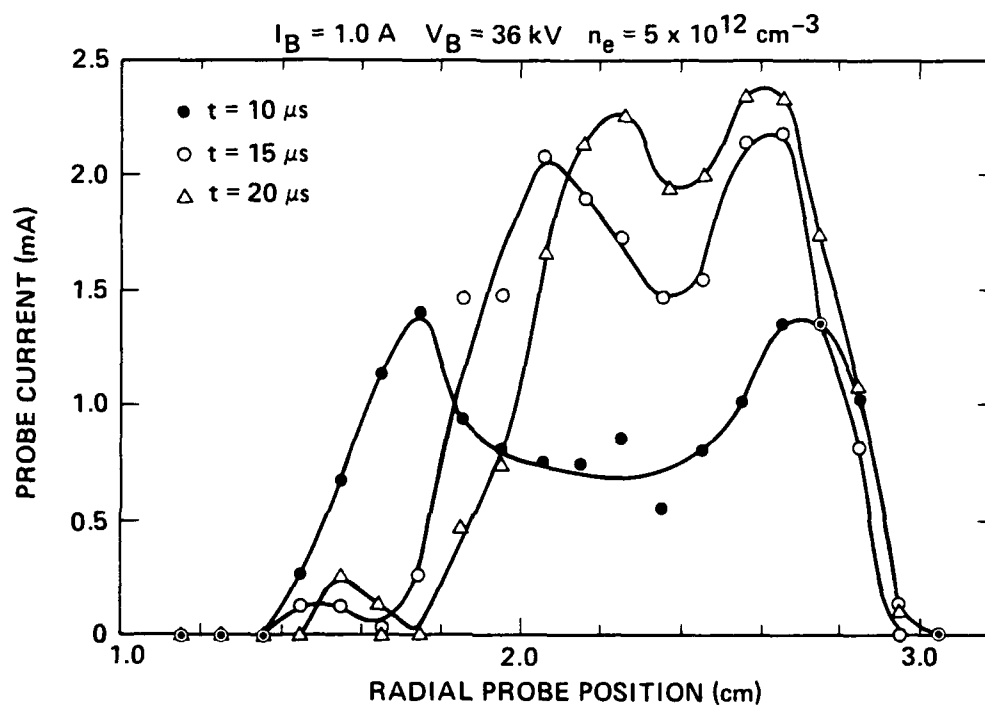


Figure 24. Temporal beam-profile evolution at low current.

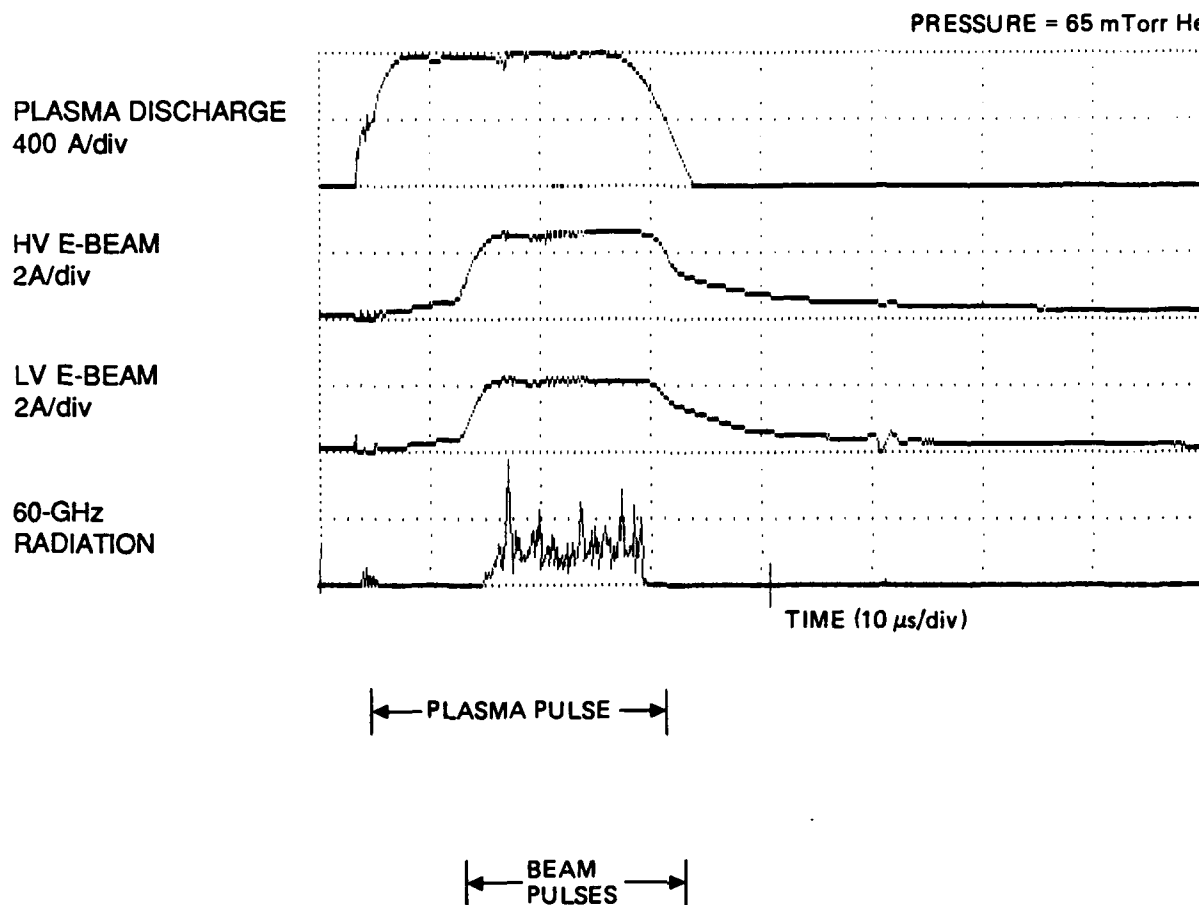


Figure 25. Radiation at 60 GHz is generated by the beam-plasma system when counterstreaming beams are injected into the plasma-loaded waveguide.

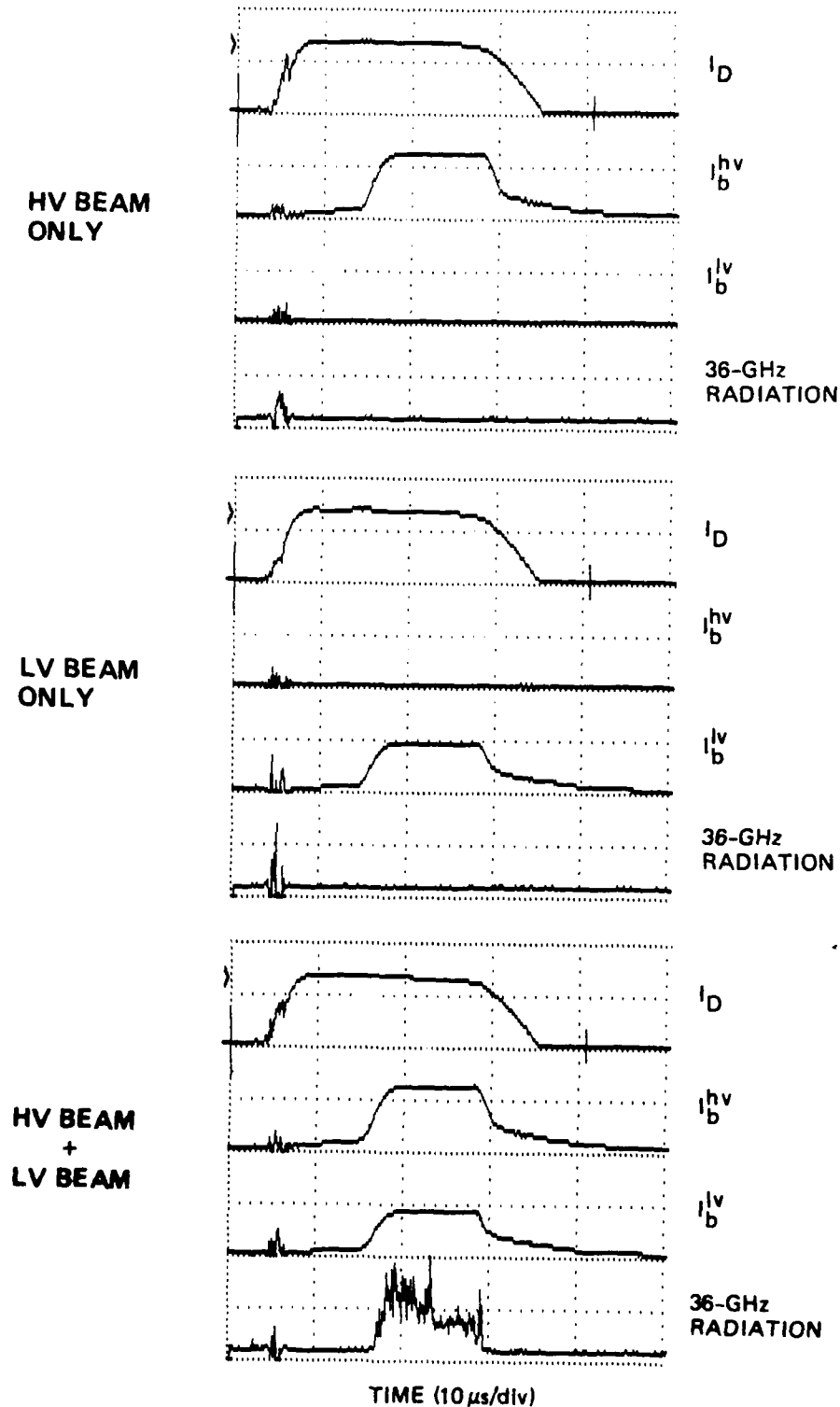


Figure 26. Simultaneous injection of both beams is required to generate mm-wave radiation. No radiation is observed when only one beam is used.

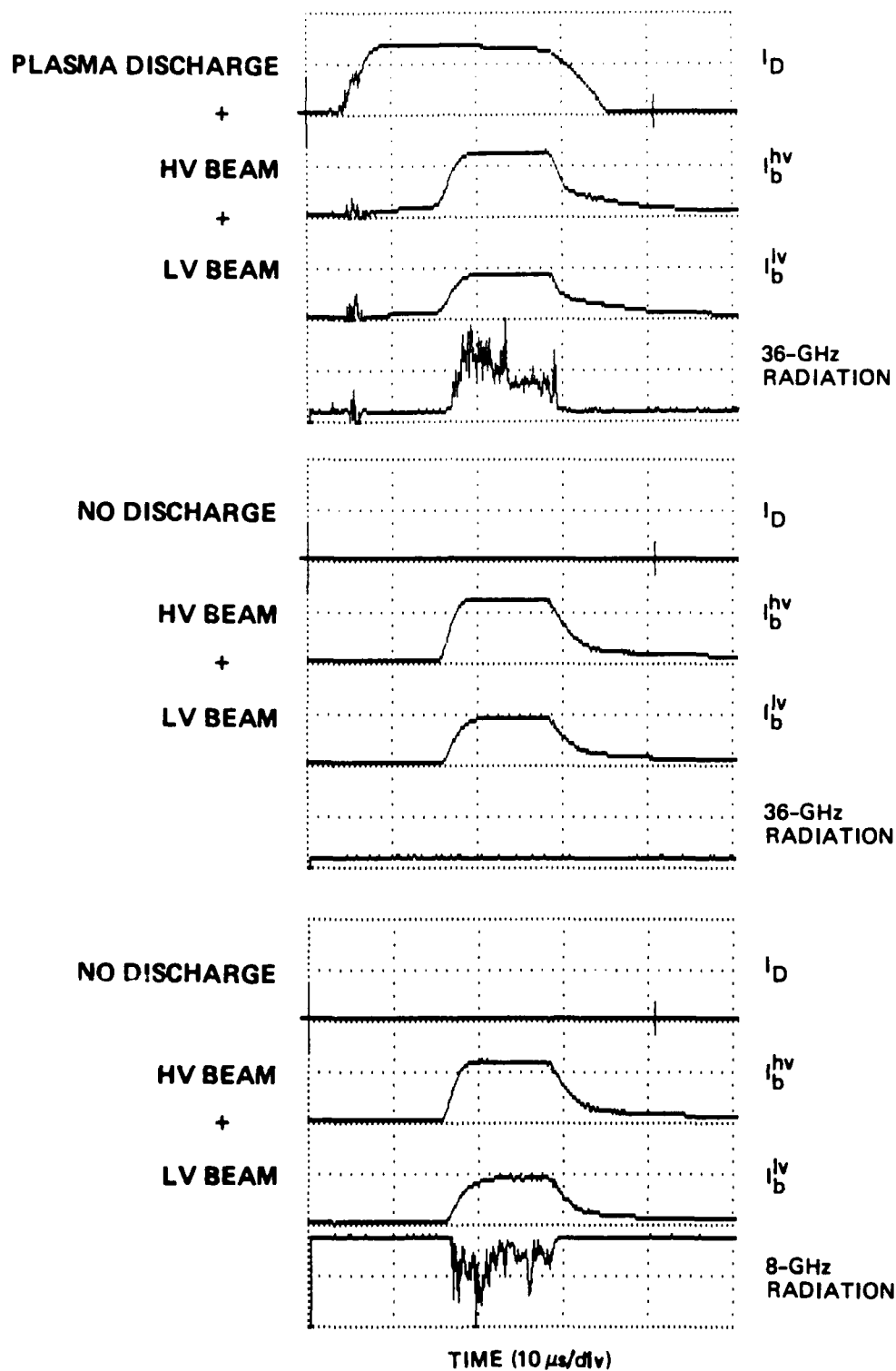


Figure 27. Output radiation shifts to low frequency when both beams are injected without the high-density waveguide discharge.

PRESSURE = 50 mTorr He

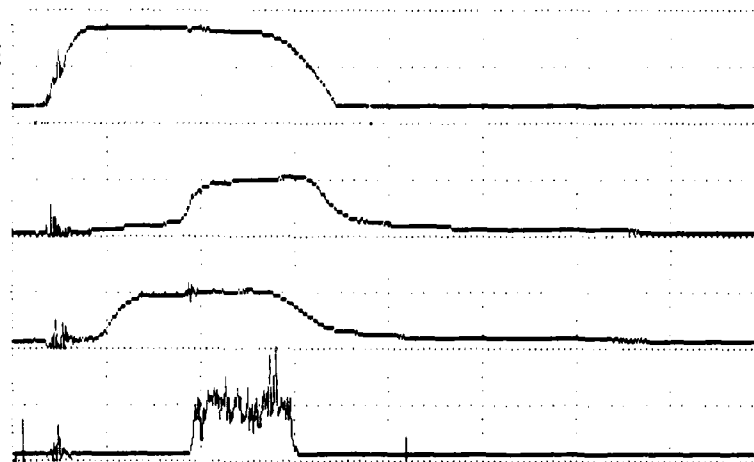
PLASMA DISCHARGE
400 A/divHV E-BEAM
2 A/divLV E-BEAM
2 A/div50-GHz
RADIATIONTIME (10 μ s/div)

Figure 28. Radiation at 50 GHz is observed only when the two beam pulses overlap in time.

radiation. In Figure 26, it is demonstrated that no radiation is observed when only one of the two beams is injected into the plasma. In Figure 27, we observe that 36-GHz radiation disappears when both beams are injected without the high-density waveguide discharge. However, even in the absence of a waveguide discharge, low-density ($2 \times 10^{11} \text{ cm}^{-3}$) plasma from the E-gun wire-anode discharges and the beams partially fills the waveguide. As shown in the lower pulse sequence in Figure 27, radiation is observed at $\sim 8 \text{ GHz}$, which is associated with twice the low-density plasma frequency. Finally, the requirement of simultaneous beam injection is dramatically demonstrated (in Figure 28) by delaying the injection of one beam relative to the other. Radiation at 50 GHz is observed in this case only when the beams overlap in time.

3.4.1 Frequency Scaling

Scaling of the millimeter-wave frequency with waveguide discharge current and plasma density was measured by varying the discharge current from 15 to 800 A and observing the output radiation with an array of waveguide band-pass and high-pass filters. The output of the filters is plotted in Figure 29 as a function of the waveguide discharge current from 200 to 800 A. The data clearly indicate that the center frequency of the radiation increases as the discharge current is increased. By noting the current value at which millimeter-wave power is received in each filter, the scaling of frequency with discharge current can be determined. These data are plotted in Figure 30, which indicate that the frequency scales as $I_0^{0.86}$.

If the frequency scales as the plasma frequency of the waveguide plasma, however, one might expect that the exponent of I_0 would be 0.5 (consistent with a linear dependence of plasma density on discharge current and a square-root dependence of plasma frequency on density). This discrepancy owes to the fact

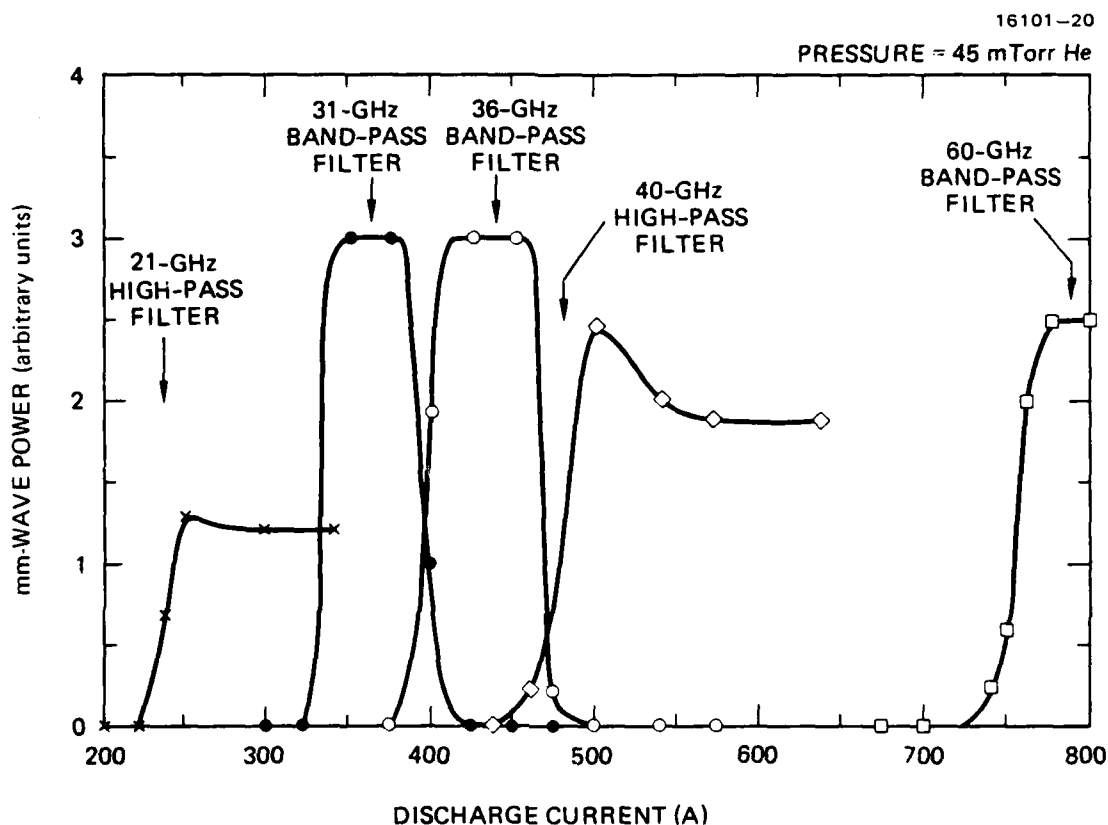


Figure 29. Frequency scaling with waveguide discharge current is determined by observing the mm-wave output with an array of waveguide high-pass and band-pass filters.

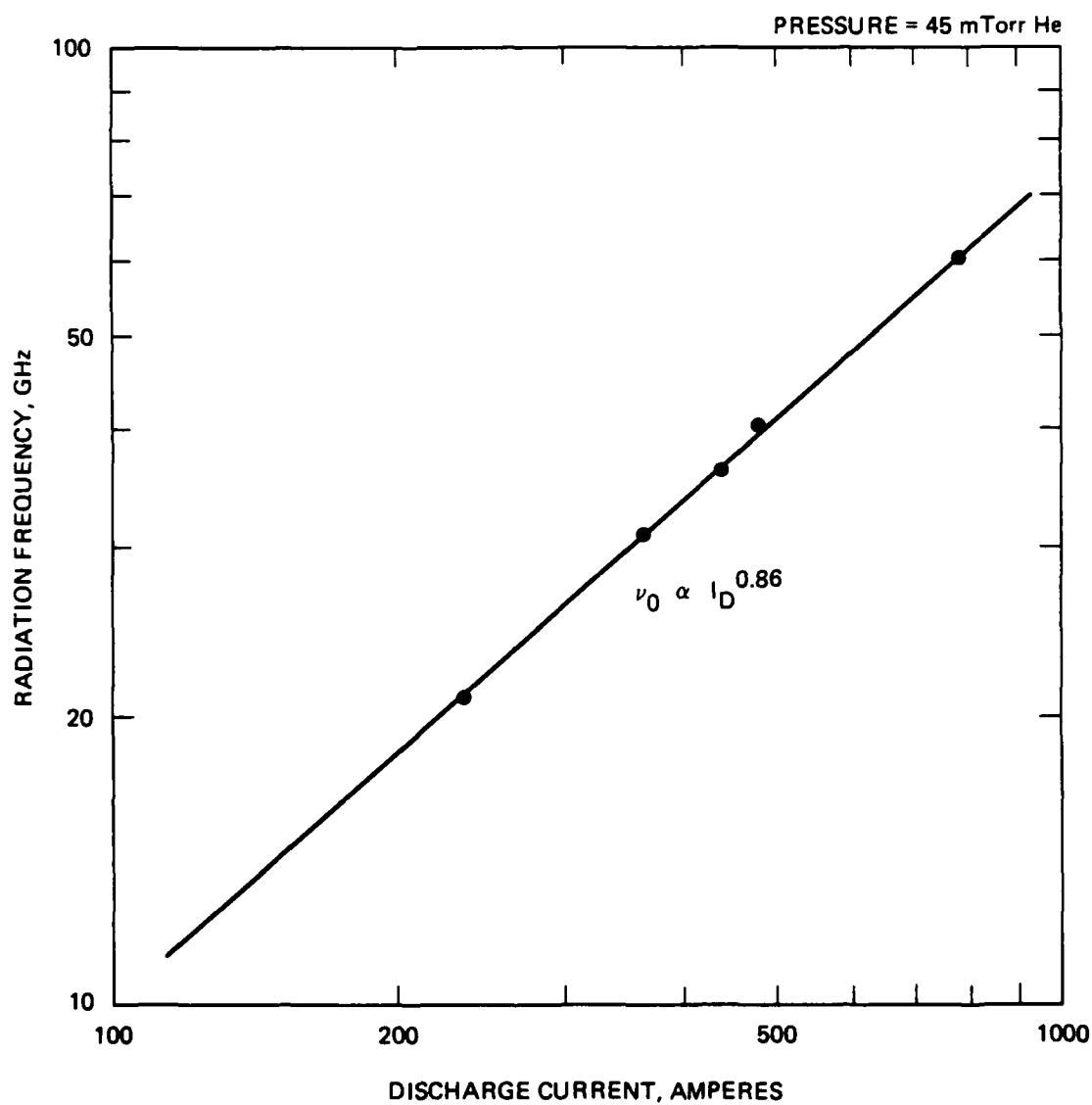


Figure 30. Frequency scaling with discharge current up to 60 GHz and 800 A.

that the plasma density does not scale linearly with discharge current. The density scaling was determined experimentally using the axial Langmuir probe, and the results are plotted in Figure 31. The data indicate that the rate of density increase with discharge current increases as the current rises above 100 A. This phenomenon occurs because, above 100 A, the cold-cathode discharge enters the so-called "abnormal-glow" regime²² where the discharge voltage increases with discharge current. Figure 32 shows this effect quite clearly. Below 100 A, the wire-anode discharge is constant at ~310 V. Above 100 A, the voltage increases to 1 kV. Therefore, as the current rises, the discharge power increases nonlinearly, and so the plasma density will increase nonlinearly as well.

Using the measured density scaling from Figure 31, the frequency scaling in Figure 30 can be renormalized to density, and the nonlinear behavior can be folded out of the data. This procedure is followed in Figure 33, but the observed millimeter-wave frequency is plotted versus the plasma frequency, which is easily calculated from the density using Eq. (4). Plotted in this manner, the data clearly show that the millimeter-wave frequency scales as twice the plasma frequency, as predicted by the three-wave-mixing theory.

We repeated the experiment at lower discharge current and slightly lower helium-gas pressure. In this regime we took great care to operate with reduced E-gun wire-anode current and beam current in order to minimize plasma production in the waveguide by the guns and beams. The raw-data scaling of frequency versus current, Figure 34, shows a better fit to the elementary $I_0^{0.5}$ scaling. Using the same procedure as that which was discussed earlier, the data were renormalized to plasma frequency and are plotted in Figure 35. As before, the output millimeter-wave frequency clearly scales as twice the plasma frequency.

To further investigate the scaling of the radiation frequency with discharge current, the experiment was repeated

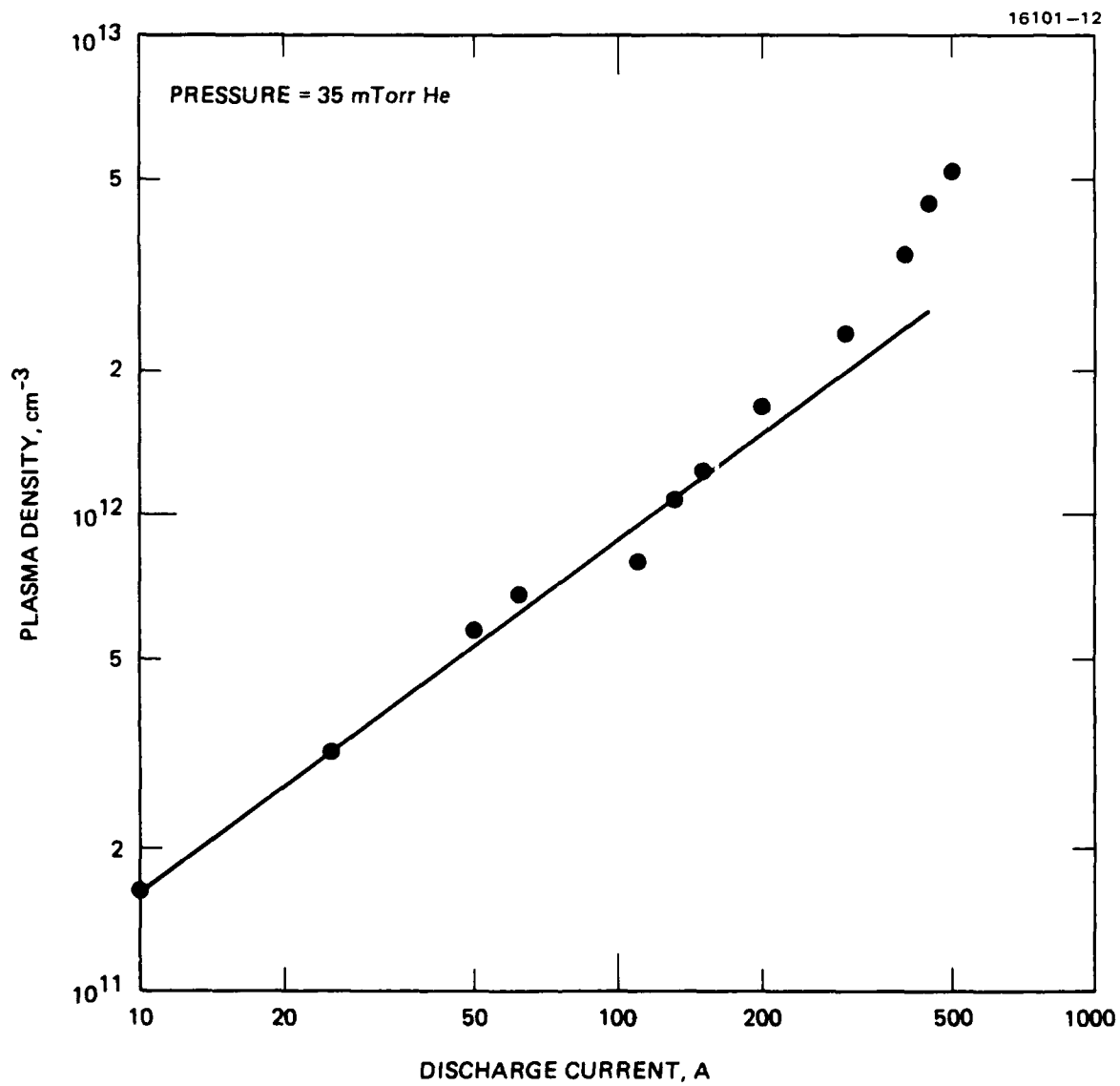


Figure 31. Plasma-density scaling with waveguide discharge current.

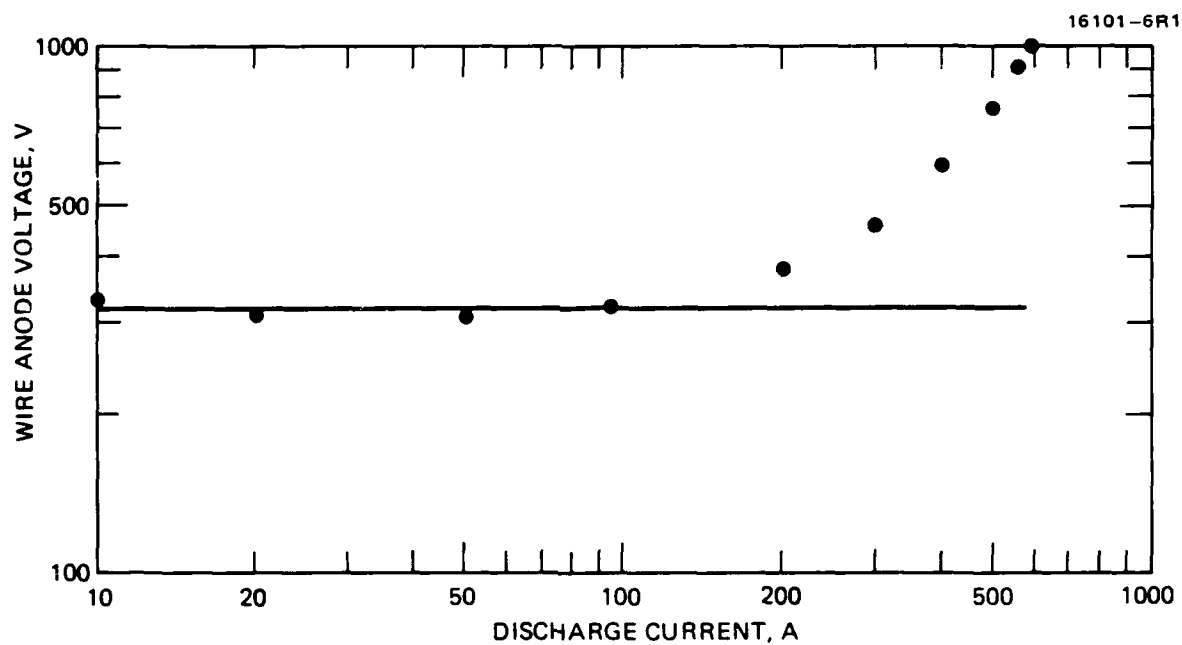


Figure 32. Wire-anode discharge-voltage scaling with discharge current.

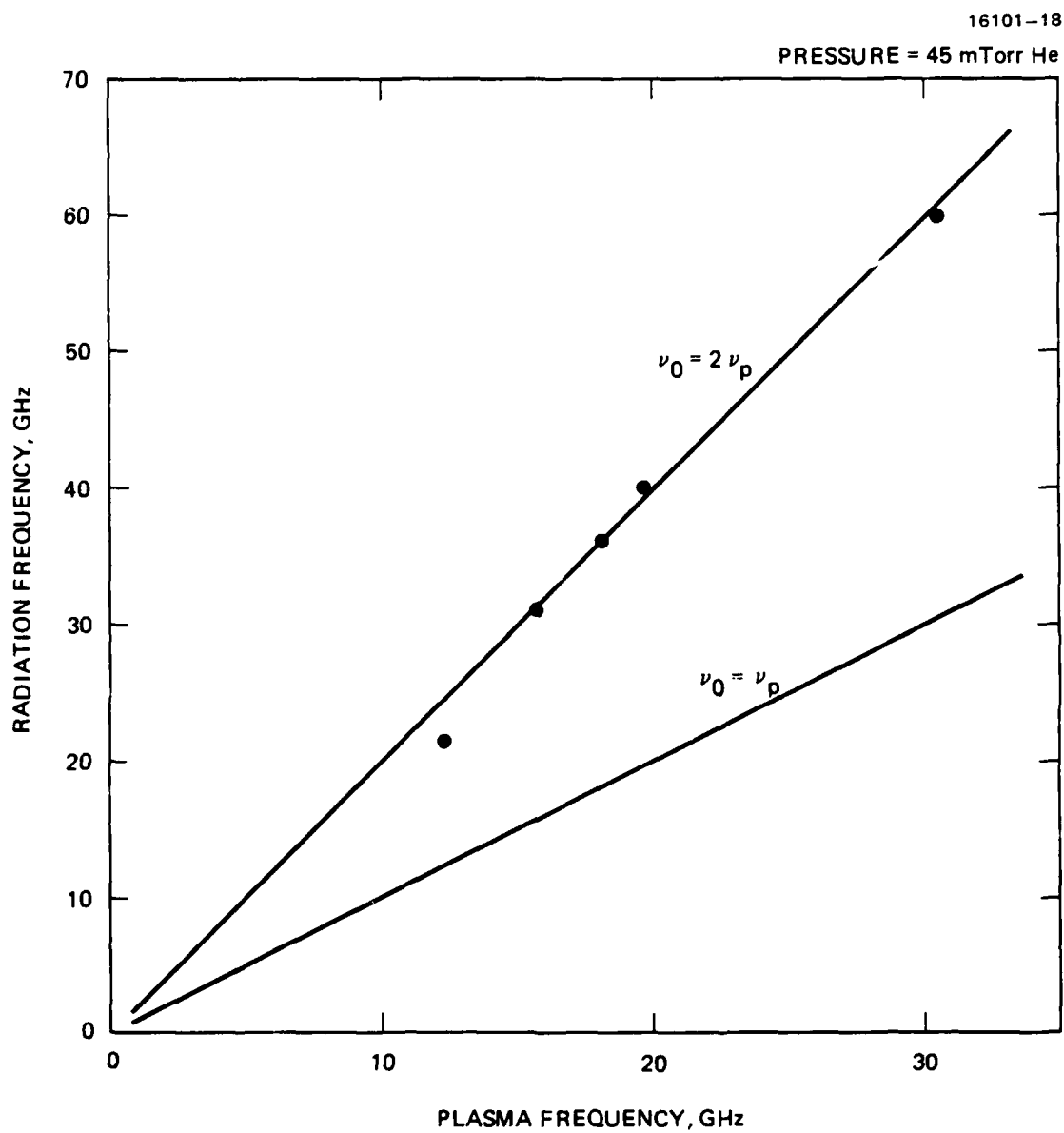


Figure 33. Output mm-wave frequency scales as $2\nu_p$.

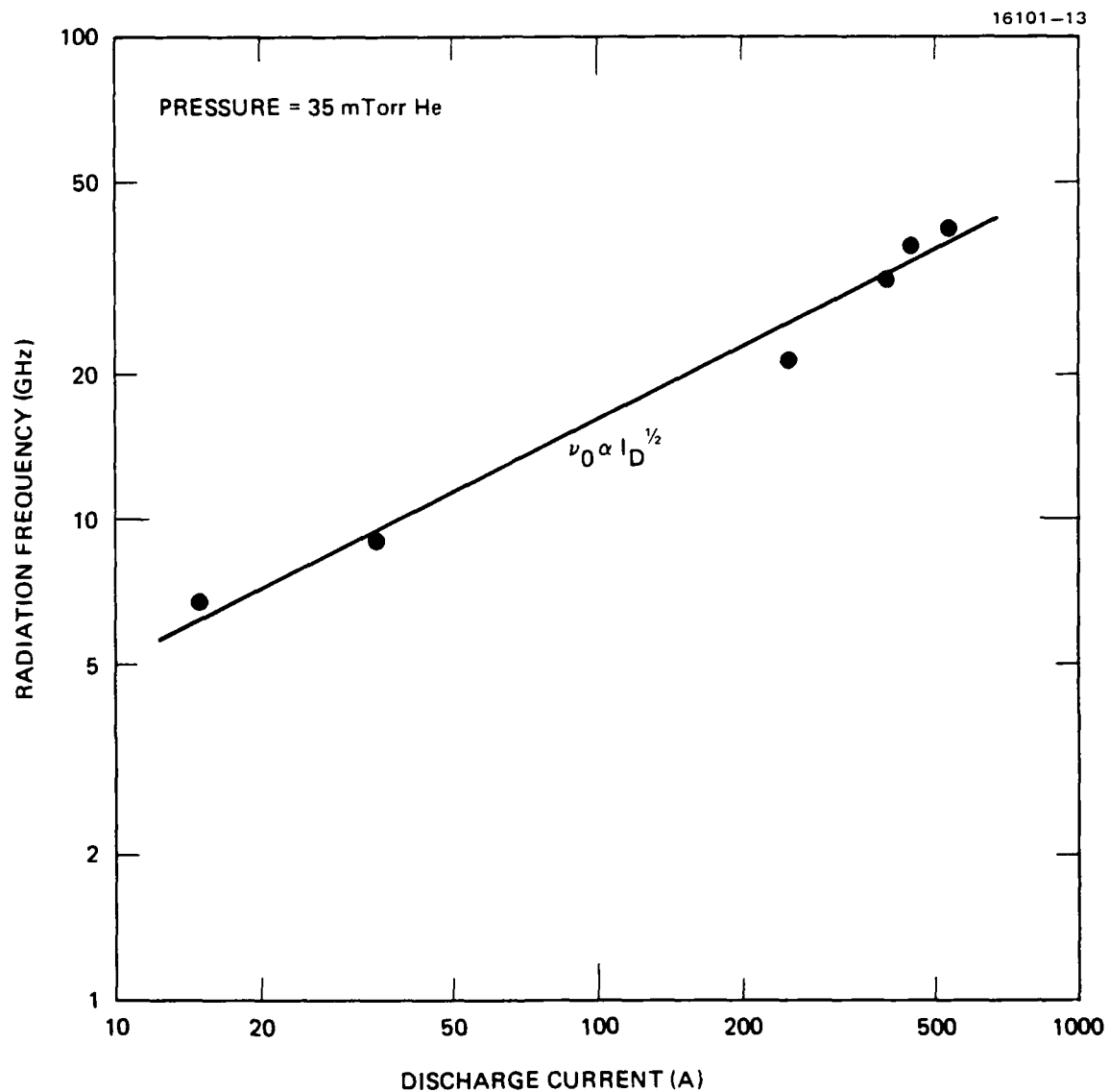


Figure 34. Frequency scaling with discharge current over a lower current range and at slightly lower gas pressure.

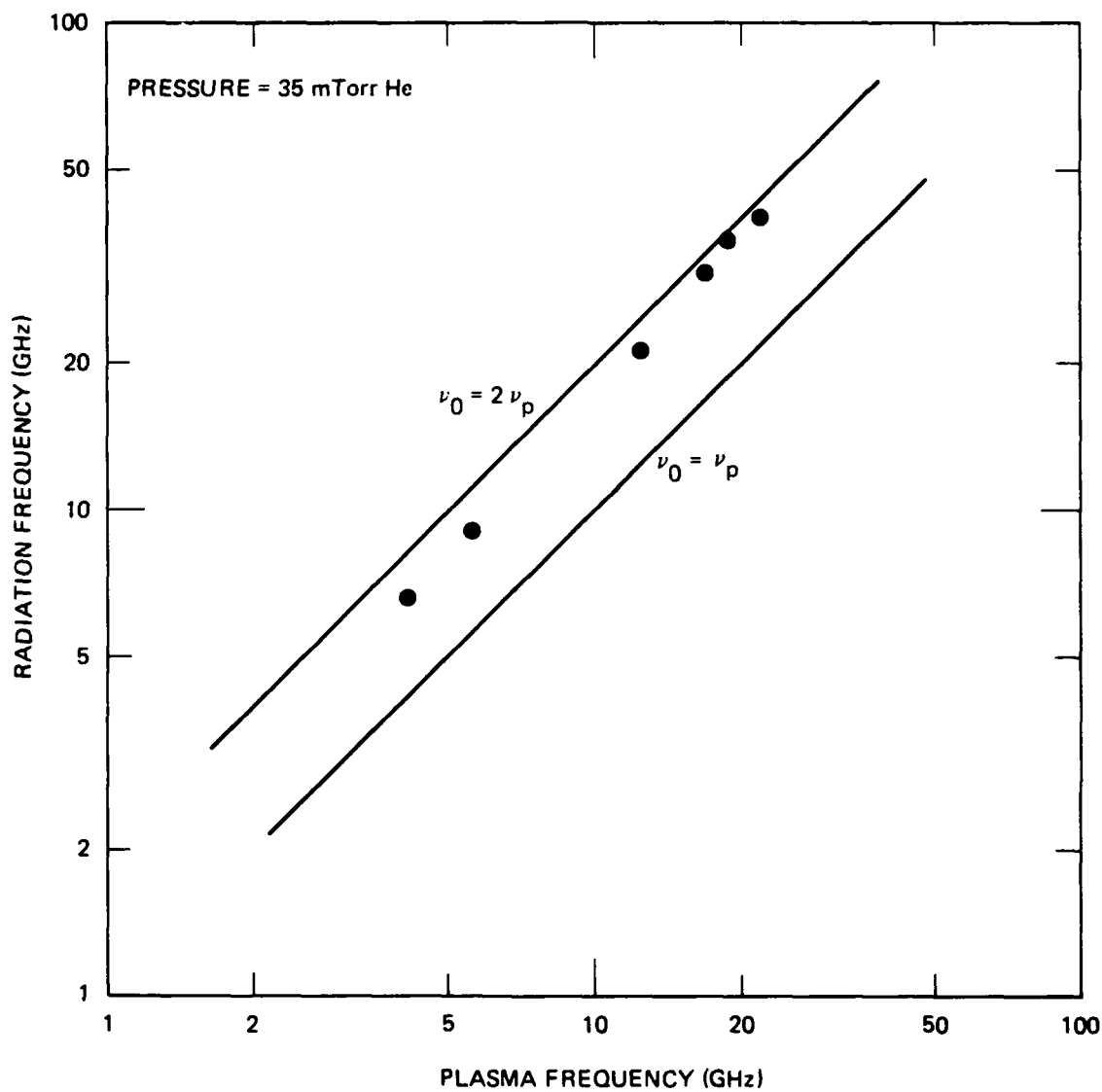


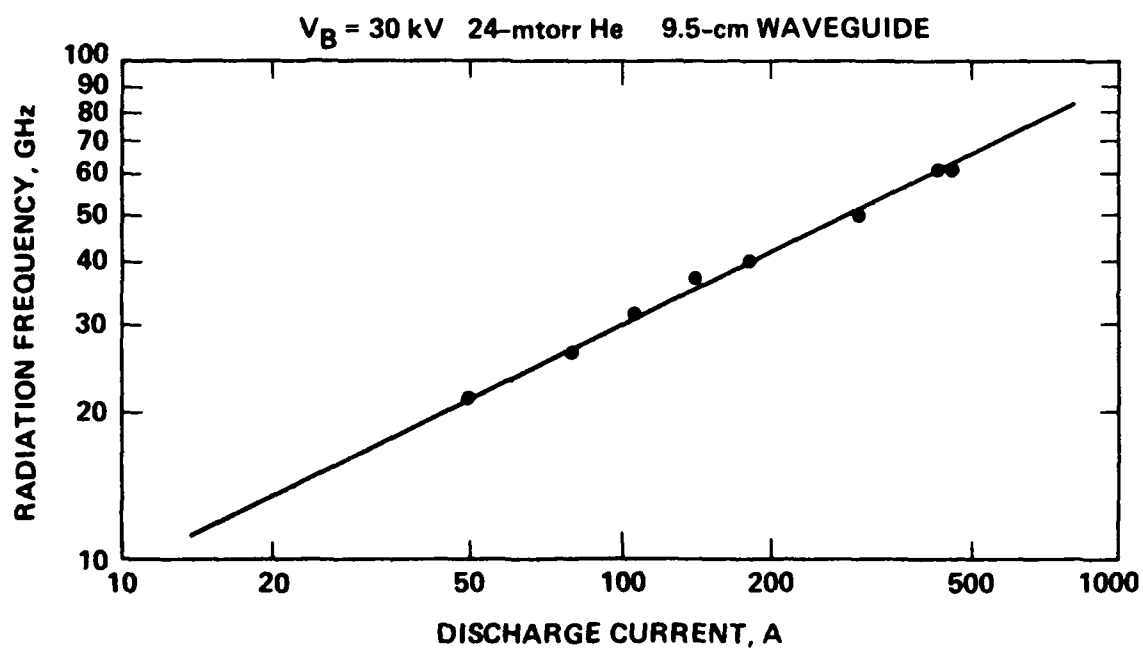
Figure 35. Output frequency also scales as $2\nu_p$ at lower plasma density.

using lower gas pressure and a 9.5-cm-diameter waveguide section. As shown in Figure 36, under these conditions we now observed the radiation frequency to scale as $I_0^{0.5}$, as was predicted from the argument above.

3.4.2 Amplitude-Modulation Scaling and Coherence

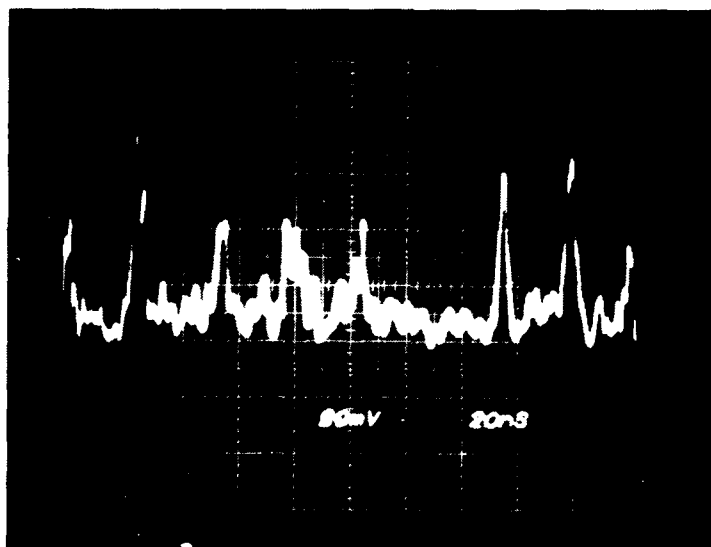
The beam-plasma system is operating in the strong turbulence regime, as discussed in Section 2.1. As shown in Figure 37, the output power is strongly modulated on a time scale that is near the ion-plasma frequency - behavior which is also characteristic of nonlinear beam-plasma instabilities. Figure 37 shows that the radiation at 35 GHz is actually emitted in seemingly random spikes with half-widths of ~ 10 ns. The spikes may be even narrower since the bandwidth limit of the oscilloscope was 100 MHz. Using the beam-plasma parameters listed in Figure 37, together with Eq. (8), we estimate the ratio of EPW energy density to plasma energy density, $W_{EPW}/n_e T_e$, to be about 7×10^{-2} . The beam-plasma interaction in the experiment is strongly turbulent, since this ratio exceeds the weak turbulence parameter, $(k_e \lambda_D)^2$, by 3 orders of magnitude. A phenomenological model of the temporal radiation modulation was developed by Rosenberg and Krall. The detailed model, which includes strong plasma turbulence effects, is presented in Section VI of Appendix B.

The millimeter-wave modulation frequency decreases as the ion mass is increased. Oscilloscope photos of the crystal detector output for five different gases (i.e., hydrogen, helium, argon, krypton, and xenon) are shown in Figure 38. These data are reduced to a quantitative form in Figure 39, where the modulation inter-pulse period and pulsewidth are plotted versus ion mass. The parameters scale approximately with the square root of the ion mass. These data clearly indicate that ion dynamics is important in determining the



OCTOBER 1996

Figure 36. Radiation frequency scales as $I_0^{1/2}$.

35-GHz
RADIATION

TIME, 40 ns/div

$$n_e = 3.8 \times 10^{12} \text{ cm}^{-3}$$

$$T_e = 5 \text{ eV}$$

$$I_b = 2.5 \text{ A}$$

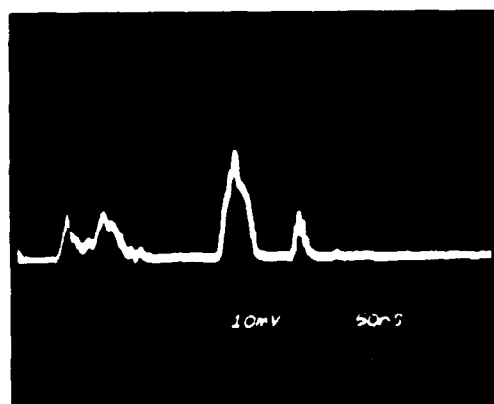
$$V_b = 30 \text{ kV}$$

$$\frac{n_b}{n_e} \cong 2.3 \times 10^{-4}$$

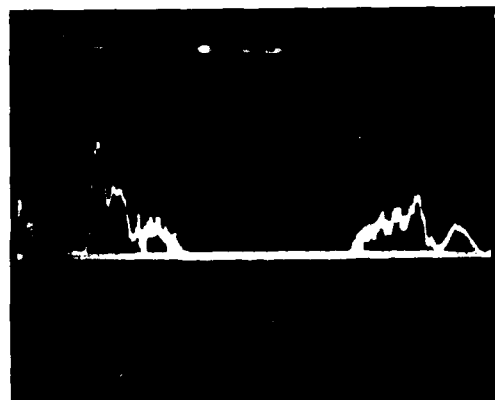
$$\frac{W_{EPW}}{n_e T_e} \cong 7 \times 10^{-2}$$

$$(k_p \lambda_D)^2 \cong 8 \times 10^{-5}$$

Figure 37. Output mm-wave radiation is strongly modulated on a time scale which is near the ion-plasma frequency. Experiment parameters corresponding to the observed 35-GHz radiation are listed below the oscilloscope waveform.

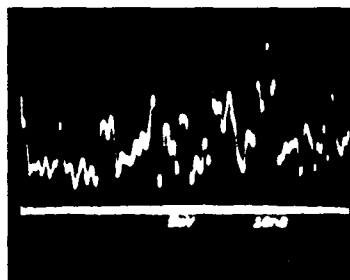


KRYPTON

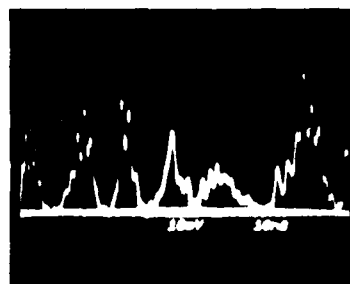


XENON

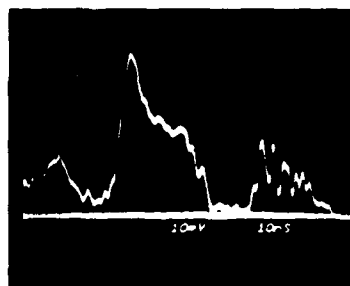
TIME (100 ns/div)



HYDROGEN



HELIUM



ARGON

TIME (20 ns/div)

Figure 38. Millimeter-wave modulation frequency decreases with ion mass.

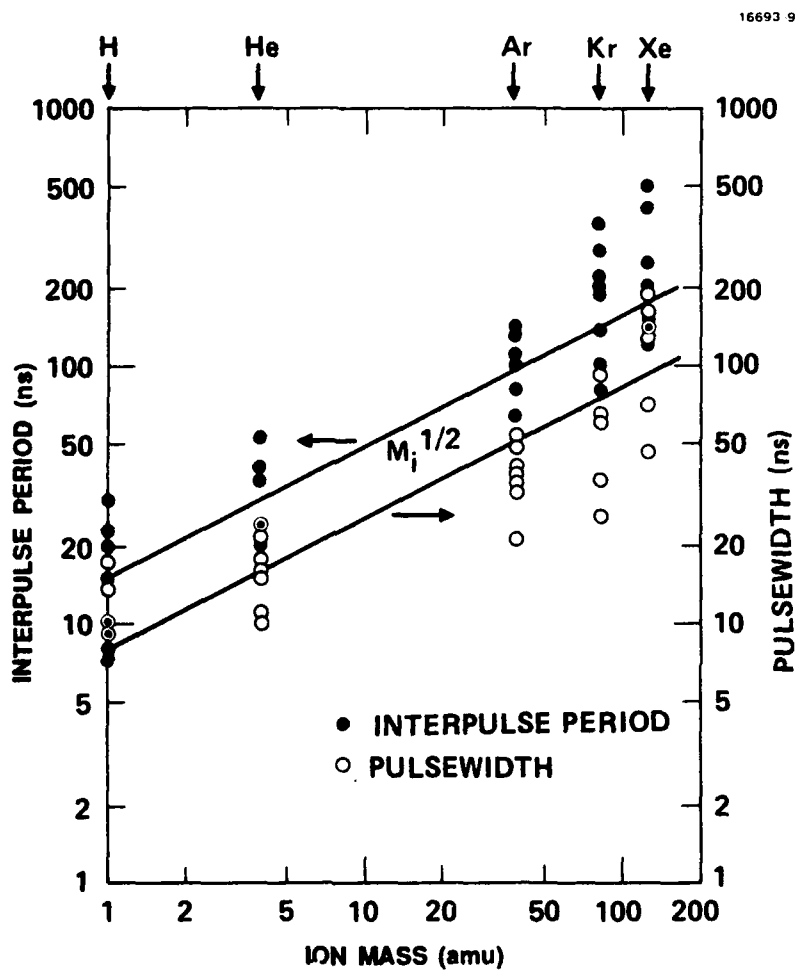


Figure 39. Millimeter-wave pulse-width and inter-pulse-period scale as $M_i^{1/2}$.

characteristics of the millimeter-wave radiation. The modulation may be caused by ion acoustic waves which are known to be generated by parametric-decay instabilities in strong-EPW-turbulent systems.

Despite the strongly modulated envelope, the millimeter-wave radiation appears to be phase coherent. We investigated the coherence of the radiation using the setup shown in Figure 40. The millimeter-wave radiation from the experiment is directed into a ring-hybrid junction which divides phase-coherent power equally at ports 2 and 4 and cancels the power at port 3. With a waveguide termination at port 2, the relative power at ports 3 and 4 provides a measure of the degree of coherence of the input signal. For example, when the output from a reflex klystron is inserted into the system, we observe $P_3/P_4 = -30$ dB, indicating that the klystron signal is highly phase coherent. When the experiment is repeated using the output from our experiment through 4 meters of waveguide, we observe $P_3/P_4 = -13$ dB. This measurement indicates that the radiation is highly coherent. The power-division ratio of only -13 dB may be caused by the larger instantaneous bandwidth (1 to 2 GHz) of the three-wave-mixing radiation relative to the narrow bandwidth of a reflex klystron.

3.4.3 Beam-Voltage Scaling

We investigated the scaling of millimeter-wave power with beam-voltage settings. This experiment was performed by holding the first E-beam voltage constant at 19.5 kV, and scanning the second E-beam voltage over a broad range while simultaneously observing the output radiation power at 35 GHz. To reduce the effects of shot-to-shot variations, and the power variations within a single pulse (i.e., modulation described earlier), an RC circuit was used to integrate the total power in each shot, and this number was then averaged over ten successive shots

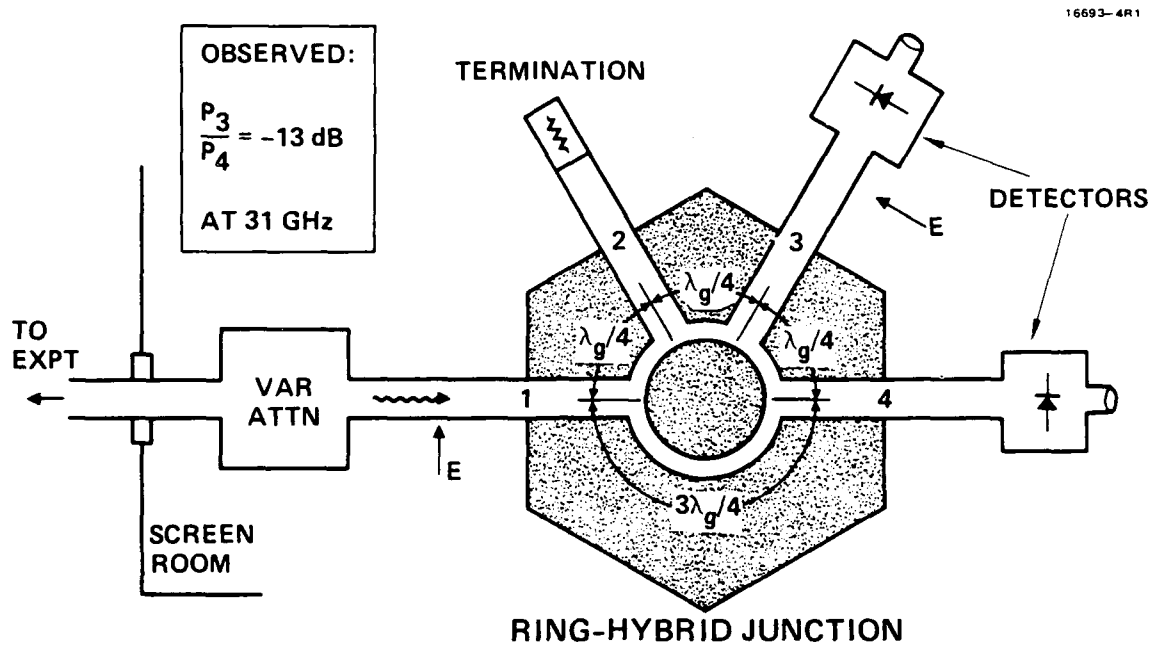


Figure 40. Phase-coherence measurement system.

using the IBM-PC computer. The results are plotted in Figure 41 for total cathode currents (sum of both E-beams) of 2.8, 3.0, 4.1, 5.6, 7.4, and 8.5 A (the cathode current in each gun is roughly twice the injected current in each beam). At the lowest current, radiation is detected only for $V_b^{LV} = V_b^{HV}$. As the beam current is increased, the beam-voltage "tuning" envelope broadens and suggests the generation of a broad spread of EPW wave numbers at high beam current. In general, however, Figure 41 shows that the radiation is optimized for almost equal beam voltages. These data contrast sharply with the solutions presented earlier, which predicted that the TM_{01} mode would be excited at $V_b^{HV} = 65$ kV for $V_b^{LV} = 18.8$ kV and $\nu_0 = 35$ GHz. Apparently, the beams are exciting higher order TM modes near the cut-off frequency of the plasma-loaded guide where $k_0 \approx 0$ and where Eq. (15) requires $V_b^{HV} = V_b^{LV}$.

Figure 42 is a comparison of voltage tuning curves at high-beam-cathode currents with $V_b^{LV} = 20$ and 30 kV. The curves nearly overlap, indicating that a substantial spreading in k -space has occurred; that is, precise beam voltage selection rules are not required since a broad k -spectrum is generated at high beam currents.

We have also set $V_b^{HV} = V_b^{LV}$ and plotted the scaling of millimeter-wave power with equal beam voltage. The results are shown in Figure 43 which indicates an optimum beam voltage of 30 kV. In this case, very little change in the optimum beam voltage setting is noted as the beam current is increased from 3.5 to 5.3 A. We repeated the experiment at higher waveguide plasma density such that the radiation center frequency is at 60 GHz. This data is shown in Figure 44. Note that at higher density and frequency, the optimum beam voltage has shifted to 41 kV.

The voltage tuning effect for $V_b^{HV} = V_b^{LV}$ can be explained by considering the EPW profile that is excited by the beams. The main requirement for high power emission is that the EPWs

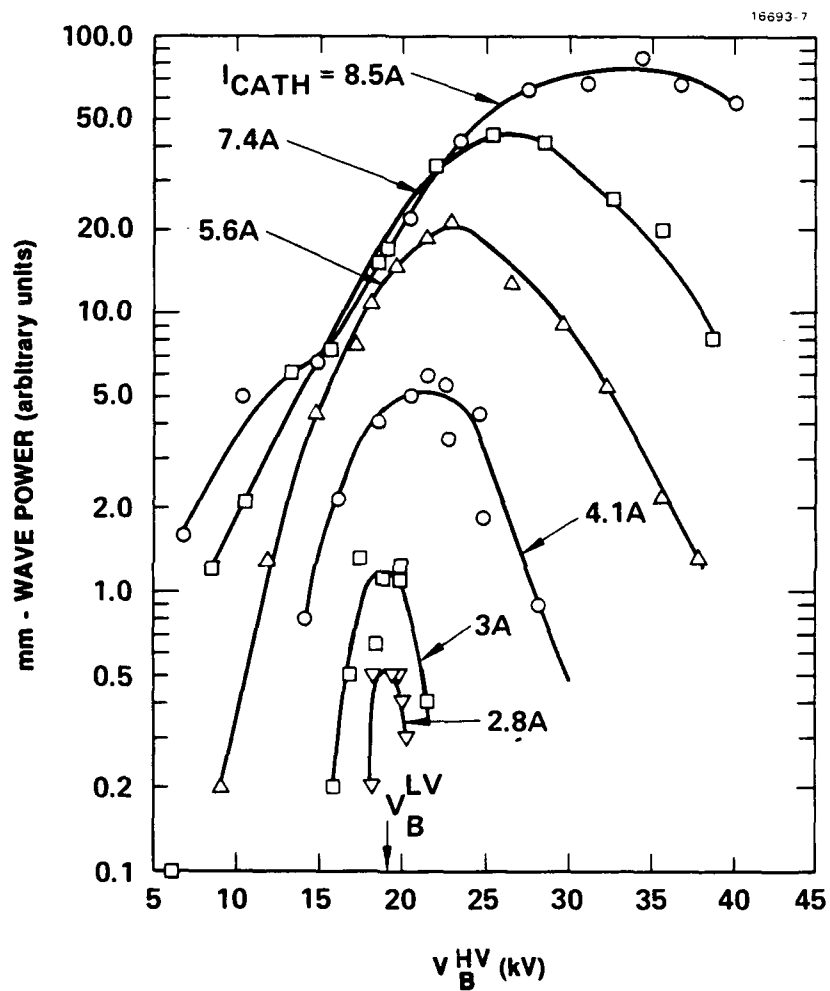


Figure 41. Beam-voltage tuning for $V_b^{\text{LV}} = 19.5$ kV.

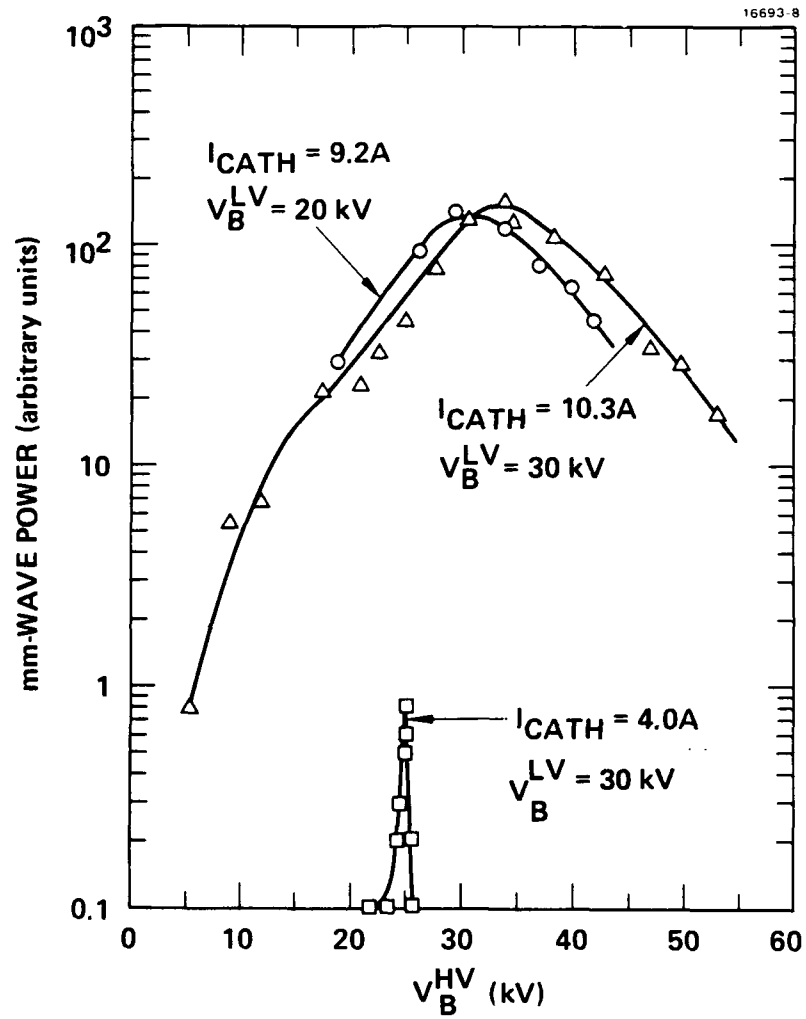


Figure 42. Beam-voltage tuning for $V_b^{LV} = 30 \text{ kV}$.

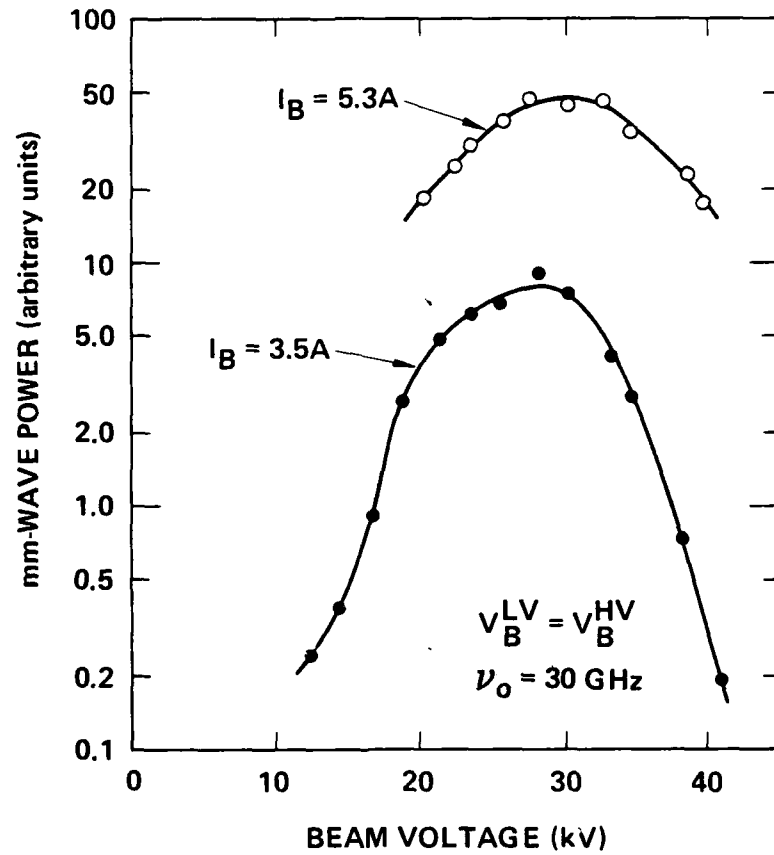


Figure 43. Millimeter-wave power scaling with beam voltage.

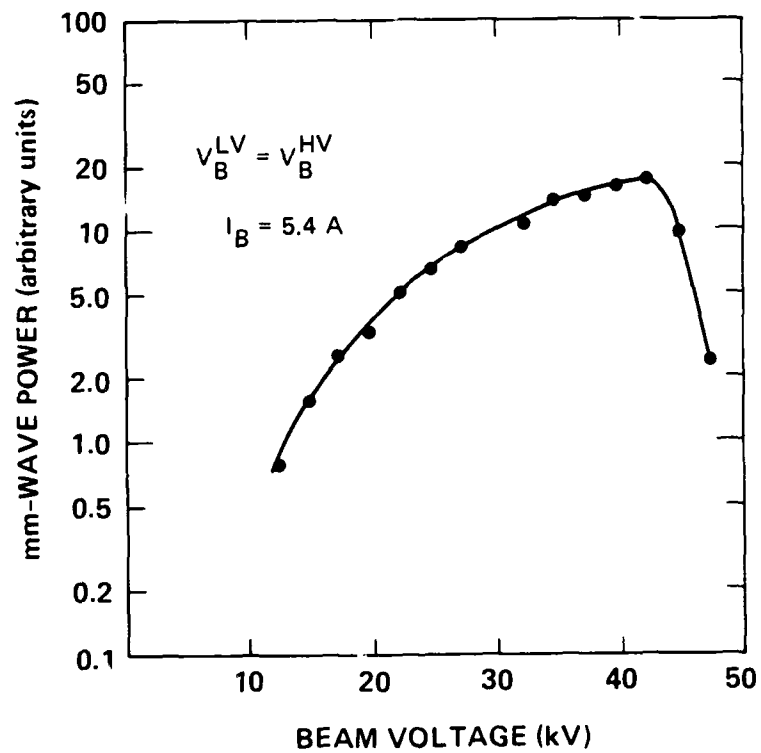


Figure 44. Millimeter-wave power scaling with beam voltage at 60 GHz.

overlap spatially so they can interact to generate the millimeter-wave radiation. In general, the EPW amplitude will grow, saturate, and then decay along the beam direction, as shown schematically in Figure 45. When the beam voltage is too low, the EPWs saturate and decay before they interact. When the voltage is too high, the EPWs require a long distance before they can grow to large amplitude. The radiation generated under either of these two conditions is less than that which would be obtained if the optimum beam voltage were used. At the optimum voltage the EPWs overlap near the waveguide midplane where they have the largest amplitude.

3.4.4 Beam-Current Scaling

Radiation power scaling with total beam current (sum of the actual injected beam currents, $I_B = I_B^{HV} + I_B^{LV}$) is plotted in Figure 46. There are three salient features of the scaling. First, there is a sharp threshold current below which we observe no detectable power. Second, once the threshold current of ~ 3.0 A is reached, the power rises rapidly over two orders of magnitude. Third, just above 3.0 A the sharply rising curve bends over to a power scaling which is approximately proportional to I_B^6 .

The current-threshold effect is controlled by electron-beam dynamics. At total beam-current values below 3 A, the current in each beam is below the Bennett-pinch current of 1.5 A. In this regime the beam channel is broad, the beam density is low, the beam-plasma interaction is weak, and the millimeter-wave power is below our detection threshold. When each beam current reaches 1.5 A (3.0-A total), however, the beam rapidly collapses, the beam density increases sharply, the beam-plasma-instability growth rate increases, and the millimeter-wave radiation suddenly rises. Once each beam becomes fully pinched with the Bennett equilibrium profile, the power rises more slowly and we observe the I_B^6 scaling for I_B up to 5.0 A.

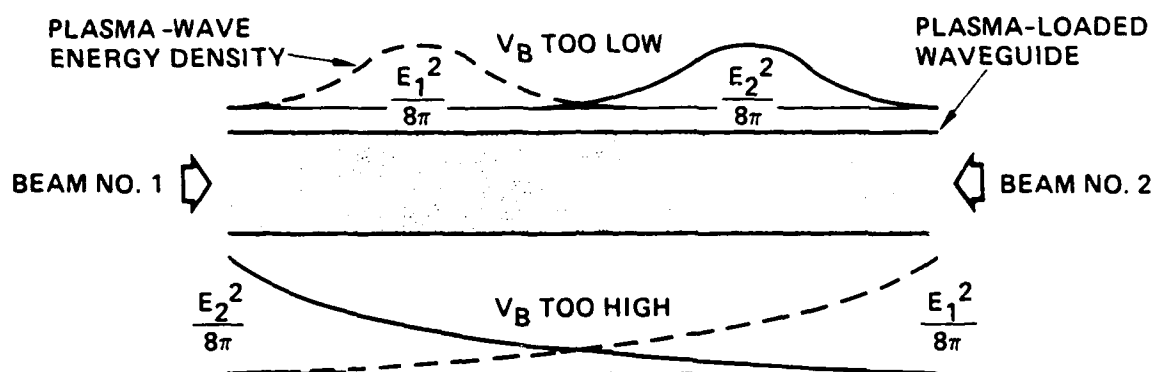


Figure 45. Radiation power is optimized for beam voltage which overlaps regions of intense plasma waves.

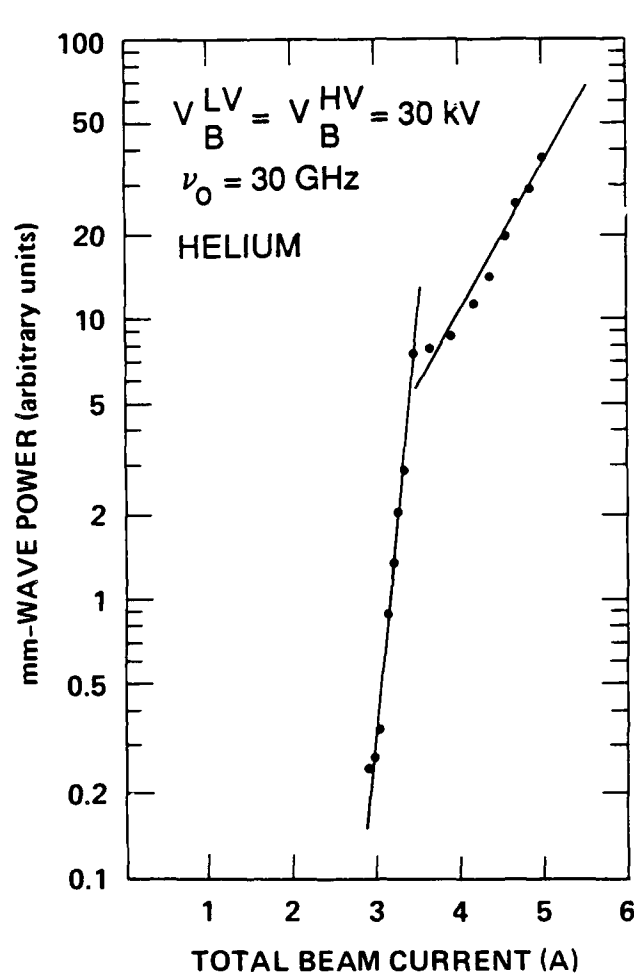


Figure 46. Millimeter-wave power scales nonlinearly with beam current.

In Figure 47 we have extended the power scaling to higher total beam currents and we have plotted the scaling for different gases including hydrogen, helium, and neon. For each gas species the same current-threshold phenomena is observed. The data also indicate that the power increases with ion mass.

The most significant result of this scaling experiment is that at the highest beam currents available the millimeter-wave power is still increasing rapidly with beam current. At 7.0 A in helium for example, we measured peak power levels of 8 kW at 31 GHz with peak efficiency of 4%. When the output is averaged over the envelope of the amplitude-modulated millimeter-wave pulse, we estimate an average conversion efficiency of about 0.4%. The efficiency estimates are based on waveguide cold tests which show that about 1% of the Ka-band radiation generated within the waveguide is coupled into the output waveguides. If the power continues to scale as I_b^6 , the efficiency will increase as I_b^5 !

3.4.5 Beam Positioning

Since the pinched-beam cross-section is so small, millimeter-wave power generation should strongly depend upon the relative beam positions inside the waveguide. To investigate this issue, we installed beam-steering coils along the waveguide as shown in Figure 48 to adjust the x-y position of each beam. As shown in Figure 49 we found that a displacement of one beam by only 2 mm increased the radiation power by 3 dB. When the beam was displaced by only 1.2 cm, the radiation level fell below our detection threshold. This simple experiment dramatically demonstrates that beam dynamics play a dominant role in the plasma three-wave mixing process.

3.5 RADIATION MODULATION CHARACTERISTICS IN 15-cm-LONG CAVITY

The radiation produced by the three-wave mixing process is strongly amplitude modulated. In the experiments described in

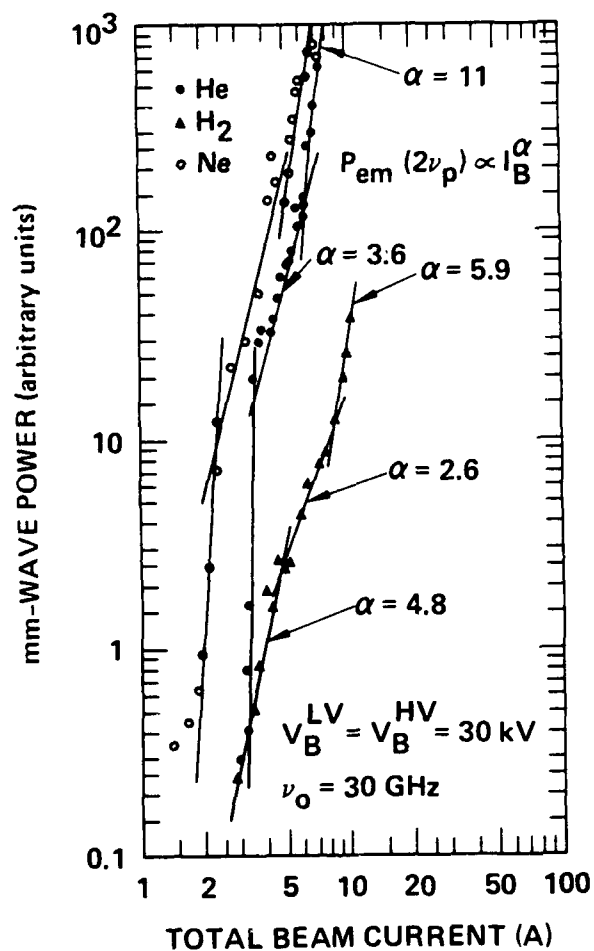


Figure 47. Millimeter-wave power scaling curves for He, H₂ and Ne.

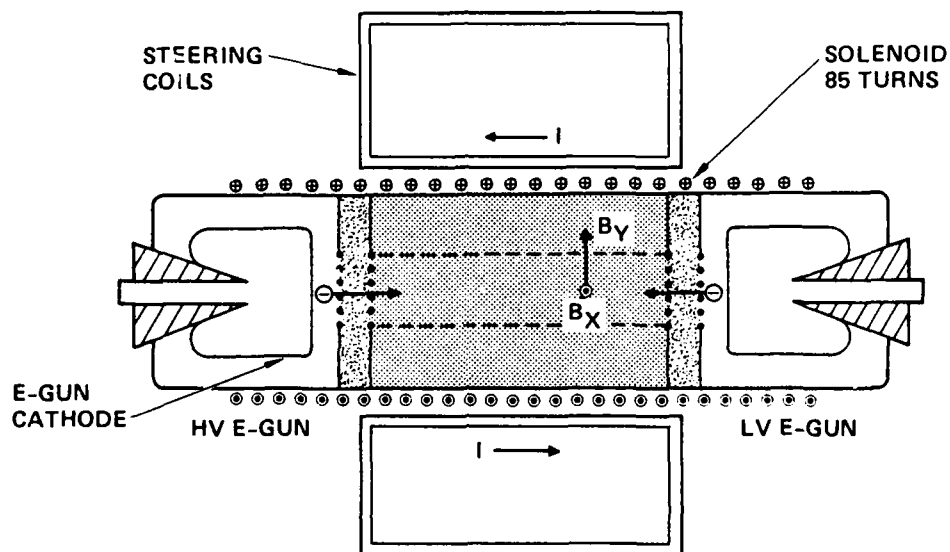


Figure 48. Beam-steering coils.

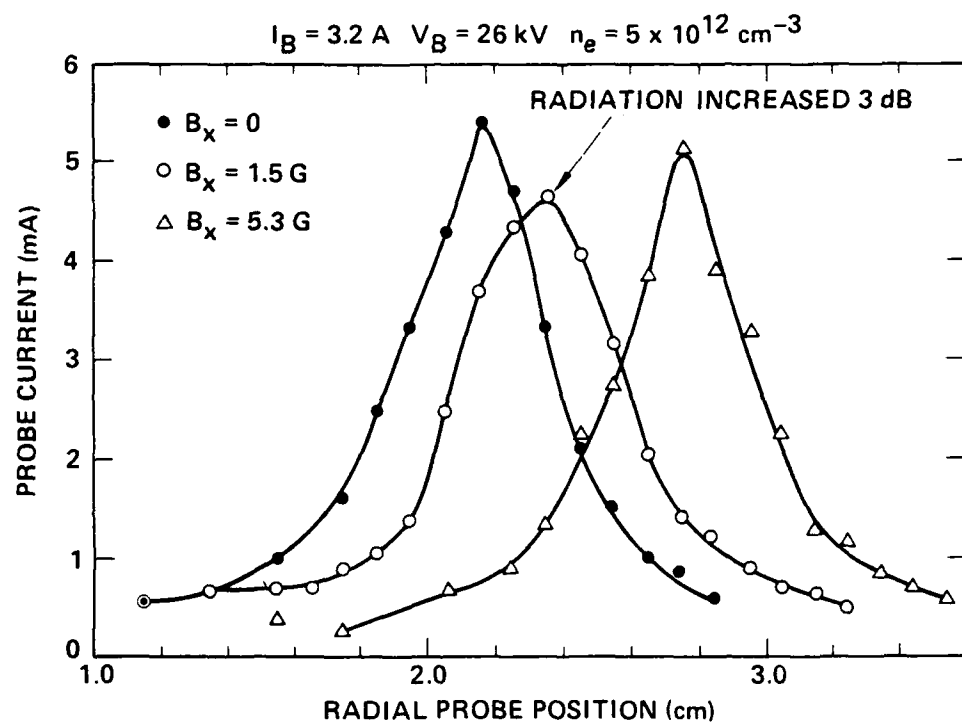


Figure 49. Beam steering optimizes output radiation.

this section, we found that the detailed modulation characteristics depend on the beam current and the waveguide plasma density. We also demonstrated that the radiation modulation is correlated with the local electrostatic oscillations in the plasma.

3.5.1 Scaling With Waveguide Plasma Density

As described in Section 3.2, the radiation modulation changes from a nearly continuous emission process at low discharge current, to a more ordered, burst emission at high discharge current. Figure 50 shows the change in the modulation of 36-GHz radiation (filter pass-band = 35 to 37 GHz) as the waveguide plasma density is increased. At 230 A, the radiation consists of many very narrow-width (5 to 25 ns wide) spikes with a short inter-pulse period (IPP) of about 10 to 50 ns. The radiation is emitted continuously and we do not observe periods when the radiation power drops to zero. However, when the discharge current is increased to 310 A, the bursts become wider (50 to 100 ns), the IPP increases to 100 to 200 ns, and the signal amplitude between bursts is low compared with the peak amplitude.

These characteristics are also exhibited at higher discharge currents. Figure 51 compares the Ka-band emission measured with waveguide discharge currents equal to 500 and 200 A. At 500 A, the emission is distributed in a series of bursts, and the signal amplitude between bursts is very low. When the discharge current is reduced to 200 A, the radiation power drops by about 14 dB and the bursts are replaced by narrow, high-frequency pulses. We believe that the frequency of millimeter-wave spikes at lower discharge current is increased because the background plasma density is lower and the parameter ϵ in Eq. (1) is higher. This will increase the growth rate of the EPWs and enhance the rate of energy transfer from the beam

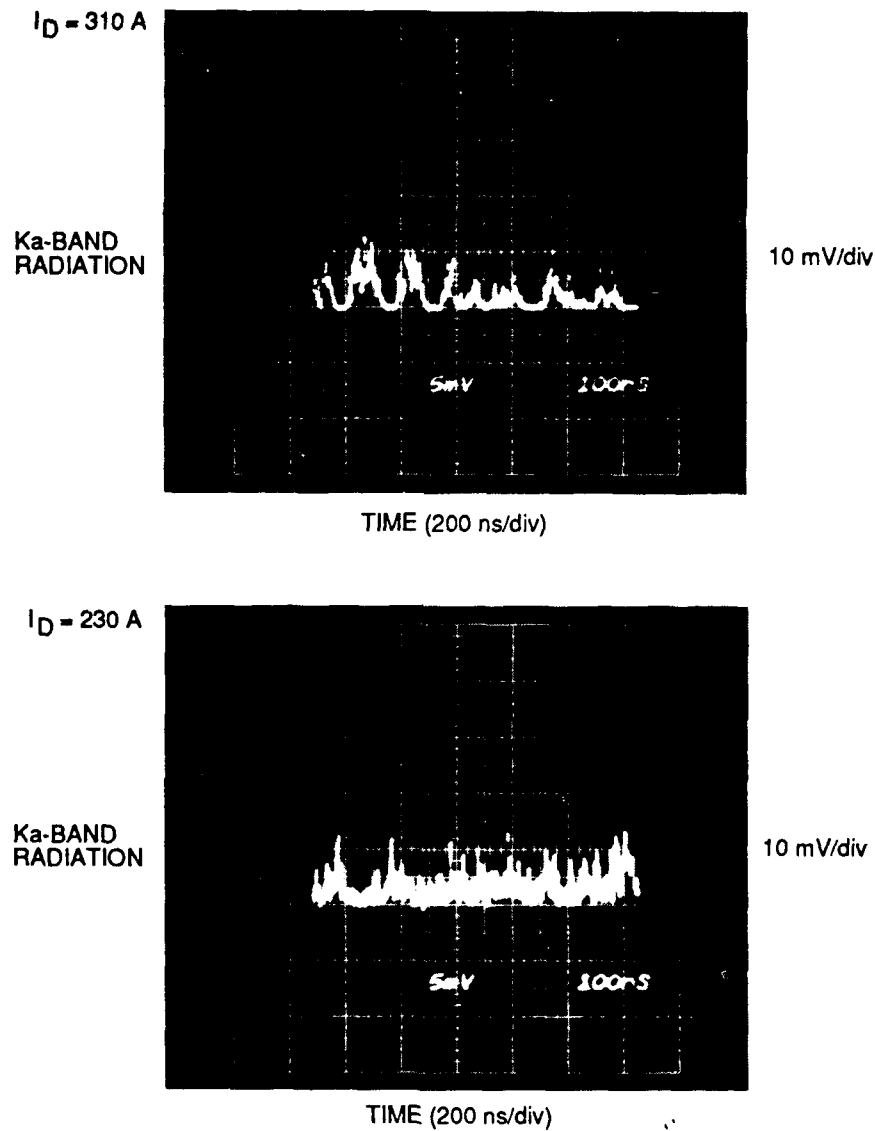


Figure 50. The modulation of Ka-band radiation is dependent on the waveguide discharge current. The total beam current was 5 A and the beam voltage was 30 kV.

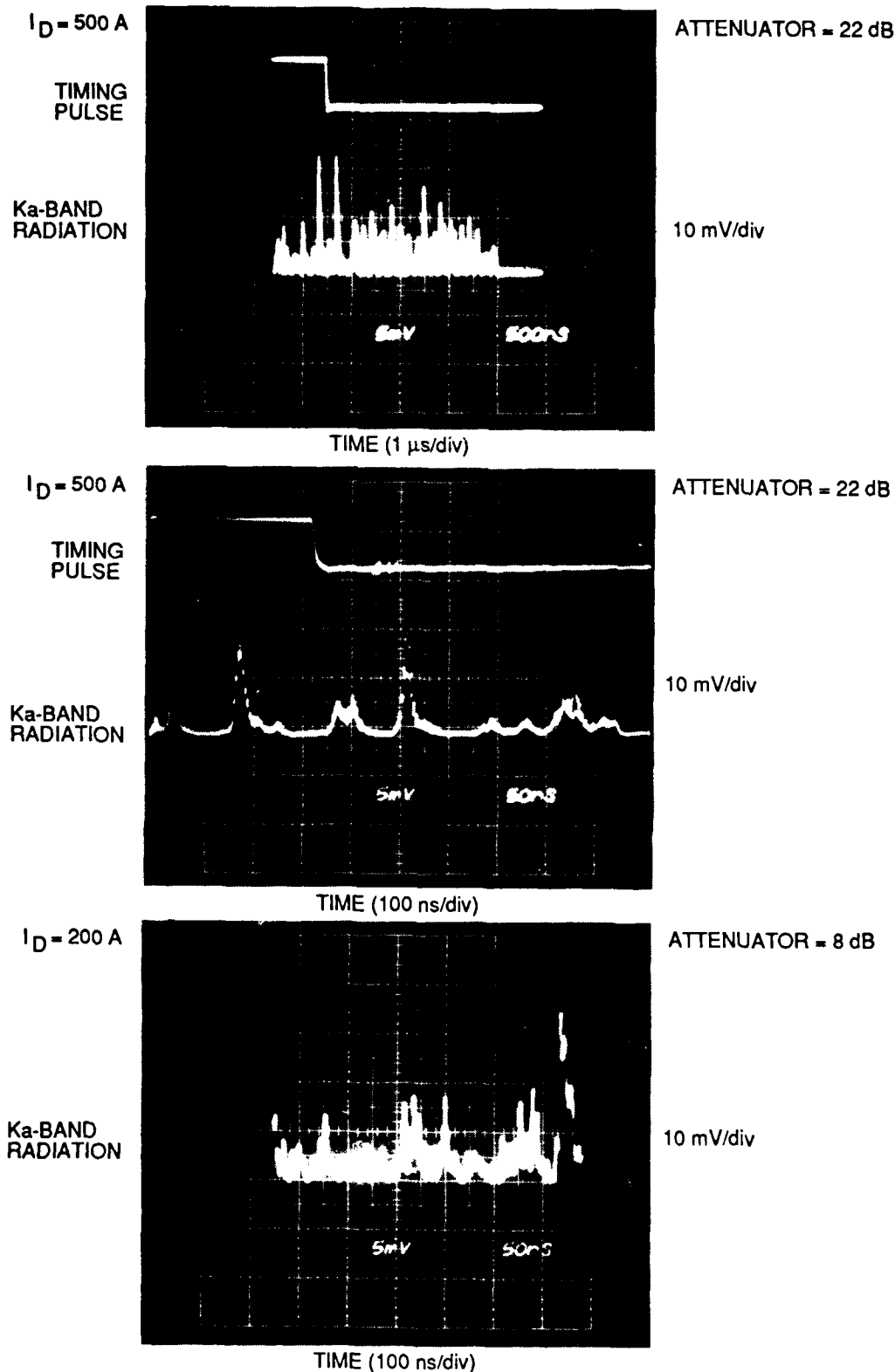


Figure 51. The Ka-band radiation is strongly modulated for a waveguide discharge current of 500 A. When the discharge current is reduced to 200 A, the radiation burst width becomes very narrow. The total beam current was 5 A and the beam voltage was 30 kV.

to the radiation field. However, since the plasma density is lower, there are fewer particles available for energy transfer and the net peak-power transferred is lower.

3.5.2 Scaling With Beam Current

As shown in Figure 52, the modulation IPP also depends on beam current. For this experiment the HV beam current (I_B^{HV}) was held constant at 2.6 A while the LV beam current was varied. At $I_B^{LV} = 2.5$ A, the emission consists of 50-ns-wide bursts and the IPP is 50 to 200 ns. When I_B^{LV} is reduced to 1.8 A, the radiation drops in power by about 15 dB (as predicted by the scaling of radiation power with beam current) and is generated in burst clusters with an IPP of 800 ns to 1 μ s; very little power is emitted between bursts. This trend continues even when I_B^{LV} is set to zero. However, voltage is still applied to the LV beam cathode, and radiation is still observed, but the IPP is now longer than 2 μ s. Radiation is produced in this case because some of the HV beam electrons reach the LV cathode and are reflected into the waveguide plasma. The reflected electrons then excite EPWs, resulting in radiation emission. When the LV beam cathode is grounded so that the HV beam electrons traverse the waveguide plasma only one time, radiation is not detected.

The change in modulation IPP and burst width with beam current may also be related to the EPW growth rate. At lower beam current the ϵ parameter is lower and the EPW growth rate is reduced, leading to a lower rate of conversion of beam energy to millimeter-waves.

3.5.3 Correlation With An Electrostatic Probe

A disk probe was used to investigate the correlation of a high-frequency probe signal with the radiation coupled out of the waveguide cavity via the X-band waveguide port. The probe

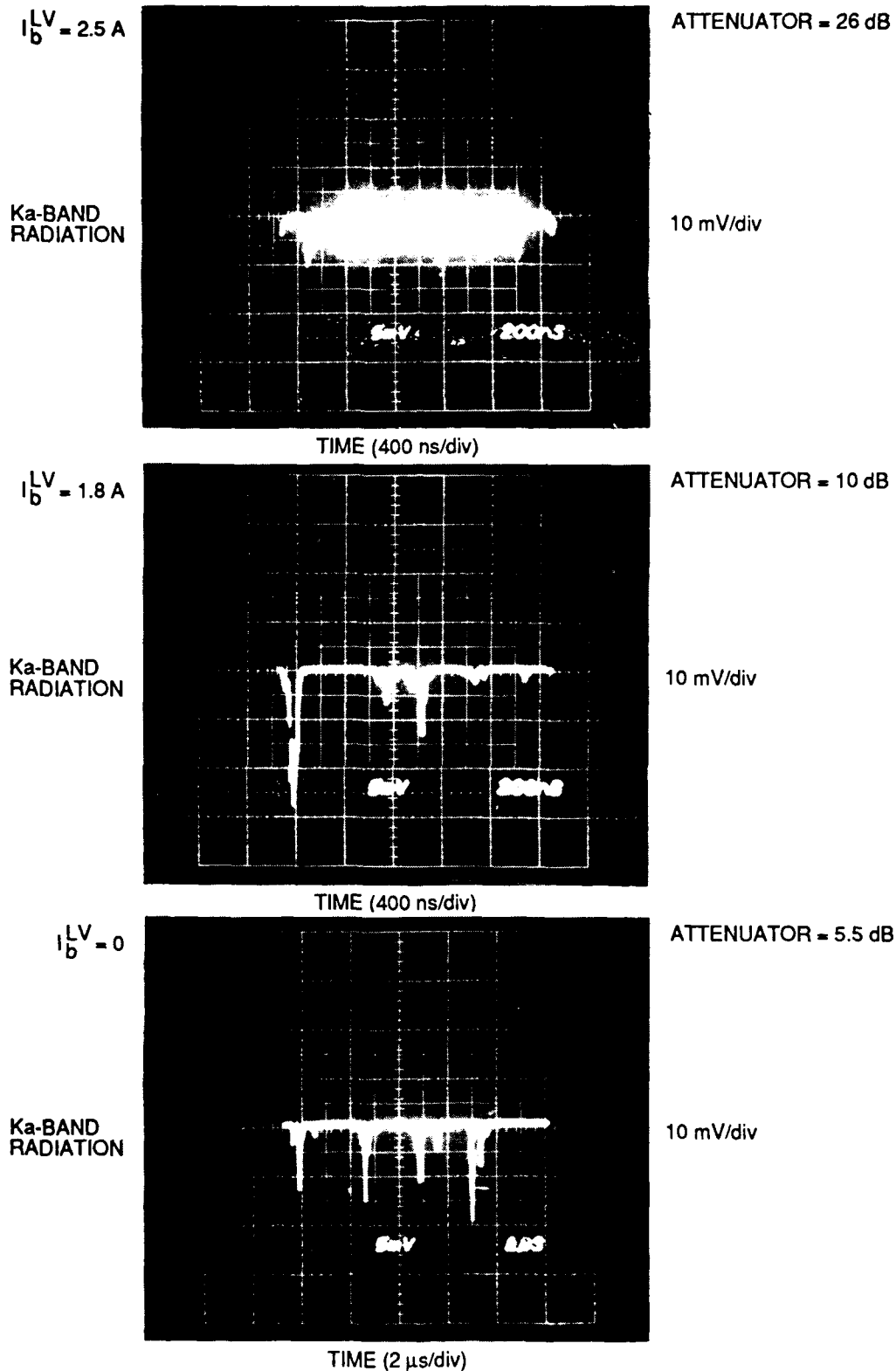


Figure 52. Ka-band modulation IPP depends on the beam current. When $I_b^{LV} = 0$, but the LV cathode is biased to reflect the HV beam electrons back into the plasma, radiation is still observed. The HV beam current was held constant at 2.6 A, the beam voltage was 20 kV and the waveguide discharge current was 500 A.

was located about 1 cm downstream of the beam injection grid shown in Figure 3 and was capacitively coupled into a 100-MHz-bandwidth oscilloscope.

The probe signal correlates well with the modulation of the 35-GHz radiation signal, as shown in Figure 53. The signals were recorded simultaneously using two oscilloscopes. The probe and radiation signals each have an IPP of about 200 ns. This is also shown in Figure 54, which displays the signals using a faster time scale. Figure 55 shows that when one of the beams is turned off, both the radiation signal falls to zero and the electrostatic (ES) probe signal is significantly reduced.

3.6 RADIATION MODULATION CHARACTERISTICS IN 1.9-cm-LONG CAVITY

Boundary conditions imposed by the waveguide cavity walls specify the allowed electrostatic (ES) and electromagnetic (EM) modes. The boundary conditions, together with the beam current and voltage, determine the allowed ES EPW modes within the system. We expect this effect to be most easily observed when the waveguide cavity dimensions are reduced to values on the order of the EPW wavelength. To investigate the radiation scaling with cavity length, we replaced the 15-cm-long waveguide cavity with a 1.9-cm-long system. The short cavity was fabricated using the same type of perforated sheet used in the 15-cm cavity. A single Ka-band waveguide output was used to couple the radiation out of the cavity.

The output radiation from the 1.9-cm-long cavity is very similar to the radiation produced in the 15-cm-long device. The radiation is strongly amplitude modulated, scales with the beam voltage, and has a threshold of about 3 A of beam current. One major difference is that the radiation power is about 20 dB lower in the shorter system. This indicates that there is insufficient distance for the E-beams to pinch and drive strong

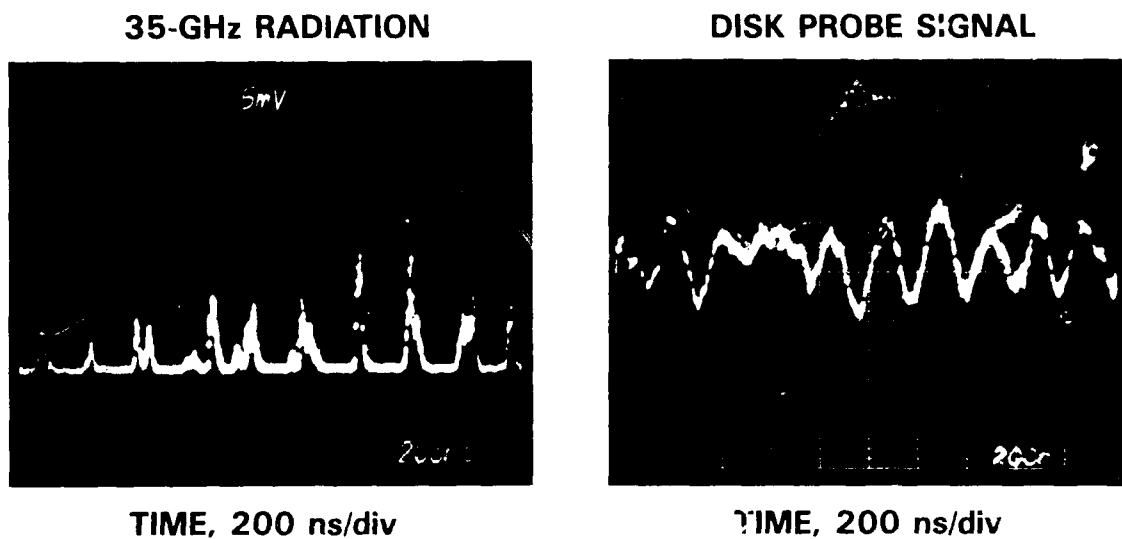


Figure 53. Electrostatic fluctuations have the same frequency components as the output radiation.

17689 4

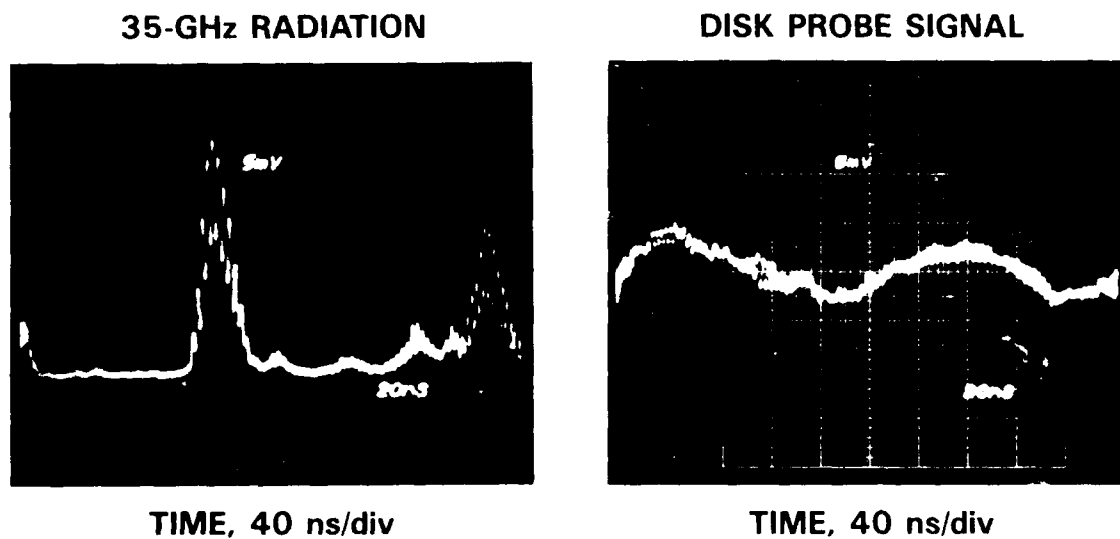


Figure 54. The radiation and the disk probe signal are compared using a faster oscilloscope time scale.

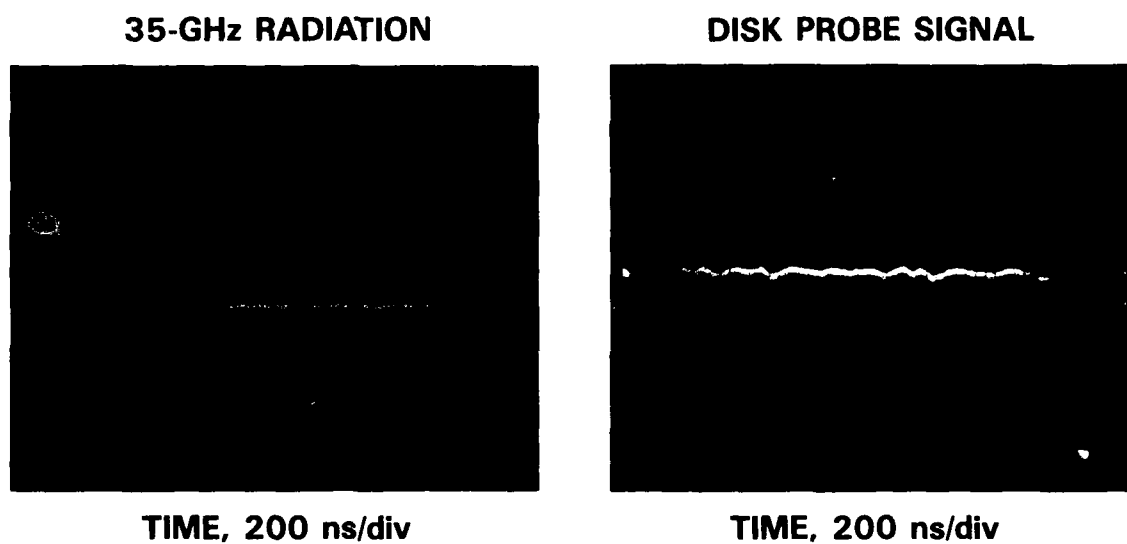


Figure 55. When only one beam is injected into the waveguide cavity, the radiation signal drops to zero and the probe signal is significantly reduced.

EPWs. For several experiments we used a gas mixture of 7% air and 93% He gas to improve the discharge stability in the small system.

3.6.1 Theoretical Discussion Of Cavity Modes

Krall and Rosenberg²³ investigated electrostatic cavity modes for a cylindrical cavity with walls fabricated from a highly transparent metal grid as shown in Figure 56. For our experimental conditions, the EPW wavelength is large compared with the grid aperture size so that we can treat the cavity walls as conducting boundaries. This boundary condition requires that the EPW electric fields vanish at the walls, and leads directly to the quantization condition that $\lambda_z = 2L/n$, where L is the length of the waveguide cavity, and n is the integral number of half-wavelengths within the cavity, $n = 1, 2, 3, \dots$. This can also be expressed in terms of the z -component of the EPW wavenumber, $k_z = n\pi/L$.

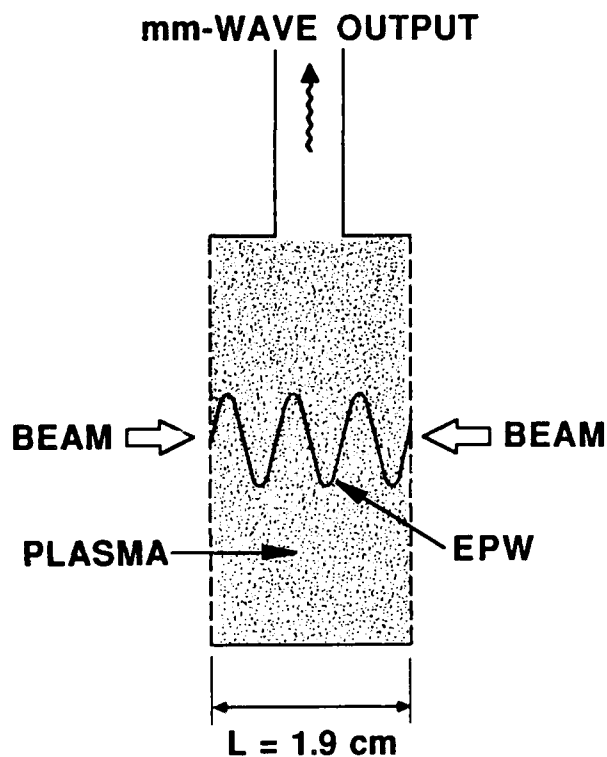
The requirement that the EPW be resonant with the beam as expressed by Eq. (2) places another constraint on the system. Combining Eq. (2) with the EPW quantization condition yields

$$v_{b,n} = \omega_p L / n\pi \quad . \quad (20)$$

Rewriting this in terms of the beam energy E_b we obtain

$$E_{b,n} = (m/2) \times (\omega_p L / n\pi)^2 \quad . \quad (21)$$

Equation (21), which was derived by M. Rosenberg,²³ requires that for fixed plasma density and device length, only certain values of beam energy can excite the allowed EPW modes. Table 2 lists the mode numbers and corresponding beam energies for 15- and 1.9-cm-long waveguide cavities. The modes are very closely spaced in beam energy in the 15-cm system, making it very



C18237

EPW QUANTIZATION: $k = \frac{n\pi}{L}$

DISPERSION: $\omega_p = kv_b$

ALLOWABLE MODES: $v_b = \frac{\omega_p L}{n\pi}$

Figure 56. The allowed EPW modes are determined by the quantization condition and the dispersion relation.

difficult to experimentally differentiate between them. Also, because the EPWs have a longer path length to grow and saturate in the 15-cm system, the spread of wave numbers is larger and k_z approaches a continuum. However, the shorter system requires smaller mode numbers and the energy spacing between modes is larger.

TABLE 2. Waveguide Cavity Mode Numbers.

	Mode number	Beam energy kV
15-cm-long cavity	30	64.3
	31	60.2
	32	56.5
	33	53.1
	34	50.1
	35	47.2
	36	44.7
	37	42.3
	38	40.1
	39	38.1
	40	36.2
	41	34.4
	42	32.8
	43	31.3
	44	29.9
	45	28.6
	46	27.4
	47	26.2
	48	25.1
	49	24.1
	50	23.2
1.9-cm-long cavity	4	58.0
	5	37.1
	6	25.8
	7	19.0
	8	14.5

3.6.2 Power Scaling With Beam Voltage

Figure 57 shows the voltage-tuning curve for the 1.9-cm-long waveguide cavity. To reduce the effects of shot-to-shot power variations, and power variations within a single pulse, we used an RC circuit to integrate the total power in each shot, and this number was then averaged over ten successive shots using the computer. Three distinct peaks are now observed rather than the broad peaks described in Section 3.4 for the 15-cm-long waveguide cavity. The three peaks correspond to the $n = 6, 7,$ and 8 modes listed in Table 2. The agreement of the physical model and the experimental results is excellent.

This experiment demonstrates that the boundary conditions imposed on the EPWs by the waveguide cavity determine the EPW modes that can be excited by the beam. This type of mode structure was not observed in the previous experiments using the 15-cm-long cavity because the modes for that system are so closely spaced. As shown in Figure 57, the 2 to 5 kV emission linewidth is sufficient to mask the presence of closely spaced modes. Another contributing factor is that the 15-cm-long cavity is many wavelengths long, as evidenced by the high mode numbers, whereas the short cavity is only a few wavelengths in length. Boundary effects are expected to be more important for the short chamber, while the longer chamber approaches a free-space simulation where the walls are well removed from the main plasma volume.

3.6.3 Modulation Envelope and Fourier Transform

The radiation emitted from the 1.9-cm-long cavity is strongly modulated with two distinctly different frequencies. Our approach to quantitatively analyze the signal was to record the crystal detector output using a fast digitizer operated at 1 GHz (effective bandwidth = 450 MHz). The digitized signal is displayed in Figure 58. The radiation bursts are now very

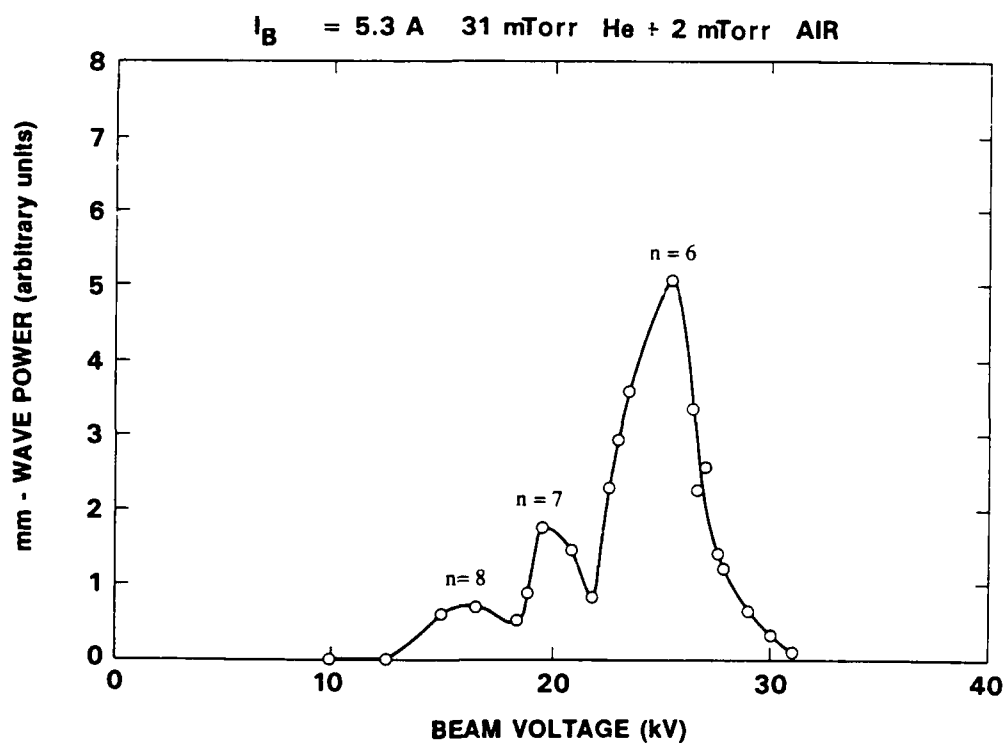


Figure 57. Radiation power scaling with beam voltage for 1.9-cm-long waveguide cavity reveals the EPW mode structure specified by the cavity longitudinal boundary conditions. Air was added to the He gas to improve the stability of the discharge.

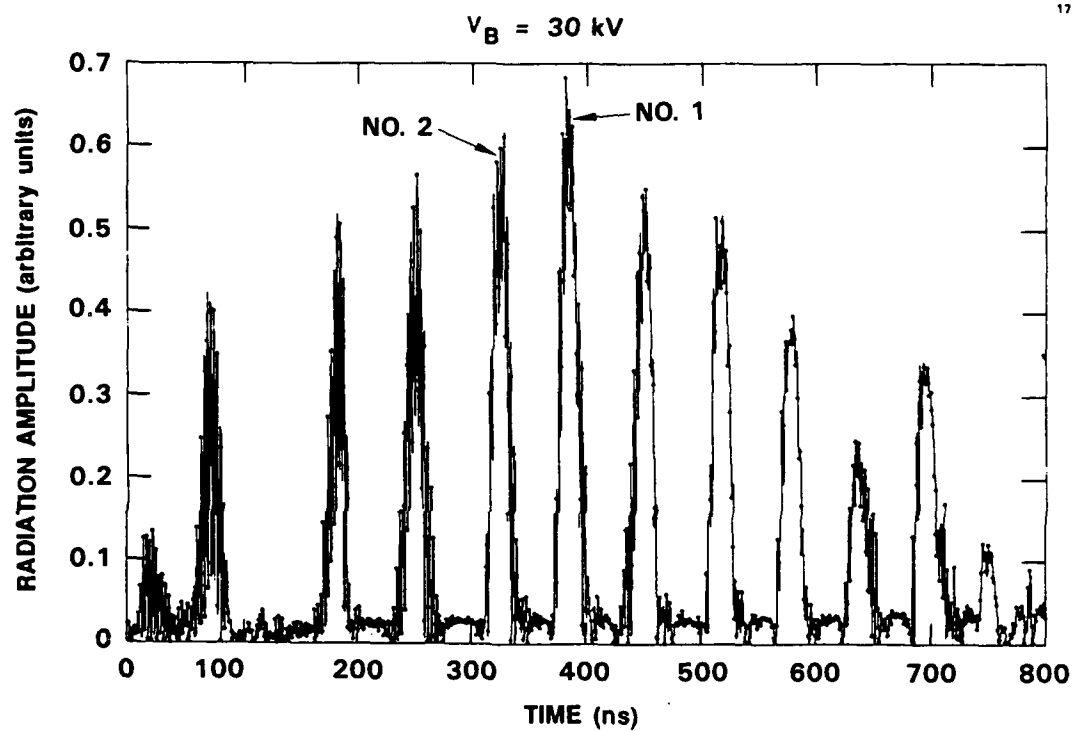


Figure 58. Radiation bursts are modulated at two different frequencies in the 1.9-cm-long waveguide cavity.

regularly spaced with a high-frequency modulation superimposed on the slower burst modulation. This is evident in Figures 59 and 60, which display two burst peaks from Figure 58 using an expanded time scale. The fast modulation depth can be a substantial fraction of the full burst amplitude, as shown in Figure 60.

The power spectrum for this data is obtained by calculating the Fast Fourier Transform using our Compaq 386/16 computer. The power spectrum is displayed on a log scale in Figure 61 and on a linear scale in Figure 62. The frequency of the slow modulation is about 14 MHz, with a second harmonic at about 28 MHz. The fast modulation peaks at 345, 356, and 371 MHz, as shown in Figure 63.

The 14 MHz modulation is controlled by the ion dynamics as described previously. The high frequency modulation near 350 MHz is a new feature that was first observed clearly in the 1.9-cm-long system. However, in contrast with the low frequency modulation, the high-frequency modulation is largely independent of the plasma and beam parameters. Subsequent experiments revealed that similar high-frequency radiation modulation is also observed using the 15-cm-long cavity.

3.7 RADIATION POWER SCALING AT LOW GAS PRESSURE

All of the previous experiments were performed using helium gas pressures in the range of 25 to 50 mTorr. Theoretical analyses by M. Rosenberg and N. Krall have shown that the modulational instability may be the dominant EPW saturation mechanism. A detailed discussion of EPW saturation is presented in Section II of Appendix B. The high gas pressures typically used in the experiment may suppress the modulational instability because the instability threshold depends on the electron-neutral collision frequency; high radiation power is generated because the instability does not limit the EPW amplitude. We

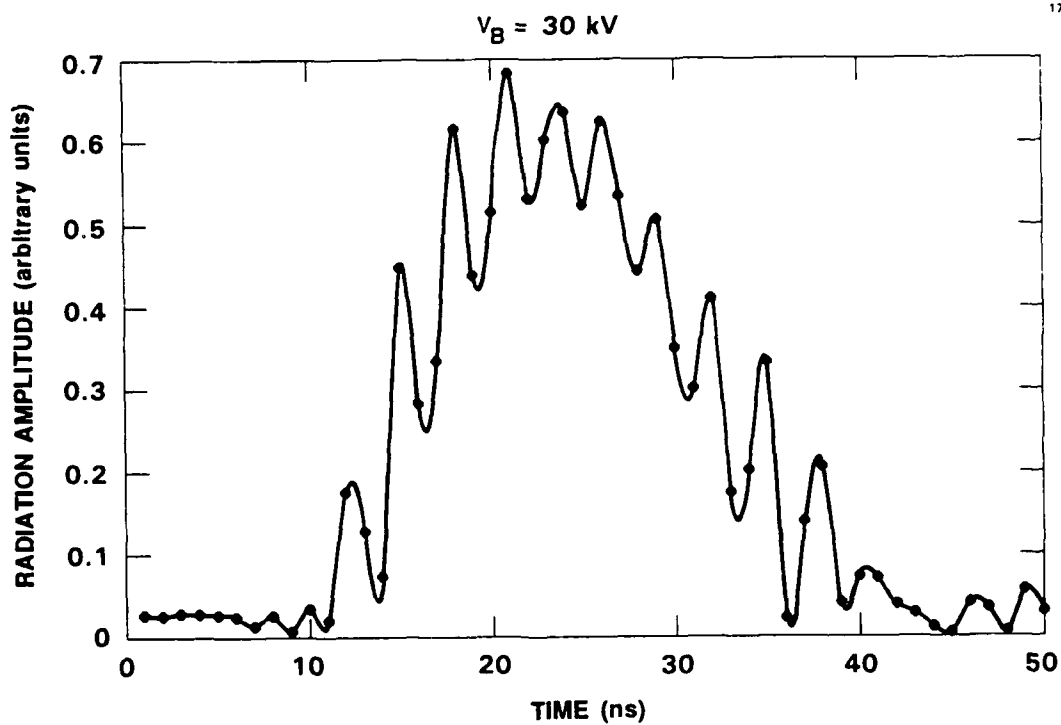


Figure 59. Peak number 1 from Figure 58 clearly shows the high- and low-frequency modulation components.

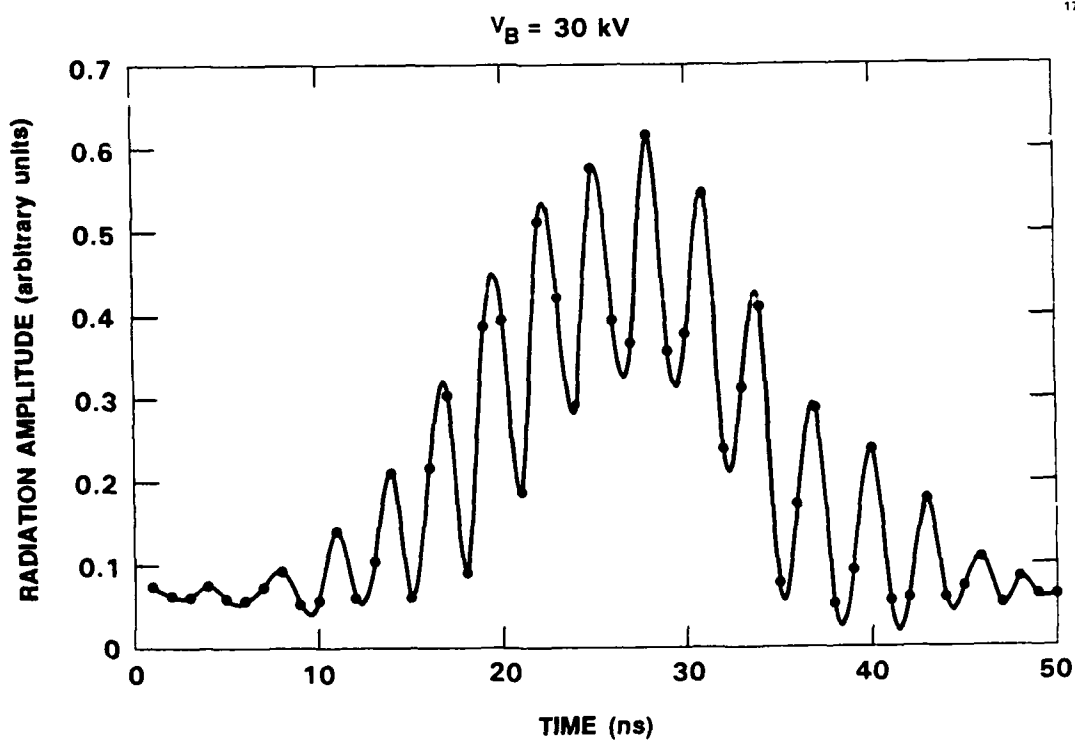


Figure 60. Peak number 2 from Figure 58.

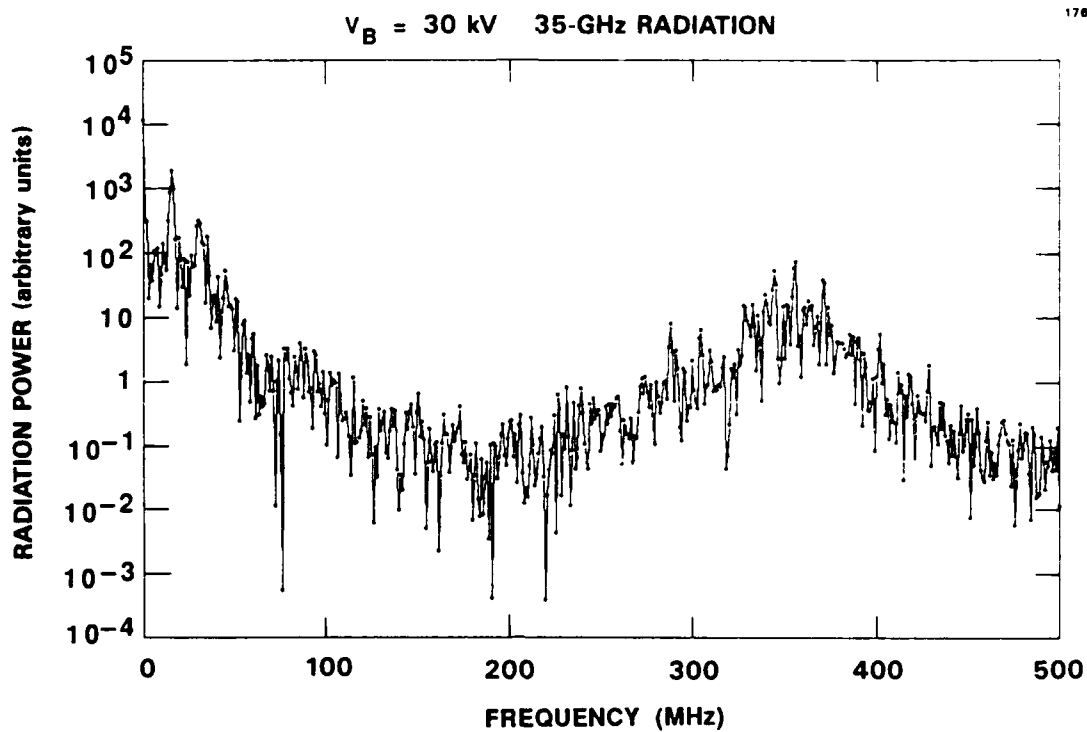


Figure 61. Two modulation frequency bands are evident in the power spectrum calculated from data shown in Figure 58.

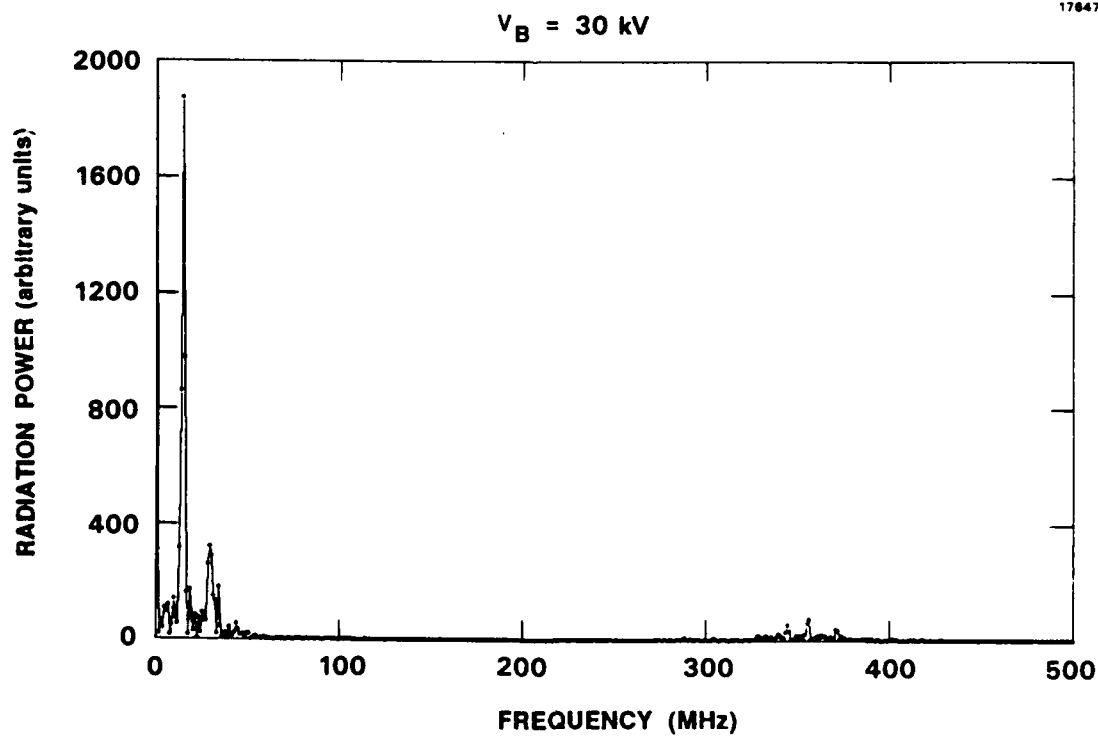


Figure 62. Display of the radiation power spectrum using a linear scale.

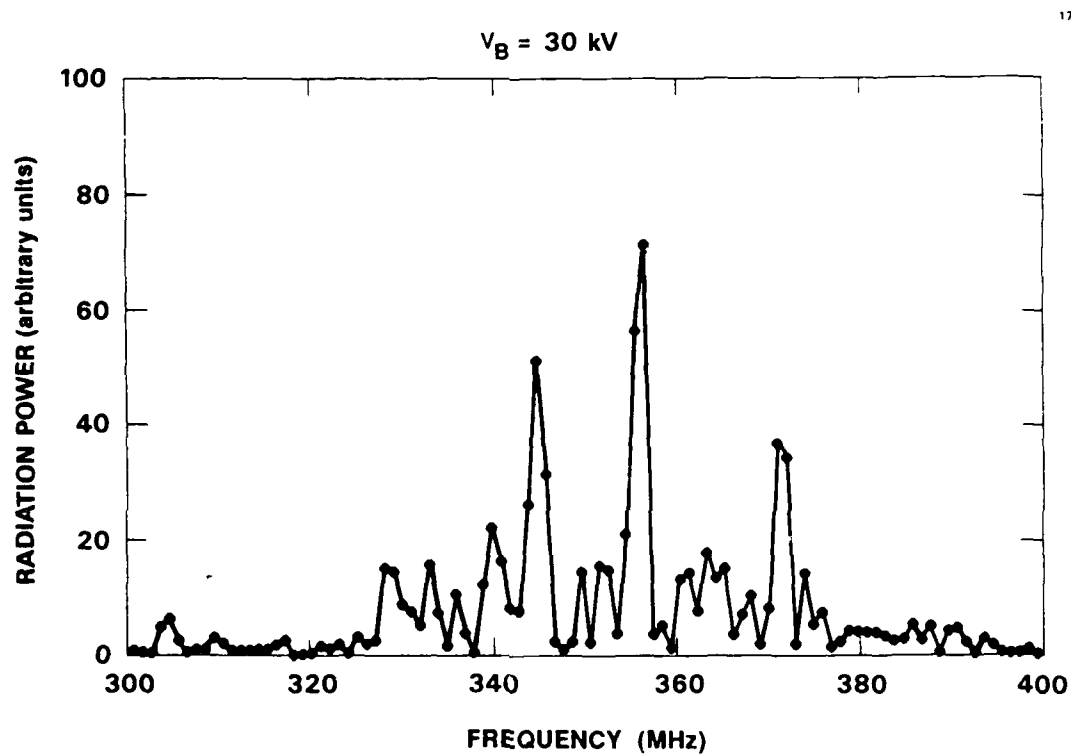


Figure 63. Display of high-frequency modulation components using an expanded scale.

investigated this by operating the 15-cm-long waveguide cavity system at reduced helium gas pressure.

3.7.1 Beam Current Scaling With Pressure

Figure 64 shows that the total beam current produced by the two-E-beam system increases as the pressure is reduced. To maximize both the influence of the modulational instability and the available beam current, we chose 12 mTorr as the operating pressure. The beam current scaling with beam discharge current at 12 mTorr is shown in Figure 65 for $V_b = 20$ kV.

3.7.2 Beam Voltage Tuning

Figure 66 displays the voltage tuning curve for 12 mTorr helium gas pressure measured using $V_b^L = V_b^H$. The maximum Ka-band power was observed for $V_b = 20$ kV. As described in Section 3.6, this voltage tuning curve does not exhibit EM power variations due to the excitation of ES cavity modes because these modes are very closely spaced for the 15-cm-long cavity. As shown in Figure 45, the scaling of millimeter-wave power with beam voltage can be explained by considering the EPW profile that is excited by the beams. The main requirement for high power emission is that the EPWs overlap spatially so they can interact to generate the millimeter-wave radiation. In general, the EPW amplitude will grow, saturate, and then decay along the beam direction. When the beam voltage is too low, the EPWs saturate and decay at the near ends of the waveguide before they interact. When the voltage is too high, the EPWs do not grow to large amplitude until they have passed each other. The radiation generated under either of these two conditions is less than that which would be obtained if the optimum beam voltage were used. At the optimum voltage the EPWs overlap near the waveguide midplane where they have the largest amplitude.

The optimum beam voltage for 12 mTorr helium gas pressure is 10 kV lower than was measured at 30 mTorr, indicating that

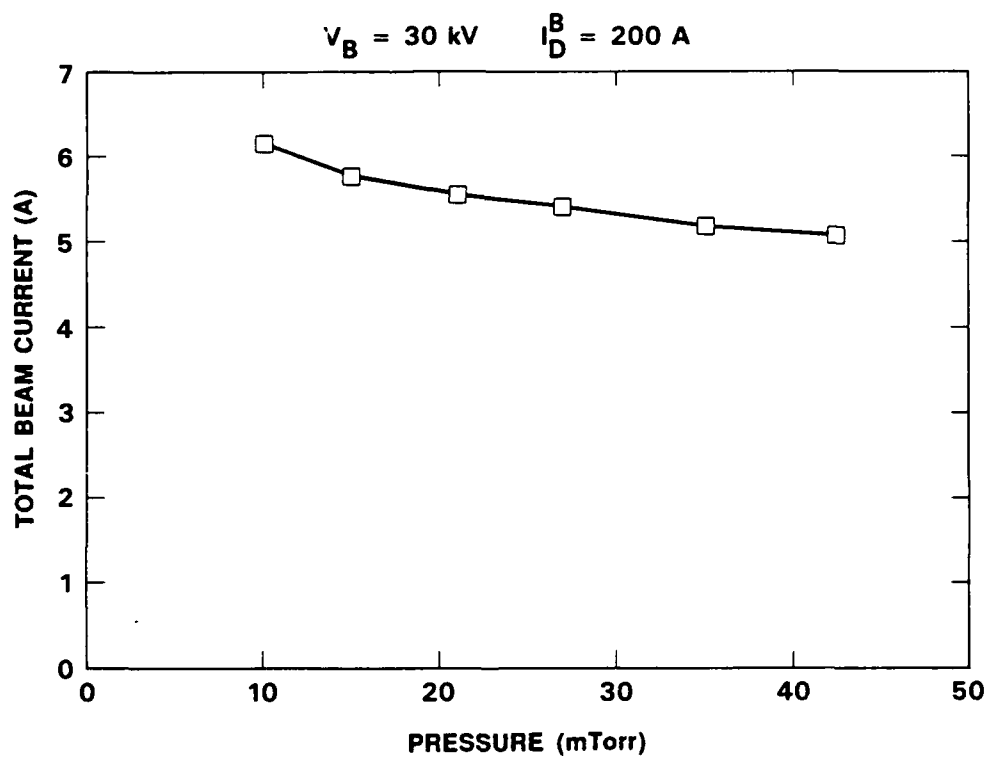


Figure 64. The beam current is maximum at low helium gas pressure.

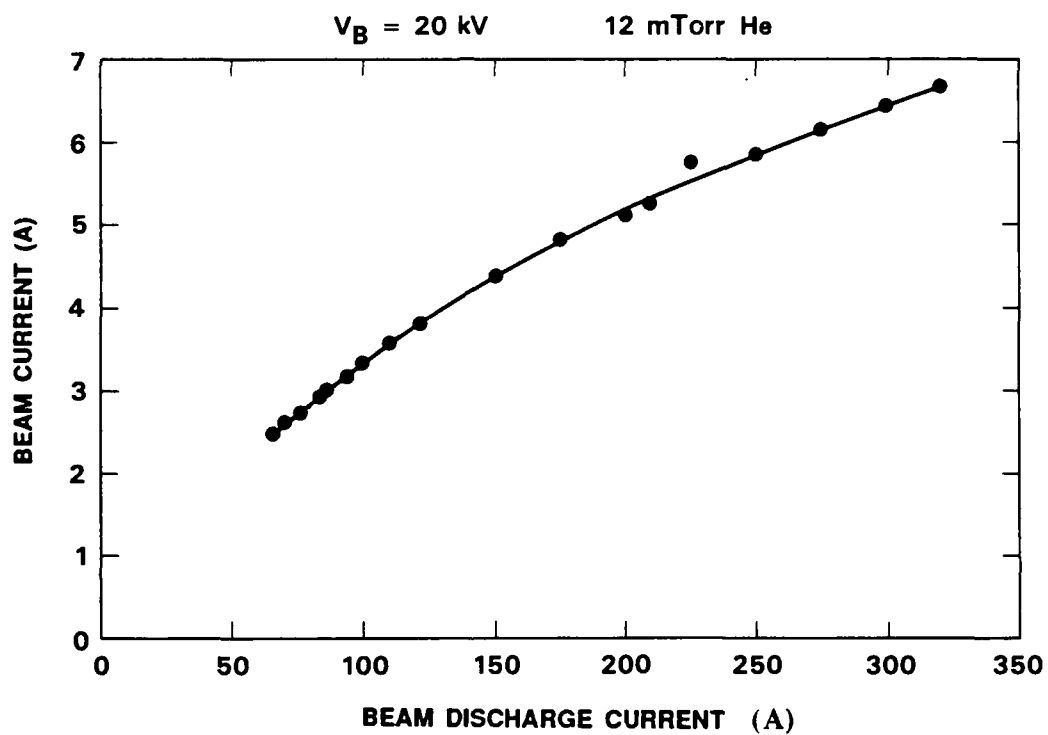


Figure 65. Beam current scaling with beam discharge current at low helium gas pressure.

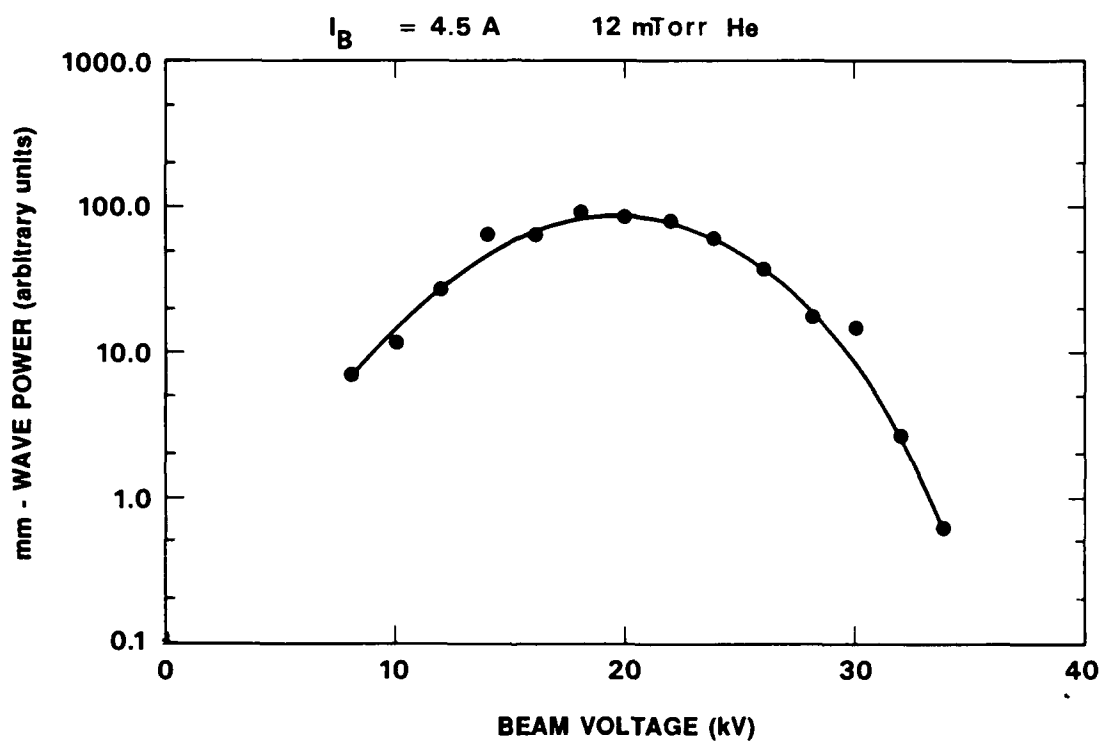


Figure 66. The radiation power scaling with beam voltage ($V_b^L = V_b^H$) shows that the power is maximized for 20 kV.

collisional effects influence the EPW excitation and the radiation generation processes. This was confirmed by recording the radiation power scaling with beam current described in the next section.

3.7.3 Saturation of Output Power at Low Gas Pressure

The radiation power scaling with total beam current is presented in Figure 67. The usual threshold is observed at $I_b = 3$ A, accompanied by a rapid increase of power with beam current until $I_b = 3.8$ A. As the beam current is raised further, the curve changes slope until the radiation nearly saturates at $I_b = 6.2$ A. This saturation behavior is not observed when higher gas pressures are used (see Section 3.4). This experiment provides direct confirmation that collisions control some aspects of the radiation generation saturation mechanisms.

3.8 ATTEMPTS TO INCREASE BEAM CURRENT FROM PLASMA-ANODE ELECTRON GUNS

The radiation power scaling with beam current measured previously demonstrated that up to the highest total beam current available, the radiation generation process had not saturated. The saturation characteristics are an indicator of the physical processes that ultimately limit the radiation power and net conversion efficiency for the three-wave mixing process. In this section we describe several different approaches we used to increase the available beam current.

3.8.1 Reduce Beam HV Gap Spacing in 1.9-cm-Long System

The Child-Langmuir space-charge-limited current in a planar diode is

$$I = (4\epsilon_0/9) (2e/m)^{1/2} (V^{3/2}/d^2) \quad , \quad (22)$$

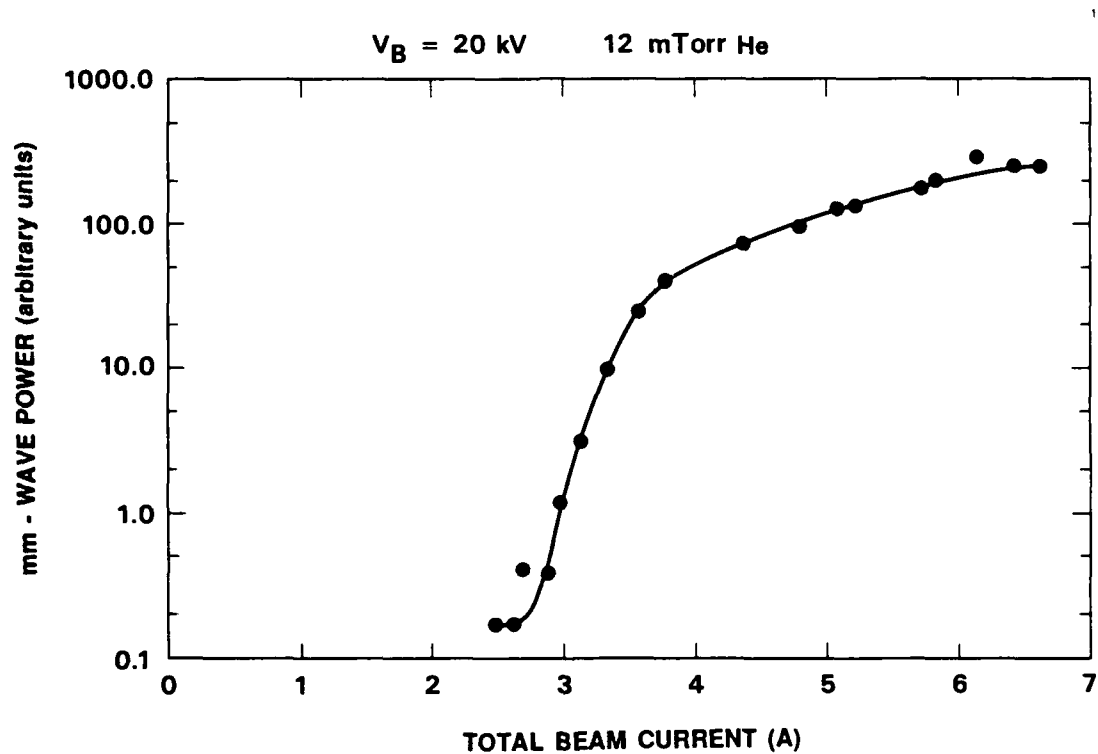


Figure 67. The radiation power begins to saturate at high beam current when low helium gas pressure is used.

where V is the gap voltage in volts, d is the gap spacing, e/m is the charge-to-mass ratio, and ϵ_0 is the permittivity of free space. Because the space-charge-limited current scales as $m^{-1/2}$, ion emission at the anode will become space-charge limited well before electron emission at the cathode. For singly charged helium ions, the space-charge-limited ion current is

$$J_i = 2.72 \times 10^{-8} (V^{3/2}/d^2) \quad . \quad (23)$$

One technique we used in an attempt to increase the space-charge-limited ion current, and consequently the E-beam current, was to decrease the gap spacing from 1.6 to 1 cm. The measured beam current scaling with beam discharge current is shown in Figure 68 for the 1.9-cm-long system with a 1-cm gap. This is compared with the scaling curve for the 15-cm-long device with a 1.6-cm-gap spacing. As expected, more beam current is produced when a small gap is used.

However, when the 1-cm-gap E-beams were installed on the 15-cm-long system, the scaling curve shown in Figure 69 was obtained. At high discharge current, we produce less beam current with the 1-cm gap, as compared with the 1.6-cm gap.

One factor is that in the 1.9-cm-long system beam electrons can easily traverse the full chamber length and interact with ions near the opposite beam cathode. The beam electrons partially cancel the ion space charge in the cathode-anode gap and thereby permit a higher net ion flux to reach the cold-cathode surface. This results in more beam current. However, when the waveguide length is increased to 15 cm, a smaller number of electrons are able to traverse the long cavity and reach the opposite cathode. This lower beam density means that less neutralization of the ion current is provided by the E-beams, fewer ions are injected to the cold-cathode, and hence lower net beam current is produced.

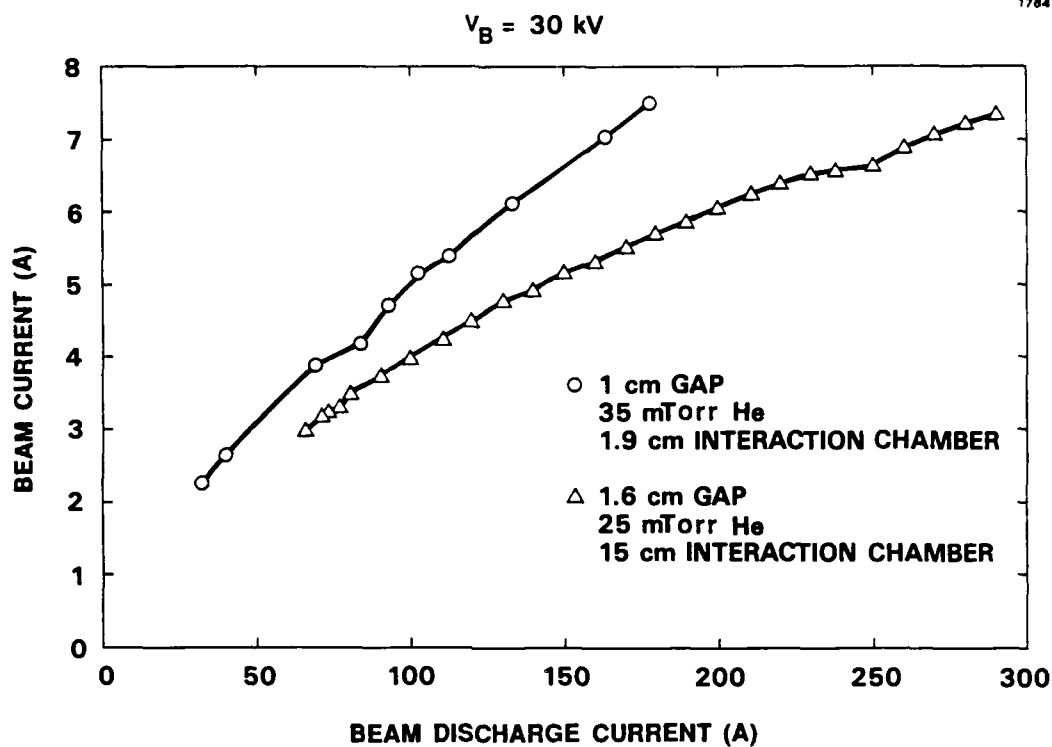


Figure 68. The electron-beam current is increased when the gap spacing is reduced in the 1.9-cm-long waveguide system.

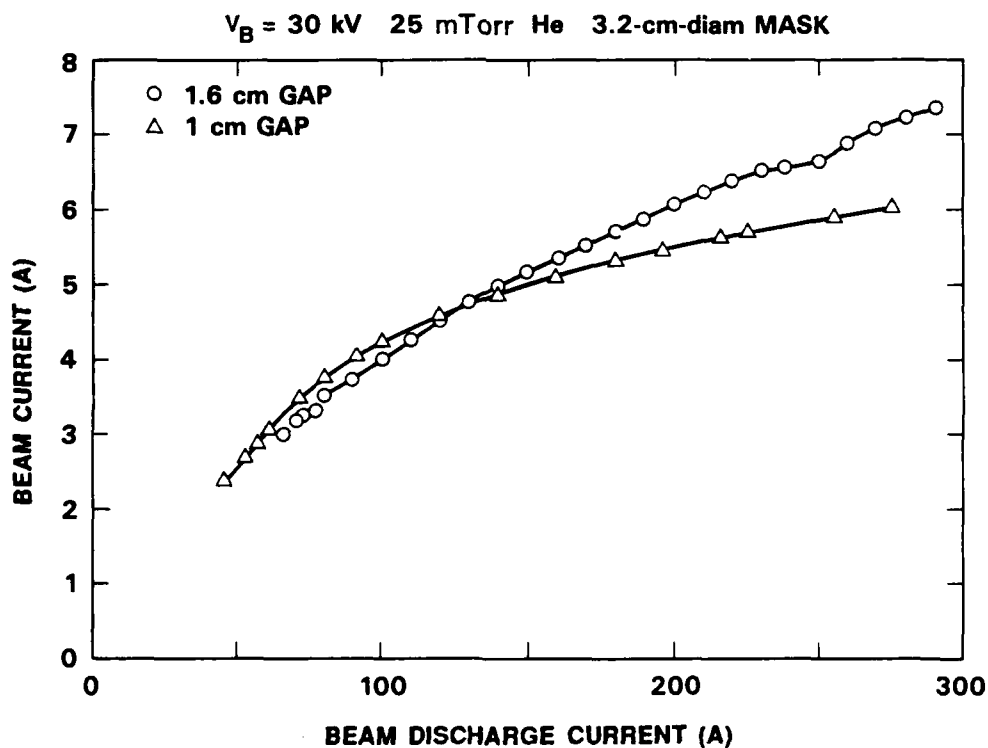


Figure 69. Reducing the gap spacing reduces the beam current in the 15-cm-long system.

This explains why more beam current can be produced in the 1.9-cm-long device as compared with the 15-cm-long system, but it does not account for the reduction in beam current at high beam discharge current as shown in Figure 69. The results indicate that we cannot increase the ion current to the cathode, and thereby increase the E-beam current, by reducing the gap spacing in the 15-cm-long system.

3.8.2 Increase Beam Mask Diameter

Another way to increase the beam current is to increase the diameter of the beam mask so that more ion current can reach the cathode surface. The space-charge-limited ion current density specified by Eq. (23) has not increased, but the beam current, which is the product of the current density and the cross-sectional area of the ion-emission surface, is now higher.

We increased the cathode mask aperture diameter from 3.2 to 4.1 cm. From the ratio of the areas of the two masks, we expect an increase in beam current of up to 64%. This is illustrated in the beam current scaling with discharge current in Figure 70 which shows that the beam current increases 2.3 A (from 4.2 to 6.5 A) for a discharge current of 100 A.

However, some of the electrons at the edge of the beam impact the sides of the waveguide cavity entrance aperture if the beam does not pinch before it reaches the cavity. The current injected into the waveguide cavity would be less than the beam current measured at the cathode, and the scaling curves would be difficult to interpret. This is apparently the situation. As shown in Figure 71, the scaling of radiation power with beam current is shifted towards higher current values when the 4.1-cm-diameter mask is used. Nonetheless, saturation of the radiation is not observed.

3.9 HOLLOW-CATHODE-PLASMA ELECTRON GUNS

An advanced electron-gun (E-gun) technique has recently been developed for a separate Hughes IR&D-funded project. The

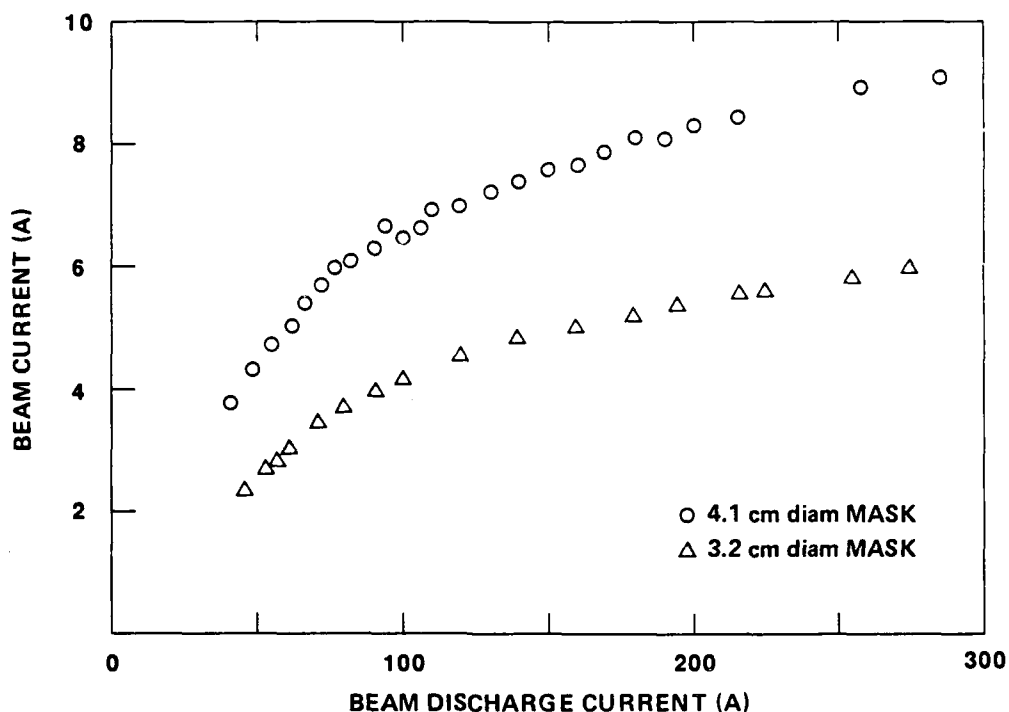


Figure 70. The emitted beam current increases when the beam mask diameter is increased.

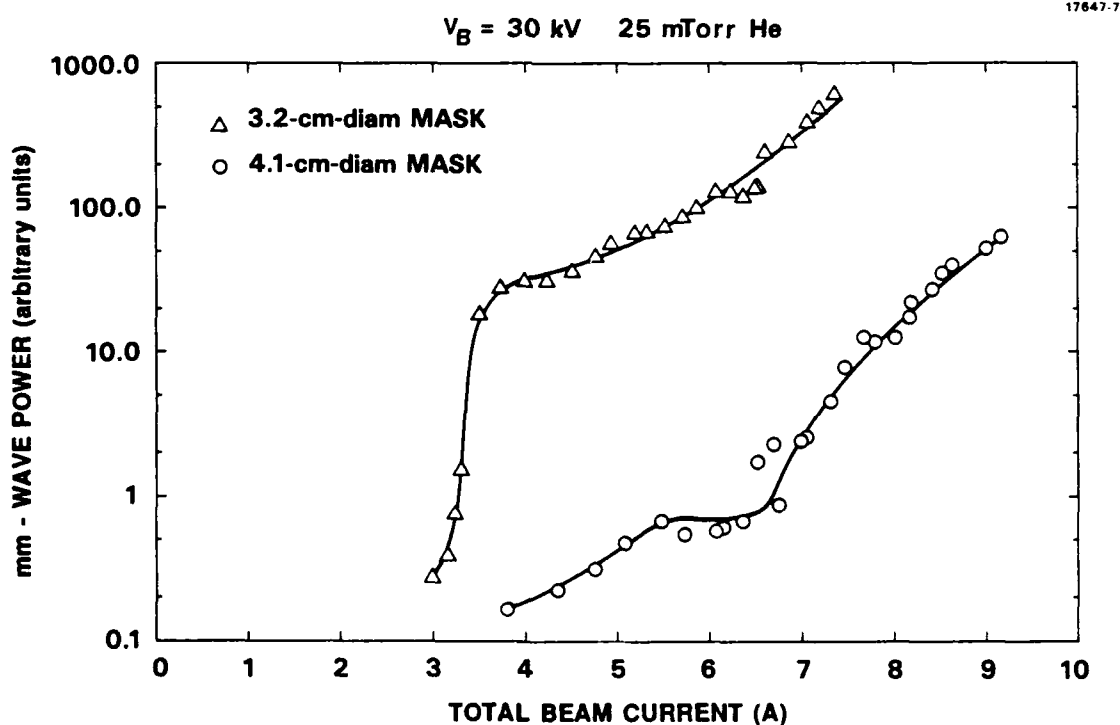


Figure 71. The radiation power scaling with beam current indicates that some of the beam current intercepts the cavity entrance aperture and is not injected into the waveguide cavity.

new gun is capable of producing much higher current density E-beams, and it has been used to demonstrate single-beam radiation emission via three-wave mixing between beam-excited and backscattered EPWs. Called the Hollow-Cathode-Plasma (HCP) E-gun, it employs a cold-cathode glow discharge in low-pressure helium gas (1 to 50 mTorr) from the inside surface of a hollow-cathode (HC) enclosure to an anode-potential grid located just outside an aperture in the HC wall, as shown in Figure 72.

The HC configuration with large cathode-to-anode area ratio provides efficient confinement of ionizing electrons inside the HC, and thus high-density plasma generation at low gas pressures. The HC plasma is modulated by applying a negative pulse to the HC relative to the anode grid with the HC-discharge pulse, as shown in Figure 72. A positively biased (~ 1 kV) keep-alive anode-wire is also inserted in the HC to maintain a low-current (10 mA) continuous discharge between pulses so that the high-current discharge pulse can be initiated on-command with low jitter (≤ 10 ns). The HC-discharge grid has a high optical transparency ($\sim 80\%$), yet ultrasmall apertures (~ 250 μm diameter). The high-density plasma ($n_e \sim 3 \times 10^{12} \text{ cm}^{-3}$ at 60 A/cm^2 current density) behind the anode-sheath at this grid provides the high-current-density electron emission in the HCP E-gun. Electrons are extracted from the plasma and accelerated to high energy by applying a high positive potential to the E-gun anode electrode, which is to the right of the HC-discharge grid in Figure 72. The beam is electrostatically focused through the aperture in the anode to form a high-current-density, circular-cross-section beam.

A proof-of-principle HCP E-gun experiment has demonstrated the generation of well-collimated intense beams at voltages up to 70 kV, currents up to 90 A, and current densities up to 20 A/cm^2 . The cathode itself has also demonstrated electron emission at a current density of 60 A/cm^2 for pulsewidths up to 100 μs . Furthermore, in a demonstration of single-beam

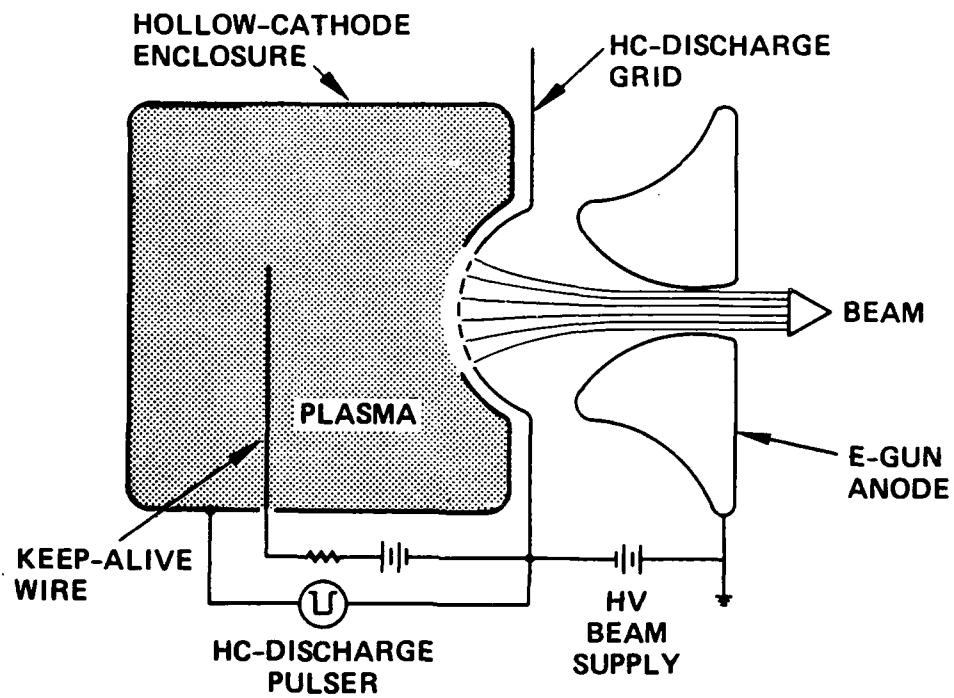


Figure 72. Hollow-cathode-plasma electron-gun configuration.

radiation generation, the proof-of-principle HCP gun injected a single 33-kV, 18-A/cm² beam into a 1.6-cm-diameter waveguide and generated broadband radiation in the frequency range from 15 to 38 GHz. The radiation output had the same modulation characteristics and tunability as was previously measured in the counterstreaming beam experiment using the 15-cm-long waveguide cavity. The current-density threshold for single-beam radiation generation operation was approximately 12 A/cm².

We adapted two new HCP E-guns to the counterstreaming-beam experiment shown in Figure 73. The 15-cm-long cylindrical waveguide with the wire-anode discharge and the X-band output waveguides were described in Section 2. Figure 74 details the HCP E-gun mechanical assembly. The HC is mounted on the same epoxy-casting high-voltage bushing that was used for the PAG. The HC anode is a fine-mesh grid that also acts as the cathode electrode for the electron beam. The E-gun anode is fabricated using the same fine-mesh grid. The E-gun grid spacing of 0.6 cm provides reliable high-voltage operation up to about 60 kV. The beam diameter at the injection point is defined by the 2.5-cm HC aperture.

The HCP E-gun circuit is shown in Figure 75. The 5 kV power supply charges the 15 μ F capacitor through a 50-k Ω resistor and a diode. When the 8451H CROSSATRON modulator switch is turned on, the full negative voltage is applied to the HC. The discharge is initiated by a few ions that stream into the hollow cathode from the wire-anode discharge within the cylindrical waveguide cavity. The hollow-cathode discharge current is varied by adjusting the capacitor-charge voltage and the current-limiting resistor (shown as 80 Ω in Figure 75). The hollow-cathode modulator is mounted on a carefully constructed deck that floats at the beam voltage (\sim 50 kV). Current transformers are used to monitor the beam and hollow-cathode discharge currents.

Figure 76 shows typical hollow-cathode discharge and beam current waveforms. We found that the discharge and beam currents

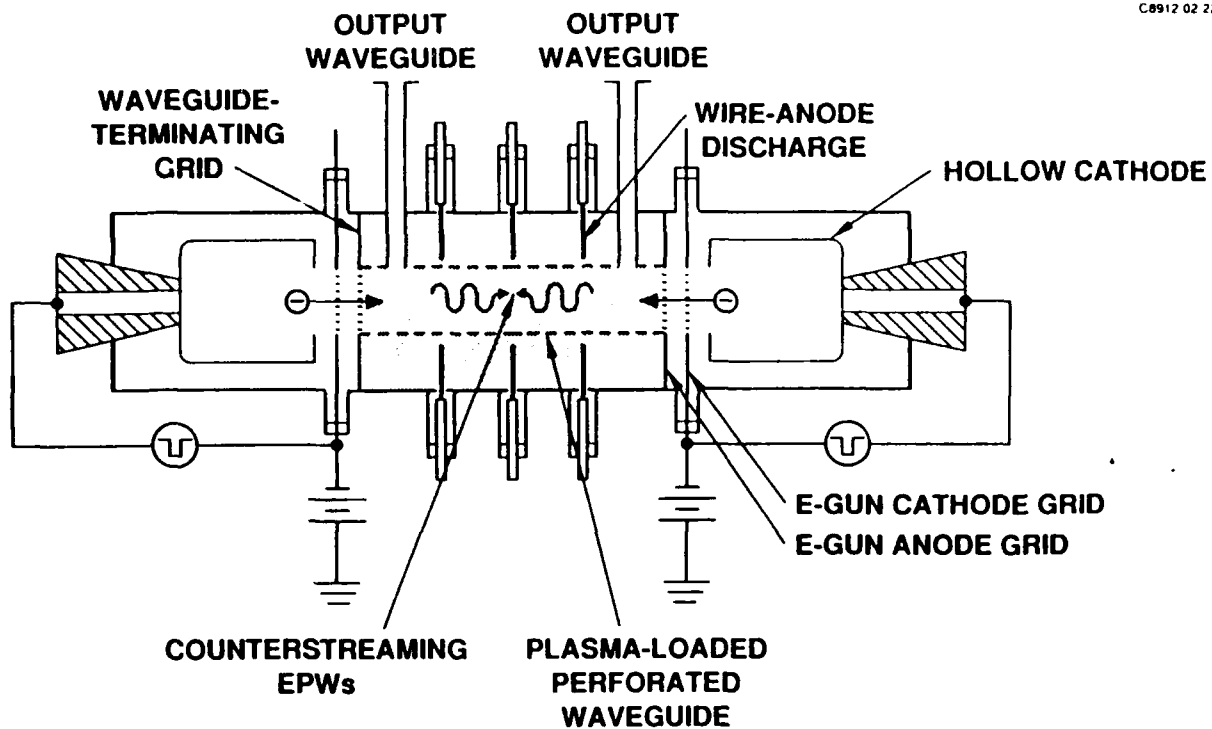


Figure 73. Three-wave mixing experiment driven by hollow-cathode-plasma electron guns.

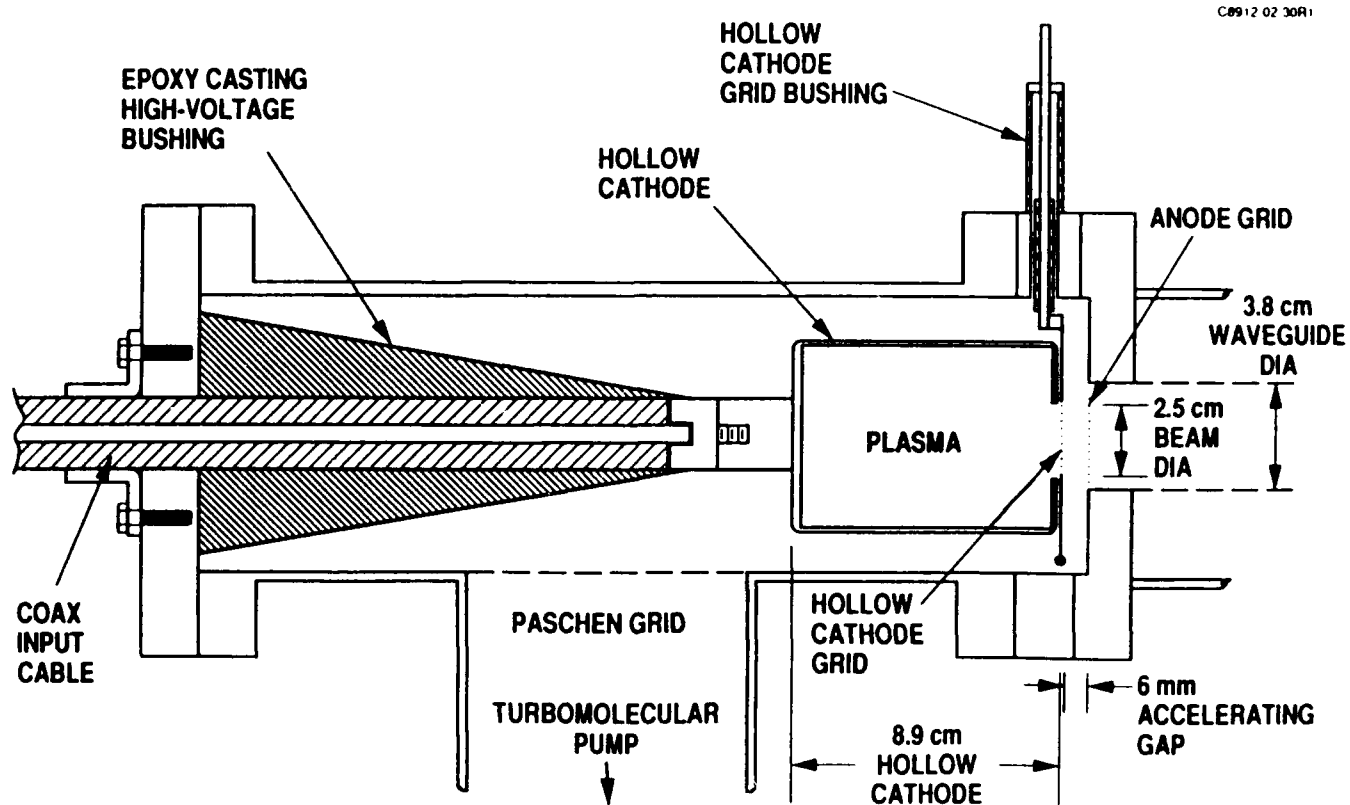


Figure 74. HCP E-gun mechanical assembly drawing.

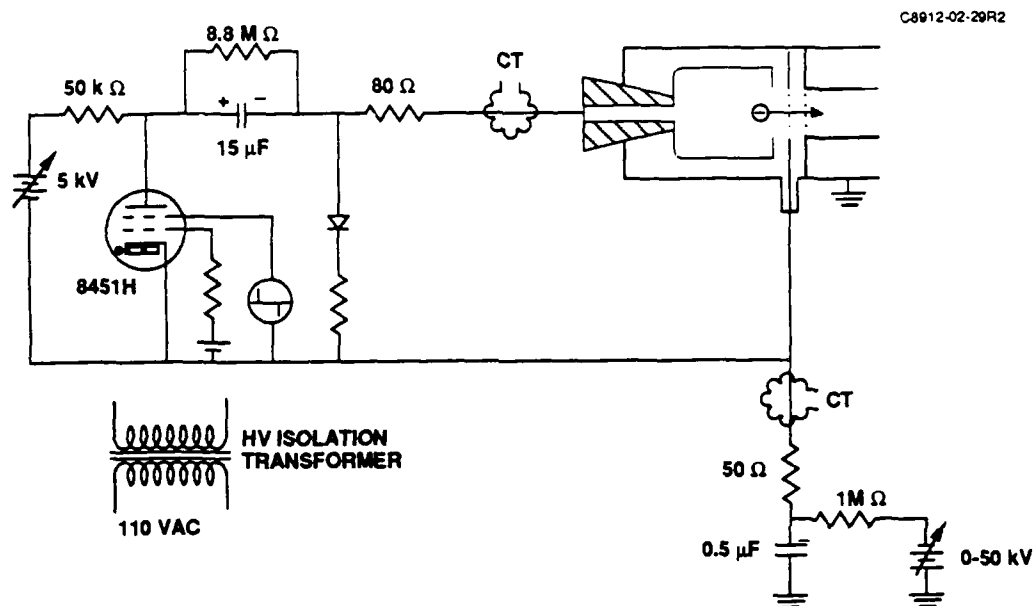


Figure 75. HCP E-gun modulator and HV circuit.

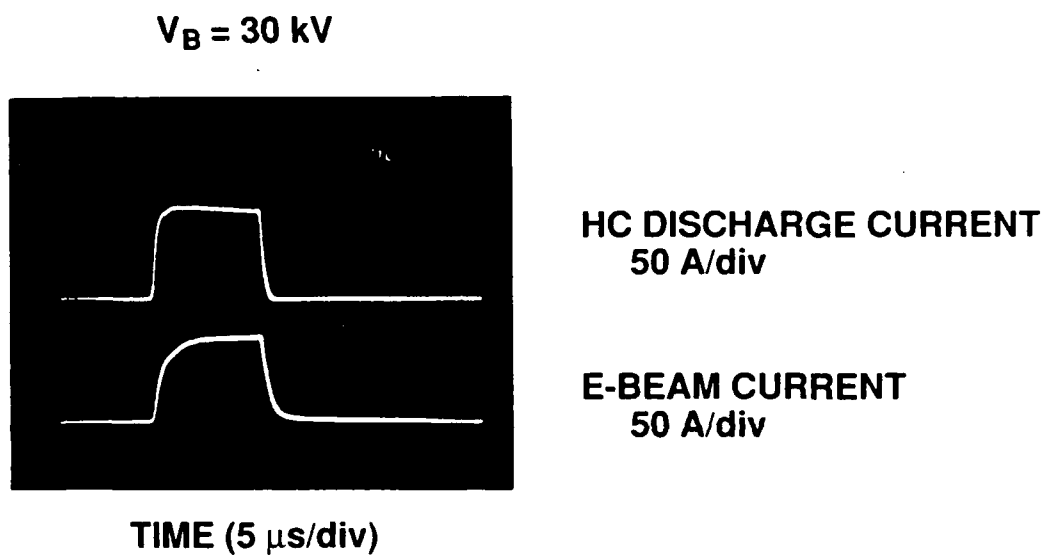


Figure 76. HCP E-gun hollow-cathode discharge and beam-current waveforms.

are approximately equal until we approach the space-charge-limited electron current for the 0.6-cm gap. This effect is clearly shown in Figure 77, which is a plot of the beam-current scaling with discharge current for a beam voltage of 30 kV.

3.10 SCALING EXPERIMENTS WITH HIGH BEAM CURRENT

We measured the Ka-band radiation-power scaling with total beam current in the HCP-E-gun-driven system for several different conditions. The radiation detection and integration circuits were described previously in Section 3.4. As shown in Figure 78, the radiation-power threshold is now 2 A of total beam current at a beam voltage of 28 kV. The cylindrical-waveguide discharge current was 400 A and the helium-gas pressure was 47 mTorr for this experiment. When the total beam current reaches about 9 A, the radiation frequency shifts from Ka-band to V-band. This is caused by beam impact ionization of the helium gas. This raises the radiation frequency beyond the calibration range of our crystal detectors.

The lower radiation threshold current is due to the smaller HCP E-gun beam diameter, and the resulting higher injected beam-current densities. The HCP E-gun has a beam output aperture of 2.5 cm, with a total area of 4.9 cm^2 . The PAG had a beam output aperture of 3.2 cm, with a total area of 8 cm^2 . Hence, when the beam current per PAG was 1.5 A, the beam current density at the injection point (prior to beam pinching) was $(1.5 \text{ A})/(8 \text{ cm}^2) = 0.19 \text{ A/cm}^2$. For an HCP E-gun beam current of 1 A per beam (for a total beam current of 2 A), the injected beam current density is 0.2 A/cm^2 . These two threshold currents are in excellent agreement.

We repeated the Ka-band radiation power scaling with beam current at reduced helium-gas pressure to reduce the beam-ionization effects. The helium-gas pressure was 26 mTorr, the cylindrical-waveguide discharge current was 60 A, and the beam

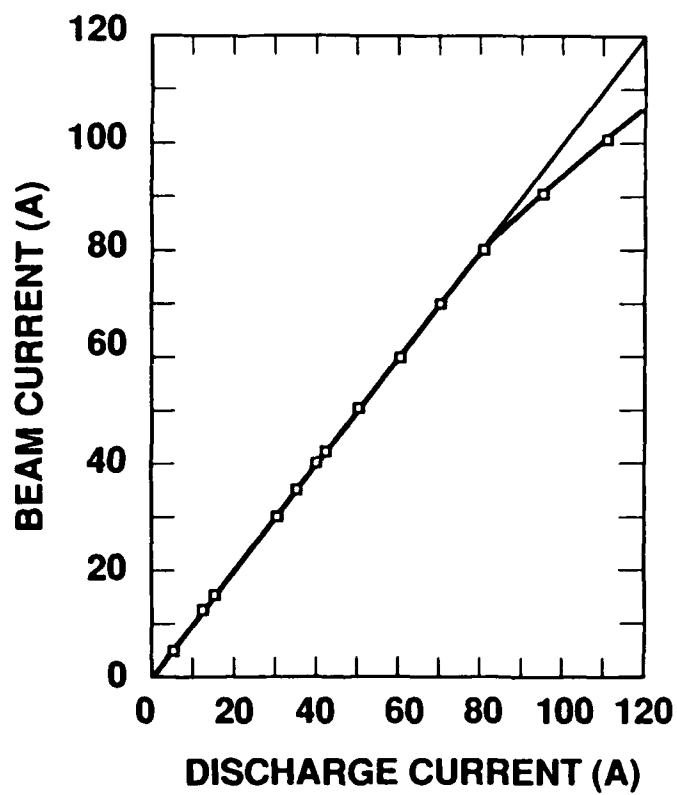


Figure 77. HCP E-gun beam-current scaling with hollow-cathode discharge current.

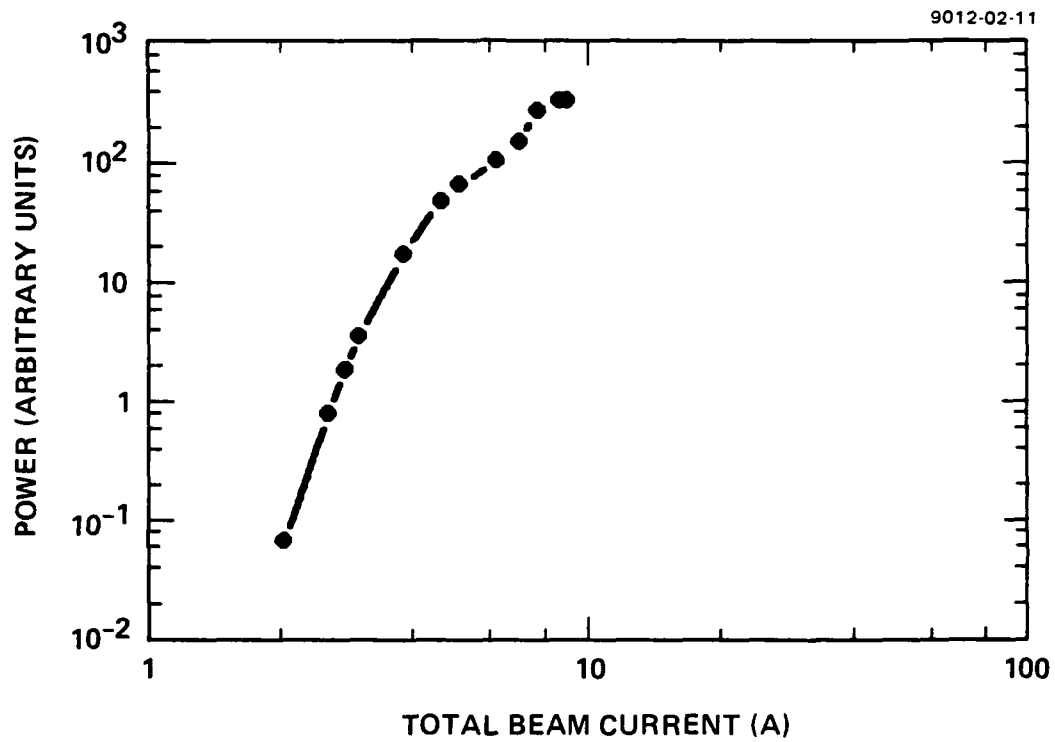


Figure 78. Radiation power scaling with total beam current.

voltage was 28 kV. As shown in Figure 79, the radiation-power threshold is now 1.3 A of total beam current (single-beam injection-current density of 0.13 A/cm²). The radiation-power scaling has two different slopes. From 1.3 to 9.3 A, the radiation power increases at $I_b^{1/2}$. However, above 9.3 A, the power scales with beam current as I_b^2 . At 13.6 A, the frequency again shifts beyond Ka-band. This is different from the scaling in Figure 46, where we found that the power increases rapidly with beam current near the beam-pinching threshold, and then increases at a slower rate above this threshold.

Beam ionization of the helium gas not only raises the plasma density within the cylindrical waveguide, but may also produce axial and radial plasma-density gradients. Density gradients will support EPWs with different frequencies, thereby spreading the EM-wave energy over a wide frequency range, and limiting the instantaneous power at any specific frequency.

3.11 TEMPORAL EVOLUTION OF RADIATION SPECTRUM

The beam-ionization effects noted in the previous section will change the radiation frequency as the beam continuously ionizes gas molecules. We investigated this process by measuring the radiation spectrum using an Hewlett-Packard 8565A spectrum analyzer. We measured the temporal variations of the radiation power at one frequency by operating the spectrum analyzer as a tuned receiver with a 3-MHz IF bandwidth. The output is recorded using a 100-megasample/second digitizer and ensemble averaged for five electron-beam pulses. After the data are recorded, the receiver frequency is changed and the process is repeated. The radiation is coupled into the RFI screen room housing our diagnostic equipment using X-band rectangular waveguide. The frequency range for the spectra extends from 6.6-GHz (limited by X-band waveguide cutoff) to 22 GHz (spectrum analyzer upper-frequency limit without external mixers).

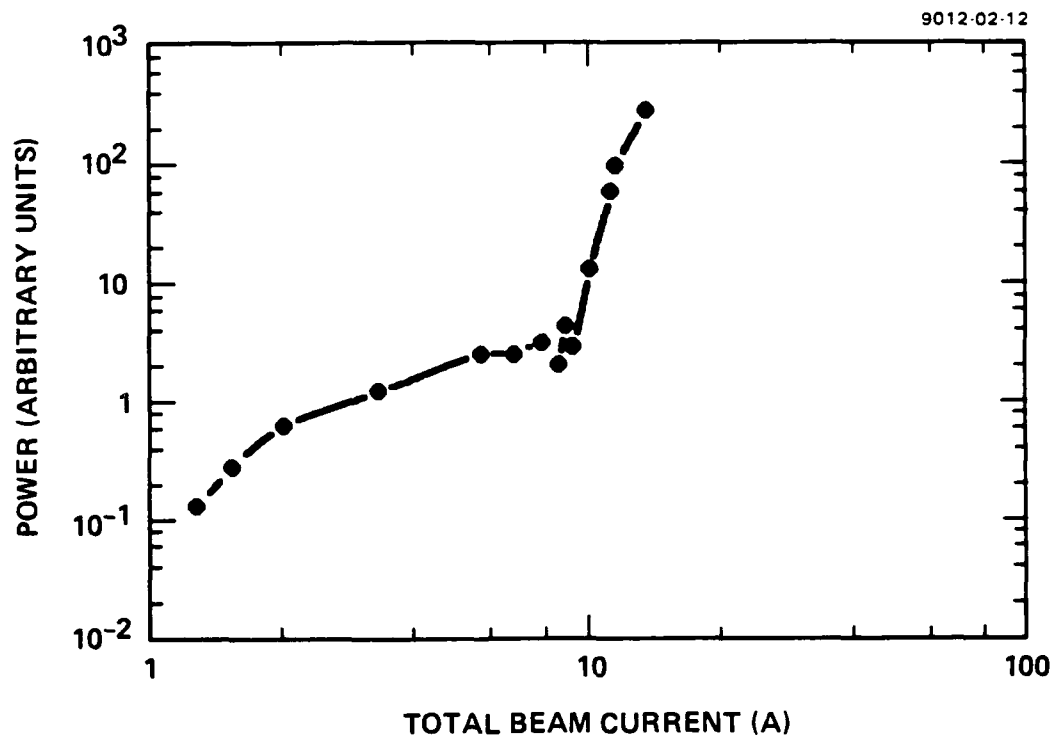


Figure 79. Radiation power scaling with total beam current at reduced helium-gas pressure.

This technique enabled us to identify the ω_p and $2\omega_p$ spectral components that are both excited by high-current beams. A typical ensemble-averaged receiver signal is shown in Figure 80. We analyze the data in two different ways. By noting the time (relative to beam turn on) at which radiation at a given frequency is first observed, we can investigate the beam-ionization effects. Alternatively, we can reconstruct a complete, temporally resolved spectrum by plotting the power at each frequency at a specified time after beam injection. Repeating this process for different times after beam injection permits us to monitor the complete evolution of the spectrum.

We investigated the temporal evolution of the ω_p and $2\omega_p$ spectral components as functions of the beam current and cylindrical-waveguide discharge current. Figures 81 and 82 are plots of the temporal evolution of the ω_p and $2\omega_p$ spectral components for total beam currents of 6 and 9.2 A, respectively. The other parameters were 28-kV beam voltage, 60-A cylindrical-waveguide discharge current, and 26-mTorr helium-gas pressure. The data in Figure 83 was measured with a cylindrical-waveguide discharge current of 300 A, a total beam current of 6 A, a beam voltage of 28 kV, and a helium-gas pressure of 26 mTorr.

Several trends are apparent in Figures 81, 82 and 83. First, we can unambiguously identify the ω_p and $2\omega_p$ spectral components for the first time. We believed, based on prior experiments,⁴ that the radiation at ω_p should be produced within our system by conversion of the EPWs on density gradients, or by EPW scattering from ion waves. However, we had been unable to identify radiation at ω_p until now. Second, we observe that beam-ionized plasma is a large fraction of the total cylindrical-waveguide plasma density. The plasma frequency changes at a rate of 0.7 GHz/ μ s for $I_b = 6$ A (Figure 81) and 1.7 GHz/ μ s for $I_b = 9.2$ A (Figure 82). When the cylindrical-waveguide discharge current is increased to 300 A (Figure 83), the plasma frequency still increases at a rate of 1 GHz/ μ s. These frequency slew rates

9012-02-13

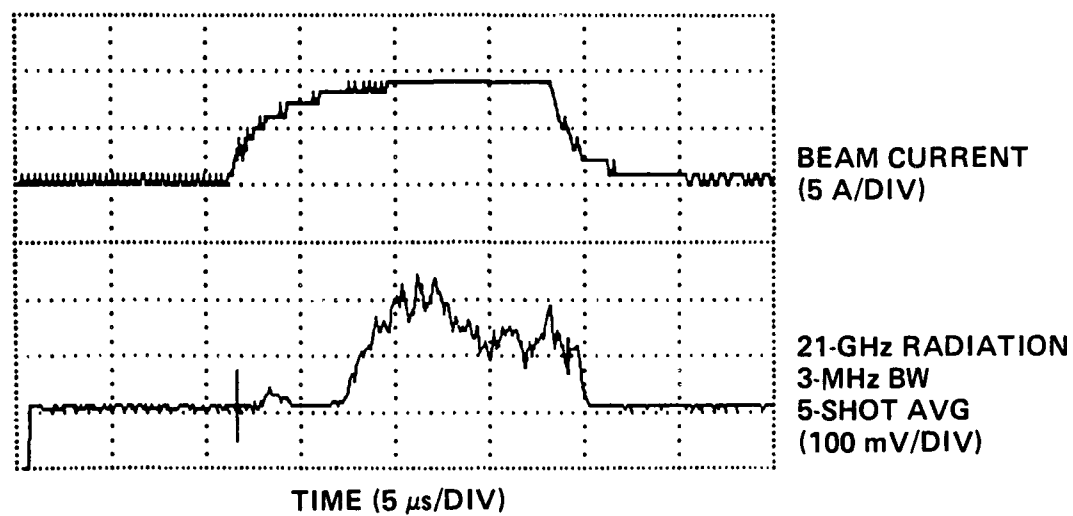


Figure 80. Radiation power at 21 GHz measured using tuned receiver.

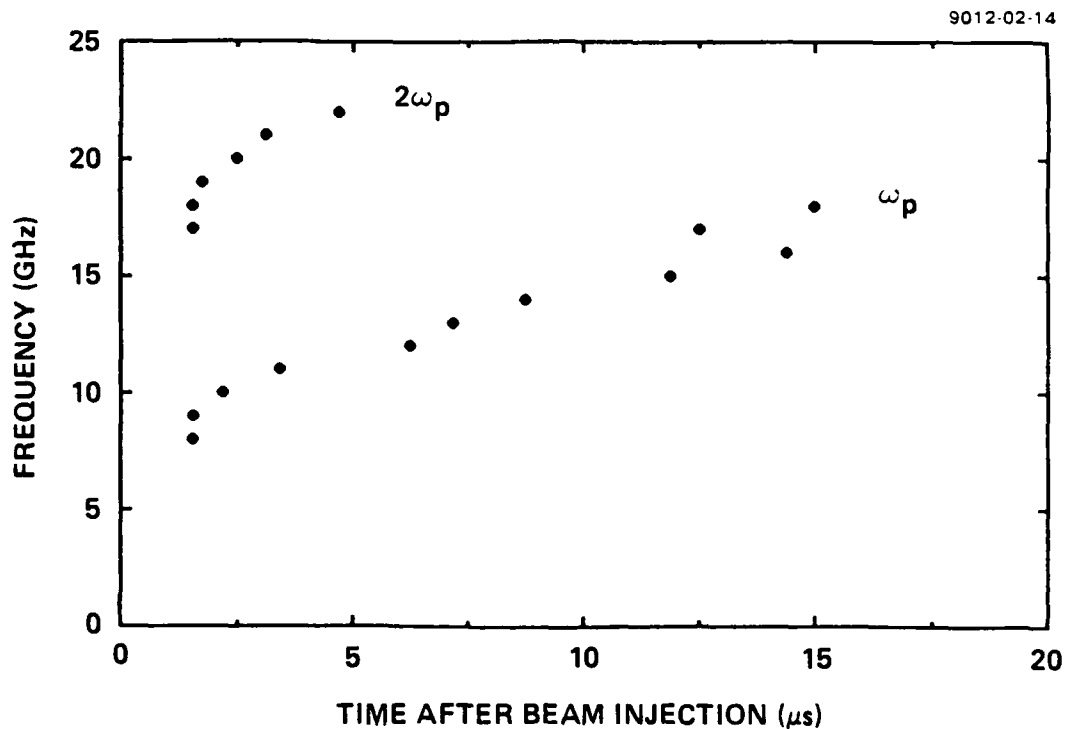


Figure 81. Temporal evolution of ω_p and $2\omega_p$ spectral components with $I_B = 6$ A. The beam voltage was 28 kV, the cylindrical waveguide discharge current was 60 A, and the helium-gas pressure was 26 mTorr.

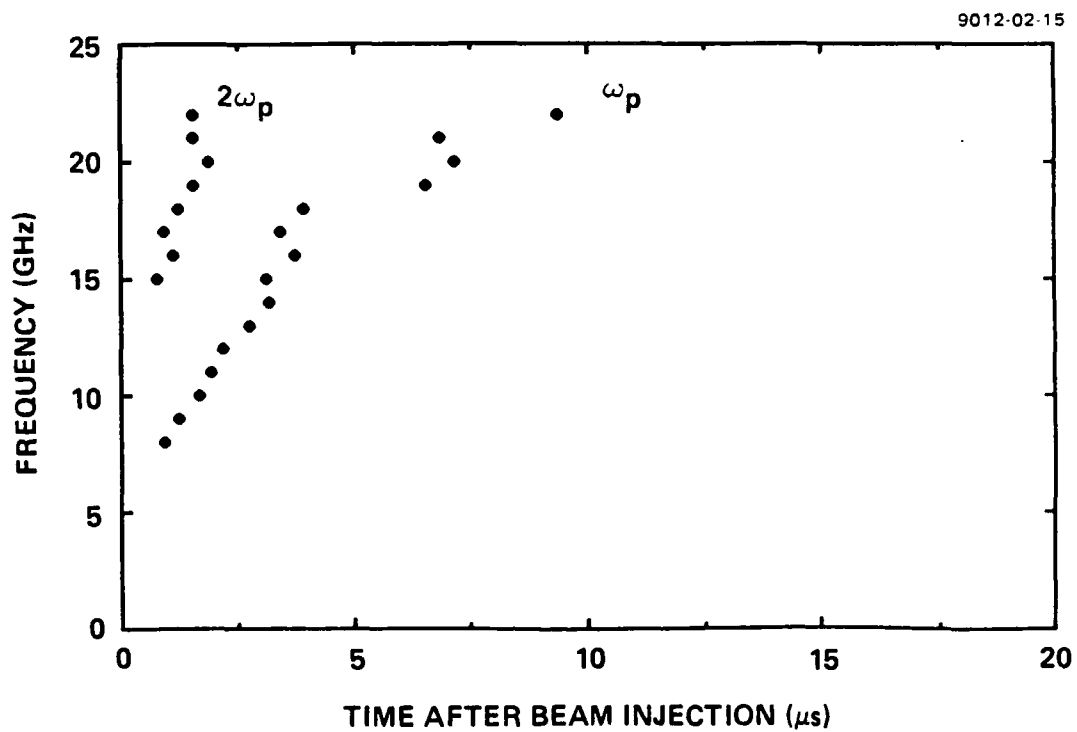


Figure 82. Temporal evolution of ω_p and $2\omega_p$ spectral components with $I_b=9.2$ A. The beam voltage was 28 kV, the cylindrical waveguide discharge current was 60 A, and the helium-gas pressure was 26 mTorr.

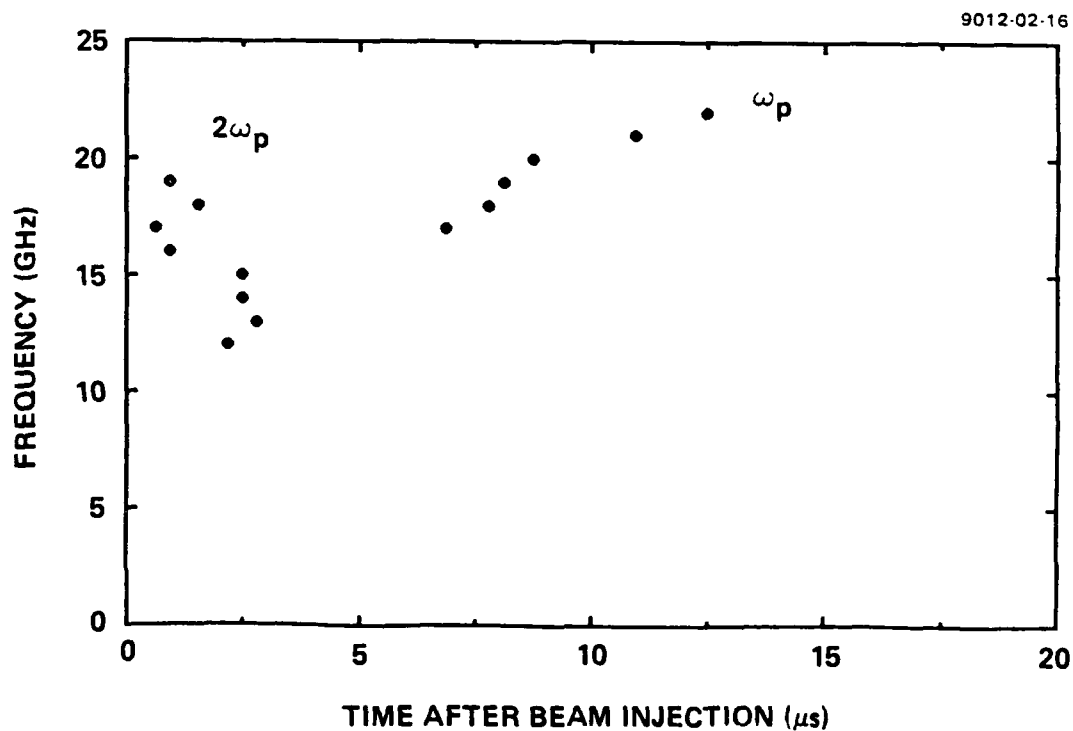


Figure 83. Temporal evolution of ω_p and $2\omega_p$ spectral components with $I_B=6$ A and $I_D=300$ A. The beam voltage was 28 kV and the helium-gas pressure was 26 mTorr.

confirm our conclusion in Section 3.10 that the radiation frequency changes substantially during a high-current beam pulse.

We used the data from the three experiments described above to reconstruct the radiation spectra at 5, 10 and 15 μ s (after beam turn on) shown in Figures 84, 85, and 86. In Figure 84, we clearly identify the ω_p (11 GHz) and the $2\omega_p$ (21 GHz) radiation peaks 5 μ s after turn on of the electron beam. Beam ionization of the helium gas raises the plasma density and the frequency of ω_p emission at 10 and 15 μ s. This also shifts the $2\omega_p$ peaks above the detection range for the spectrum analyzer. As shown in Figure 85, the radiation bandwidth increases when the beam current is raised to 9.2 A. The ω_p -radiation frequency also increases during the beam pulse because beam ionization contributes to the plasma density.

When the cylindrical-waveguide discharge current is increased to 300 A, the ω_p peaks are all centered at about 18 GHz and the frequency does not change appreciably during the beam pulse. As expected, the radiation power at $2\omega_p$ is mainly at 36 GHz. This demonstrates that the beam ionization effects are minimized for high discharge currents and low beam currents; the beam-ionized plasma is a small fraction of the total plasma density.

3.12 RADIATION PRODUCED BY INTERACTION OF SINGLE ELECTRON BEAM WITH BACKGROUND PLASMA

A single electron beam can produce radiation at $2\omega_p$ if the beam-excited EPWs grow to large amplitude, and then produce counterpropagating EPWs. For example, a large-amplitude EPW can parametrically decay into a backward-propagating EPW and an ion wave. Another process is backscattering of an EPW by density perturbations caused by the intense EPW electric field. This process is diagrammed in Figure 87.

We observe radiation produced by the interaction of a single electron beam with the background plasma. The radiation is strongly amplitude modulated, with the same characteristics

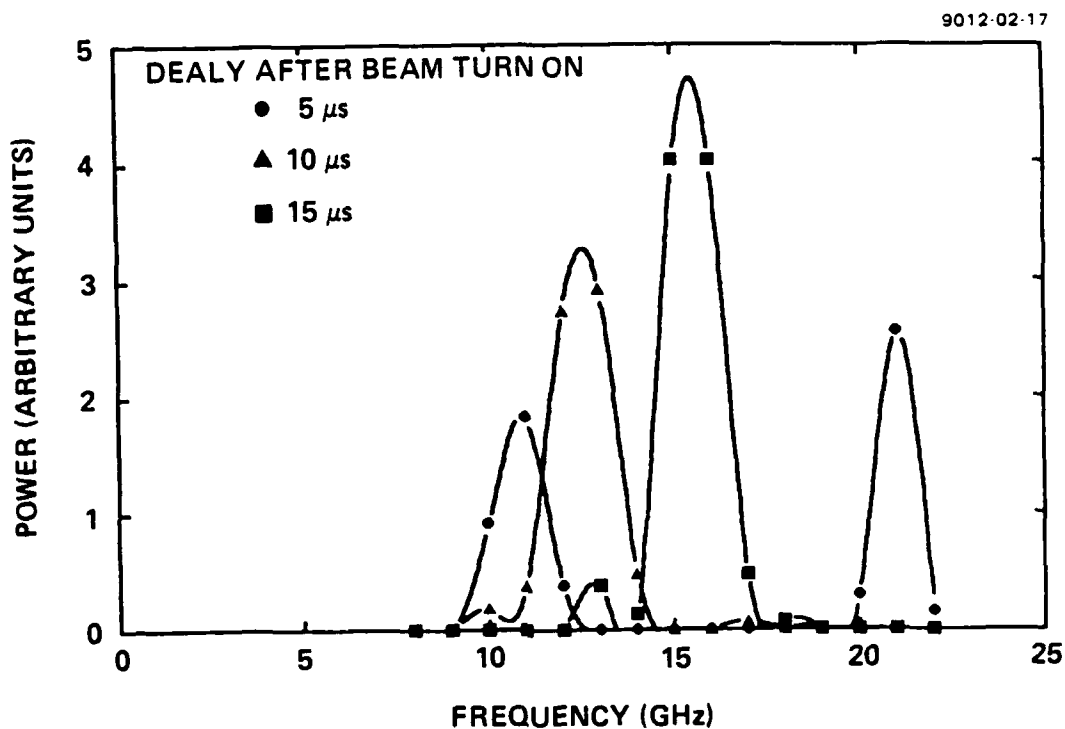


Figure 84. Radiation spectrum measured using tuned receiver with 60-A discharge current, 6-A total beam current, 28-kV beam voltage, and 26 mTorr helium-gas pressure. At 5 μ s after beam turn on, radiation peaks are observed at 11 (ω_p) and 21 GHz ($2\omega_p$).

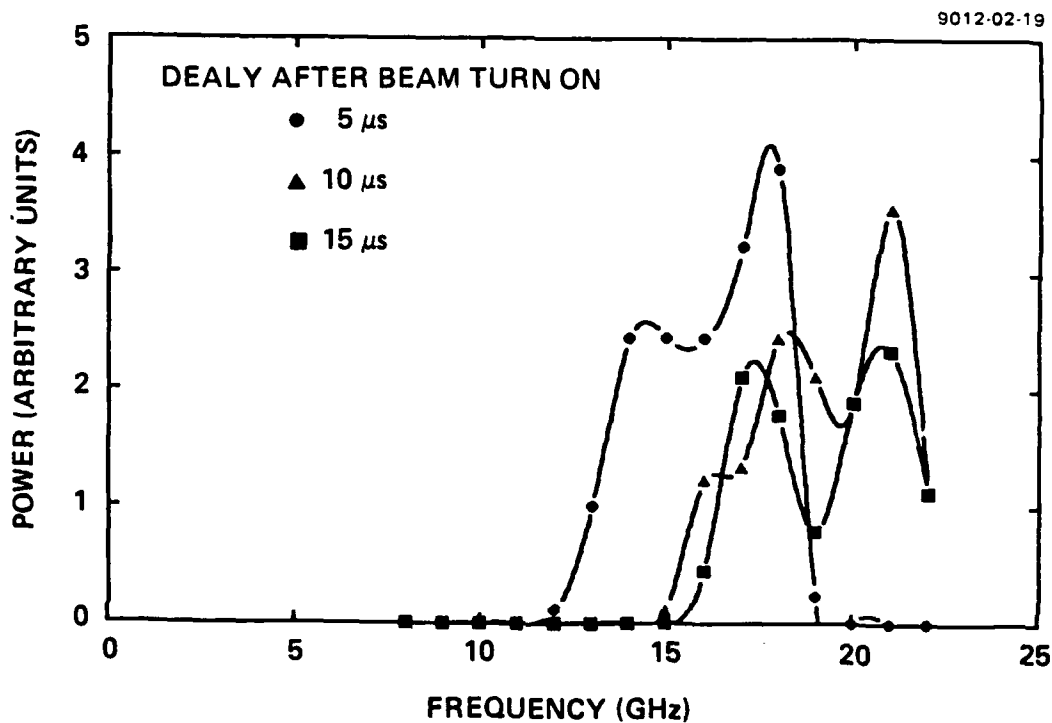


Figure 85. Radiation spectrum with 60-A discharge current, 9.2-A total beam current, 28-kV beam voltage, and 26 mTorr helium-gas pressure.

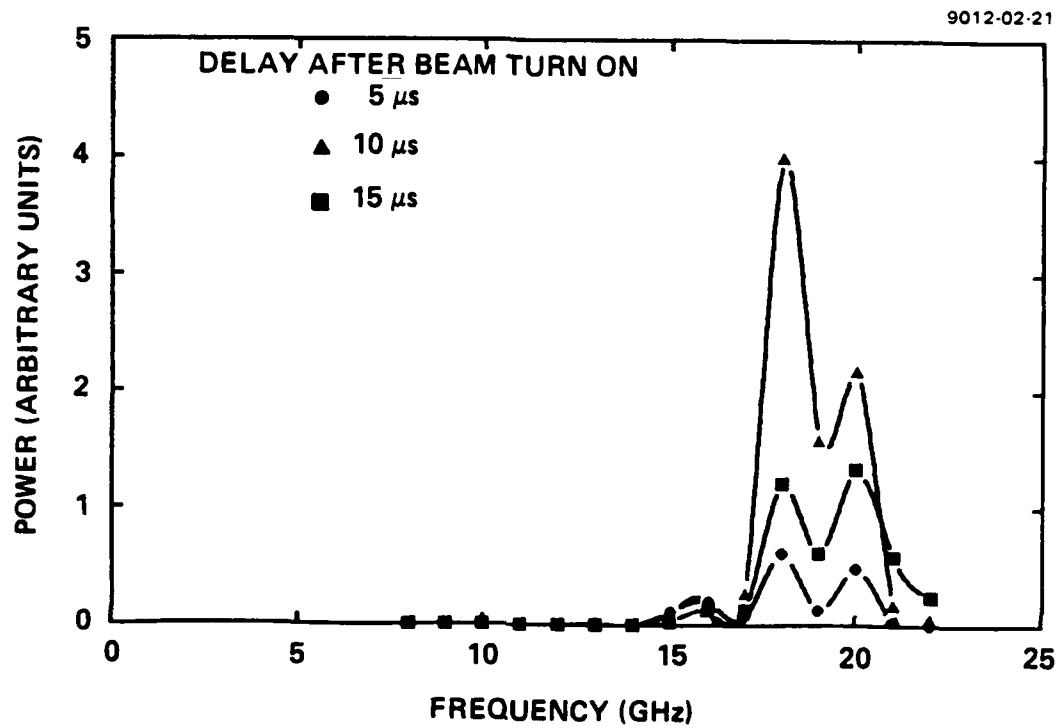


Figure 86. Radiation spectrum with 300-A discharge current, 6-A total beam current, 28-kV beam voltage, and 26-mTorr helium-gas pressure.

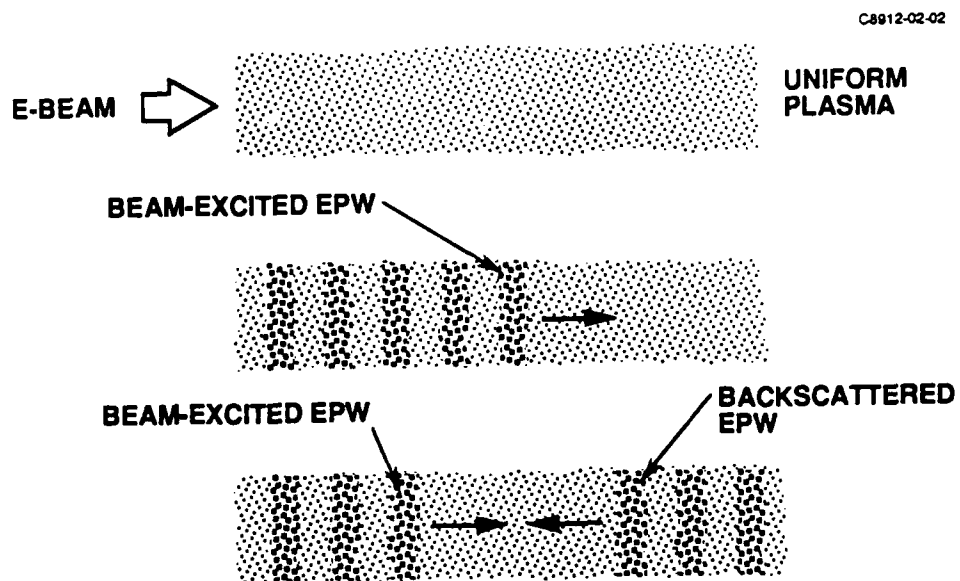


Figure 87. An intense electron beam can produce backscattered EPWs.

described earlier for the counterstreaming-beam case. The beam-current threshold for single-beam radiation is about 9.2 A. This is consistent with our earlier experiments using PAGs in which no single-beam radiation was observed up to the maximum single-beam current of about 7 A. Figure 88 shows the scaling of single-beam, Ka-band radiation power with beam current from 9.2 to 15.4 A and a beam voltage of 28 kV. From 13.5 to 15.4 A, the power increases as $I_b^{2.9}$ until the radiation frequency increases beyond the 40-GHz upper-frequency limit for calibrated power measurements. This frequency shift occurred despite our efforts to reduce beam ionization by operating with only 17-mTorr helium-gas pressure and 7 A of cylindrical waveguide discharge current.

3.13 ORBITRON EXPERIMENTS AT THE UNIVERSITY OF TENNESSEE

Under the auspices of the present contract on plasma three-wave mixing, AFOSR also sponsored one week of joint experiments between HRL and the University of Tennessee (UT) to investigate Orbitron radiation mechanisms in the Plasma Science Laboratory at UT. The results of the investigation, which was conducted March 10 through 14, 1986, are related to plasma-three-wave mixing. In fact, we found that the observed radiation from pulsed-plasma Orbitrons is generated by three-wave mixing.

An Orbitron is a cold-cathode glow-discharge plasma device that employs a fine-wire anode (Figure 89) to generate an electrostatic trap for electrons. Because of the small anode cross section, electrons execute many transits across the diameter of the device before they can be collected by the anode. A glow discharge may therefore be established at low gas pressures where the ionization mean-free-path is long compared to the size of the device. The Orbitron-configuration was conceived in 1963 by McClure¹² as a simple ion source for particle accelerators. In recent years, the wire-anode discharge has been used as an ionization gauge, as a pre-ionizer for high-power

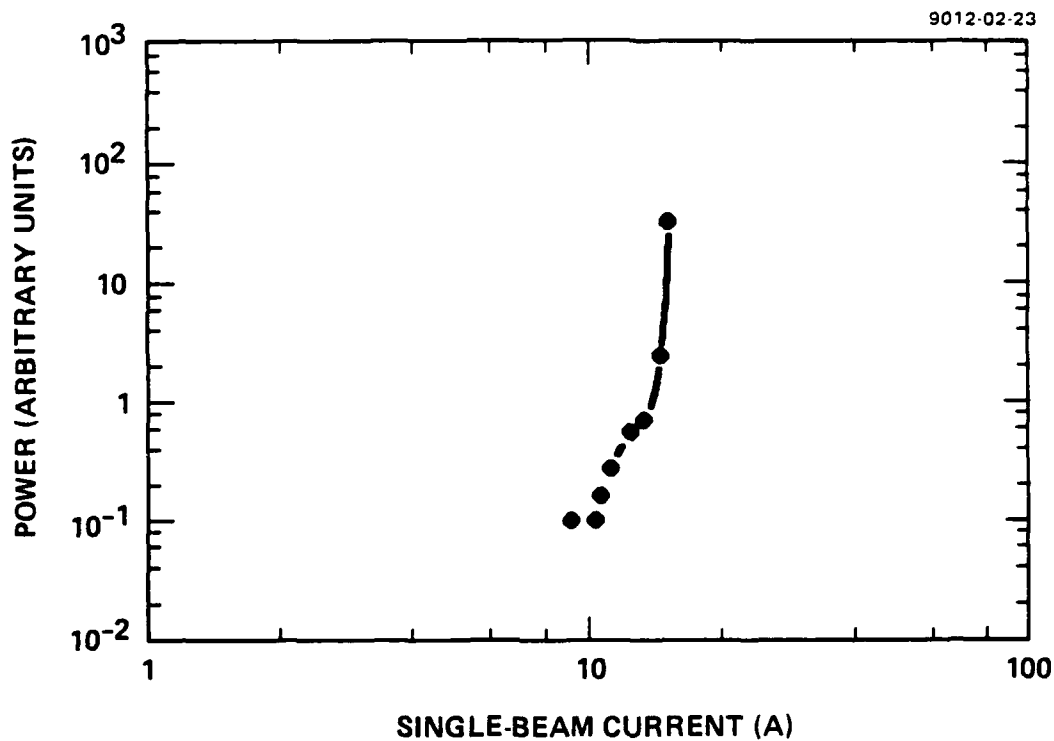


Figure 88. Radiation power scaling with single-beam current. The beam voltage was 28 kV, the cylindrical-waveguide discharge current was 7 A, and the helium-gas pressure was 17 mTorr.

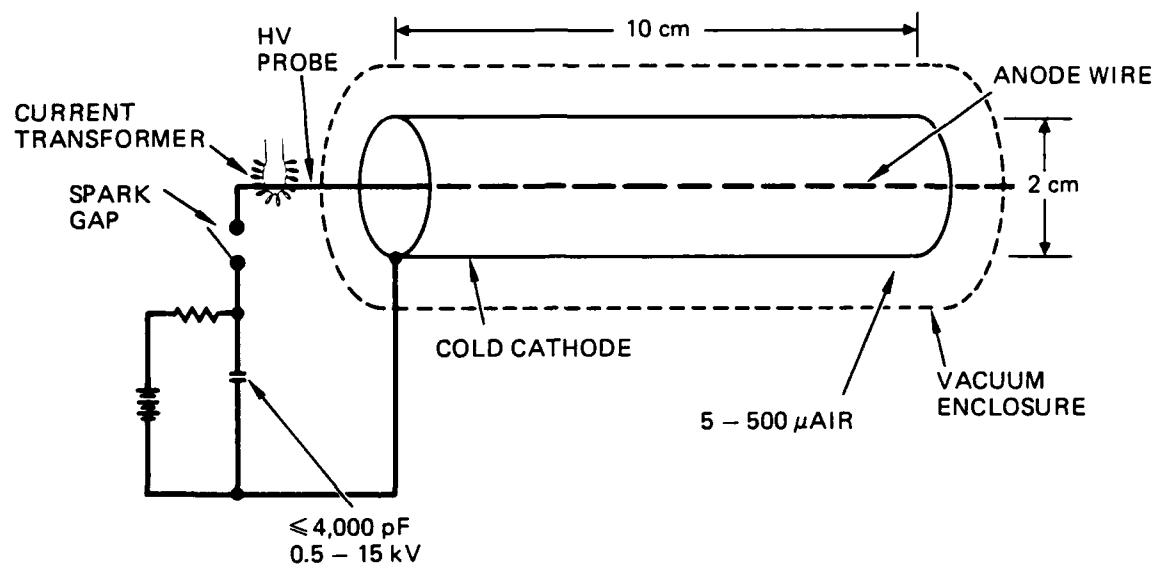


Figure 89. UT Orbitron configuration and drive circuit.

switch devices,¹³ and as a microwave-to-millimeter-wave source.¹¹ Professor Igor Alexeff from the University of Tennessee has observed emission at low microwave frequencies (~1 GHz) when the wire is driven by a low-voltage (~500 V) dc power supply; and he has also observed short-pulse emission at millimeter-wave frequencies when the wire is pulsed to high voltage (~10 kV) by discharging a small capacitor across the source as shown in Figure 89.

Prof. Alexeff has attributed the observed radiation to emission from electrons that become trapped about the anode wire. In his model, the emission frequency corresponds to the frequency of rotation about the wire, which is given by

$$\nu_o = \frac{1}{2\pi r} \left(\frac{eV}{m_e \ln(r_2/r_1)} \right)^{1/2}, \quad (24)$$

where r_2 is the cathode radius and r_1 is the wire-anode radius. This equation is plotted in Figure 90 as a function of wire voltage for several orbit diameters. The most important features of this orbit-radiation model are that the frequency increases with wire voltage and that very small orbit diameters are required in order to obtain high-frequency emission at low wire voltage. Prof. Alexeff usually employs very fine wires and has reported emission from electrons with orbit diameter nearly equal to the wire diameter.

Two types of Orbitron devices were investigated at UT: plasma-filled Orbitrons which use a pulsed glow discharge, and vacuum Orbitrons, which use thermionic emission from a hot filament. Both devices generated observable radiation with power efficiency on the order of 10^{-6} to 10^{-5} .

The vacuum Orbitron (Figure 91) was operated cw and generated rather low-frequency (1 to 2 GHz), low-power ($\ll 1$ mW) radiation which was essentially independent of the applied wire voltage over the range from 1 to 3 kV (Figure 92). From Figure 90,

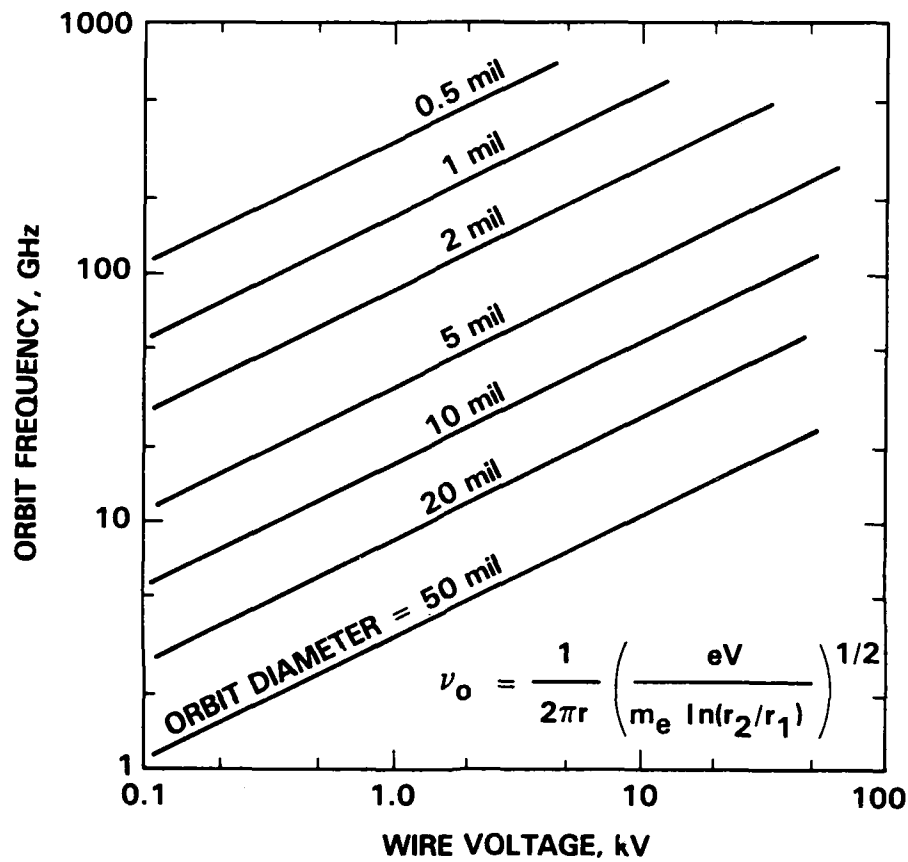
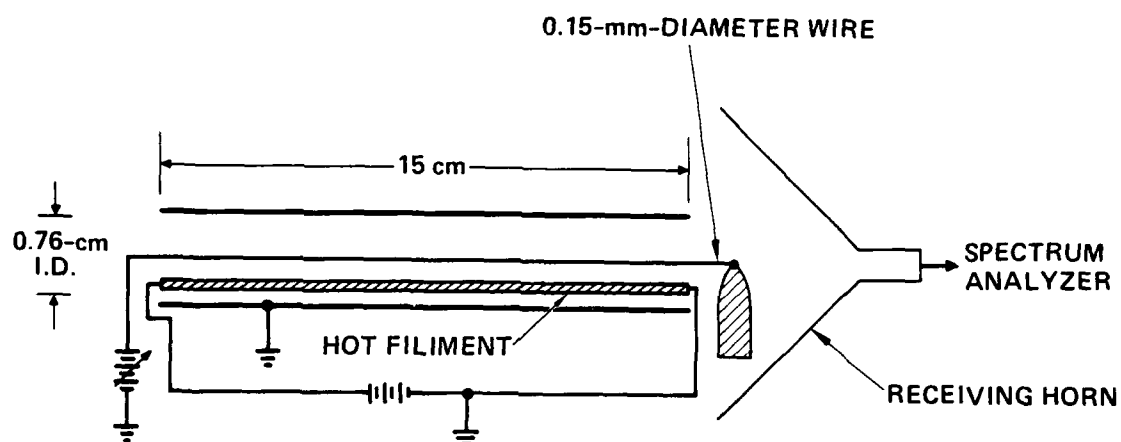
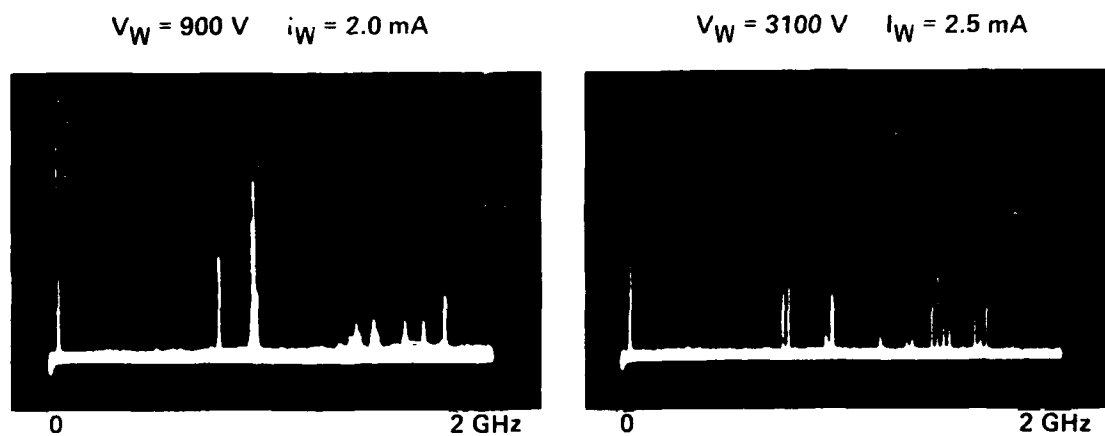


Figure 90. Theoretical orbitron-frequency scaling with wire voltage.



- ORBIT FREQUENCY AT WIRE SURFACE = 69 GHz WITH $V_W = 3100$ V
- RADIAL "BOUNCE" FREQUENCY = 2.2 GHz WITH $V_W = 3100$ V
- ELECTRONS CAN COUPLE TO TEM MODES ONLY AT 2 GHz

Figure 91. Vacuum-orbitron experiment.



FREQUENCY, 200 MHz/div

MAX POWER = -50 dBm

FREQUENCY, 200 MHz/div

MAX POWER = -40dBm

NO RADIATION OBSERVED ABOVE 2 GHz

Figure 92. Low-frequency ($\leq 2 \text{ GHz}$) emission from vacuum orbitron.

elementary Orbitron theory would predict emission around 69 GHz when a 0.15-millimeter-diameter anode wire is driven at 3100 V. Since the observed 1-to 2-GHz radiation was well below the cut-off frequency of TM or TE waveguide modes in the 7.6-millimeter-diameter cathode/waveguide, it appears likely that the radiation is generated by large-diameter (\gg anode-wire-diameter) electron orbits with a significant radial-velocity component, which couple to the radial electric field of a TEM, coaxial-waveguide mode.²⁴ In fact, the radial "bounce" frequency for electrons across the inside diameter is 2.2 GHz (at $V_w = 3100$ V) which is close to the observed output frequency. Such TEM modes can propagate at low frequency without cut-off.

To investigate the more interesting plasma-filled Orbitrons, which reportedly generate higher frequency and power, we instrumented several different Orbitrons with current and voltage diagnostics (current transformer and high-voltage probe) to accurately measure discharge parameters simultaneously with the observation of microwave emission. As shown in Figure 93, we found that in each discharge pulse, the wire-anode-discharge voltage falls and the current rises as the driving capacitor discharges. By observing the output of many detectors simultaneously, we found that the frequency actually increases with time even though the wire voltage is decreasing. This phenomena is demonstrated in Figure 94(a), which shows the frequency increase from 2 to 30 GHz as the discharge current increases. At higher capacitor charging voltage ($V_{c2} > V_{c1}$) in Figure 94(b), the frequency increases from 8 to 90 GHz in only 110 ns! As shown in both traces, the radiation is also emitted in narrow spikes that are about 10-ns wide.

The highest frequency observed from the pulsed-plasma orbitrons was 110 GHz. As shown in Figure 95, two detectors were used simultaneously to measure the frequency: a LHe-cooled InSb detector and a D-band (110 to 140 GHz) crystal detector. Frequency discrimination was achieved by using fine-wire mesh

16101-22

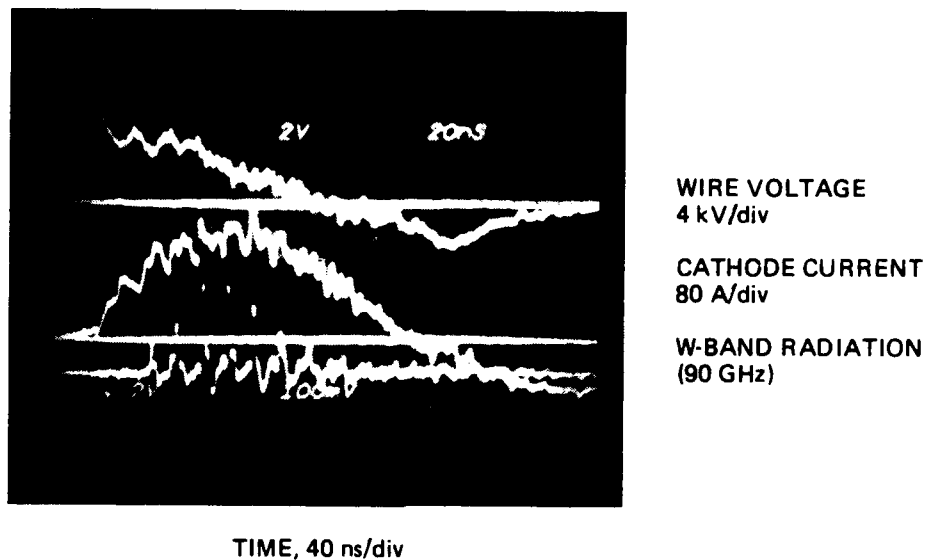


Figure 93. Orbitron discharge voltage and current during the discharge pulse.

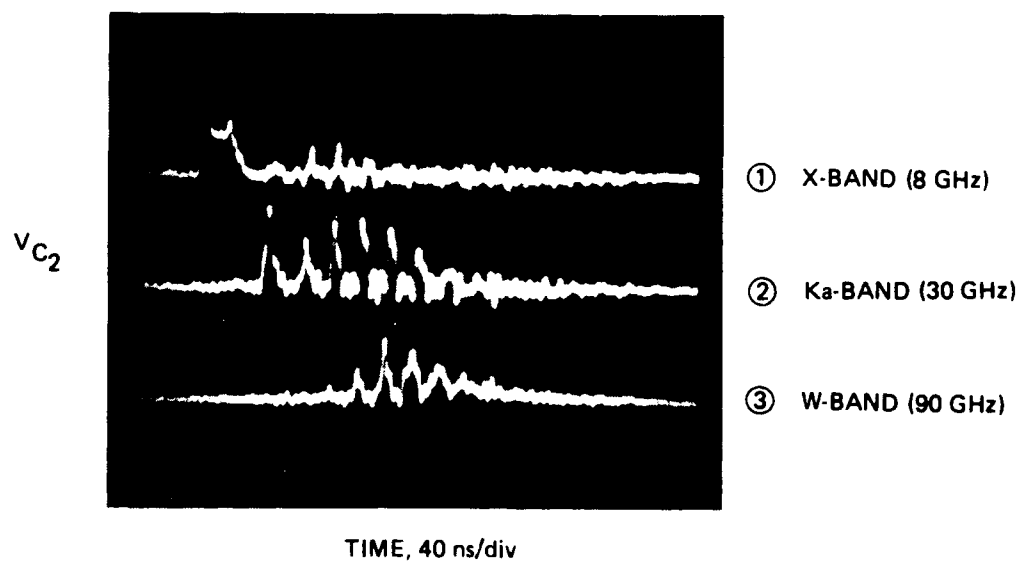
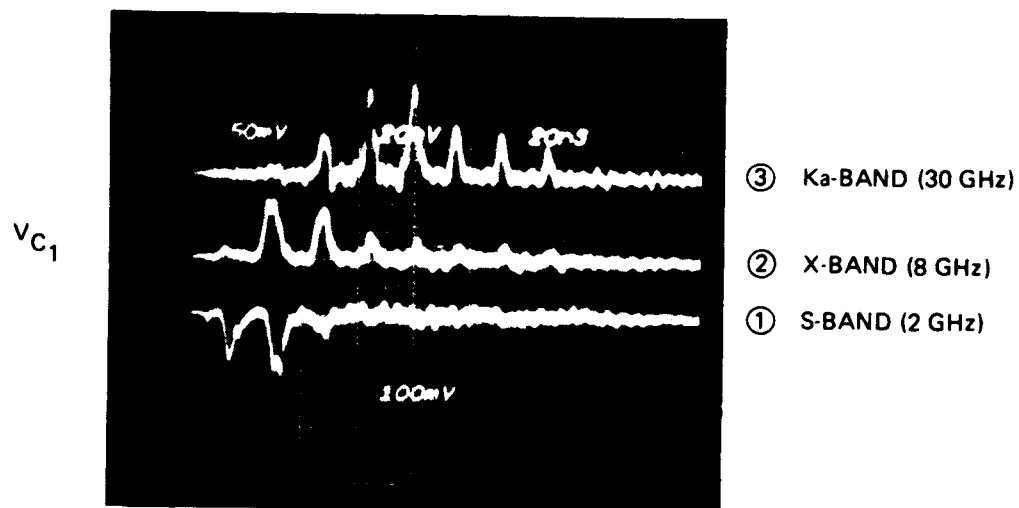


Figure 94. Orbitron emission frequency increases with time in each discharge pulse even though the wire voltage is decreasing.

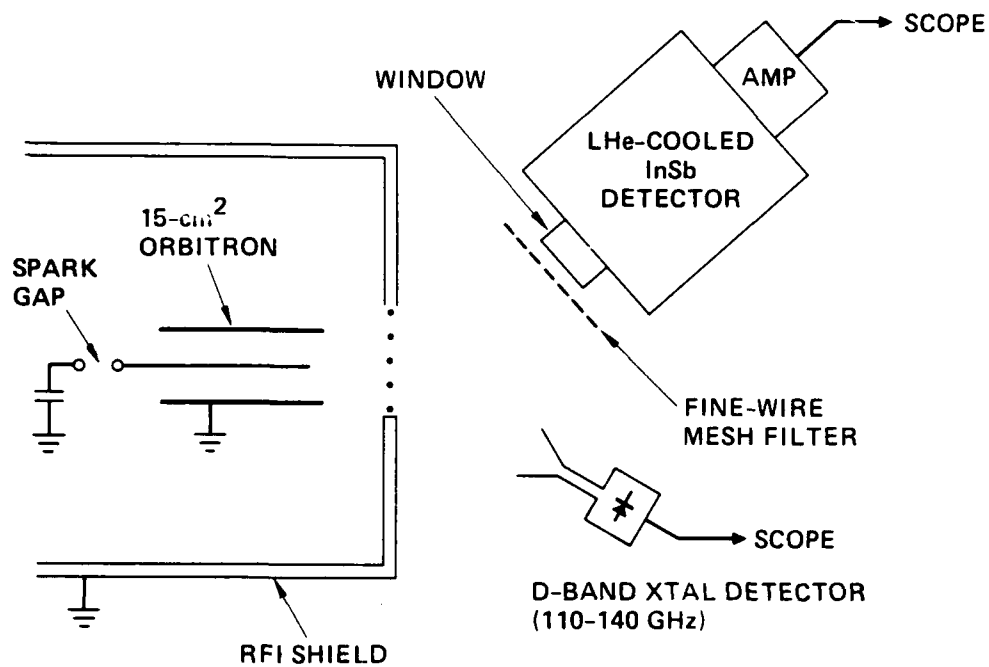


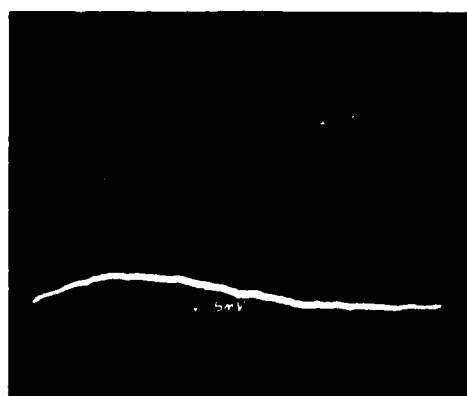
Figure 95. Highest frequency observed is 110 GHz.

filters in front of the InSb detector, and by using the D-band crystal detector as a high-pass filter. Figure 96 shows the response of the two detectors simultaneously. The appearance of an output signal from the InSb detector, with two dense filters (20 lines/mm and 13 lines/mm in series) placed over its input window, would suggest that the 15-cm² Orbitron was radiating terahertz frequencies. However, the D-band detector has just turned on under these experimental conditions, indicating that the radiation is actually near 110 GHz. The InSb detector output is misleading because the wire-mesh filters do not cut-off sharply at a particular frequency, and because the LHe-cooled InSb detector is extremely sensitive--it can easily detect IR radiation from a human placed in front of its input window. The wire-mesh filters do heavily attenuate the 110-GHz radiation, but the sensitive InSb detector is able to record the attenuated signal.

Finally, we measured the scaling of the emission frequency as a function of discharge current for two Orbitron tubes having total cathode areas of 15 and 60 cm². Using the same experimental technique as that shown in Figure 29 we found the frequency to scale as the square-root of the discharge current, as shown in Figure 97.

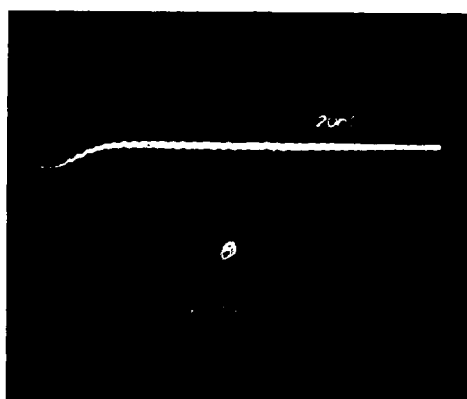
The lines through the data points in Figure 97 are not just best-fit curves to the data: they represent the prediction of plasma three-wave-mixing theory for the Orbitron geometry. The theoretical curves were generated by a model that calculates the plasma density from the measured cathode current density, assuming a cold-cathode discharge with a secondary-electron-emission coefficient, γ , of 0.2. Using this model, the plasma density is

$$n_e = \frac{I_D}{A_c (1+\gamma) e v_s} \quad , \quad (25)$$



InSb DETECTOR
20 LINE/mm AND
13 LINE/mm
FILTERS IN SERIES

TIME, 200 ns/div



D-BAND
DETECTOR
1-M Ω
TERMINATION

TIME, 40 ns/div

→ | ← 50-ns RADIATION PERIOD

Figure 96. InSb detector records 110-GHz signal through two filters.

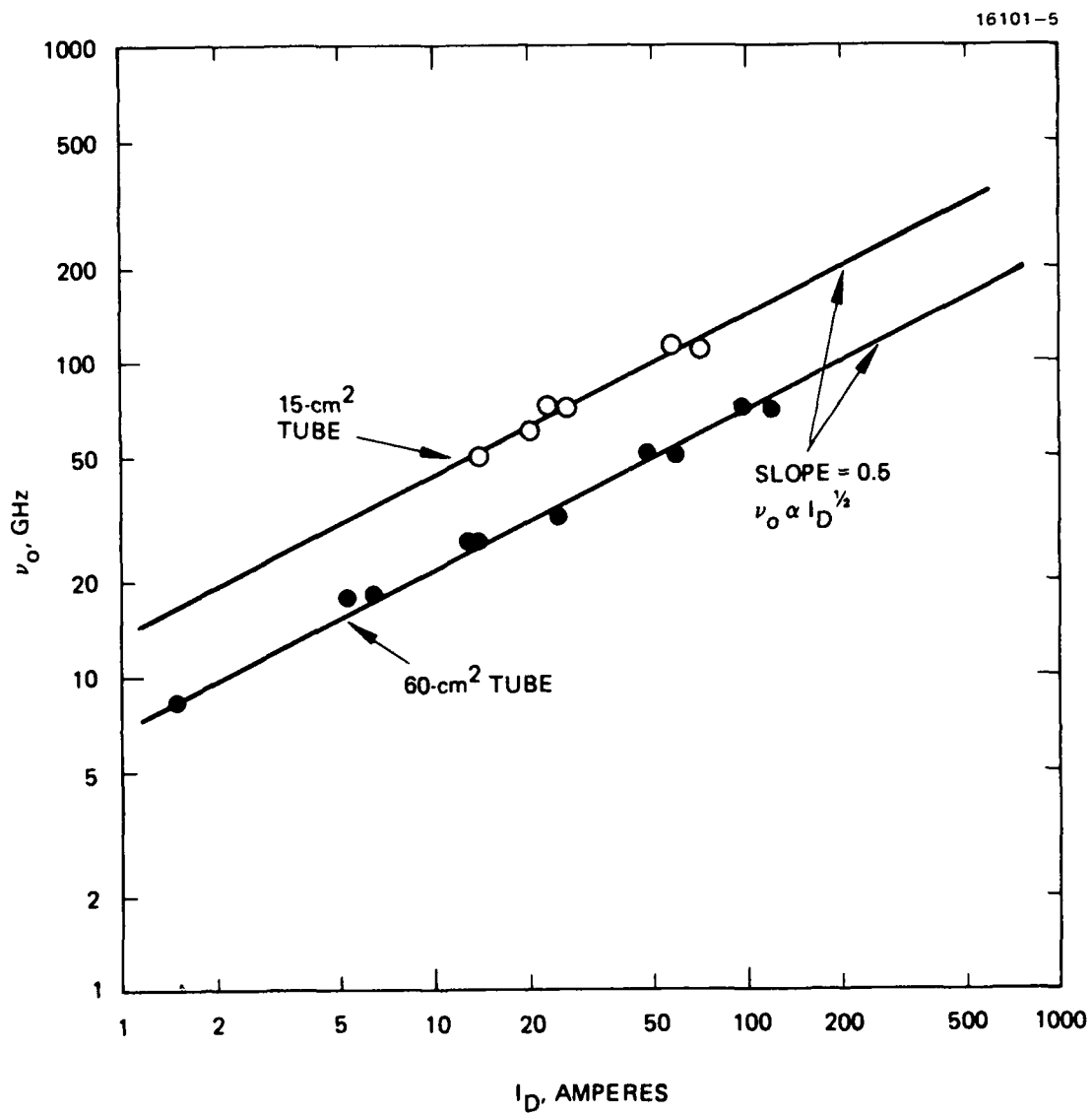


Figure 97. Orbitron frequency scales as the square-root of the discharge current as predicted by plasma-three-wave-mixing theory.

where A_c is the cathode area and v_s is the ion-sound speed given by $(T_e/M_i)^{1/2}$. Inserting Eq. (25) into Eq. (4), we find the plasma frequency to be

$$\omega_p = \left(\frac{4\pi e I_D}{A_c m_e (1+\gamma) (T_e/M_i)^{1/2}} \right)^{1/2} \quad (26)$$

According to three-wave-mixing theory, the Orbitron frequency would then scale as

$$\nu_o = 2\nu_p = \frac{1}{\pi} \left(\frac{4\pi e I_D}{A_c m_e (1+\gamma) (T_e/M_i)^{1/2}} \right)^{1/2} \quad (27)$$

The two theoretical curves in Figure 98 are Eq. (27) with $A_c = 15$ and 60 cm^2 , $T_e = 5 \text{ eV}$, and $M_i = 14$ (nitrogen). The agreement between the data points and the theoretical model is remarkable. This experiment was later repeated at HRL using a 7.3-cm-diameter Orbitron with a 250-cm^2 cathode area. Similar results were obtained with good agreement with Eq. (27), as shown in Figure 98. However, in this experiment we also used different gas species and demonstrated the predicted $M_i^{1/4}$ ion-mass scaling.

Apparently, plasma-filled Orbitron radiation is driven by high-energy discharge electrons (emitted by secondary emission from the cathode surface) that excite counterpropagating EPWs. These waves couple via plasma three-wave mixing to a radiation field at twice the plasma frequency. This result explains the scaling with discharge current and the rapid frequency "chirp" with time in each discharge pulse as the discharge current and plasma density increase. When the plasma is removed and electrons are provided by a thermionic source, only low-frequency TEM modes are observed. Radiation which is consistent with

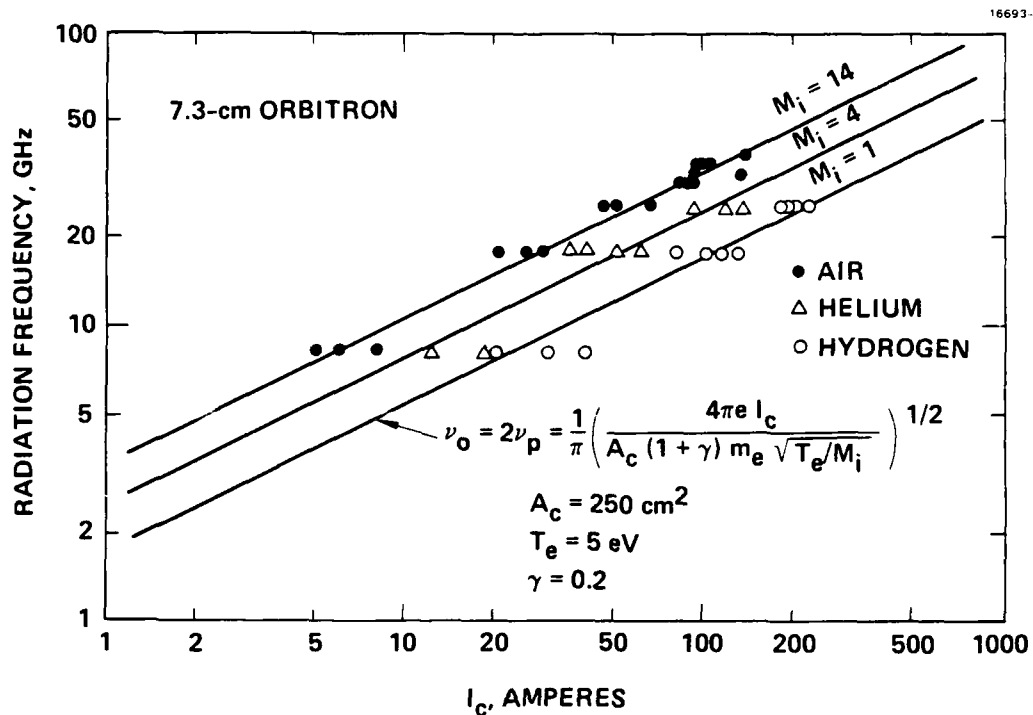


Figure 98. Frequency scaling with current and ion mass using a 7.3-cm-diameter orbitron at Hughes Research Laboratories

electron orbits at the surface of the fine wire as described by Eq. (24) was not observed under any circumstances. Coupling to a radiation field would not be expected in this case anyway since the boundary conditions at the surface of the wire require the E_d field to be zero.

Finally, we investigated frequency scaling at HRL using the 7.3-cm Orbitron with two-thirds of the cathode area covered by a Kapton mask such that electrons would be emitted only from the remaining active-cathode area on one side. In this configuration, three-wave mixing should be inhibited since the discharge electrons can no longer counterstream. However, with the cathode masked we still observed radiation. The millimeter-wave power was reduced by a factor of 20 to 40, and the output frequency scaled as ν_p rather than as $2\nu_p$, as shown in Figure 99. In this case, we believe that the radiation is generated by linear mode conversion from one plasma wave as it interacts with the radial plasma-density gradient.

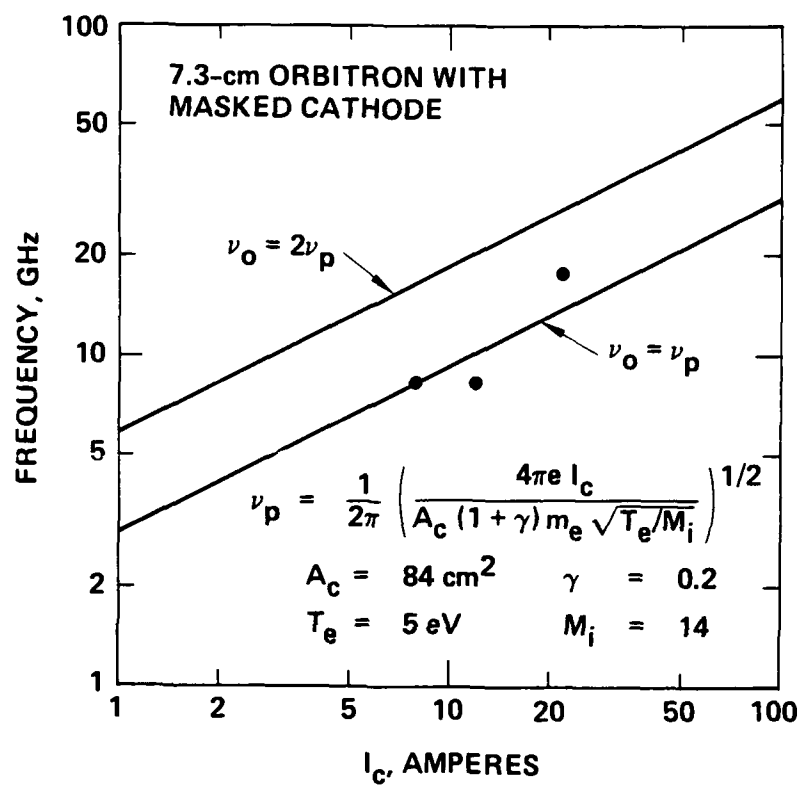


Figure 99. Frequency scaling with masked cathode.

SECTION 4

INTERACTIONS

- 4.1 The following paper was presented at the 1985 APS Plasma Physics Division Meeting in San Diego, California, on 5 November 1985.

"Millimeter-Wave Generation Via Plasma Three-Wave Mixing,"
by R.W. Schumacher.

- 4.2 Orbitron experiments were conducted jointly with Prof. Igor Alexeff of the University of Tennessee on 10-14 March 1986. A seminar on plasma physics research at Hughes Research Laboratories was given to UT staff and students during the visit. The seminar included a discussion of plasma three-wave mixing.

- 4.3 During 1985, technical interaction between Hughes personnel and Drs. Nicholas Krall and Marlene Rosenberg of JAYCOR led to a new AFOSR-sponsored program on plasma-three-wave-mixing theory (in support of our experiment) at JAYCOR.

- 4.4 A technical presentation on plasma three-wave mixing was given to Dr. Alan Garscaden from Wright-Patterson Air Force Base during his visit to Hughes Research Laboratories in August, 1985.

- 4.5 The following papers were presented at the 1986 APS Plasma Physics Division Meeting in Baltimore, Maryland on 6 November 1986.

"Millimeter-Wave Generation Via Plasma Three-Wave Mixing,"
by J. Santoru and R.W. Schumacher.

"Orbitron Radiation-Mechanism Experiments At The University of Tennessee (UT)," by R.W. Schumacher

"Plasma-Anode E-Gun", by A.J. Palmer, R.J. Harvey, R.W. Schumacher, F.A. Dolezal, D.J. Gregoire, and J. Santoru

- 4.6 The following paper was presented at the 1986 IEEE International Conference on Plasma Science in Saskatoon, Saskatchewan on 20 May 1986.

"Millimeter-Wave Generation Via Plasma Three-Wave Mixing," by R.W. Schumacher and J. Santoru

- 4.7 During 1986-1987, technical presentations on plasma three-wave mixing were given to the following organizations:

- Air Force Wright Avionics Laboratory (Dr. Alan Garscaden and Mr. Dave Hime)
- Rome Air Development Center (Mr. Dirk Bussey)
- Naval Research Laboratory (Dr. Robert Parker)
- Massachusetts Institute of Technology
- New York Polytechnique Institute (Prof. Erich Kunhardt)
- University of Southern California (Prof. Martin Gundersen)
- Naval Air Development Center (Mr. John Oakley).

- 4.8 Technical presentations were made to the Radar Systems Group and the Ground Systems Group of Hughes Aircraft Company during 1986-1987.

4.9 The three-wave-mixing process investigated during this program has led to the development of the Plasma Wave Tube. This device incorporates a counterpropagating electron plasma wave topology to achieve multi-octave tunability in the microwave and millimeter-wave frequency range.

4.10 The following papers were presented at the 1987 APS Plasma Physics Division Meeting in San Diego, California, on 5 November 1987.

"Scaling of Millimeter-Wave Radiation Generated by Counterstreaming Beams in a Plasma-Filled Waveguide," by R.W. Schumacher and J. Santoru.

"Plasma-Anode Electron Gun (PAG) Scaling," by J. Santoru, R.W. Schumacher, R.J. Harvey, and A.J. Palmer.

4.11 The following papers were presented at the 1987 IEEE International Conference on Plasma Science in Arlington, Virginia, on 1 June 1987.

"Scaling of Millimeter-Wave Radiation Generated by Counterstreaming Beams in a Plasma-Filled Waveguide," by R.W. Schumacher and J. Santoru.

"Plasma-Anode E-Gun," by J. Santoru, R.W. Schumacher, A.J. Palmer, R.J. Harvey, F.A. Dolezal, and D.J. Gregoire.

4.12 During 1987 - 1988 separate technical presentations on plasma-three-wave mixing were given to members of the Air Force Wright Aeronautical Laboratories (Mr. Anthony White, Mr. Ken Helberg, and Mr. Jack Tehan).

4.13 The following paper was presented at the 1988 IEEE International Conference on Plasma Science in Seattle, Washington, on 8 June 1988.

"Saturation of the Plasma Three-Wave-Mixing Process," by J. Santoru and R.W. Schumacher.

4.14 The following paper was presented at the 1989 IEEE International Conference on Plasma Science in Buffalo, New York on 24 May 1989.

"Millimeter-Wave Radiation Generated Via Plasma Three-Wave Mixing Using High-Current-Density Counterstreaming Electron Beams," by J. Santoru and R.W. Schumacher.

4.15 The following paper was presented at the 1989 APS Plasma Physics Division Meeting in Anaheim, California on 15 November 1989.

"Saturation of the Three-Wave-Mixing Process," by R.W. Schumacher, J. Santoru and D.M. Goebel.

4.16 Continuous technical interactions between Hughes personnel and Dr. Marlene Rosenberg and Dr. Nicholas Krall included meetings at HRL, at JAYCOR, and at each APS and IEEE meeting mentioned above. We have also had close collaborations on the two radiation-generation papers included in the appendices of this report.

SECTION 5

PUBLICATIONS AND PATENTS

The following publications are in preparation:

1. "Electromagnetic-Wave Generation in a Counterstreaming-Beam-Plasma System," by R.W. Schumacher, J. Santoru, M. Rosenberg, and N.A. Krall. To be submitted to Physical Review Letters. A preliminary version of this paper is reproduced in Appendix A.
2. "Millimeter-Wave Generation Via Plasma Three-Wave Mixing," by R.W. Schumacher, J. Santoru, M. Rosenberg, and N.A. Krall. To be submitted to Physics of Fluids. A preliminary version of the paper is reproduced in Appendix B.
3. "Plasma-Anode Electron Gun," by R.W. Schumacher, J. Santoru, R.J. Harvey, and A.J. Palmer. To be submitted to Journal of Applied Physics. A copy of this paper is reproduced in Appendix C.
4. "Orbitron Radiation Mechanisms," by R.W. Schumacher. To be submitted to Physical Review Letters.
5. "Millimeter-Wave Generation Via Plasma Three-Wave Mixing, II," by R.W. Schumacher, J. Santoru, M. Rosenberg, and N.A. Krall. To be submitted to Physics of Fluids.

The following patent application has been submitted:

1. "Improved Plasma Wave Tube," Patent Disclosure No. PD-87441, by R.W. Schumacher and J. Santoru. This invention was made using scaling relationships developed with AFOSR support under this contract.

SECTION 6

RESEARCH PERSONNEL

The following personnel at Hughes Research Laboratories have been associated with the research effort:

1. Robert W. Schumacher (Principal Investigator)
Senior Staff Physicist (213) 317-5439.
2. Joseph Santoru (Co-Principal Investigator)
Member of the Technical Staff (213) 317-5838.
3. Dan M. Goebel
Member of the Technical Staff (213) 317-5941.
4. Ronnie M. Watkins
Development Engineer, Specialist (213) 317-5424.

REFERENCES

1. C. Chin-Fatt and H.R. Griem, Phys. Rev. Lett. 25, 1644 (1970).
2. P. Leung, J. Santoru, A.T. Wong, P.Y. Cheung, Physics of Auroral Arc Formation, Geophysical Monograph Series 25, 387 (1981).
3. M. Schneider and M.Q. Tran, Phys. Lett. 91A, 25 (1982).
4. P.Y. Cheung, A.Y. Wong, C.B. Darrow, S.J. Qian, Phys. Rev. Lett. 48, 1348 (1982).
5. D. Bohm and E.P. Gross, Phys. Rev. 75, 1851 and 1864 (1949).
6. M.A. Lampert, J. Appl. Phys. 27, 5 (1956).
7. F.W. Crawford, "Microwave Plasma Devices - Promise and Progress," Proc. IEEE 59, 4 (1971).
8. T.M. O'Neil, J.H. Winfreg, J.H. Malmberg, Phys. Flu. 14, 1204 (1979).
9. S. Kainer, J.M. Dawson, R. Shanny, Phys. Flu. 15, 493 (1972).
10. S.A. Self, M.M. Shoucri, F.W. Crawford, J. Appl. Phys. 42, 704 (1971).
11. I. Alexeff and F. Dyer, Phys. Rev. Lett. 45, 351 (1980).
12. G.W. McClure, "Low-pressure glow discharge," Appl. Phys. Lett. 2, p. 233 (1963).
13. J.R. Bayless and R.J. Harvey, U.S. Pat. No. 3, 949, 260 (1976) (Assigned to Hughes Aircraft Company).
14. D. Pigache and G. Fournier, "Secondary-emission electron gun for high-pressure molecular lasers," J. Vac. Sci. Tech. 12, 1197-1199 (November/December 1975).
15. G. Wakalopoulos, "Ion Plasma Electron Gun," U.S. Pat. No. 3, 970, 892, Hughes Aircraft Company, July 20, 1976.
16. P.F. Little, "Secondary Effects," Band XXI, Vol. XXI, Handbook Der Physics (1956). Also see A.G. Hill et al., Phys. Rev. 55, 463-470 (March 1939).

17. R.W. Schumacher and R.J. Harvey, "CROSSATRON Modulator Switch," Conference Record of the Sixteenth IEEE Power Modulator Symposium," p. 139, Arlington, Virginia, June 1984.
18. R.W. Schumacher and R.J. Harvey, "CROSSATRON Modulator Switch: A Long-Life Component for Pulsed-Power Systems," Fifth IEEE Pulsed-Power Conference.
19. J.R. Pierce, "Theory and Design of Electron Beams," 2nd. Ed. Van Nostrand, New York (1954).
20. R.J. Harvey, "Plasma-Anode Electron Gun," Hughes Aircraft Company patent disclosure No. 84050, U.S. patent pending.
21. N.A. Krall and A.W. Trivelpiece, "Principles of plasma physics," p 495, McGraw Hill, New York (1973).
22. John H. Ingold, Gaseous Electronics, Chapter 2, Edited by M.N. Hirsh and H.J. Oskam, p. 19-64 (Academic Press, New York, 1978).
23. M. Rosenberg and N. Krall, Bull. Am. Phys. Soc. 32, 1885 (1987).
24. J.M. Burke, W.M. Manheimer, E. Ott, Bull. Am. Phys. Soc., 30, p. 1511 (1985).

APPENDIX A

ELECTROMAGNETIC-WAVE GENERATION IN A COUNTERSTREAMING-
BEAM-PLASMA SYSTEM

This paper will be submitted to Physical Review Letters.

ELECTROMAGNETIC-WAVE GENERATION IN A COUNTERSTREAMING-BEAM-PLASMA SYSTEM

R.W. Schumacher and J. Santoru
Hughes Research Laboratories, Malibu, CA 90265

M. Rosenberg,^(a) and N.A. Krall
Krall Associates, Del Mar, CA 92014

^(a)Consultant; presently at Center for Astrophysics and Space Sciences,
University of California, San Diego, La Jolla, CA 92037

ABSTRACT

Radiation from 8 to 60 GHz is generated with high efficiency ($\lesssim 4\%$) by injecting counterstreaming, high-power (30 keV, 4 A) electron beams into an unmagnetized, plasma-loaded waveguide. The radiation is emitted at twice the plasma frequency and is amplitude modulated on the ion plasma frequency time scale. A turbulence theory model is consistent with the radiation characteristics and power scalings.

PACS numbers: 52.25.Sw, 52.40.Mj, 52.35.Mw

The generation of electromagnetic radiation at twice the plasma frequency ($2\omega_{pe}$) by the coupling of electron-beam-excited plasma waves has been studied for several years.^{1,2} Prior experiments used low-voltage, low-current counterstreaming electron beams and reported beam-to-radiation conversion efficiencies $\leq 0.01\%$. To the best of our knowledge, this investigation is the first to use high-power ($\lesssim 90$ keV, $\lesssim 4$ A) beams in a plasma-loaded waveguide to generate kilowatt radiation power levels at millimeter-wave frequencies with an efficiency $\lesssim 4\%$.

Our experimental apparatus is shown in Figure 1a. Two cold-cathode secondary-emission electron guns inject counterstreaming electron beams into an unmagnetized, plasma-loaded ($n_e \leq 10^{13}$ cm⁻³), cylindrical (3.8-cm diameter and 15.2-cm long) microperforated waveguide cavity with background-gas pressure of 10 - 50 mTorr. The plasma is produced by a 12-wire wire-anode discharge^{3,4} in the annular space surrounding the waveguide cavity. The microperforations are large compared to a Debye length, but small compared to the electromagnetic wavelength; radiation remains trapped in the guide while plasma and ionizing electrons can pass through freely. Radiation is coupled out of the cavity through rectangular X-band waveguides, oriented to align the TE₁₀ rectangular waveguide mode with the axial electric field of a TM mode in the circular waveguide. The radiation is analyzed by a network of microwave and millimeter-wave filters, attenuators, and calibrated detectors. The experiment is operated with 10- to 25- μ s-wide discharge and beam pulses at a repetition rate of 1 Hz.

Radiation from 8 to 60 GHz is observed when two counterstreaming electron beams are injected into the plasma-loaded waveguide. As shown in Figure 1b, radiation is observed only when the beams overlap temporally, and the beam currents exceed a threshold value described below. Radiation

frequencies as high as 60 GHz are produced when the plasma discharge current is raised to 800 A. The radiation is emitted in bursts as shown in Figure 1c. The burst width and interburst periods are each a few inverse ion-plasma-frequency (ω_{pi}^{-1}) time periods, as confirmed by operation with hydrogen, helium, argon, krypton, and xenon background gases. The radiation is generated at twice the plasma frequency as shown in Figure 1d. Radiation from a single beam is not observed up to the maximum single beam current of 4 A.

We investigated the scaling of the radiation power output, P , as a function of the beam energy E_b and current I_b . We used analog RC integration circuits to measure the average power during the beam pulses, and then we averaged the integrated power for ten shots. The power is optimum when the beams have comparable energy, especially at low beam current, as shown in Figure 2a. In addition, P maximizes at an optimal beam energy (Figure 2b) that increases with radiation frequency (30 keV at 30 GHz; 40 keV at 60 GHz). Figure 2c displays the averaged output power scaling with beam current for both beams operating at 30 kV. The threshold total beam current ($I_b = I_{b1} + I_{b2}$) is about 3 A.

Single-beam propagation experiments using disk probes show that the threshold is related to the self Bennett pinch⁵ of each beam. Above the 3-A threshold current at the 30-kV beam voltage, the beam full-width at half maximum decreases from 2.7-cm diameter at the beam injection point to about 0.5-cm diameter 15 cm downstream as shown in Figure 2d. The beam collapse threshold is consistent with the Bennett pinch condition, and the beam profile fits a Bennett profile with a perpendicular beam temperature of 15 eV. When the counterstreaming beams pinch, the beam densities increase, raising P above our detection threshold. Above the threshold current, there is a sharp

rise in radiation power as the total beam current is increased to 3.5 A; at higher currents, the power scales as $I_b^{6.6}$ as shown in Figure 2c. This scaling varies between $I_b^{3.6}$ and $I_b^{6.6}$, depending on the experimental parameters. At $I_b = 7$ A in a helium discharge, the peak radiation power level in the waveguide cavity is 8 kW at 31 GHz and the peak beam-to-radiation conversion efficiency is 4%. The efficiency calculation is based on waveguide cold tests which show that about 1% of the Ka-band radiation generated within the waveguide is coupled into the output waveguides.

We developed a theoretical model which explains many features of the experiment. Each electron beam excites a spectrum of unstable electron plasma waves with frequency $\omega \sim \omega_{pe}$, axial wavenumber $k = \omega_{pe}/v_b$, and spectrum width of $\Delta k \sim (\omega_{pe}/v_b)(n_b/n_e)^{1/3}$ via a strong hydrodynamic beam-plasma instability, with growth rate⁶ $\delta \sim (2)^{-4/3}(3)^{1/2}\omega_{pe}(n_b/n_e)^{1/3}$, where n_b and v_b are the beam density and beam velocity, respectively. Since the beams counterstream, the waves excited by the two beams counterpropagate axially. The beam-excited waves saturate by beam trapping⁷ at an energy density $W_0 = E_0^2/8\pi \sim n_b E_b (n_b/n_e)^{1/3}$, where E_0 is the wave electric field amplitude, and $E_b = 0.5m_e v_b^2$ is the beam energy. When the time scale for beam trapping, several times δ^{-1} , is comparable to the beam's transit time across the waveguide cavity, L/v_b , the waves excited by both beams overlap spatially and saturate within the waveguide cavity. Radiation is generated when two counterpropagating waves interact and then couple to an electromagnetic TM mode of the cylindrical waveguide. The energy and momentum conservation rules for this three-wave process gives $\omega_3 = \omega_1 + \omega_2 \sim 2\omega_{pe}$, and $k_3 = k_1 + k_2 \sim 0$ for the axial wavenumbers (since $k_1 \sim -k_2$), where 3 refers to the TM mode, and 1 and 2 refer to the beam-excited plasma waves.

This model explains why radiation is seen only when the background plasma and both beams are present. The absence of radiation from a single beam indicates that other radiation mechanisms, such as scattering of electron plasma waves off density fluctuations or emission from solitons, are weaker processes in this system than the three-wave interaction. The requirement that the beams have comparable energy for maximum radiation output is consistent with energy and momentum conservation for the three-wave process since the phase velocity of the beam excited waves is $< c$. The voltage-tuning curves broaden at higher beam currents, as shown in Figure 2a, because the width of the wavenumber spectrum of the beam-excited waves increases as $n_b^{1/3}$. The observation of optimal beam energy for maximum radiation output, as shown in Figure 2b, follows from the requirement that the beam-excited waves saturate within the length of the guide. This yields an optimal coupling energy of $E_b \sim (m_e/2)(L\omega_{pe}/15)^2(n_b/n_e)^{2/3}$, which gives 20 keV for $n_b/n_e = 5 \times 10^{-4}$, and 46 keV for $n_b/n_e = 2 \times 10^{-3}$, where $n_e = 3 \times 10^{12} \text{ cm}^{-3}$. These values are consistent with the experimental results.

The radiated power is also predicted to scale strongly with beam current. From weak turbulence theory, the power density of $2\omega_{pe}$ radiation generated in the three-wave interaction is⁸

$$\Sigma \sim \frac{4\pi\sqrt{3}}{5} \frac{\omega_{pe}^2}{n_e m_e c^3} \int_{\sqrt{3}\omega_{pe}/c}^{k_{De}} dk (W_k)^2 (\omega_{pe}/kc)^2, \quad (1)$$

where W_k is the energy density per unit wavenumber of the beam-excited waves and k_{De} is the Debye wavenumber. Multiplying equation (1) by the interaction volume, $V = A_b L$, where A_b is the cross-sectional area of the

pinched beam, and using $W_k = W_0/\delta k$, where $\delta k = \Delta k/(N)^{1/2}$ is the half width of the plasma-wave spectrum after N e-foldings, yields

$$P = \Sigma V \sim \omega_{pe}(n_b/n_e)^{7/3}(v_b/c)^7(n_e m_e c^2 A_b L)(N)^{1/2}. \quad (2)$$

If the beam profile is determined from self-focusing⁵, $n_b A_b T_b \propto I_b^2$, and the equation of state for the beam is $n_b \sim T_b$, corresponding to two-dimensional adiabatic compression, equation (2) scales as $P \propto I_b^{7/3}$. To derive this expression we also used $n_b A_b \propto I_b/v_b$ where n_b is the pinched beam density and v_b is constant. If the beam energy is optimized so that $v_b \propto n_b^{1/3}$ as discussed above, the power scales as $P \propto I_b^6$. The peak power estimated from equation (2) is about 0.2 kW, using $n_e = 3 \times 10^{12} \text{ cm}^{-3}$, $n_b/n_e = 3.3 \times 10^{-3}$, $E_b = 35 \text{ keV}$, $L = 15 \text{ cm}$, $A_b = \pi r_b^2$, with the beam radius $r_b = 0.25 \text{ cm}$, and $N = 6$. The peak power estimate and the power scaling with beam current are reasonably consistent with the experimental observations.

The temporal modulation of the radiation amplitude can be understood by noting that the saturated beam-excited waves can drive the modulational instability⁹ on the ω_{pi}^{-1} time scale since W_0 is greater than the modulational instability threshold of $4v_{en}/\omega_{pe}$, where v_{en} is the electron-neutral collision frequency. The nonlinear development of this instability leads to Langmuir wave collapse and the formation of ion density fluctuations on the ω_{pi}^{-1} time scale. The beam-excited waves scatter off these fluctuations, damping the wave growth.^{10,11} When the density fluctuations decay (e.g., via convection¹²), the beam can again excite electron plasma waves, and the cycle repeats. The radiation power is cyclical on the same time scale as the growth and decay of the ion density fluctuations, which is of the order of ω_{pi}^{-1} . The

modulation time period is proportional to $m_i^{1/2}$, in agreement with the experiment.

Acknowledgements

We wish to acknowledge the expert technical assistance of R. Watkins in the design and assembly of the experimental apparatus. We appreciate Dr. R. Barker's support throughout the project. This research was funded by Air Force Office of Scientific Research under contract number F49620-85-C-0059.

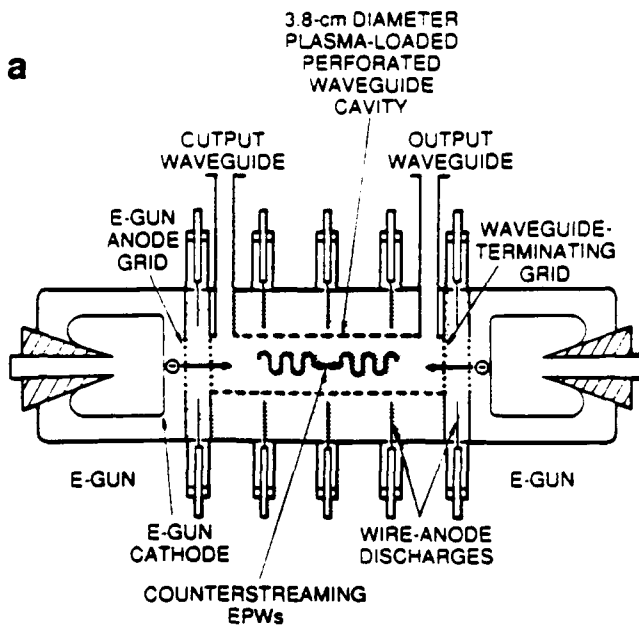
References

1. P. Leung, J. Santoru, A.Y. Wong, and P.Y. Cheung, in Physics of Auroral Arc Formation, edited by S.I. Akasofu and J.R. Kan (American Geophysical Union, Washington, D.C., 1981).
2. T. Intrator, N. Hershkowitz, and C. Chan, *Phys. Fluids* **27**, 527 (1984).
3. G.W. McClure, *Appl. Phys. Lett.* **2**, 233 (1963)
4. I. Alexeff and F. Dyer, *Phys. Rev Lett.* **45**, 351 (1980)
5. W.H. Bennett, *Phys. Rev.* **45**, 890 (1934).
6. B.I. Aronov, A.A. Rukhadze, and M.E. Chogovadze, *Soviet Physics-Technical Physics* **17**, 877 (1972).
7. T.M. O'Neil, J.H. Winfrey, and J.H. Malmberg, *Phys. Fluids* **14**, 1204 (1971).
8. S.A. Kaplan and V.N. Tsytovich, *Plasma Astrophysics* (Pergamon Press, Oxford, 1973).
9. V.E. Zakharov, *Sov. Phys. JETP* **35**, 908 (1972).
10. A.A. Galeev, R.Z. Sagdeev, V.D. Shapiro, and V.I. Shevchenko, *Sov. Phys. JETP* **45**, 266 (1977).
11. H.P. Freund, I. Haber, P. Palmadesso, and K. Papadopoulos, *Phys. Fluids*, **23**, 518 (1980).
12. P.Y. Cheung and A.Y. Wong, *Phys. Rev. Lett.*, **55**, 1880 (1985).

Figure Captions

Figure 1: (a) Beam-plasma experiment. (b) Waveguide discharge current, beam currents, and 50-GHz detector output. (c) Detector output showing radiation burst width and burst period in an argon plasma. (d) Scaling of radiation frequency with background plasma frequency.

Figure 2: (a) Radiation power scaling with E_{b2} for different beam currents. E_{b1} was held constant at 19 keV. (b) Radiation power scaling with beam energy ($E_{b1} = E_{b2}$) for two different total beam currents. (c) Radiation power scaling with beam current. (d) Electron beam profiles.

**b**

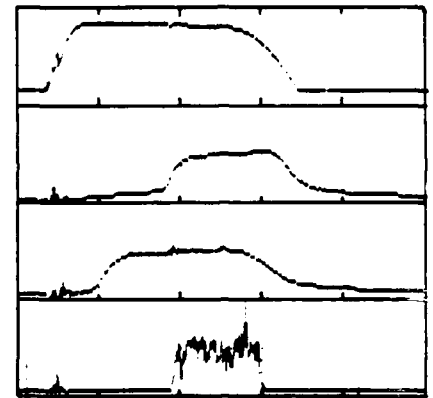
16101-7R1

WAVEGUIDE
DISCHARGE
CURRENT
400A/DIV

BEAM #1
BEAM CURRENT
4A/DIV

BEAM #2
BEAM CURRENT
4A/DIV

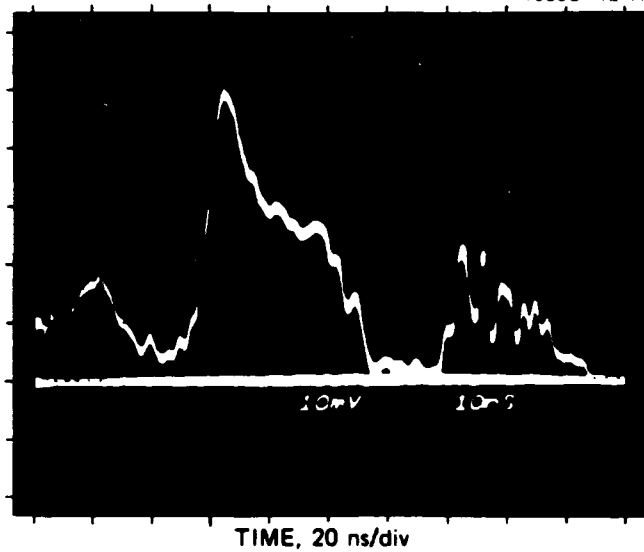
50-GHz DETECTOR
OUTPUT



TIME, 10 μ s/div

c

16693-12R1

**d**

16101-11R1

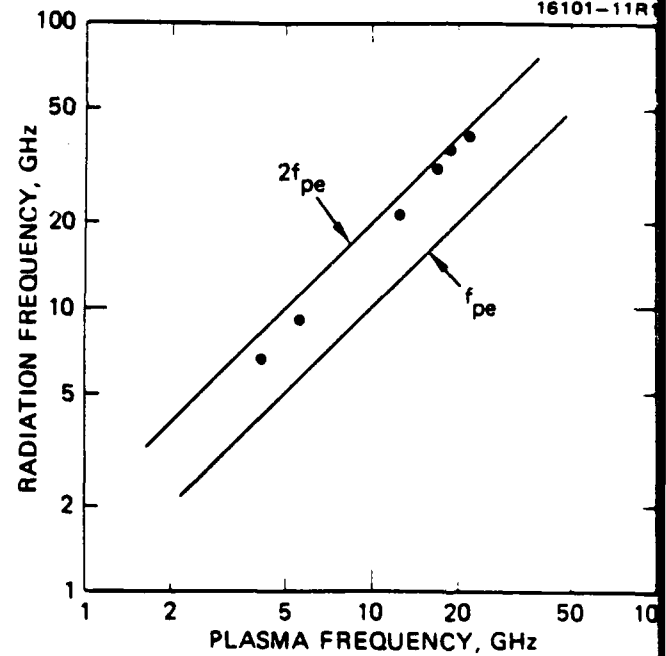


Figure 1

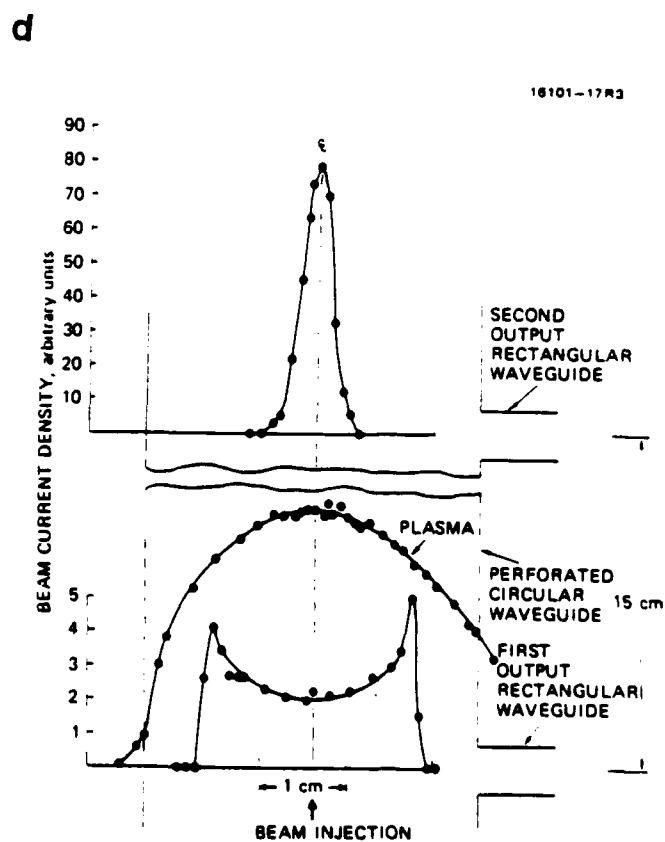
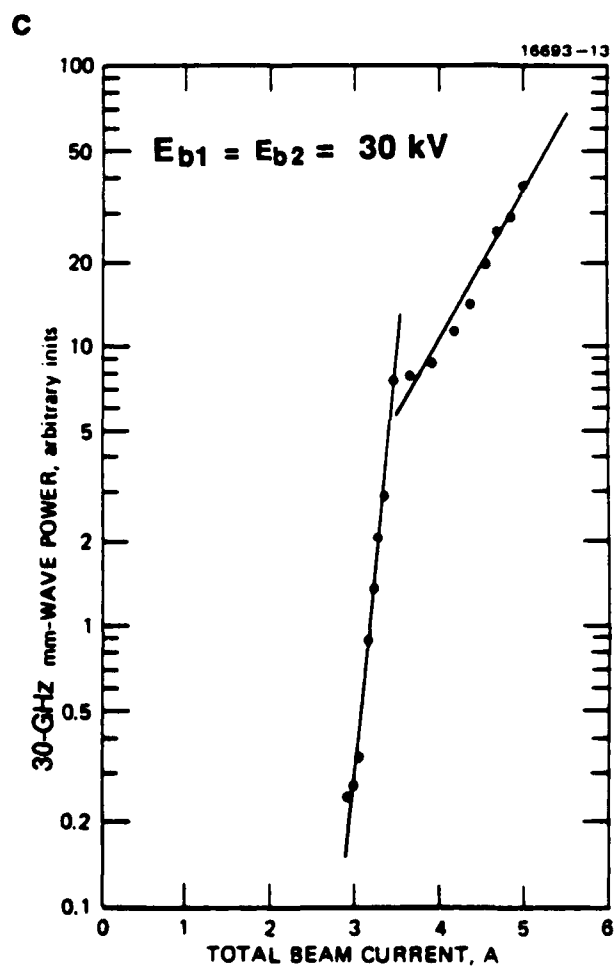
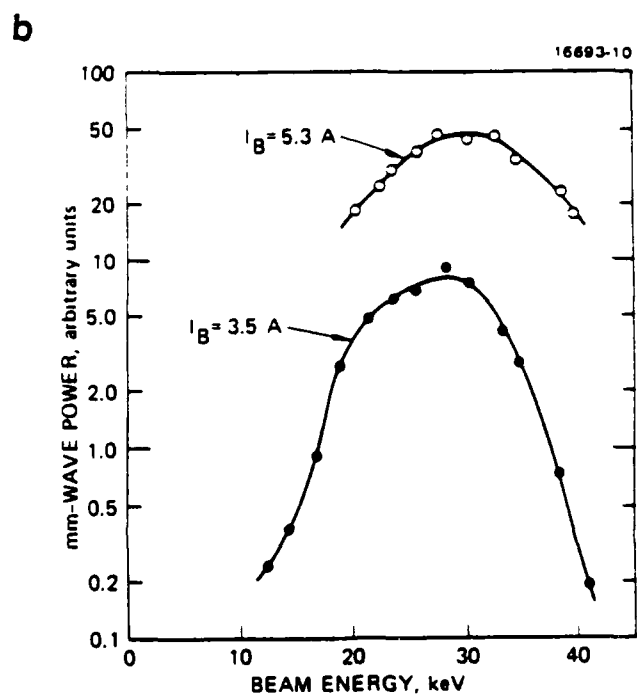
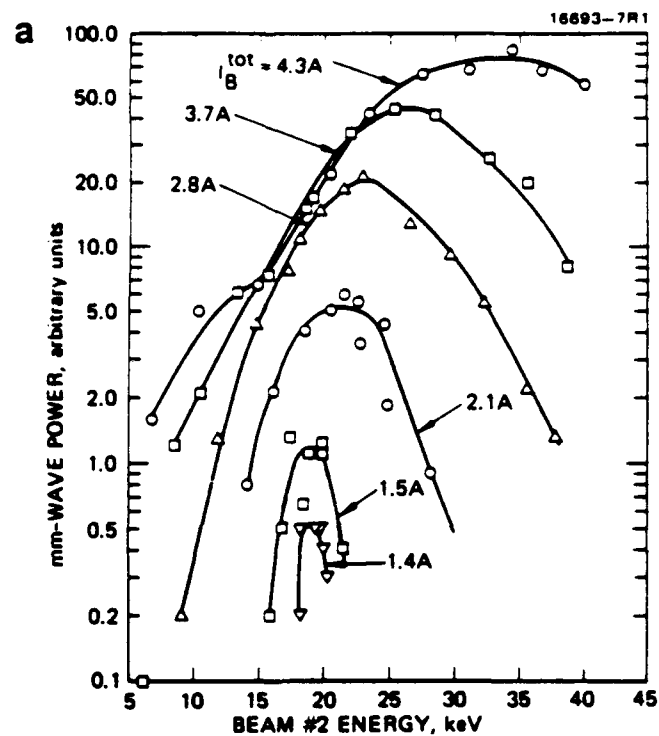


Figure 2

APPENDIX B

ELECTROMAGNETIC-WAVE GENERATION THROUGH PLASMA THREE-WAVE MIXING

This paper will be submitted to Physics of Fluids.

Electromagnetic-wave generation through plasma three-wave mixing

R.W. Schumacher and J. Santoru
Hughes Research Laboratories, 3011 Malibu Canyon Road, Malibu, CA 90265

M. Rosenberg^{a)} and N.A. Krall
Krall Associates, 1070 America Way, Del Mar, CA 92014

(Received

Radiation from 8 to 60 GHz is generated by injecting counterstreaming electron beams (≤ 90 kV) into an unmagnetized, plasma-loaded circular waveguide. The beams excite counterpropagating electron plasma waves (EPWs), and the nonlinear coupling of those waves generates an electromagnetic mode at twice the plasma frequency, $2\omega_{pe}$. The self (Bennett) pinch of each beam dominates both beam dynamics and the scaling of radiation power with beam current. No radiation is detected below the pinch threshold at 1.5 A. At larger currents, the radiation power increases as the sixth power of the total beam current. No saturation is observed up to beam currents of 3.5 A, where the peak power in the plasma-loaded waveguide is estimated to be 8 kW. The radiation power is optimized when the

^{a)} Consultant; now at the Center for Astrophysics and Space Science, University of California at San Diego, La Jolla, CA 92093.

beams have comparable energy. The beam energy that optimizes the radiation power increases with frequency from 30 keV at 30 GHz to 41 keV at 60 GHz. The radiation is amplitude-modulated at low ($40 \text{ MHz} < \omega_{pi}$) frequencies. The low-frequency modulation scales as the square root of the ion mass, which is consistent with the excitation of ion-acoustic instabilities. A phenomenological model developed for this system shows that, initially, each beam excites EPWs by means of a strong, hydrodynamic beam-plasma instability. The waves saturate by beam trapping. The saturated EPWs drive the nonlinear modulational instability, which grows on the time scale of the ion plasma frequency. The EPWs then scatter off the associated density perturbations, the beam decouples from the EPWs, and the radiation ceases. When the density perturbations relax, the process begins anew.

I. INTRODUCTION

The generation of electromagnetic radiation by an electron beam propagating through a background plasma has been studied intensely for many years. Areas of investigation range from space plasmas (e.g., type-III solar radio bursts¹) to high-power microwave generators.^{2,3} In an unmagnetized plasma, the electron beam can drive unstable electron plasma waves (EPWs) at the plasma frequency ω_{pe} ($\omega_{pe} = 2\pi f_{pe}$). Beam-excited EPWs can then participate in various radiation-generating mechanisms.

Radiation-generating mechanisms may involve the nonlinear mixing or beating of beam-excited EPWs with each other or with other waves in the plasma. For example, one such mechanism, which produces radiation near the plasma frequency, involves the scattering of an EPW off an ion-acoustic wave or off an ion density gradient, thereby converting the EPW to an

electromagnetic wave.⁴⁻¹⁴ At least two other nonlinear mechanisms produce radiation at multiples of the plasma frequency. One uses the interaction of two counterpropagating EPWs to generate radiation at $2\omega_{pe}$.^{15,16} The other mechanism is associated with strong plasma turbulence and soliton collapse.¹⁷⁻²⁰

Prior experiments that explored the physics of $2\omega_{pe}$ radiation generated by the EPW-EPW interaction used low-voltage, low-current counterstreaming electron beams to excite the EPWs.^{15,16} EPW growth and propagation properties were studied, together with the characteristics of the $2\omega_{pe}$ radiation. The radiation power levels were very low (about -60 dBm), with poor beam-to-electromagnetic-wave conversion efficiencies.¹⁵

This paper describes an experimental and theoretical investigation of the generation of microwave and millimeter-wave radiation in a beam-plasma system. The experimental approach is to drive a plasma-loaded waveguide cavity with counterstreaming electron beams. The beams excite counterpropagating EPWs, which then couple to generate electromagnetic radiation at twice the plasma frequency, $2\omega_{pe}$. To the best of our knowledge, our investigation is the first to use high-power (≤ 90 keV, ≤ 6 A) beams in a high-density, plasma-loaded waveguide to generate substantial radiation power levels (≤ 8 kW) at millimeter-wave frequencies with efficiencies as high as a few percent.

Our experimental parameters were quite different from those of previous counterstreaming electron-beam experiments. Table I compares our key parameters and results with those of two such experiments. We used higher plasma density, higher background-neutral pressures, and higher beam energies, obtaining a conversion efficiency for electron-beam power to $2\omega_{pe}$ -radiation power that is orders of magnitude larger than previously reported. We varied our experimental parameters over wide ranges to identify the physical processes responsible for that difference. Independent control of waveguide plasma density, gas species, beam voltage, and beam current allowed a careful parametric study of the beam, EPW, and radiation physics. Theoretical analyses were applied to explain the experimental phenomena that we observed.

II. THEORETICAL BACKGROUND

Beam-plasma phenomena are attractive for generating radiation because of the ease with which intense, high-frequency EPWs can be excited when a high-power electron beam is injected into a dense plasma. However, the problem of efficiently coupling the power in the electrostatic waves to a radiation field has hindered previous attempts to use plasmas in radiation sources or amplifiers.²¹ We overcame the difficulty by using a nonlinear wave-interaction mechanism that we call "plasma three-wave mixing," in which the beam-excited slow EPWs couple to generate a fast electromagnetic wave at $2\omega_{pe}$ that easily radiates out of the plasma. In our experiment, we inject moderate-energy (≤ 90 keV) electron beams into an unmagnetized, plasma-loaded circular waveguide from opposite ends. The electron beams excite counterpropagating EPWs at the plasma frequency ω_{pe} . Such quasi-electrostatic waves couple nonlinearly to produce electromagnetic waves at twice the plasma frequency, $2\omega_{pe}$.

Our theoretical analyses focus on the physics of the beam-plasma instabilities and wave-wave interactions related to our experiment, including beam propagation, linear beam-plasma instability, wave saturation, wave-wave coupling, and strong plasma turbulence. We list a set of representative experimental parameters in Table II, which we designate the standard case for our experiment. Some of those parameters could be varied independently over a wide range; the corresponding scalings are discussed in subsequent sections. Table III lists dimensionless parameters that bound and delineate the physics of our experiment. Physical concepts and general theoretical expressions relevant to the parameter regime shown in Table III are reviewed here. In subsequent sections, we discuss the application of those concepts to the interpretation of the experimental observations.

A. Beam dynamics

As each electron beam propagates in the plasma, it generates a poloidal self-magnetic field, whose associated Lorentz force pinches the beam. That gives rise to a specific beam profile which can be compared with the experimental beam profile. The threshold current for magnetic pinching to occur is given by the Bennett pinch condition,²²

$$I_b^2 \geq 3.2 \times 10^{-10} n_b A_b T_{b\perp}, \quad (1)$$

where I_b is the beam current in amperes, n_b is the beam density in inverse cubic centimeters, A_b is the cross-sectional area of the beam in square centimeters, and $T_{b\perp}$ is the transverse beam temperature in electron volts. Electrostatic forces between beam electrons are neglected, because the beam is charge-neutralized by the background plasma. That is, we have satisfied the condition for space-charge neutralization of the beam,²³ $4\pi\sigma\tau_b \gg (L/r_b)^2$, where σ is the plasma conductivity, τ_b is the beam pulsewidth, L is the waveguide cavity (and beam propagation) length, and r_b is the beam radius.

In addition, return currents can be neglected, since the beam pulsewidth is much longer than the magnetic diffusion time²³: that is, $\tau_b \gg 4\pi\sigma r_b^2/c^2$, where c is the speed of light in vacuum. The pinching length, or the distance the beam travels before it becomes fully pinched, is of the order of the inverse betatron wavenumber,²⁴

$$k_\beta^{-1} \sim r_b (I_A/2I_b)^{1/2}, \quad (2)$$

where the Alfvén current $I_A = 1.70 \times 10^4 \beta\gamma$ amperes, $\beta = v_b/c$, v_b is the beam velocity, and $\gamma = (1 - \beta^2)^{-1/2}$.

B. Beam-plasma instability

Each electron beam propagating through the circular-waveguide plasma excites EPWs by means of the Cerenkov beam-plasma instability. In our experiment, the electron beams are weak ($\epsilon \equiv n_b/n_e \ll 1$ where n_b and n_e are the beam and background plasma densities, respectively) and cold ($\Delta v_b/v_b \ll \epsilon^{1/3}$, where Δv_b is the beam thermal speed). They excite EPWs (with angular frequency ω and axial wavenumber k_z) that satisfy the Cerenkov resonance condition, $\omega = k_z v_b$, as predicted by linear hydrodynamic theory.²⁵⁻²⁷ Since each electron beam is weak, its interaction with the background waveguide plasma is stronger than the mutual two-stream interaction of the beams.

The plasma-loaded waveguide behaves essentially like a slow-wave structure: each beam, with directed axial speed v_b (where $v_b < c$), interacts resonantly with the slow, quasi-electrostatic modes of the plasma-loaded waveguide. The electromagnetic field structure of the excited EPW has components E_z , E_r , and B_θ . The modes are quasi-electrostatic, since the magnetic field component is much smaller than the electric field components, of the order of δ_b/ω_{pe} , where δ_b is the growth rate of the Cerenkov beam-plasma instability.²⁸ The finite size of the waveguide cavity limits the allowed values of the axial (k_z) and the radial (k_\perp) wavenumbers, which follow from boundary conditions on the electromagnetic-field components at the conducting wall of the cavity. The quantization conditions are

$$k_z = \frac{p\pi}{L}, \quad (3a)$$

$$k_\perp = \mu_{nm}/R, \quad (3b)$$

where p is the integer, μ_{nm} corresponds to the m^{th} root of the n^{th} -order Bessel function $J_n(\mu_m)$, R is the cavity radius, and L is the cavity length.

The spectrum of Cerenkov-excited, axisymmetric EPWs for $r_b = R$ is²⁸

$$\omega = k_{oz} v_b + i\delta_b = \omega_{pe} + i\delta_b , \quad (4a)$$

$$\delta_b = \frac{\sqrt{3}-i}{2} \omega_{pe} \left[\frac{\epsilon}{2\gamma} \left(\frac{k_{\perp}^2 + k_{oz}^2/\gamma^2}{k_{\perp}^2 + k_{oz}^2} \right) \right]^{1/3} , \quad (4b)$$

where k_{oz} is the axial wavenumber satisfying the Cerenkov resonance condition. When the beam radius is small relative to the cavity radius ($r_b \ll R$) and concentric within the cavity, axisymmetric modes ($n = 0$) are preferentially excited because they have maximum E_z on axis.²⁹

The linear spatial growth rate for the Cerenkov-unstable EPWs in an infinite system is³⁰

$$k_{\perp} = \sqrt{3/2} (\epsilon E_b / T_e)^{1/3} k_{oz} , \quad (5)$$

where E_b is the beam energy and T_e is the electron temperature of the background plasma.

C. Wave saturation

Nonlinear theory shows that the EPW gains energy from the electron beam until it is saturated by beam trapping, which is the broadening of the beam velocity distribution.^{26,27} The phase velocity v_{ph} of the growing, beam-excited EPW lies slightly below the beam velocity:

$$v_{ph} \sim v_b (1 - \epsilon^{1/3} 2^{-4/3}) . \quad (6)$$

As the wave grows, it traps and slows beam electrons. The wave stops growing when its field amplitude saturates. The saturated energy density \bar{W}_0 of the EPW is

$$\bar{W}_0 = \bar{E}_0^2 / 8\pi = n_b E_b (\epsilon/2)^{1/3} , \quad (7)$$

where \bar{E}_0 is the saturated EPW electric field. The fraction of beam energy converted into EPW energy is thus $(\epsilon/2)^{1/3}$.

The initial growth and saturation of the EPW by beam trapping is rapid, occurring on the time scale of a few Cerenkov beam-plasma instability growth times. Since $\epsilon^{1/3} > \sqrt{m_e/m_i}$, where m_e and m_i are the electron and ion masses, respectively, such a time scale is faster than the inverse ion plasma frequency, implying that ion dynamics are not important at this stage.

If the saturated field amplitude of the beam-excited waves is large enough, nonlinear parametric instabilities involving ion dynamics, such as the modulational instability or the parametric decay instability, can occur on the ion time scale.³¹⁻³³ The modulated instability occurs when the ponderomotive force associated with the spatial gradient of the saturated wave intensity is strong enough to overcome either thermal dispersion or collisional effects. The ratio $W_0/n_e T_e$, where $W_0 = E^2/8\pi$ and $n_e T_e$ is the background-plasma energy density, quantifies the strength of the wave energy. In our experiment, the collisional contribution dominates and the threshold for the modulational instability is given by³⁴

$$W_0/n_e T_e > 4\nu_e/\omega_{pe}, \quad (8)$$

where ν_e is the electron collision frequency. The maximum linear growth rate of the modulational instability δ_{mod} is

$$\delta_{\text{mod}} \sim \omega_{pi} \left(\frac{W_0}{3n_e T_e} \right)^{1/2} \quad (9)$$

where ω_{pi} is the ion plasma frequency.

D. Strong plasma turbulence

When Eq. (8) is satisfied, the plasma is in the strongly turbulent regime characterized by the nonlinear development of the modulational instability, which involves Langmuir wave collapse. Zakharov's equations³¹ provide a theoretical model for Langmuir wave collapse (for $W_0/n_e T_e < 1$) and have been well studied.³⁵ The essence of the nonlinear development of the modulational instability is the transfer of energy in long-wavelength, beam-excited EPWs to shorter-wavelength, EPWs and density fluctuations. The shorter-wavelength EPWs are then subject to Landau damping.

In our experiment, the beam-excited EPWs would generate a ponderomotive force, which displaces plasma from regions of maximum electric field, forming a density fluctuation δn whose magnitude is of the order of $-|E|^2/16\pi T_e$, where E is the amplitude of the EPW electric field. Those low-density regions, or "cavitons,"³⁶ act as resonant cavities in which the EPWs are trapped. The plasma may evolve into a state characterized by the presence of rapidly collapsing electric fields and cavitons (supersonic time scale for $W_0/n_e T_e > \sqrt{m_e/m_i}$).

Strong plasma turbulence has been shown theoretically to have macroscopic consequences for the development of beam-plasma interactions.^{32,37-43} In a turbulent plasma, the long-wavelength, beam-excited EPWs can scatter off the ion density fluctuations associated with the collapsing cavities. The effective collision frequency for such scattering is^{38,40}

$$\nu_{\text{eff}} \sim \alpha \omega_{pe} (\delta n/n_e) , \quad (10)$$

where α is a numerical factor of order one. Computer simulations⁴⁰ give $\alpha \sim 1/3$ to $1/4$. The scattering detunes the Cerenkov beam-plasma resonance, which can then be retarded or quenched. As a result, the beam decouples from the plasma throughout the period of strong turbulence. However, the ion density fluctuations eventually dissipate — for example, through electron-ion

collisions or convection. Since the beam pulsewidth is longer than the characteristic ion-dissipation period in our experiment, the evolution of the beam-excited spectrum may be cyclic, with the period controlled by the ion dissipation time.^{41,44}

E. Radiation mechanisms

Microwaves and millimeter waves are generated by the interaction of three waves in the plasma-loaded waveguide. Two are counterpropagating quasi-electrostatic EPWs at ω_{pe} that are Cerenkov-excited by the counterstreaming electron beams. The third is a TM mode at $2\omega_{pe}$ that easily radiates out of the plasma. The electromagnetic-wave frequency is controlled by changing the background plasma density.

The kinematics of the plasma three-wave mixing follows from energy and momentum conservation relations for the waves.⁴⁵

$$\text{Energy conservation:} \quad \omega_3 = \omega_1 + \omega_2 \sim 2\omega_{pe} , \quad (11)$$

$$\text{Momentum conservation:} \quad k_{3z} = k_{1z} + k_{2z} \quad (12)$$

$$\text{Electromagnetic-wave dispersion:} \quad \omega_3^2 = \omega_{pe}^2 + \omega_c^2 + k_{3z}^2 c^2 , \quad (13)$$

$$\text{EPW dispersion:} \quad \omega_1 \sim \omega_{pe}, \omega_2 \sim \omega_{pe} . \quad (14)$$

Here ω_3 is the electromagnetic waveguide mode frequency, ω_1 and ω_2 are the frequencies of the beam-excited EPWs, ω_c is the vacuum waveguide cutoff frequency for the circular-waveguide TM mode, k_1 and k_2 are the EPW wavenumbers, and k_3 is the electromagnetic wavenumber.

In weak-turbulence theory, the emission power density for plasma three-wave mixing is⁴⁵

$$\Pi(2\omega_{pe}) \sim \frac{4}{5} \pi \sqrt{3} \left(\frac{\omega_{pe}^2}{n_e m_e c^3} \right) \int_{\sqrt{3} \omega_{pe}/c}^{k_D} W_k^2 \left(\frac{\omega_{pe}}{ck} \right)^2 dk , \quad (15)$$

where k_D is the inverse Debye length and W_k is the energy density of the EPWs per unit wavenumber k .

The total $2\omega_{pe}$ radiation power, $P(2\omega_{pe})$, is given by

$$P(2\omega_{pe}) = \Pi(2\omega_{pe})V_{int} , \quad (16)$$

where V_{int} ($\sim A_b L$, with A_b being the beam cross-sectional area) is the spatial volume in which the three-wave interaction takes place. The conversion efficiency η of beam power to $2\omega_{pe}$ radiation power is given by

$$\eta = P(2\omega_{pe})/P(2 \text{ beams}) , \quad (17)$$

where $P(2 \text{ beams}) = \sum_{i=1}^2 n_{bi} E_{bi} v_{bi} A_{bi}$ is the power in the two counterstreaming electron beams.

III. EXPERIMENTAL APPARATUS

In this section, we describe the experimental configuration, electron guns, and diagnostic instruments.

A. Experimental configuration and parameters

We investigated radiation generation using the beam-plasma-waveguide system shown in Fig. 1. Two electron beams are counterinjected into an unmagnetized, plasma-loaded circular waveguide, where they generate counterpropagating EPWs. The EPWs couple nonlinearly by

means of three-wave mixing to generate a TM waveguide mode, which then propagates down the waveguide in the direction of the slower beam (as a consequence of momentum conservation). Consistent with energy conservation, the radiation frequency is centered at twice the plasma frequency. Table IV lists our beam, plasma, and other operating parameters.

Figure 2 diagrams the experimental apparatus. High-density plasma ($\leq 10^{13} \text{ cm}^{-3}$) is generated by a 12-wire wire-anode discharge⁴⁶⁻⁴⁸ in the annular space surrounding a 3.8-cm-diameter, 15.2-cm-long microperforated waveguide with a background-gas pressure ranging from 1 to 50 mTorr. The microperforations allow both ionizing discharge electrons and background plasma to penetrate the waveguide, thus loading it with a high-density, quiescent plasma. The microperforations are large compared with a Debye length but small compared with the electromagnetic wavelength; therefore, radiation remains trapped in the waveguide but plasma can pass through freely.

Both ends of the cylindrical-waveguide cavity are terminated by highly transparent grids (80%). Radiation is coupled out of the cavity through rectangular X-band waveguides that are oriented to align the electric-field vector of the TE₁₀ rectangular-waveguide mode with the axial electric field of a TM mode in the circular waveguide.

B. Electron guns

Secondary-emission electron guns^{49,50} are used to generate the electron beams. As shown in Fig. 2, each gun employs a separate wire-anode discharge in the region between the waveguide and the electron-gun cathode. The plasma in each discharge is partially confined between the waveguide-terminating grid on one side and a similar grid on the opposite side near the cathode. The latter grid also serves as the anode for the electron gun.

A fraction of the ions produced in the plasma are extracted through the anode grid and then accelerated to the flat cathode (which is continuously held at negative high voltage), where they

bombard the molybdenum electrode surface and produce secondary electrons. Those electrons are accelerated back through the cathode-anode gap, forming a high-energy beam. After passing through the anode grid and the waveguide-terminating grid, electron beams are injected into the waveguide with low loss (~36%) to the grids. Finally, the beams propagate through the plasma-loaded waveguide, where ion charge in the plasma neutralizes the electron space-charge, allowing the beams to propagate without requiring the use of magnetic focusing-fields.

The utility of the secondary-emission electron gun is based on the high secondary-emission yield, which is obtained when high-energy ions strike gas-covered cathode-electrode materials. For example, the secondary-emission yield varies from 5 to 15 when helium ions in the 35- to 150-kV range strike a molybdenum cathode in the presence of 20 mTorr of helium gas.⁵¹

The electron-beam current is controlled at low voltage by modulating the ≤ 1 -kV wire-anode discharge at the ground potential of the anode electrode. Because the plasma is confined within the gridded anode structure (for ion current less than the space-charge-limited current, plasma electrons are unable to overcome the ≤ 1 -kV discharge-cathode drop to penetrate the gridded structure), plasma closure of the high-voltage gap cannot occur and long-pulse ($\gg 1 \mu\text{s}$) operation is achieved. Modulation of the plasma source controls the ion flux incident on the cathode, which in turn controls the beam current. A monoenergetic beam is obtained throughout the beam pulse because the electron beam is switched on and off by the plasma source rather than the high-voltage supply for the cathode. Low-energy electrons produced from the rise and fall of the cathode voltage in conventional pulsed beams are not present. All of this is achieved without heater power and without high-vacuum-environment requirements, because the metallic cathode used in the secondary-emission electron guns cannot be poisoned.

The apparatus is typically operated with 10- to 25- μs -wide flat-top pulses at a pulse repetition frequency of 1 Hz. A 25- μs pulse-forming network (PFN) is employed to drive current pulses up to 800 A in the main waveguide-plasma-discharge section. A higher-impedance 18- μs PFN drives the wire-anode discharge in electron-gun 2. Ignitrons are used as closing switches to

discharge both PFNs. The wire-anode discharge in electron-gun 1 is modulated by a circuit consisting of a capacitor and a Hughes-built XTRON-3 CROSSATRON® modulator switch.^{52,53} The Hughes CROSSATRON is an advanced thyatron-like device that both closes and opens under grid control, so square-wave pulses can be obtained in hard-tube-modulator fashion without having to use a fixed-pulselength PFN. The electron-gun wire-anode current pulses are typically 10 to 150 A. Finally, capacitors are used to continuously maintain high voltage on the electron-gun cathodes through 1-k Ω current-limiting resistors.

C. Diagnostic instruments

Each discharge and high-voltage beam circuit is instrumented with high-voltage probes and current transformers. Those diagnostic instruments, as well as Langmuir probes, are interfaced with an 11-channel, PC-based data acquisition system and an oscilloscope array, which are housed in a radio frequency interference (RFI) screen room. The output waveguides are also fed into the screen room, where the radiation is analyzed by a network of microwave and millimeter-wave detectors, filters, attenuators, and mixers. Figure 3 is a schematic of the detection system. The maximum sampling rate of the analog-to-digital (A/D) converters in the computerized data acquisition system is 1 GHz.

One axial and two radial Langmuir probes are employed to determine the plasma parameters in the plasma-loaded waveguide. Each probe consists of a 1-mm-diameter tantalum disk, which only negligibly perturbs the discharge. The radial probes are also used to measure the electron-beam profiles. One electron gun is removed and the axial probe is installed temporarily to measure the axial plasma-density profile. Figure 4 presents the profiles that result when the center anode wires are either disconnected from the modulator or driven through 47- Ω resistors. When the center wires are disconnected, all the current is collected by the eight end-wires and the profile is more uniform. When the center wires collect discharge current, the profile is more strongly peaked

near the midplane. Plasma leakage from each electron-gun wire-anode discharge also contributes to profile uniformity near the ends of the waveguide.

IV. BEAM DYNAMICS

Our measurements of the radial profile of a single beam indicate that the beam is focused as it propagates through the plasma-loaded waveguide. The equilibrium beam profile, threshold current, and focusing length are consistent with the Bennett condition for magnetic pinching.

A. Beam focusing

Radial plasma-density and electron-beam profiles measured at the rectangular output waveguide sections using disk probes are presented in Fig. 5. The electron-beam profile (50 keV, 5 A) reveals a well-collimated beam that converges rather than diverges as it propagates through the plasma-loaded waveguide. At the beam-injection end of the waveguide (near the first rectangular output waveguide), the beam current profile rises sharply at the edges and falls toward the axis. That profile is related to the ion density profile in the wire-anode-discharge section of the electron gun. The density is higher at the edge near the wires and lower near the axis. The 3.18-cm-diameter anode grid defines the beam diameter within the 3.81-cm-diameter waveguide.

At the opposite end of the waveguide (near the second rectangular output waveguide), as shown in Fig. 5, the beam has focused after passing through the waveguide plasma. The full width at half maximum has decreased from 2.7 to 0.45 cm, and the beam current density on axis has increased by a factor of about 8 despite beam attenuation by the plasma.

The beam current threshold for the self-focusing effect is the Bennett condition for magnetic pinching [Eq. (1)]. Using $\beta = 1/3$ and $T_{b\perp} = 10$ eV (see Sec. IV B) yields a beam current

threshold of $I_b \sim 1.8$ A. That value agrees with the experimentally determined threshold for beam focusing.

B. Radial electron beam profile

The radial electron-beam profile changes to a Bennett profile under the force exerted by the self-magnetic field. A Bennett profile, which results when the pinching force is balanced by beam thermal pressure or small-angle electron-neutral scattering,^{54,55} has the form

$$n_b(r) = \frac{n_{b0}}{(1 + r^2/a^2)^2}, \quad (18)$$

where r is the radial position relative to the center of the beam, n_{b0} is the beam density at $r = 0$, and the Bennett radius a is given by

$$a = [2 (2)^{1/2} \lambda_{Db}/\beta] \left(\frac{T_{b\perp}}{T_{b\perp} - T_e} \right)^{1/2}, \quad (19)$$

where λ_{Db} is the beam Debye length.

A typical radial electron-beam profile measured 15 cm downstream of the beam-injection point is presented in Fig. 6 for $n_e = 2 \times 10^{11} \text{ cm}^{-3}$, $E_{b1} = 35.5 \text{ keV}$, and $I_{b1} = 2.6 \text{ A}$. The figure demonstrates that the Bennett profile, specified by Eq. (18), agrees very well with the measured data; the best-fit value for the Bennett radius is 0.3 cm. Equation (19) can then be used to infer the perpendicular beam temperature $T_{b\perp}$. Using measured values of $n_b = 4 \times 10^9 \text{ cm}^{-3}$ and $T_e = 5 \text{ eV}$ in Eq. (19) yields $T_{b\perp} = 10 \text{ eV}$. If the beam current is adjusted to a value just below the Bennett pinch threshold, a temporal collapse in the radial electron-beam profile results,

as shown in Fig. 7. The initially broad, inverted profile evolves toward the pinched-beam condition over a period of 10 μ s.

Magnetic self-focusing has been used to explain beam pinching and the equilibrium beam diameter. Two additional factors should also be considered. One is the pinching length, given by Eq. (2), which should be less than the maximum beam propagation pathlength of 16.5 cm. For the conditions listed in Fig. 6 (2.6 A, 35.5 keV, 0.3-cm-radius beam), the pinching length is 10.5 cm. The second factor is that each counterstreaming electron beam will partially cancel the magnetic field produced by the other electron beam. However, since the two beams do not overlap precisely, a net magnetic field will be produced.

V. RADIATION SCALINGS

Microwave and millimeter-wave radiation is generated in our experiment when two counterstreaming electron beams are injected into the plasma-loaded waveguide; the plasma discharge alone produces no background radiation. Employing the detection techniques diagrammed in Fig. 3, we recorded radiation at frequencies up to 60 GHz. As Fig. 8 shows, 60-GHz radiation was observed over a 13- μ s period within the envelope of the electron-beam pulses, which overlap the pulse of the circular-waveguide cavity plasma-discharge current I_d . Moreover, the figure demonstrates that no background radiation was emitted from the plasma discharge before the beams were injected.

A high-density plasma and simultaneous injection of both beams are required to generate microwave and millimeter-wave radiation. As Fig. 9 shows, no radiation is produced when just one beam is injected into the plasma. That condition holds for current values up to the maximum single-electron-beam current of 6 A. Delayed injection of one beam demonstrates the necessity of

simultaneous injection of both beams. The plots in Fig. 10 record radiation at 50 GHz only when the beams overlap in time.

The necessity of simultaneous injection suggests that the radiation-generating mechanism involves the coupling of counterpropagating EPWs excited by the beams. If the radiation at $2\omega_{pe}$ were due to soliton emission, we would expect to see radiation when a single beam is present. The coupling of a single electron beam with plasma has been observed to generate radiation at $2\omega_{pe}$ in certain strongly turbulent regimes; indeed, radiation at $2\omega_{pe}$ has been observed in some single-beam/plasma experiments.^{19,56,57}

A. Radiation-frequency scaling with plasma density

The frequency of the radiation is controlled by the density of the waveguide plasma and is equal to twice its plasma frequency. As shown in Fig. 11, 36-GHz radiation is observed when the high-density waveguide discharge is on but disappears when both beams are injected without the discharge. However, even in the absence of a waveguide discharge, the waveguide is partially filled by low-density ($2 \times 10^{11} \text{ cm}^{-3}$) plasma from beam ionization as well as diffusion from the electron-gun wire-anode discharges. As demonstrated in the lower pulse sequence in Fig. 11, radiation appears at about 8 GHz, which is twice the frequency of the low-density plasma.

The scaling of the radiation frequency with the waveguide discharge current and plasma density was measured by varying the discharge current from 200 to 800 A and recording the output radiation with an array of waveguide bandpass and high-pass filters. The filter output is plotted in Fig. 12 as a function of the waveguide discharge current from 200 to 800 A. The data indicate that the center frequency increases with the discharge current. By plotting radiation frequency as a function of the discharge current value at which millimeter-wave power is received in each filter, we can determine the scaling of frequency with discharge current.

To minimize plasma production in the waveguide by the guns and beams, we performed the scaling experiment at low discharge current and low helium-gas pressure as well as reduced electron-gun wire-anode and beam current. The scaling of radiation frequency with discharge current presented in Fig. 13 shows a good fit to $I_d^{1/2}$ scaling. Such scaling is expected with low gas pressure because the discharge voltage remains constant as the discharge current is increased; under those conditions, $n_e \propto I_d$ and $\omega_{pe} \propto I_d^{1/2}$. As shown in Fig. 14, the radiation frequency scales as twice the waveguide plasma frequency, supporting the premise that the radiation-generating mechanism is plasma three-wave mixing. To further investigate radiation frequency scaling, we repeated the experiment using lower gas pressure, higher discharge current, and a 9.5-cm-diameter waveguide section. Figure 15 shows that the radiation frequency scaled as $I_d^{1/2}$, in agreement with the above argument.

B. Radiation-power scaling with electron-beam energy

We investigated the scaling of radiation power with electron-beam energy by holding the energy of electron-beam 1 constant at 19.5 keV and scanning the energy of electron-beam 2 over a broad range while simultaneously recording the output radiation power at 35 GHz. To reduce the effects of shot-to-shot variations and fluctuations of radiation power during a single pulse (i.e., amplitude modulation, described in Sec. VI), we used an RC integration circuit to measure the total radiation power in each shot. The resulting value was then averaged over ten successive shots. The results are plotted in Fig. 16 for total cathode currents (the sum of both electron beams) of 2.8, 3.0, 4.1, 5.6, 7.4, and 8.5 A. For each electron gun, the cathode current is roughly twice the injected beam current. At the lowest current, radiation is detected only for $E_{b1} = E_{b2}$. As the beam current is increased, the beam-energy tuning envelope broadens. In general, Fig. 16 shows that for low beam current, the radiation peaks when the beam energies are

nearly equal, providing further evidence that the $2\omega_{pe}$ radiation is produced by the coupling of counterpropagating EPWs.

Plasma three-wave mixing satisfies energy and momentum conservation according to Eqs. (11)–(14). The frequency of the electromagnetic wave is $\omega_3 = 2\omega_{pe}$ and its phase velocity is greater than c . The momentum conservation law, Eq. (12), imposes constraints on the wavenumbers of the interacting EPWs. The beam-excited waves, ω_1 and ω_2 , are slow, having axial phase velocities approximately equal to the beam velocity v_b . To satisfy momentum conservation, it is necessary to have $k_{1z} \sim -k_{2z}$, implying that $v_{b1} \sim v_{b2}$, consistent with the Cerenkov resonance condition. Energy tuning, which is a signature of the three-wave mixing process in the nonrelativistic regime, is evident in the curve shown in Fig. 16, in which the radiation power clearly peaks when the beam energies are approximately equal. At the higher beam currents, the tuning curve broadens, presumably owing to the spreading of the k spectrum of the beam-excited waves [$\Delta k_z/k_z \sim (n_b/n_e)^{1/3}$].

The energy tuning effect was further investigated by setting $E_{b1} = E_{b2} (= E_b)$ and plotting the radiation power as a function of beam energy. The results at 30-GHz output frequency, shown in Fig. 17, indicate an optimum beam energy of 30 keV. The optimum value changes very little as the total beam current ($I_b = I_{b1} + I_{b2}$) increases from 3.5 to 5.3 A. When the experiment was repeated at higher waveguide plasma density with a radiation frequency of 60 GHz, the optimum beam energy shifted to 41 keV (Fig. 18).

The scaling of radiation power with beam energy could be related to the mechanism for EPW saturation. For efficient coupling and high-power radiation emission, the EPWs excited by each beam must overlap spatially. The EPWs essentially travel with the beam because their group velocity v_g is of the order of the beam velocity; for maximum output radiation, the EPWs generated by each beam should reach saturation within the waveguide length. Each beam excites an EPW with $\omega \sim \omega_{pe}$ and $k_z = \omega_{pe}/v_b$. For the standard-case parameters (Table II), the instability growth rate δ_b is about $0.07 \omega_{pe}$, with $k_z \sim 9 \text{ cm}^{-1}$ and $\Delta k_z/k_z \sim (n_b/n_e)^{1/3} = 0.1$, where Δk_z is the half-

width of the beam-plasma instability in k_z space. The beam-plasma instability is in the strong hydrodynamic regime; thus, the EPW saturation mechanism must be beam trapping. Each beam traps in the potential of the unstable EPW that is excited within a few beam-plasma instability growth times. Equating the wave saturation time to the transit time for the beam to reach the midpoint of the waveguide ($6/\delta_b \sim L/2v_b$) yields

$$\beta \sim (L\omega_{pe}/15c)(n_b/n_e)^{1/3}, \quad (20)$$

where $\beta = v_b/c$. For $n_b/n_e = 0.001$ and $n_e = 3 \times 10^{12} \text{ cm}^{-3}$, we obtain $\beta \sim 0.3$ and $E_b \sim 30 \text{ keV}$, which is consistent with the voltage tuning data shown in Fig. 17. Equation (20) also predicts the trend shown in Fig. 18, since the optimum voltage should shift to higher beam energies as either n_b or n_e is increased.

C. Radiation-power scaling with electron-beam current

The scaling of radiation power with total beam current (the sum of the two injected beam currents), plotted in Fig. 19, has three salient features. First, there is a sharp threshold at 3 A of total beam current, below which we observe no power. (The lowest detectable power is $\sim 100 \mu\text{W}$ for this experiment.) That threshold is also apparent in Fig. 10. No radiation is produced during the early portion of the electron-beam 2 pulse, even with 0.5-A current from electron-beam 1; however, radiation is observed when the electron-beam 1 current is increased to 2 A. Second, at about 3 A, the power rises rapidly over two orders of magnitude. Third, just above 3 A, the sharply rising curve shifts to a power scaling that is approximately proportional to I_b^6 , where $I_b = I_{b1} + I_{b2}$. From the I_b^6 power scaling, we can conclude that the beam-to-radiation conversion efficiency scales as I_b^5 .

In Fig. 20, we extended the power scaling to higher total beam currents and plotted the scaling for helium, hydrogen, and neon gases. The same threshold-current phenomenon is observed for each gas species. The data also indicate that the power increases with ion mass. The most significant result is that, at the highest beam currents available, the radiation power is still increasing rapidly with beam current. At 7 A in helium, we estimate peak power levels in the circular-waveguide cavity to be 8 kW at 31 GHz, with a peak beam-to-radiation conversion efficiency of 4%. This efficiency calculation is based on cold tests of the circular, microperforated waveguide, which show that only about 1% of the $K\alpha$ -band radiation generated in the waveguide is transmitted to the X-band output ports.

Estimates based on weak-turbulence theory are reasonably consistent with the magnitude and scaling of the observed $2\omega_{pe}$ radiation. The weak-turbulence expression for the magnitude of the $2\omega_{pe}$ -radiation emission power density, $\Pi(2\omega_{pe})$, is given by Eq. (15). To evaluate that expression, we assume, first, that the energy density of the EPWs, W_0 , is constant over a region of k_z space corresponding to the half-width δk of the beam-excited plasma wave spectrum after N e-foldings: $\delta k = \sqrt{N} (n_b/n_e)^{1/3} k_{oz}$, where k_{oz} is the axial wavenumber of the beam-excited wave, satisfying $\omega_{pe} = k_{oz}v_b$. Second, we assume that W_0 is the saturated wave energy density due to beam trapping given by Eq. (7). The emission power density is now integrated to yield

$$\Pi(2\omega_{pe}) \sim \sqrt{N} \omega_{pe} (n_b/n_e)^{7/3} (v_b/c)^7 n_e m_e c^2 . \quad (21)$$

Multiplying Eq. (21) by the interaction volume $A_b L = \pi r_b^2 L$ (where r_b is the pinched-beam radius) yields the total $2\omega_{pe}$ power radiated. To calculate the peak radiated power, we use $n_e = 3 \times 10^{12} \text{ cm}^{-3}$, $E_b = 35 \text{ keV}$, and $n_b/n_e \sim 0.003$ ($I_{b1} = I_{b2} = 3.5 \text{ A}$), assuming a pinched-beam radius of $r_b \sim 0.25 \text{ cm}$. With those values, the peak radiated power is estimated to be of the order of 0.2 kW. That peak is below the inferred experimental value. However, the experimental

value is based on cold tests of the waveguide; moreover, the theory itself is based on saturated amplitudes that can have error bars of an order of magnitude.

We compare the above estimate with an estimate for radiation at $2\omega_{pe}$ from cylindrically symmetric solitons. The power emitted per soliton is given in Refs. 14 and 17 as

$$P(2\omega_{pe}) = \sqrt{3} \pi \omega_{pe} \frac{E_0^2}{8\pi} \left(\frac{v_e}{c}\right) \lambda_D^3, \quad (22)$$

where E_0 is the amplitude of the soliton electric field and v_e is the thermal speed. Using $E_0^2/8\pi = n_e T_e$, with $n_e = 3 \times 10^{12} \text{cm}^{-3}$ and $T_e = 5 \text{ eV}$, gives a power output of about $4 \mu\text{W}$ per soliton. That value is about nine orders of magnitude smaller than the measured peak power.

From Eq. (21), the scaling of radiation power with beam density is given by

$$P(2\omega_{pe}) \propto n_b^{7/3} v_b^7 A_b. \quad (23)$$

If the beam profile is determined from self-focusing ($n_b A_b T_b \propto I_b^2$) and the equation of state of the beam is $n_b \propto T_b$ (corresponding to two-dimensional adiabatic compression), then Eq. (23) scales as $P \propto I_b^{7/3}$. To derive that expression, we also used $n_b A_b \propto I_b/v_b$, where n_b is the pinched-beam density and v_b is constant. If the beam energy is optimized so that $v_b \propto n_b^{1/3}$, as discussed in Sec. V.B, the power scales as $P \propto I_b^6$, which is reasonably consistent with the experimental scaling. If beam pinching is a factor in radiation generation, then the magnitude of the radiation power should depend on the relative beam position in the waveguide, since the pinched-beam cross sections are small. To investigate that issue, we installed beam-steering magnetic-field coils along the waveguide to adjust the radial position of each beam. As shown in Fig. 21, a displacement of one beam by just 2 mm increased the radiation power by a factor of 2. However, when the beam was displaced by 1.2 cm, the level of radiation fell below our detection threshold. Further

measurements and theoretical analyses of counterstreaming electron-beam dynamics are required to resolve this scaling issue.

VI. RADIATION CHARACTERISTICS

Our experiment produces strongly amplitude-modulated radiation. It is emitted as bursts with interburst periods and burstwidths that depend on the background gas species. Figure 22 demonstrates that the radiation is strongly modulated with a frequency near the ion-plasma frequency.

The millimeter-wave modulation frequency decreases with greater ion mass. Oscilloscope photographs of the crystal detector outputs for five different gases (hydrogen, helium, argon, krypton, and xenon) are presented in Fig. 23. The same data are shown quantitatively in Fig. 24, where the modulational interburst periods and burstwidths are plotted as functions of ion mass. The parameters scale approximately with the square root of the ion mass. The data clearly indicate the importance of ion dynamics in determining the characteristics of the radiation. For example, the modulation could be caused by ion-acoustic waves, known to be generated by nonlinear parametric instabilities in systems with strong EPW turbulence.

A. Nonlinear parametric instabilities

To understand how the radiation is modulated on the ion time scale, we consider the role of strong plasma turbulence. When the saturated EPW amplitude becomes sufficiently large, nonlinear parametric processes involving the ion dynamics can occur. The threshold for the modulational instability [given by Eq. (8)] depends on the electron-neutral collision frequency and is $W_0/n_e T_e > 0.004$ for standard-case parameters. Using the saturated EPW energy density \bar{W}_0

estimated from beam trapping (with $n_b/n_e = 0.001$, $E_b = 30$ keV, and $T_e = 10$ eV) yields $\bar{W}_0/n_e T_e \sim 0.2$, which is larger than the threshold for the modulational instability. Beam trapping occurs on the time scale of a few beam-plasma instability growth periods, so the saturated EPW amplitude is reached before the modulational instability can grow.

The linear growth rates for the modulational instability and the parametric decay instability can be calculated using the following one-dimensional linear dispersion relation for the parametric instabilities, including electron and ion collisions⁵⁸⁻⁶¹:

$$[\omega^2 + 2iv_i\omega - (\omega_k^i)^2] [(\omega + iv_e)^2 - \Delta^2] + (k^2 e^2 E_0^2 / 4m_e m_i) (\Delta / \omega_k^e) = 0, \quad (24)$$

where v_i and v_e are the effective ion and electron collision frequencies, respectively; $\omega_k^i = kc_s$ is the ion-acoustic frequency, c_s being the ion sound speed; $\Delta = \omega_0 - \omega_k^e$ is the frequency mismatch, ω_0 being the pump EPW frequency (i.e., the beam-excited wave satisfying $\omega_{pe} = k_{0z} v_b$); $E_0^2/8\pi$ is the energy density of the pump EPW; and $\omega_k^e = \omega_{pe} [1 + (3/2)k^2 \lambda_D^2]$.

Figure 25(a) shows, for a helium plasma, the growth rate for the modulational instability γ_{mod} calculated for $E_0^2/8\pi n_e T_e = 0.05$, $\omega_0 = \omega_{pe}$, and $v_e/\omega_{pe} = 2 \times 10^{-3}$. Figures 25(b), (c), and (d) show the growth rate of the modulational instability with the same parameters for argon, krypton, and xenon plasmas, respectively. The maximum growth is inversely proportional to the square root of the ion mass. Figure 26 shows the effect of electron collisions on the growth rate of the modulational instability. The parameters are $E_0^2/8\pi n_e T_e = 0.1$ and $\omega_0 = \omega_{pe}$, and the electron collision frequencies are (a) $v_e/\omega_{pe} = 0$, (b) $v_e/\omega_{pe} = 2 \times 10^{-3}$, (c) $v_e/\omega_{pe} = 4 \times 10^{-3}$, and (d) $v_e/\omega_{pe} = 8 \times 10^{-3}$. Collisions reduce the growth of the instability, but do not quench it for our range of experimental parameters.

These estimates suggest that, in our experiment, the modulational instability plays a role in the development of the beam-plasma instability. For standard-case parameters, the amplitude of the beam-excited waves, saturated by beam trapping, is much larger than the threshold for the

instability. Collisions reduce the growth rate just slightly. For a helium plasma, standard-case growth times for the linear stage of the modulational instability are of the order of several ω_{pi}^{-1} ~several nanoseconds, which is much larger than the beam pulsewidth of 20 μ s. Hence, effects of the modulational instability should be manifest in the radiation emitted from the plasma.

B. Phenomenological model of temporal modulation of radiation

We invoke strong plasma turbulence effects to explain the observed temporal modulation of the $2\omega_{pe}$ radiation. Figures 25, 26, and 27 demonstrate that the modulation occurs on the ion time scale, the same as for the development of nonlinear parametric instabilities.

Computer simulations and phenomenological models describing the nonlinear stabilization of beam-plasma interactions due to strong turbulence were presented in Refs. 37-39, and 42. Quasi-steady-state models for the case of continuous beam injection were also proposed in those studies. Our experiment can be considered steady state, since the beam pulsewidth ($\tau_b = 20 \mu$ s) is much longer than the time scale for the development of parametric instabilities, 10 to 100 ω_{pi}^{-1} .

In the quasi-steady state, the waves generated by the modulational instability can affect the dissipation of the beam-excited wave. In particular, finite amplitude ion density perturbations and cavities provide a mechanism for dissipating the long-wavelength, beam-excited EPWs. It involves the scattering of EPWs off density fluctuations (the Davison-Oberman high-frequency resistivity)⁶² into the nonresonant wavenumber regime, where the EPWs can be damped by either Landau damping or resonance broadening.^{38,40}

Motivated by the phenomenological approaches of Refs. 37 through 39, we developed a phenomenological model for the temporal evolution of the beam-plasma radiation-generation system. The following scenario describes relaxation oscillations about a quasi-steady state, involving the growth and decay of the ion density fluctuations. Initially, each electron beam excites EPWs by means of a strong, hydrodynamic beam-plasma instability. Beam trapping

saturates the waves on the short electron time scale, of the order of several beam-plasma growth times. The saturated EPWs with energy density \bar{W}_0 drive the modulational instability, whose linear growth occurs on the ion time scale of several tens of ω_{pi}^{-1} . Since $\bar{W}_0 > \sqrt{m_e/m_i}$, the nonlinear development of the modulational instability (i.e., Langmuir collapse) can occur supersonically.

In this scenario, EPWs scatter off the ion density perturbations and cavities, with an effective collision frequency governed by $\nu_{\text{eff}} \sim \alpha \omega_{pe} (\delta n/n_e)$ [Eq. (10)]. If the density fluctuations are large enough that ν_{eff} is greater than the beam-plasma instability growth rate, δ_b , the plasma becomes transparent to the beam. As the density fluctuations decay such that $\delta_b > \nu_{\text{eff}}$, the EPWs are again excited by the beam and the cycle repeats. Since the $2\omega_{pe}$ radiation is produced by the coupling of the beam-excited waves, the output radiation power is also cyclic on the time scale of the growth and decay of the ion density fluctuations.

The phenomenological model describing the temporal evolution of our beam-plasma-radiation system comprises the following coupled nonlinear equations, which assume the same parameters for both beams:

$$\frac{dW_1}{dt} = \delta_b W_1 - \nu_{\text{eff}}(W_s) W_1, \quad (25)$$

$$\frac{dW_2}{dt} = \nu_{\text{eff}}(W_s) W_1 - \gamma_e W_2, \quad (26)$$

$$\frac{dW_s}{dt} = \gamma_{\text{mod}}(W_1) W_s - \gamma_i W_s, \quad (27)$$

$$\frac{dW_T}{dt} = \gamma_T W_1^2 - \gamma_c W_T, \quad (28)$$

where W_1 is the energy density of the beam-excited waves (normalized to $n_e T_e$), W_2 is the normalized energy density of the shorter-wavelength EPWs, $W_s = (\delta n/n_e)^2$ is the normalized

energy density of the ion density fluctuations, and W_T is the normalized energy density of the electromagnetic waves with frequency $2\omega_{pe}$.

The linear beam-plasma instability growth rate δ_b is given by $\delta_b = \sqrt{3}/2 (n_b/2n_e)^{1/3}$. The growth rate of the modulational instability is $\gamma_{mod} = \omega_{pi}(W_1/3)^{1/2}\Theta(W_1 - W_{th})$, where Θ is the Heaviside function with argument $(W_1 - W_{th})$, and W_{th} is the threshold energy density for the modulational instability, given by $W_{th} = 4v_e/\omega_{pe}$. The rate of plasmon scattering on density fluctuations is taken as $v_{eff} = W_s^{1/4}/4$, whereas, the shorter-wavelength plasma waves are assumed to be damped by Landau damping, denoted by γ_e . The ion fluctuations are assumed to decay by convection,^{63,64} $\gamma_i = kc_s$, since the ion-neutral collision rate and the electron Landau damping rate are relatively small in our experimental range. The rate of three-wave mixing, γ_T , is given by

$$\gamma_T = \frac{4\pi\sqrt{3}}{5} \sqrt{N} \omega_{pe} \left(\frac{v_b}{c}\right)^3 \left(\frac{v_e}{c}\right)^2 \left(\frac{n_e}{n_b}\right)^{1/3}, \quad (29)$$

which follows from Eq. (15), assuming that the spectral width of the W_1 waves, with wavenumber $k_1 = \omega_{pe}/v_b$, is given by $(\Delta k_1/k_1) = (n_b/n_e)^{1/3} / \sqrt{N}$, after N e-foldings. The rate of radial convection of the electromagnetic waves in the waveguide is $\gamma_c = c/R$.

Figures 27 and 28 show solutions of Eqs. (25)-(28) for helium and argon plasmas, respectively. The parameters are $n_b/n_e = 0.001$, $n_e = 3 \times 10^{12} \text{cm}^{-3}$, $T_e = 5 \text{ eV}$, $E_b = 35 \text{ keV}$, $N = 6$, $R = 2 \text{ cm}$, and $v_e/\omega_{pe} = 0.001$. The ion decay rate γ was modeled by $\gamma_i = 4kc_s = 4(\omega_{pe}/v_b)c_s$, which corresponded well with the time scale between radiation bursts. The Landau damping rate was modeled by a constant, $\gamma_e = 0.01 \omega_{pe}$, which corresponds to a wavelength of the W_2 waves, k_2 , of the order of $k_2\lambda_{De} \sim 0.2$. The solutions are initialized with $W_1 = 0.1$, $W_2 = 0.3$, $W_s = 0.08$, and $W_T = 2 \times 10^{-4}$.

As shown in Fig. 27 for helium, the radiation burstwidth is of the order of $<10 \text{ ns}$ and the interburst period is of the order of 20 ns , both values being reasonably consistent with the experimental data for helium presented in Fig. 23. The radiation burstwidth is controlled by the

modulational-instability growth time, and the interburst period is controlled by the dissipation of the ion density fluctuations. Both scale as $m_i^{1/3}$ to $m_i^{1/2}$, consistent with the experimental data in Figs. 23 and 24. Figure 28 shows results for argon for the same parameters as for the helium case of Fig. 27. The burstwidth is <15 ns and the interburst period ~ 35 ns, also reasonably consistent with the data shown in Fig. 23. The bursts appear to be more regular than those shown in the oscilloscope photographs in Fig. 23, presumably because the simple model ignores the variation of background plasma parameters, which can result from strong turbulence, as well as the spatial evolution of the system. Temporal measurements of the ion density fluctuations in the system would help to confirm the validity of the model.

VII. RESULTS AND DISCUSSION

Our beam-plasma radiation-generation experiment has the following temporal evolution. By means of a strong, hydrodynamic, Cerenkov beam-plasma instability, each electron beam excites EPWs on a fast time scale — of the order of $(n_b/n_e)^{-1/3} \omega_{pe}^{-1}$. The beam-excited EPW is saturated by beam trapping, also on a fast time scale — of the order of several beam-plasma instability growth times. Radiation at twice the plasma frequency is generated through plasma three-wave mixing of counterpropagating EPWs. The energy density of the EPWs, W_o , at saturation is large enough to drive the modulational instability, which develops on the slower ion time scale — of the order of $\omega_{pi}^{-1} (W_o/n_e T_e)^{-1/2}$. Strong plasma turbulence, with Langmuir collapse and ion density fluctuations, develops supersonically, since $W_o/n_e T_e > (m_e/m_i)^{1/2}$. Beam-excited EPWs scatter from the ion density fluctuations and shift out of resonance with the beam, causing the beams to decouple from the EPWs. The ion fluctuations then decay (for example, by means of convection or collisions) and the beams can again couple to the plasma and excite EPWs. The entire cycle repeats on the ion-dissipation time scale, which is much shorter than the beam pulsewidth.

Theoretical analyses of the physical processes operating in our experiment appear to be consistent with several key experimental results. The dynamics of a single beam is consistent with magnetic pinching. The Bennett pinch condition is consistent with the experimental beam current threshold for beam focusing. The radial beam profile can be fit with a Bennett profile, whose radius is consistent with theory. The mechanism responsible for radiation emission is consistent with the weak-turbulence theory of plasma three-wave mixing. Momentum and energy conservation for that process is exhibited by energy tuning. Beam trapping estimates are consistent with the observed peaking of radiation power with beam energy. Estimates of the millimeter-wave radiation power and beam-to-radiation conversion efficiency calculated using weak-turbulence theory are reasonably consistent with the experimentally measured power. A phenomenological model to explain the temporal modulation of the radiation on the ion time scale is consistent with the pulsed characteristics of the radiation as well as the magnitude and scaling of the burst and interburst periods.

The conversion efficiency of beam-to- $2\omega_{pe}$ -radiation power is much higher in our experiment than in previous counterstreaming electron-beam experiments, as indicated in Table I. The dependence of the radiation emission power density on $n_b E_b$ appears to be the primary source of the difference. That density, from Eq. (15), is

$$\Pi(2\omega_{pe}) \sim \omega_{pe}(v_b/c)^3 W_0 (W_0/n_e m_e c^2) . \quad (30)$$

Here W_0 is proportional to the beam energy density and is equal to $\xi n_b E_b$, where $\xi \sim (n_b/n_e)^{1/3}$, for a cold beam, with wave saturation by beam trapping. The dependence of Π on beam energy is then $\Pi \sim E_b^{3.5}$. Since previous experiments used beam energies of the order of 100 to 400 eV and we use beam energies of 30 keV, the radiation emission power density should be higher by a factor of about 4×10^6 to 5×10^8 assuming other parameters are the same. Similarly, the beam-to- $2\omega_{pe}$ -radiation conversion efficiency will be higher by a factor of E_b^2 , an increase of 10^4 to 10^5 .

This points toward favorable scaling of the three-wave mixing radiation mechanism to the higher beam energy regime.

ACKNOWLEDGMENT

We are indebted to R. Watkins, Hughes Research Laboratories, Plasma Physics Department, for his expert technical assistance in fabricating and maintaining the experimental apparatus. This work was supported by the Air Force Office of Scientific Research under Contract F49620-85-C-0059.

REFERENCES

1. K. Papadopoulos, Rev. Geophys. Space Phys. **17**, 624 (1979).
2. J. Benford, "High power microwave simulator development," Microwave J., p. 97 (December 1987).
3. M.V. Kuzelev, F. Kh. Mukhametzyanov, M.S. Rabinovich, A.A. Rukhadze, P.S. Strelkov, and A.G. Shkvarunets, Sov. Phys. JETP **56**, 780 (1982).
4. L.D. Bollinger and H. Bohmer, Phys. Rev. Lett. **26**, 535 (1971).
5. L.D. Bollinger and H. Bohmer, Phys. Fluids **15**, 693 (1972).
6. J.R. Apel, Phys. Rev. Lett. **19**, 744 (1967).
7. J.R. Apel, Phys. Fluids **12**, 640 (1969).
8. D.A. Whelan and R.L. Stenzel, Phys. Rev. Lett. **47**, 95 (1981).
9. D.A. Whelan and R.L. Stenzel, Phys. Fluids **28**, 958 (1985).
10. R.E. Aamodt and W.E. Drummond, Plasma Phys. **6**, 147 (1964).
11. P.A. Sturrock, Plasma Phys. **2**, 158 (1961).

12. P.A. Sturrock, R.H. Ball, and D.E. Baldwin, *Phys. Fluids* **8**, 1509 (1965).
13. T.J.M. Boyd, *Phys. Fluids* **7**, 59 (1964).
14. K. Papadopoulos and H. Freund, *Space Sci. Rev.* **24**, 511 (1979).
15. P. Leung, J. Santoru, A.Y. Wong, and P.Y. Cheung, in *Physics of Auroral Arc Formation*, Geophysical Monograph Series, Vol. 25, edited by S.I. Akasofu and J.R. Kan (American Geophysical Union, Washington, D.C., 1981).
16. T. Intrator, N. Hershkowitz, and C.Chan, *Phys. Fluids* **27**, 527 (1984).
17. K. Papadopoulos and H.P. Freund, *Geophys. Res. Lett.* **5**, 881 (1978).
18. M.V. Goldman, G.F. Reiter, and D.R. Nicholson, *Phys. Fluids* **23**, 388 (1980).
19. P.Y. Cheung, A.Y. Wong, C.V. Darrow, S.J. Qian, *Phys. Rev. Lett.* **48**, 1348 (1982).
20. A.Y. Wong and P. Cheung, *Phys. Rev. Lett.* **52**, 1222(1984).
21. F.W. Crawford, *Proc. IEEE* **59**, 4 (1971).
22. W.H. Bennett, *Phys. Rev.* **45**, 890 (1934).

23. R.N. Sudan, in *Handbook of Plasma Physics*, edited by M.N. Rosenbluth and R.Z. Sagdeev; (North-Holland and Elsevier, New York, 1983), Vol. 2, *Basic Plasma Physics II*, edited by A.A. Galeev and R.N. Sudan.
24. A.S. Halstead and D.A. Dunn, *J. Appl. Phys.*, **37**, 1810 (1966).
25. R.J. Briggs, *Electron Stream Interaction with Plasmas*, (MIT Press, Cambridge, Mass., 1964).
26. T.M. O'Neil, J.H. Winfreg, and J.H. Malmberg, *Phys. Fluids* **14**, 1204 (1971).
27. S. Kainer, J.M. Dawson, and R. Shanny, *Phys. Fluids* **15**, 493 (1972).
28. B.I. Aronov, A.A. Rukhadze, and M.E. Chogovadze, *Sov. Phys. Tech. Phys.* **17**, 877 (1972).
29. T. Tajima, *Phys. Fluids* **22**, 1157 (1979).
30. S.A. Self, M.M. Shoucri, and F.W. Crawford, *J. Appl. Phys.* **42**, 704 (1971).
31. V.E. Zakharov, *Sov. Phys. JETP* **35**, 908 (1972).
32. R.Z. Sagdeev, *Rev. Mod. Phys.* **51**, 1 (1979).
33. D.R. Nicholson, *Introduction to Plasma Theory* (Wiley, New York, 1983), Chap. 7.

34. C.N. Lashmore-Davies, Nucl. Fusion **15**, 213 (1975).
35. M.V. Goldman, Rev. Mod. Phys. **66**, 709 (1984).
36. H.C. Kim, R.L. Stenzel, and A.Y. Wong, Phys. Rev. Lett., **33**, 886 (1974).
37. K. Papadopoulos, Phys. Fluids **18**, 1769 (1975).
38. A.A. Galeev, R.Z. Sagdeev, V.D. Shapiro, and V.I. Shevchenko, Sov. Phys. JETP Lett. **24**, 21 (1976).
39. H.P. Freund, I. Haber, P. Palmadesso, and K. Papadopoulos, Phys. Fluids **23**, 518 (1980).
40. A.A. Galeev, R.Z. Sagdeev, V.D. Shapiro, and V.I. Shevchenko, Sov. Phys. JETP **46**, 711 (1977).
41. H.L. Rowland, Phys. Fluids **23**, 509 (1980).
42. H.L. Rowland and K. Papadopoulos, Phys. Rev. Lett. **39**, 1276 (1977).
43. R.A. Smith, M.L. Goldstein, and K. Papadopoulos, Astrophys. J. **234**, 348 (1979).
44. B.A. Alterkop, A.S. Volokitin, and V.P. Tarakanov, Sov. Phys. Dokl. **22**, 302 (1977).
45. S.A. Kaplan and V.N. Tsytovich, *Plasma Astrophysics* (Pergamon, Oxford, 1973).

46. I. Alexeff and F. Dyer, Phys. Rev. Lett. **45**, 351 (1980).
47. G.W. McClure, Appl. Phys. Lett. **2**, 233 (1963).
48. J.R. Bayless and R.J. Harvey, U.S. Patent No. 3 949 260 (1976) (assigned to Hughes Aircraft Company).
49. D. Pigache and G. Fournier, J. Vac. Sci. Technol. **12**, 1197 (1975).
50. G. Wakalopoulos, U.S. Patent No. 3 970 892, (20 July 1976), (assigned to Hughes Aircraft Company).
51. P.F. Little, "Secondary effects," in *Encyclopedia of Physics/Handbuch der Physik*, edited by S. Flugge (Springer-Verlag, Berlin, 1956), Vol. XXI, *Electron-Emission Gas Discharges I/elektronen-Emission Gasentladungen I*, pp. 574-663.
52. R.W. Schumacher and R.J. Harvey, "CROSSATRON Modulator Switch," *Conference Record of the Sixteenth IEEE Power Modulator Symposium*, IEEE 84 CH2056-0, 1984, pp. 139-151.
53. R.W. Schumacher and R.J. Harvey, "CROSSATRON Modulator Switch: A Long-Life Component for Pulsed-Power Systems," Fifth IEEE Pulsed-Power Conference.
54. E.P. Lee, Phys. Fluids **19**, 60 (1976).

55. J.D. Lawson, *The Physics of Charged Particle Beams* (Clarendon Press, Oxford, 1977), p. 273.
56. M. Schneider and M.Q. Tran, Phys. Lett. **91A**, 25 (1982).
57. K.G. Kato, G. Benford, and D. Tzach, Phys. Fluids **26**, 3636 (1983).
58. G.L. Payne, D.R. Nicholson, R.M. Downie, and J.P. Sheerin, J. Geophys. Res. **89**, 10921 (1984).
59. D.R. Nicholson, G.L. Payne, R.M. Downie, and J.P. Sheerin, Phys. Rev. Lett. **52**, 2152 (1984).
60. J.C. Weatherall, J.P. Sheerin, D.R. Nicholson, G.L. Payne, M.V. Goldman, and P.J. Hansen, J. Geophys. Res. **87**, 823 (1982).
61. W. Kruer and J.M. Dawson, Phys Fluids **15**, 446 (1972).
62. J. Dawson and C. Oberman, Phys. Fluids **5**, 517 (1962).
63. P.Y. Cheung and A.Y. Wong, Phys. Rev. Lett. **55**, 1880 (1985).
64. P.Y. Chueng and A.Y. Wong, Phys. Fluids **28**, 1538 (1985).

TABLE I. Comparison of key parameters and results of previous and current counterstreaming electron-beam experiments.

Experiment	Radiation frequency, (= $2f_{pe}$) (GHz)	Background-neutral pressure (mTorr)	Beam energy, E_b (keV)	Conversion efficiency of beam-to- $2f_{pe}$ radiation, $\eta = \frac{P(2f_{pe})}{2n_b e E_b v_b A_b}$
Leung et al. ¹⁵	2	~0.1	0.1	~ 10^{-10} (Ar) ^a
Intrator et al. ¹⁶	0.6	≤ 0.02	0.35	~ 2×10^{-4} (Xe)
Current experiment	8-60	>25	30	<0.04 (He)

^aEstimated from data in Ref. 15.

TABLE II. Standard-case parameters for current experiment.

Waveguide cavity

Length $L = 15$ cm

Radius $R = 1.9$ cm

Background helium gas

Pressure $P \sim 40$ mTorr

Neutral density $n_n \sim 1.5 \times 10^{15} \text{ cm}^{-3}$

Ambient plasma

Electron density $n_e = 3 \times 10^{12} \text{ cm}^{-3}$

Ion density $n_i = n_e$

Electron temperature $T_e = 5$ eV

Ion temperature $T_i \leq 0.1$ eV

Plasma frequency $\omega_{pe} \sim 10^{11} \text{ s}^{-1}$

Collisionless skin depth $\delta_0 = c/\omega_{pe} \sim 0.3$ cm

Electron Debye length $\lambda_D \sim 0.001$ cm

Electron-neutral collision frequency $\nu_{en} \sim 10^8 \text{ s}^{-1}$

Ion-neutral collision frequency $\nu_{in} \sim 10^6 \text{ s}^{-1}$

Electron-ion collision frequency $\nu_{ei} \sim 10^7 \text{ s}^{-1}$

Conductivity $\sigma = \omega_{pe}^2/4\pi \nu_{en} \sim 10^{13} \text{ s}^{-1}$

Electron beams

Pulsewidth $\tau_b = 20$ μs

Energy $E_{b1} = E_{b2} = 30$ keV

Density $n_b/n_e \sim 0.001$

TABLE III. Dimensionless parameters for current experiment (helium).

Collisions

$$v_{en}/\omega_{pe} \sim 10^{-3}$$

$$v_{ei}/\omega_{pe} \sim 5 \times 10^{-4}$$

$$v_{in}/\omega_{pe} \sim 10^{-5}$$

Ion temperature

$$T_i/T_e < 0.02$$

Mass ratio

$$\sqrt{m_e/m_i} \sim 0.01$$

Thermal dispersion

$$k_{oz}\lambda_D = 0.01$$

Beam pulsewidth \cdot h

$$\omega_{pi}\tau_b \sim 2 \times 10^4$$

$$\tau_p v_b/L \sim 10^4$$

Beam energy

$$E_b/T_e \sim 6 \times 10^3$$

$$\beta = v_b/c \sim 1/3$$

Beam thermal spread

$$\Delta v_b/v_b \sim 0.02$$

Beam density

$$(n_b/n_e)^{1/3} \sim 0.1$$

TABLE IV. Operating parameters of current experiment.

Background-neutral gas

H₂, He, Ne, Ar, Kr, or Xe at 1–65 mTorr; typically He at 24 mTorr

Ambient plasma

Electron density $n_e = 2 \times 10^{11} \text{ cm}^{-3}$ to 10^{13} cm^{-3}

Electron beams

Energy $E_b \leq 90 \text{ keV}$, typically 20–50 keV

Current $I_b \leq 3.5 \text{ A}$

Temperature $T_b \geq 15 \text{ eV}$

Current density $J_b \leq 4 \text{ A/cm}^2$

Beam density $n_b \leq 6 \times 10^9 \text{ cm}^{-3}$, $0.03\% \leq n_b/n_e \leq 3\%$

Circular waveguide cavity

3.8-cm diameter, 15.2-cm length

FIGURE CAPTIONS

- FIG. 1. Beam-plasma-waveguide system: \vec{k}_1 and \vec{k}_2 are the wavenumbers of the beam-excited EPWs and \vec{k}_3 is the wavenumber of the resultant electromagnetic wave.
- FIG. 2. Experimental beam-plasma apparatus.
- FIG. 3. Radiation diagnostic instruments and power measurement system.
- FIG. 4. Axial plasma-density profiles.
- FIG. 5. Radial plasma-density and electron-beam profiles measured across the diameter of the circular waveguide at two axial positions that correspond to the output waveguide locations.
- FIG. 6. Measured radial beam profile at 15 cm downstream of beam-injection point and best-fit Bennett profile. The experimental parameters are $n_e = 2 \times 10^{11} \text{ cm}^{-3}$, $E_{b1} = 35.5 \text{ keV}$, and $I_{b1} = 2.6 \text{ A}$.
- FIG. 7. Temporal beam-profile evolution at low electron-beam current. Time t is measured relative to the electron beam turn-on time; $n_e = 5 \times 10^{12} \text{ cm}^{-3}$, $E_b = 36 \text{ keV}$, and $I_b = 1.0 \text{ A}$.
- FIG. 8. Radiation at 60 GHz is generated by the beam-plasma system when counterstreaming electron beams are injected into the plasma-loaded waveguide. The background helium-gas pressure is 65 mTorr.

FIG. 9. Simultaneous injection of both beams is required to generate millimeter-wave radiation. No radiation is observed when only one beam is used. (a) Only electron-beam 1 is injected into the background plasma. (b) Only electron-beam 2 is injected. (c) Both beams are injected.

FIG. 10. Radiation at 50 GHz is generated only when the two beam pulses overlap in time. The background helium gas pressure is 50 mTorr.

FIG. 11. Output radiation shifts to low frequency when both beams are injected without the high-density waveguide discharge. (a) Both beams injected into the background plasma. (b) Background discharge turned off, both beams injected, no 36-GHz radiation. (c) Background discharge turned off, both beams injected, 8-GHz radiation observed.

FIG. 12. Radiation-frequency scaling with waveguide discharge current is determined by analyzing the millimeter-wave output with an array of waveguide high-pass and bandpass filters. The helium gas pressure is 45 mTorr.

FIG. 13. Radiation frequency f scaling with waveguide discharge current, with a helium gas pressure of 35 mTorr.

FIG. 14. Radiation frequency f scales as $2f_{pe}$, with a helium gas pressure of 35 mTorr.

FIG. 15. Radiation frequency f scales as $I_d^{1/2}$ in a 9.5-cm-diameter circular-waveguide cavity with a helium-gas pressure of 24 mTorr and a beam voltage of 30 keV.

- FIG. 16. Beam-energy tuning for $E_{b1} = 19.5$ keV, as a function of E_{b2} and the total beam cathode current.
- FIG. 17. Millimeter-wave power scaling with beam energy for $I_b = 3.5$ and 5.3 A. The radiation frequency is 30 GHz, I_b is the sum of I_{b1} and I_{b2} , and $E_{b1} = E_{b2}$.
- FIG. 18. Millimeter-wave power scaling with beam energy at 60 GHz. The radiation frequency here is higher than that in Fig. 17 because we increased the waveguide plasma density. The total beam current is 5.4 A and $E_{b1} = E_{b2}$.
- FIG. 19. Millimeter-wave power scales nonlinearly with total beam current. The radiation frequency is 30 GHz, $E_{b1} = E_{b2} = 30$ keV, and the background gas is helium.
- FIG. 20. Millimeter-wave power scaling for helium, hydrogen, and neon gases. The radiation frequency is 30 GHz and $E_{b1} = E_{b2} = 30$ keV.
- FIG. 21. Beam steering optimizes output radiation. The beam current I_b for a single beam is 3.2 A, $n_e = 5 \times 10^{12} \text{ cm}^{-3}$, and $E_b = 26$ keV.
- FIG. 22. Millimeter-wave radiation is strongly amplitude modulated on a time scale near the ion-plasma frequency. Experimental parameters corresponding to the measured 35 -GHz radiation are listed below the oscilloscope waveform.
- FIG. 23. Millimeter-wave modulation frequency decreases with ion mass.
- FIG. 24. Millimeter-wave burstwidth and interburst period scale as $m_i^{1/2}$.

FIG. 25. Linear growth rate of the modulational instability as a function of instability wavenumber. The parameters are $E_0^2/8\pi n_e T_e = 0.05$, $\omega_0 = \omega_{pe}$ and $v_e/\omega_{pe} = 2 \times 10^{-3}$ for (a) helium, (b) argon, (c) krypton and, (d) xenon. .

FIG. 26. Linear growth rate of the modulational instability as a function of instability wavenumber. The parameters for helium are, $\omega_0 = \omega_{pe}$, $E_0^2/8\pi n_e T_e = 0.1$, for (a) $v_e/\omega_{pe} = 0$, (b) $v_e/\omega_{pe} = 2 \times 10^{-3}$, (c) $v_e/\omega_{pe} = 4 \times 10^{-3}$, and (d) $v_e/\omega_{pe} = 8 \times 10^{-3}$.

FIG. 27. Solutions of Eqs. (25)-(28) for a helium plasma. The parameters are $n_b/n_e = 0.001$, $n_e = 3 \times 10^{12} \text{cm}^{-3}$, $T_e = 5 \text{ eV}$, $E_b = 35 \text{ keV}$, $N = 6$, $R = 2 \text{ cm}$, $v_e/\omega_{pe} = 0.001$, $\gamma_i = 4(\omega_{pe}/v_b)c_s$, $\gamma_e = 0.01 \omega_{pe}$. The solutions are initialized with (a) $W_1 = 0.1$, (b) $W_2 = 0.3$, (c) $W_s = 0.08$, and (d) $W_T = 2 \times 10^{-4}$.

FIG. 28. Solutions of Eqs. (25)-(28) for an argon plasma. The parameters are $n_b/n_e = 0.001$, $n_e = 3 \times 10^{12} \text{cm}^{-3}$, $T_e = 5 \text{ eV}$, $E_b = 35 \text{ keV}$, $N = 6$, $R = 2 \text{ cm}$, $v_e/\omega_{pe} = 0.001$, $\gamma_i = 4(\omega_{pe}/v_b)c_s$, $\gamma_e = 0.01 \omega_{pe}$. The solutions are initialized with (a) $W_1 = .01$, (b) $W_2 = 0.3$, (c) $W_s = 0.08$, and (d) $W_T = 2 \times 10^{-4}$.

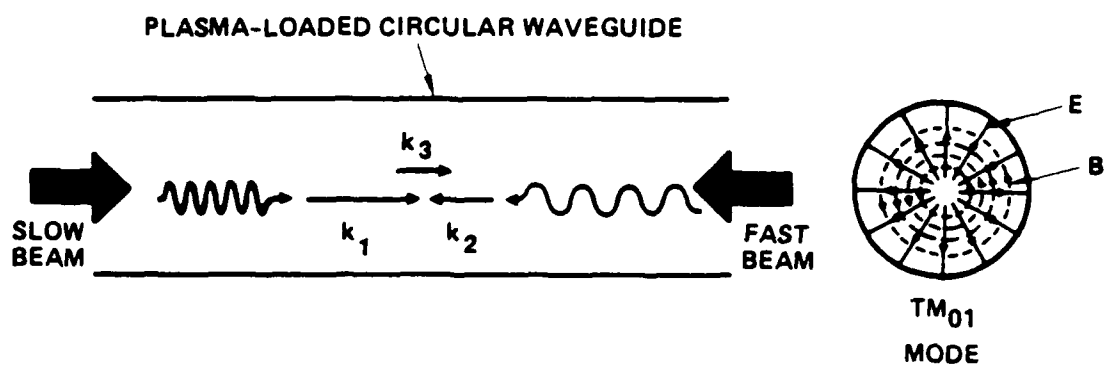


Figure 1

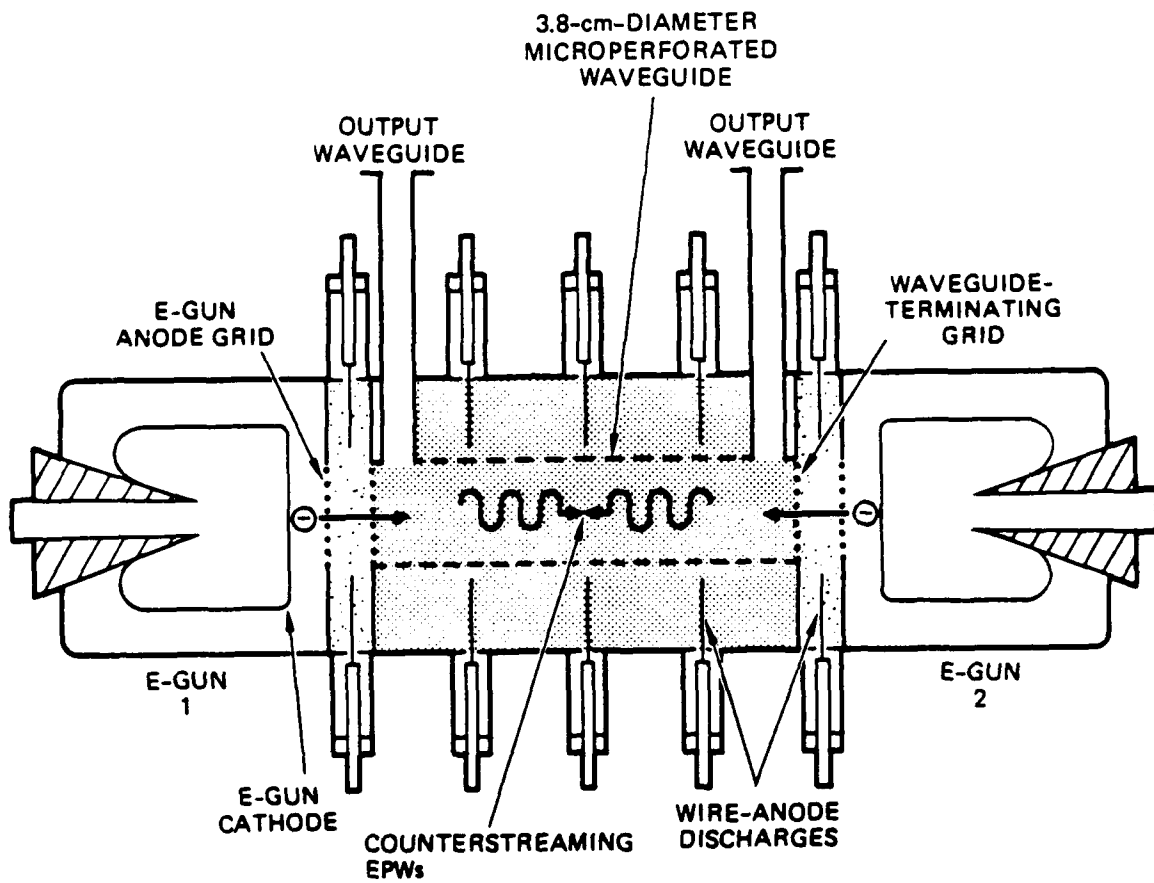


Figure 2

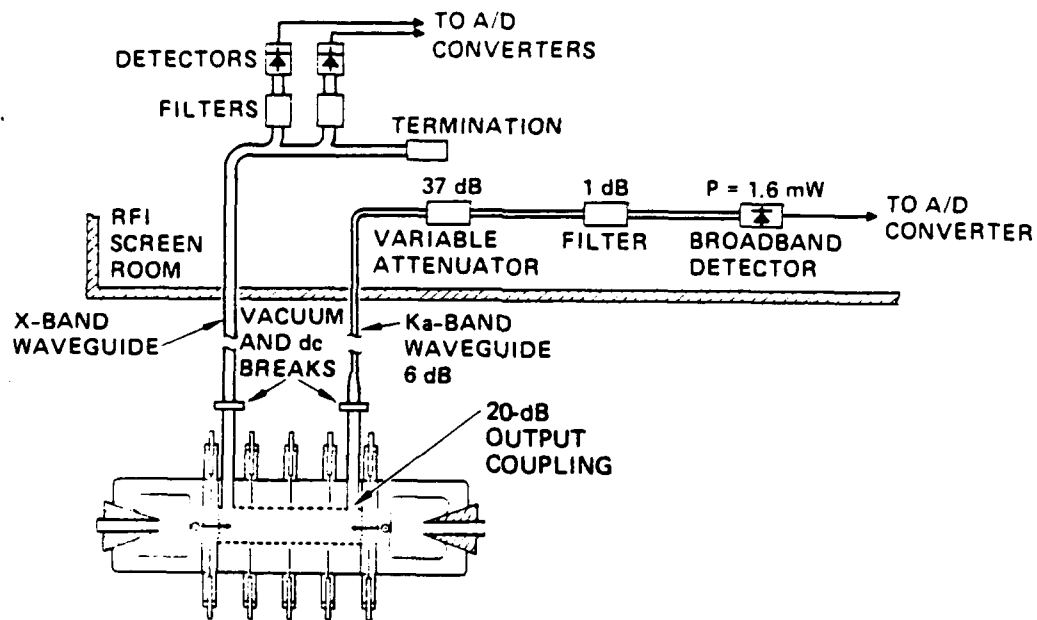


Figure 3

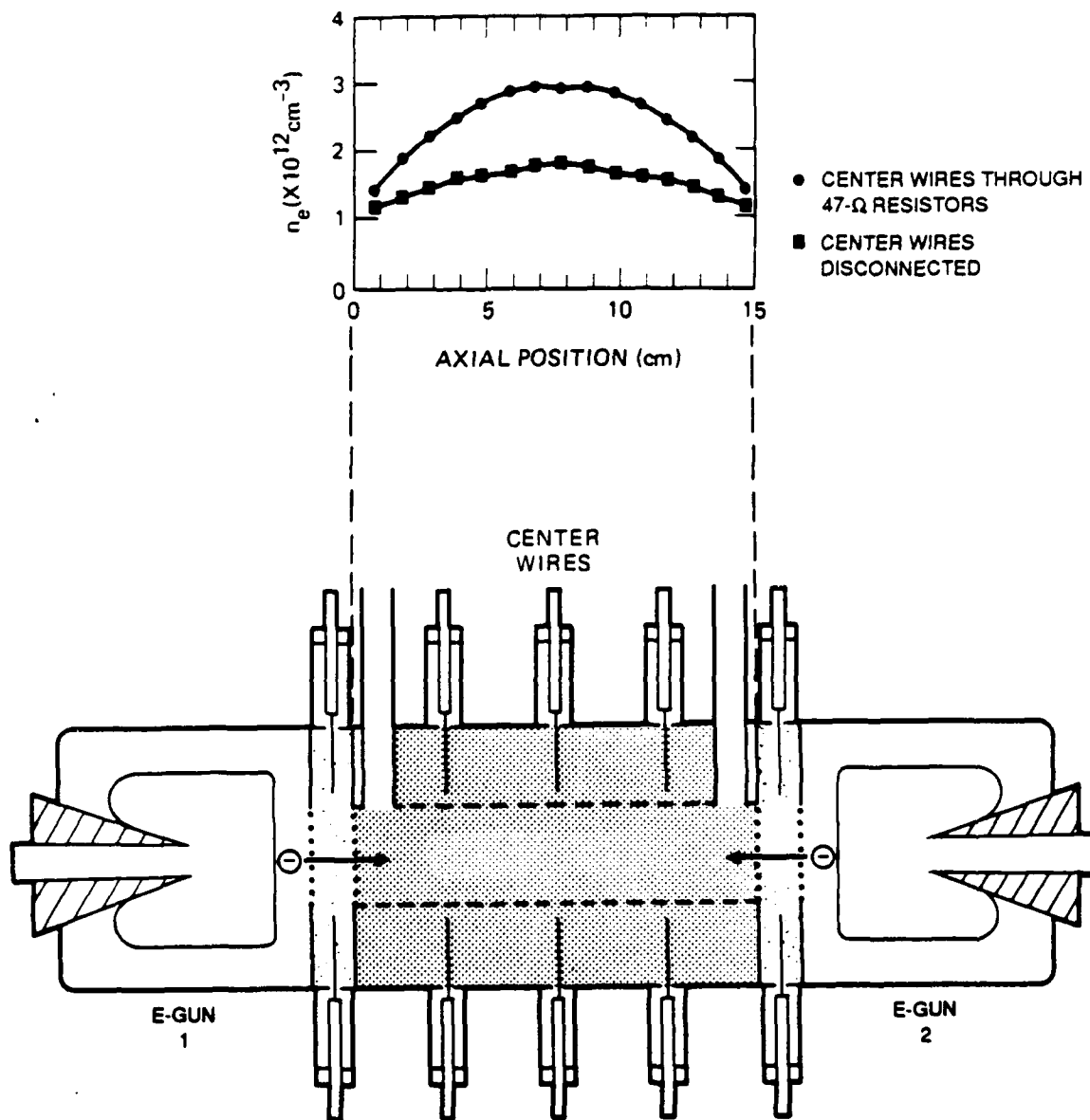


Figure 4

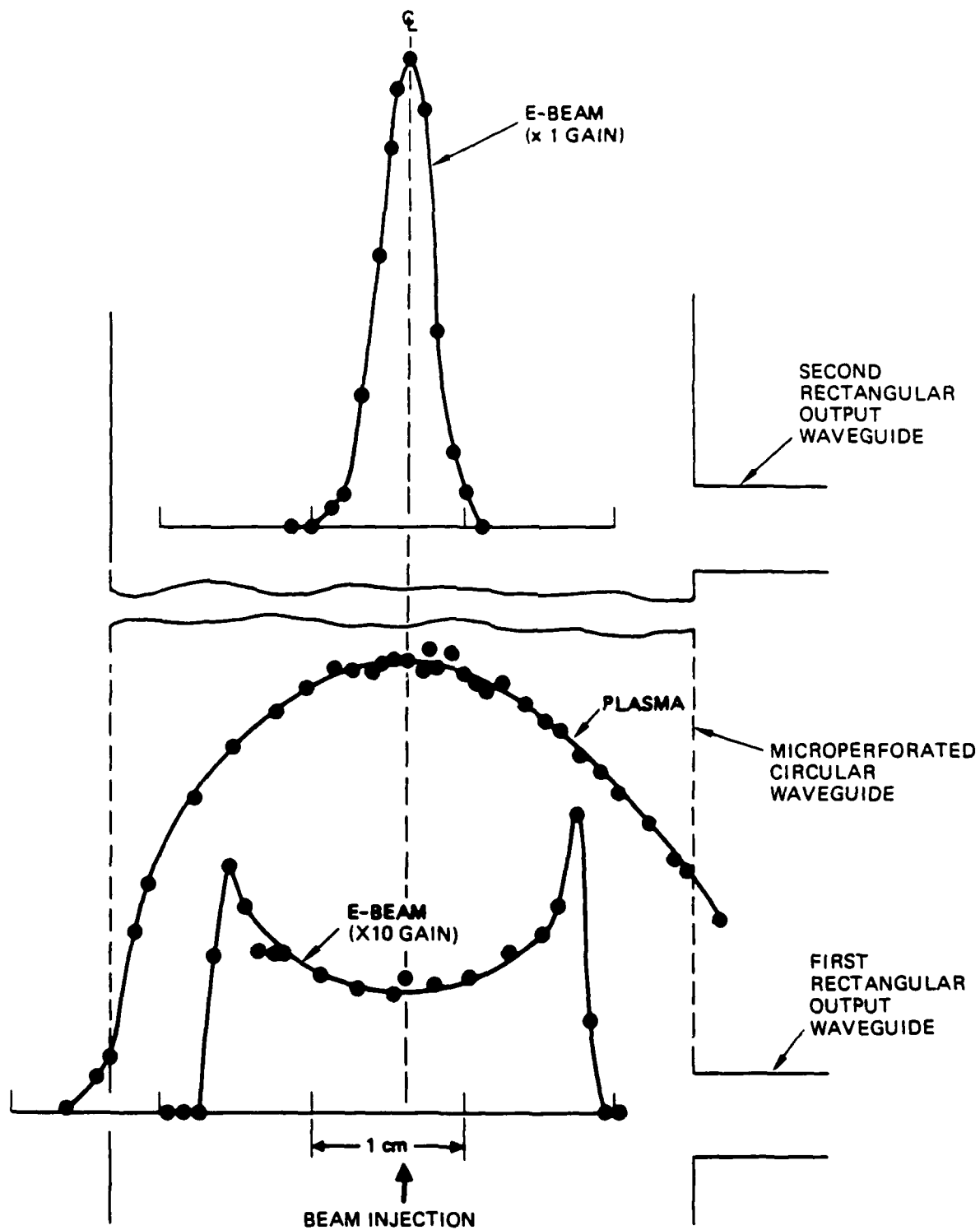


Figure 5

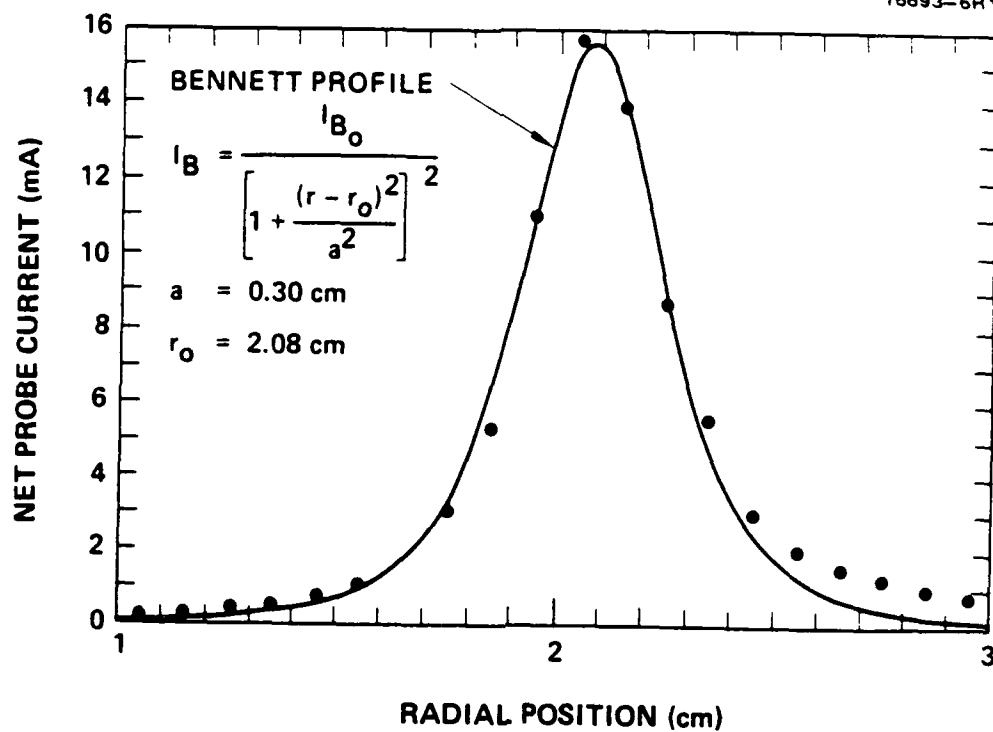


Figure 6

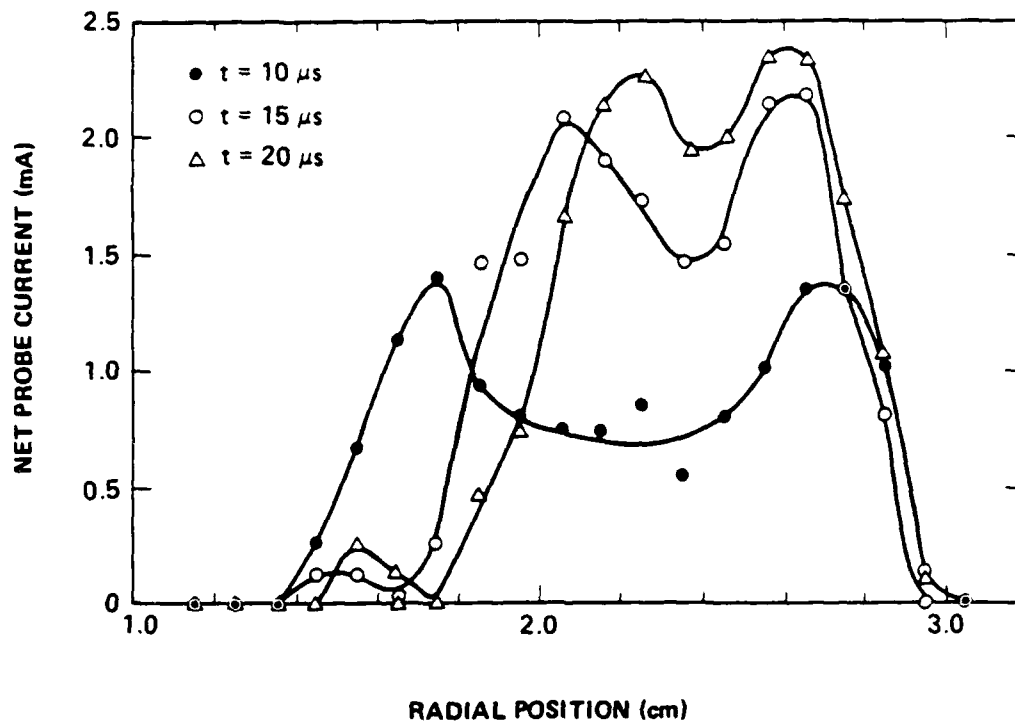


Figure 7

16101-10R1

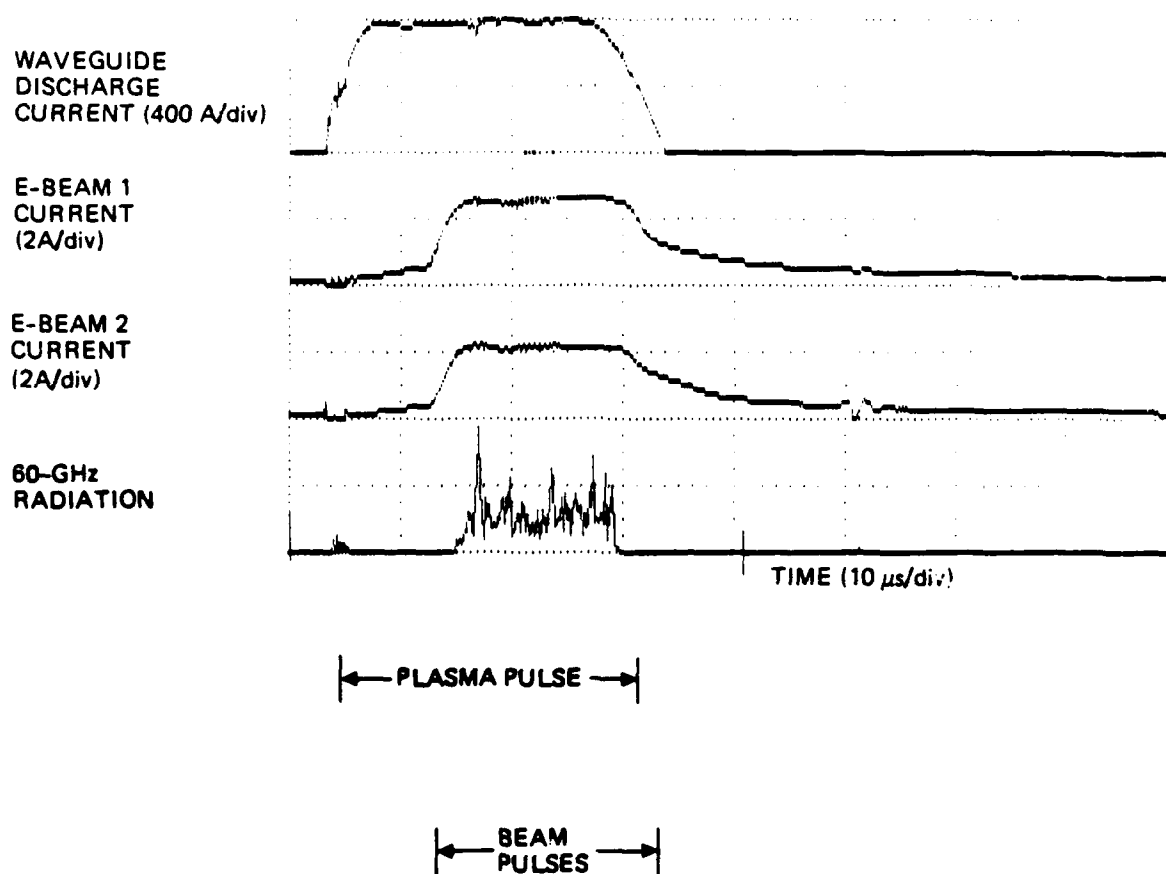


Figure 8

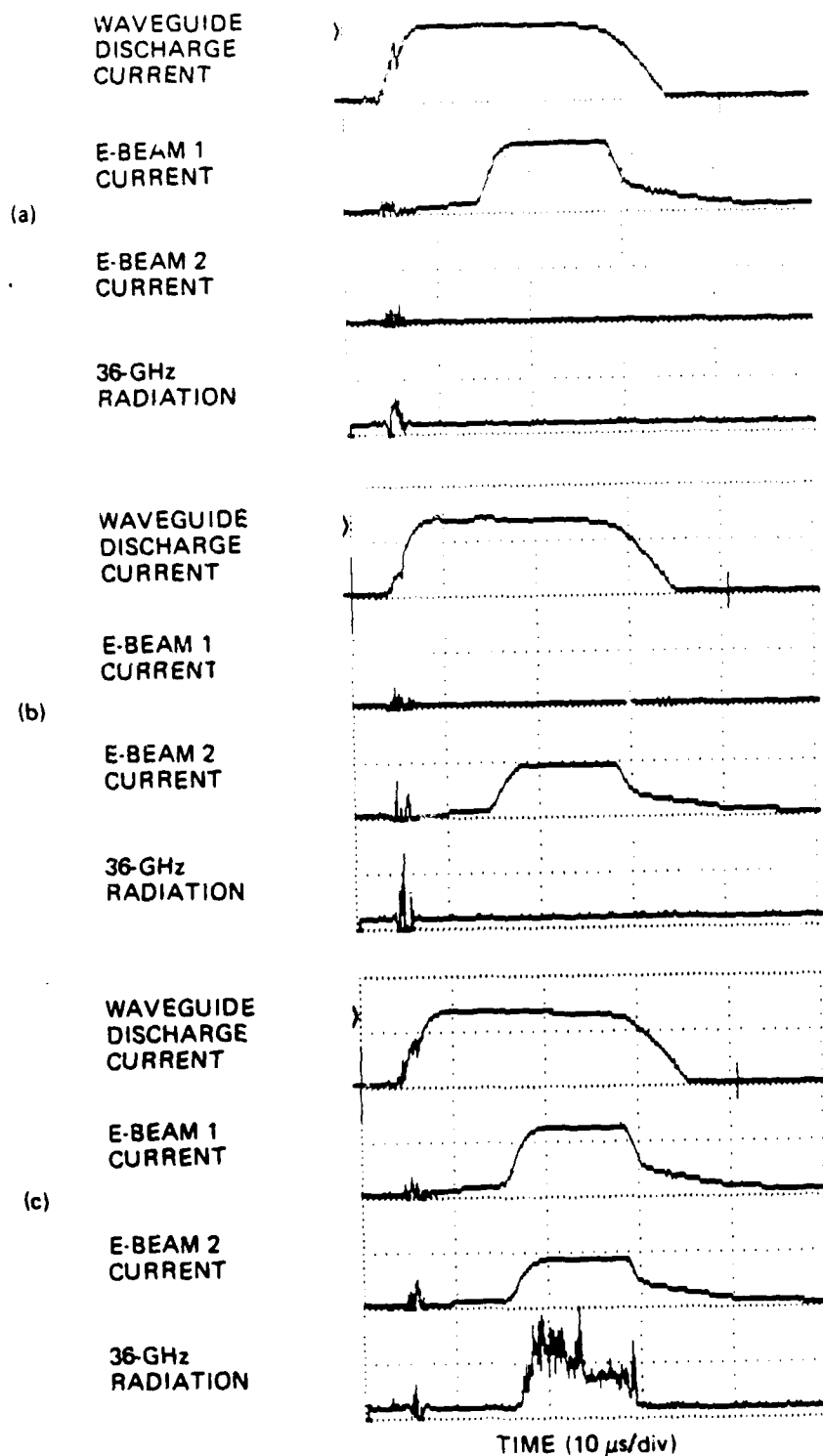


Figure 9

16101-7R2

WAVEGUIDE CURRENT
DISCHARGE (400 A/div)

E-BEAM 1 CURRENT
(2 A/div)

E-BEAM 2 CURRENT
(2 A/div)

50-GHz
RADIATION

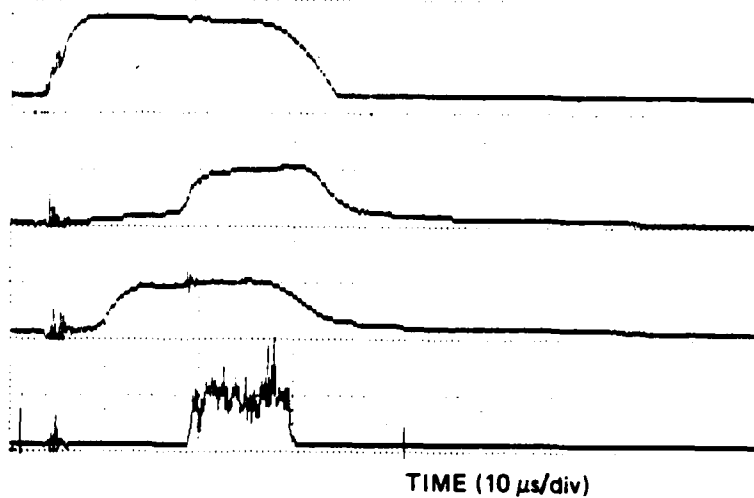


Figure 10

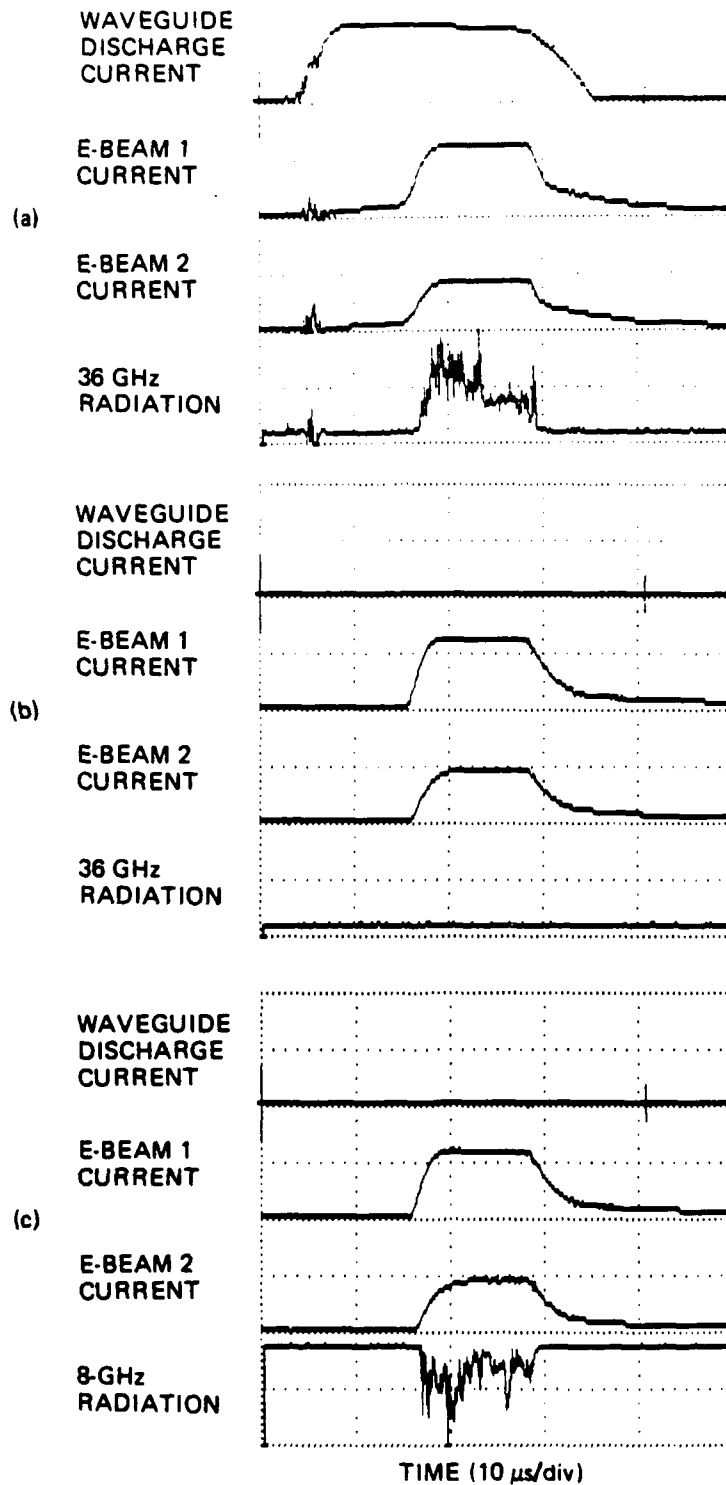


Figure 11

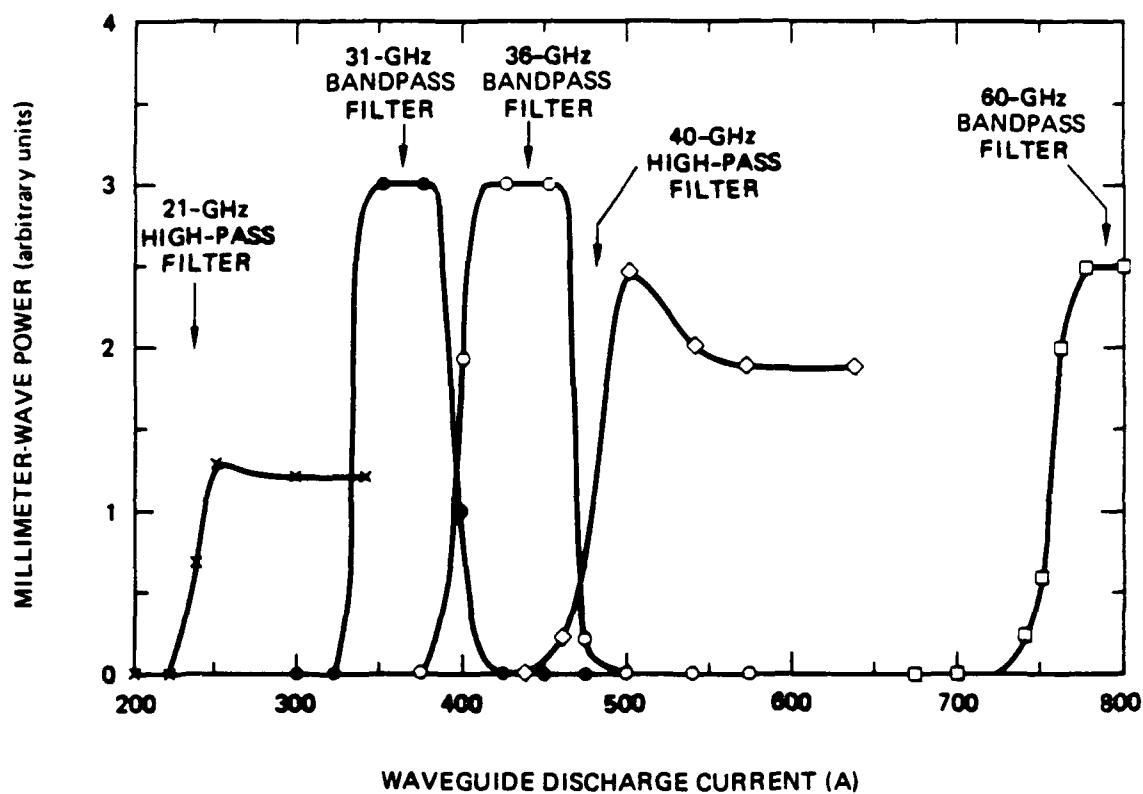


Figure 12

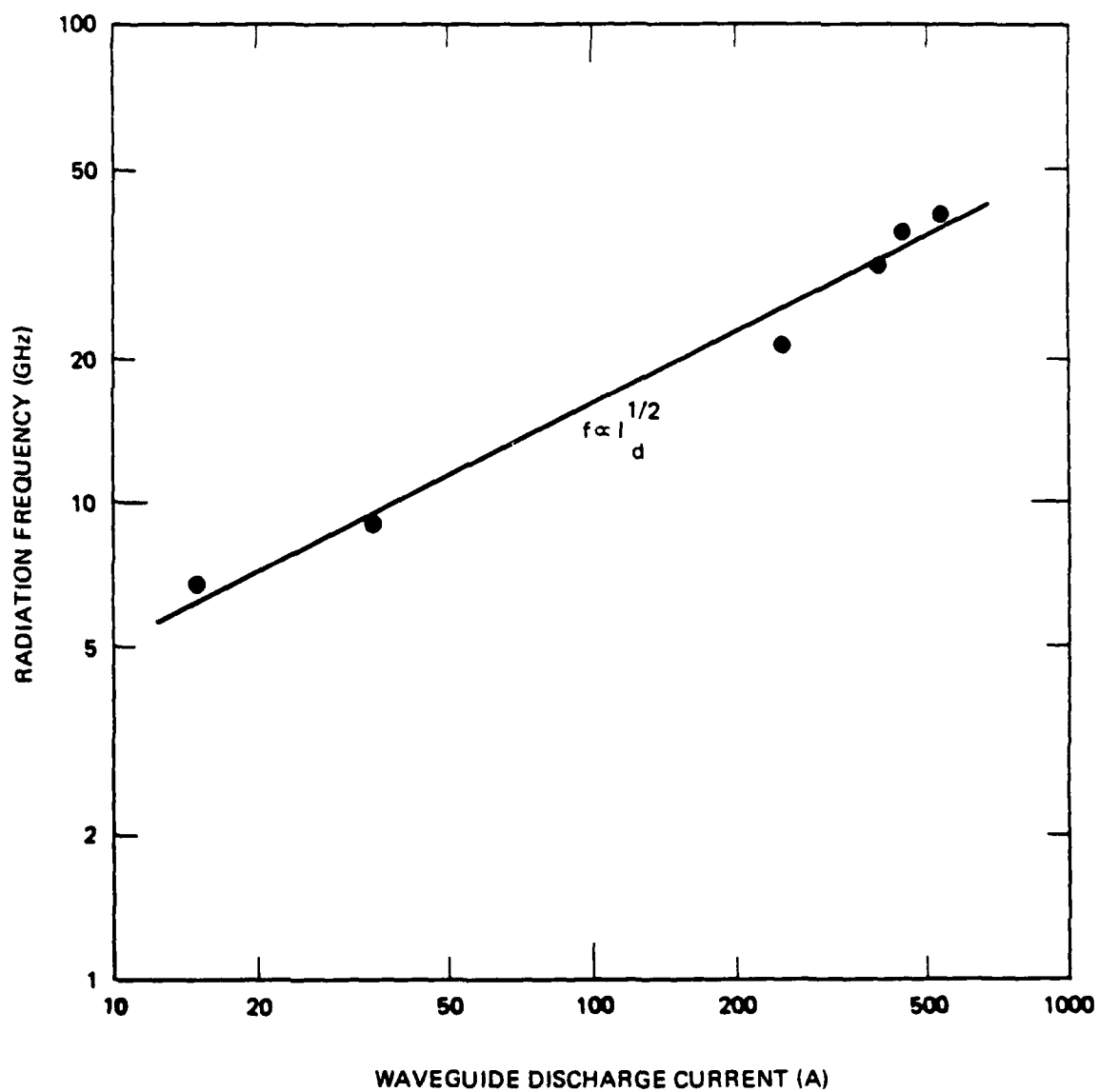


Figure 13

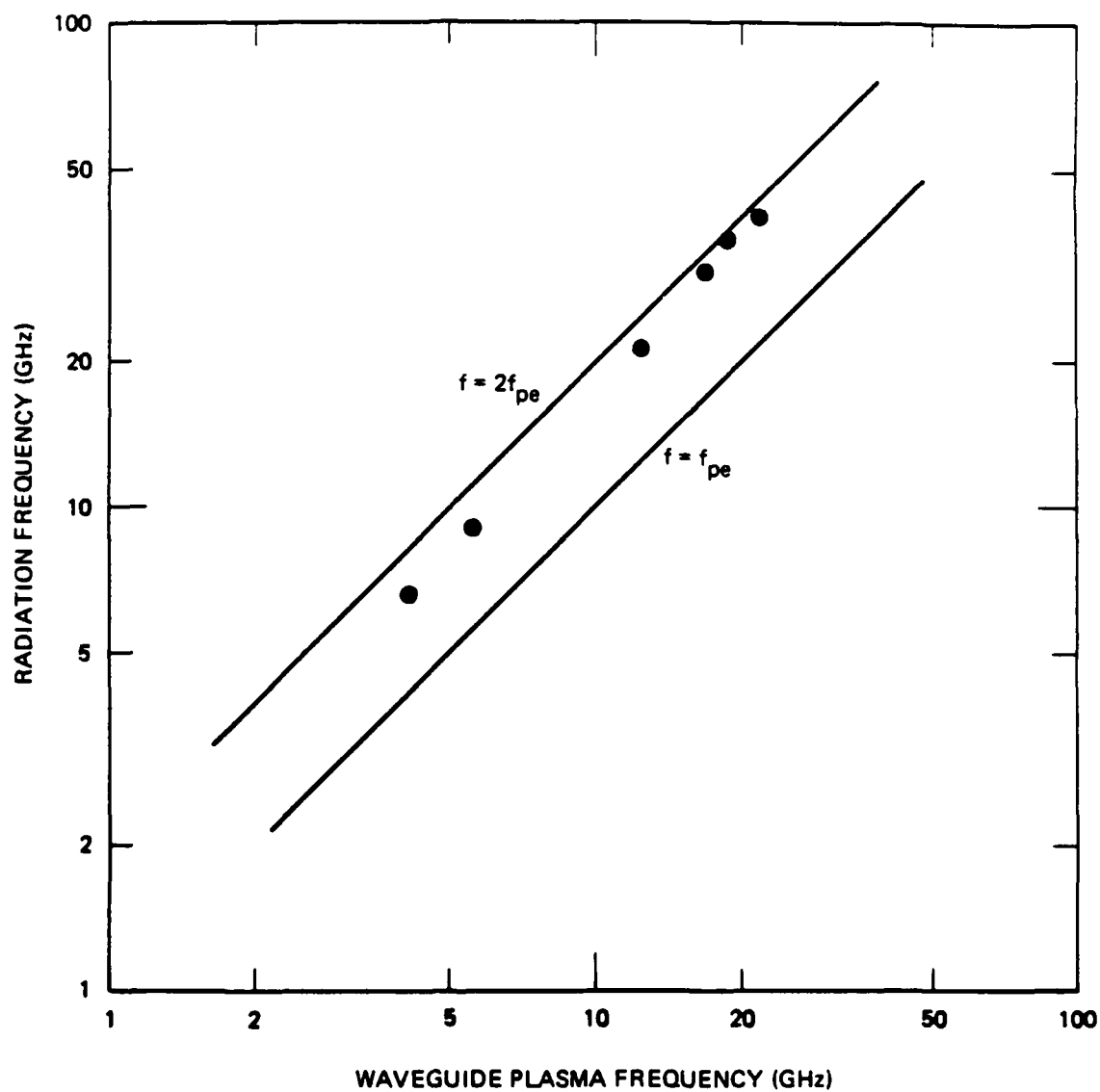


Figure 14

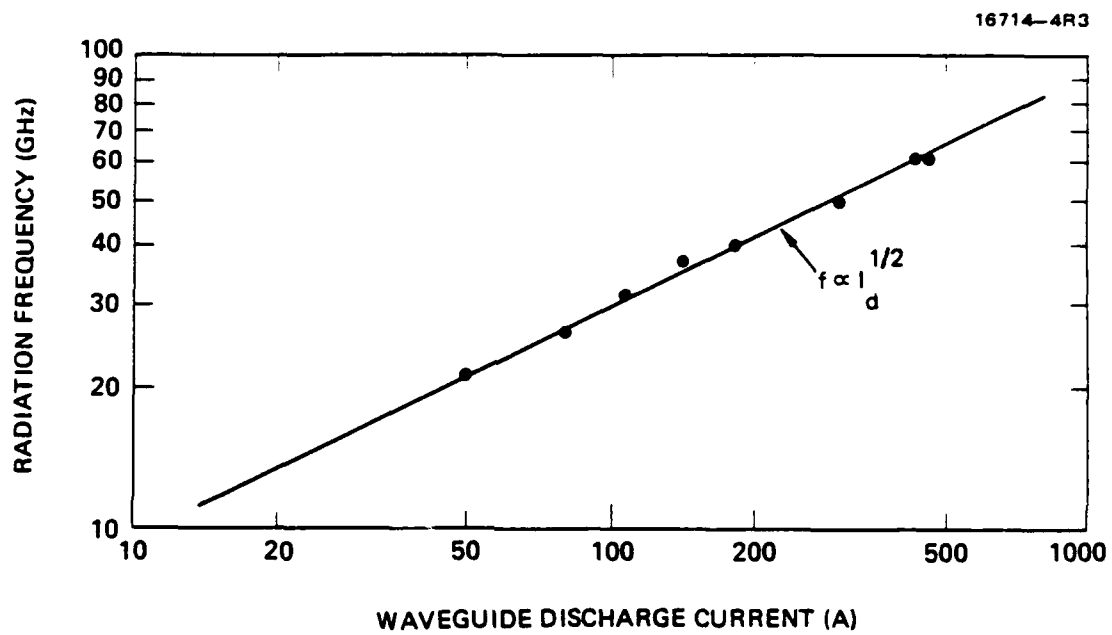


Figure 15

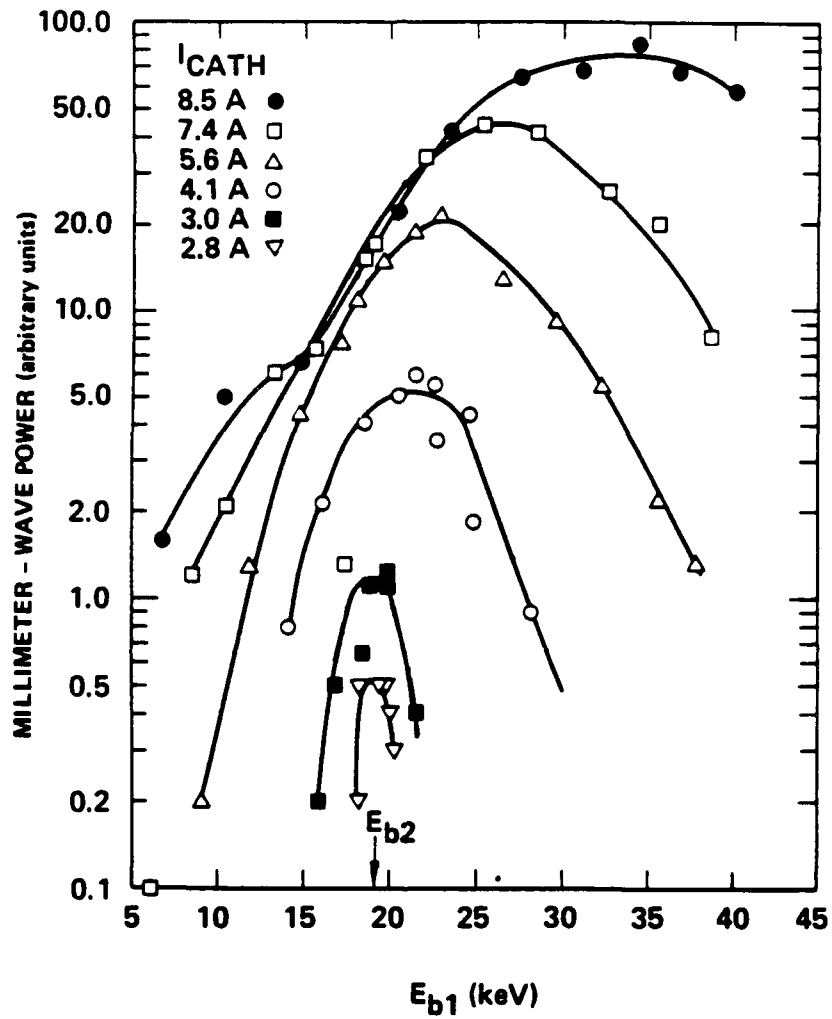


Figure 16

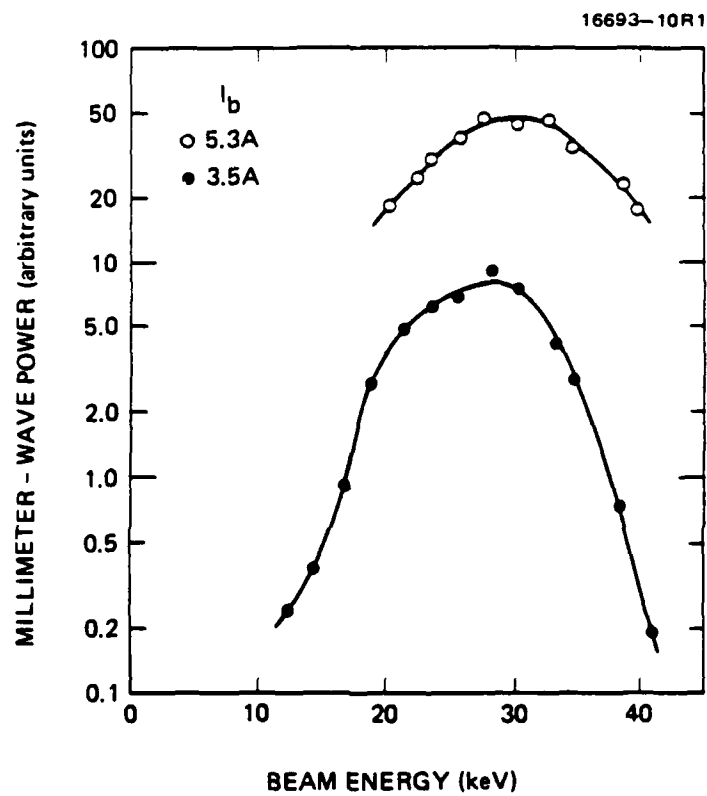


Figure 17

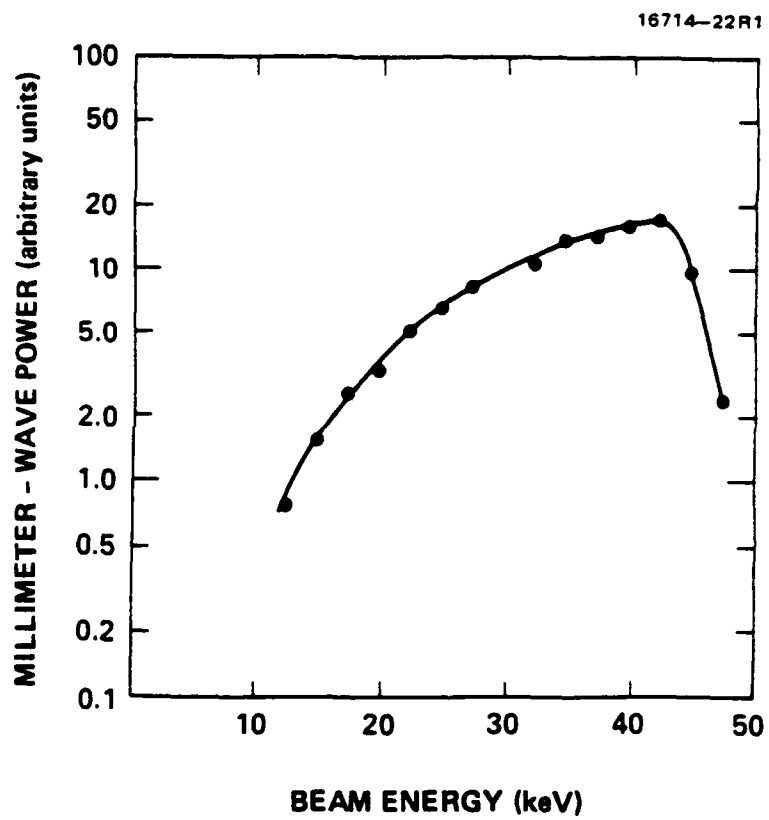


Figure 18

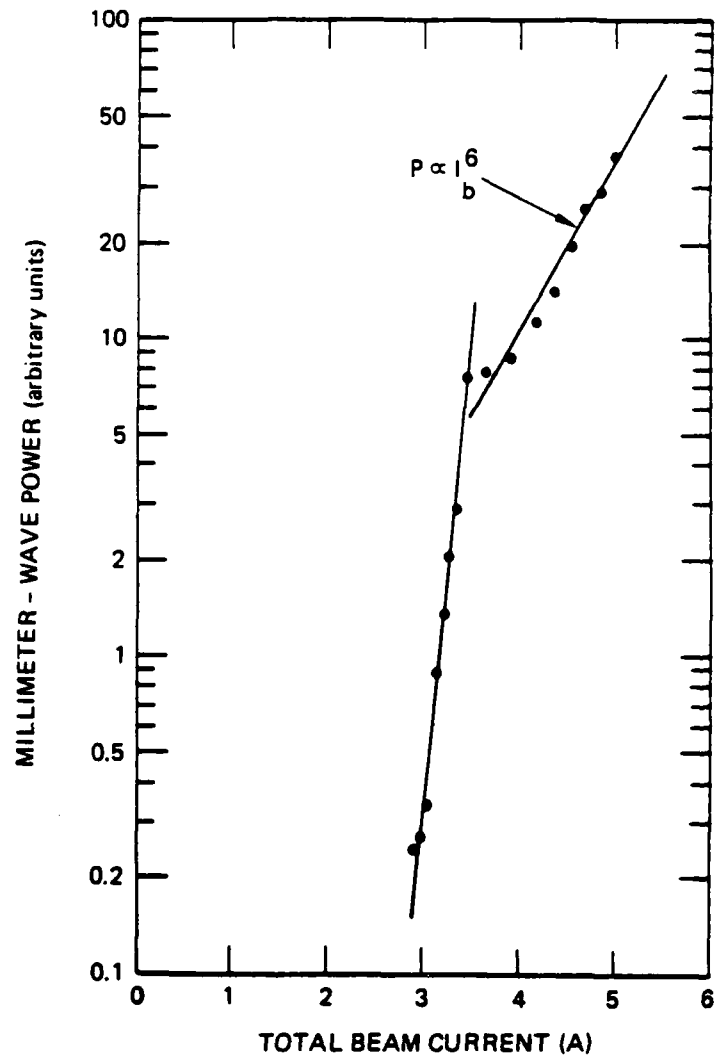


Figure 19

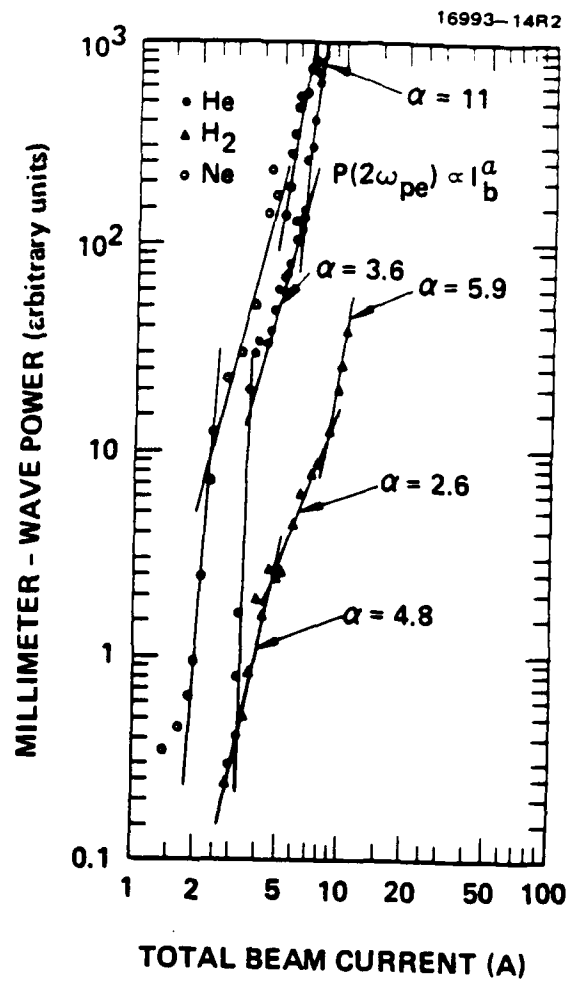


Figure 20

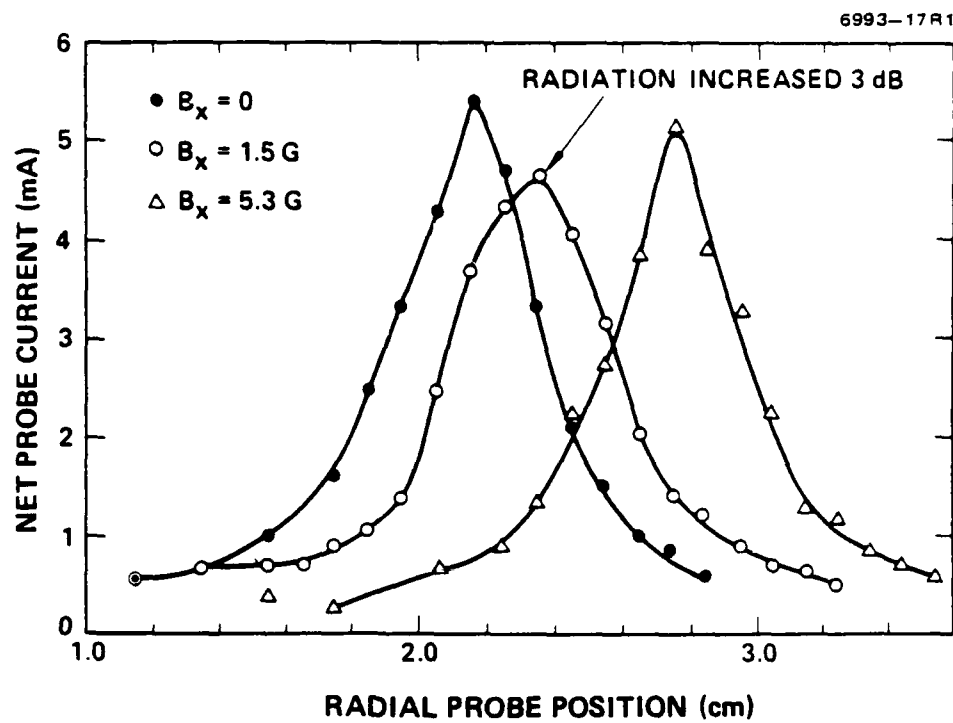
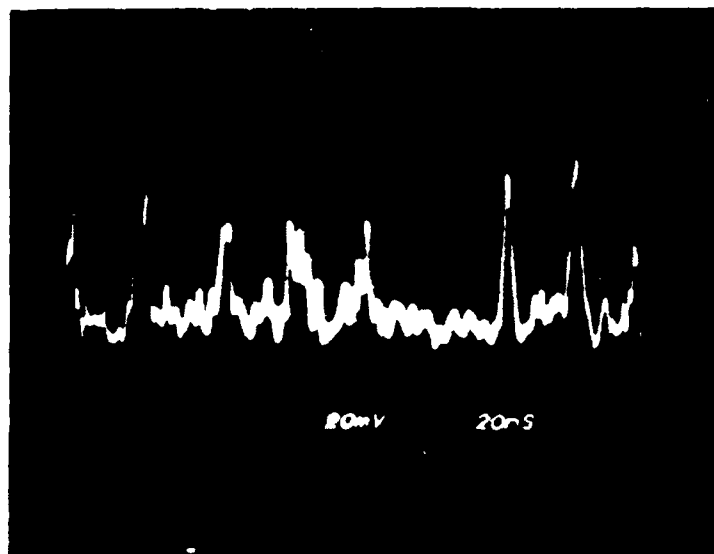


Figure 21

16101-14R1



35-GHz
RADIATION

TIME (40 ns/div)

$$n_e = 3.8 \times 10^{12} \text{ cm}^{-3}$$

$$T_e = 5 \text{ eV}$$

$$I_b = 2.5 \text{ A}$$

$$E_b = 30 \text{ keV}$$

$$\frac{n_b}{n_e} \sim 2.3 \times 10^{-4}$$

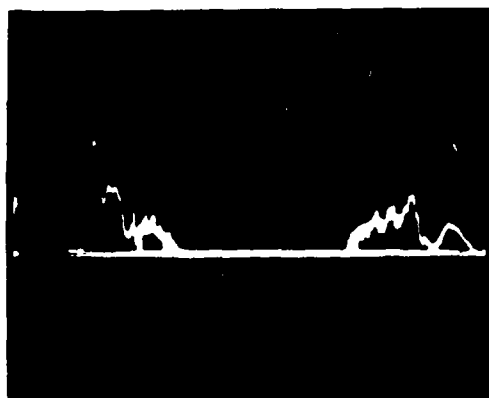
$$\frac{W_o}{n_e T_e} \sim 7 \times 10^{-2}$$

$$(k\lambda_D)^2 \sim 8 \times 10^{-5}$$

Figure 22

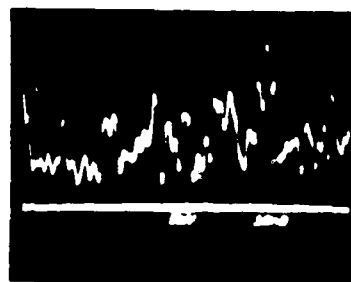


KRYPTON

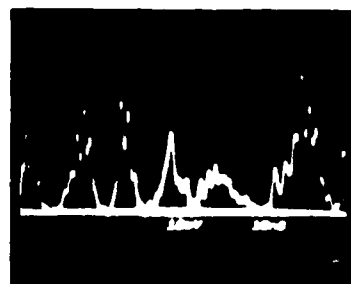


XENON

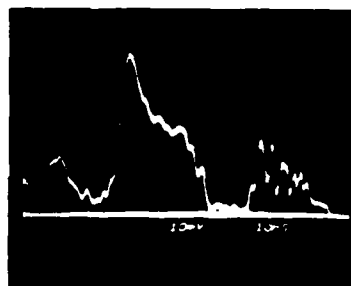
TIME (100 ns/div)



HYDROGEN



HELIUM



ARGON

TIME (20 ns/div)

Figure 23

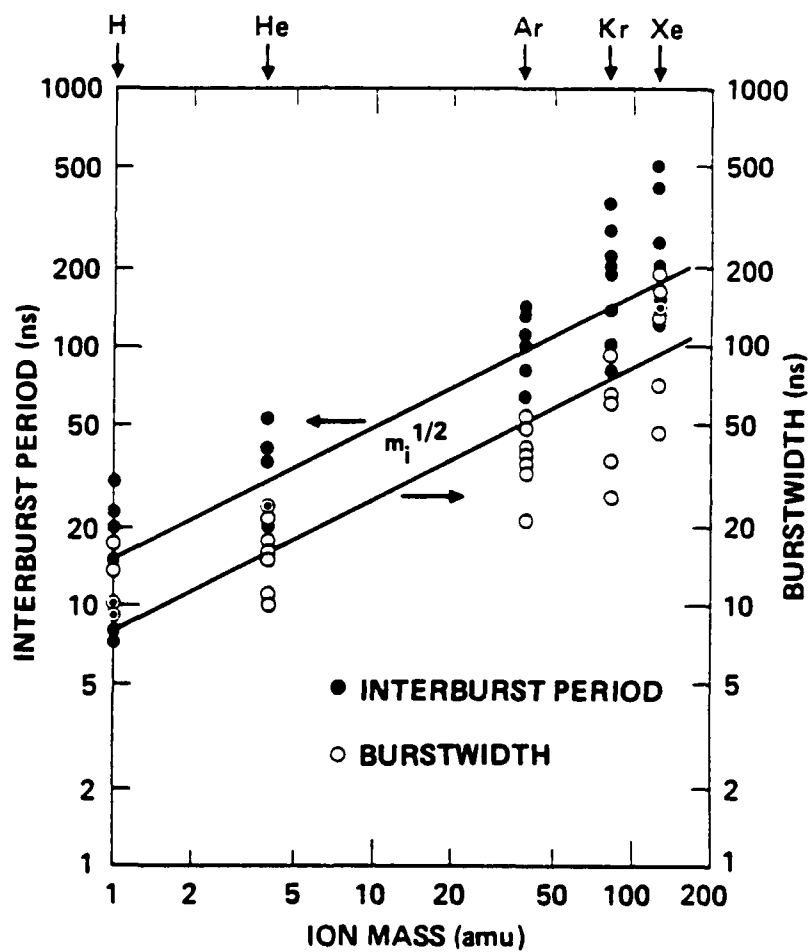


Figure 24

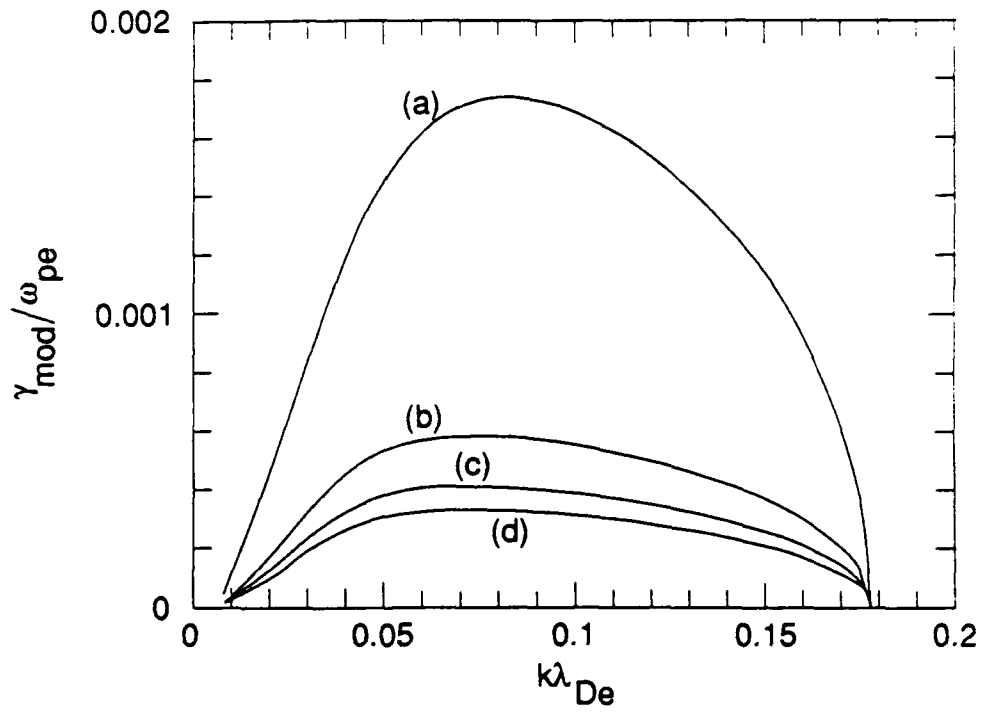


Figure 25

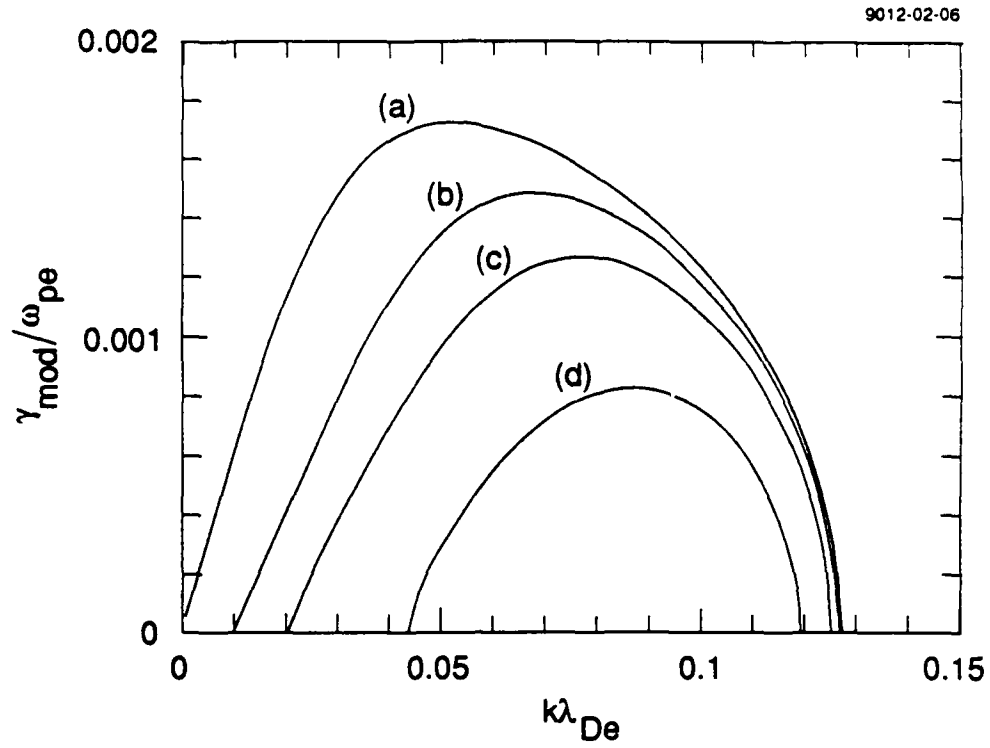


Figure 26

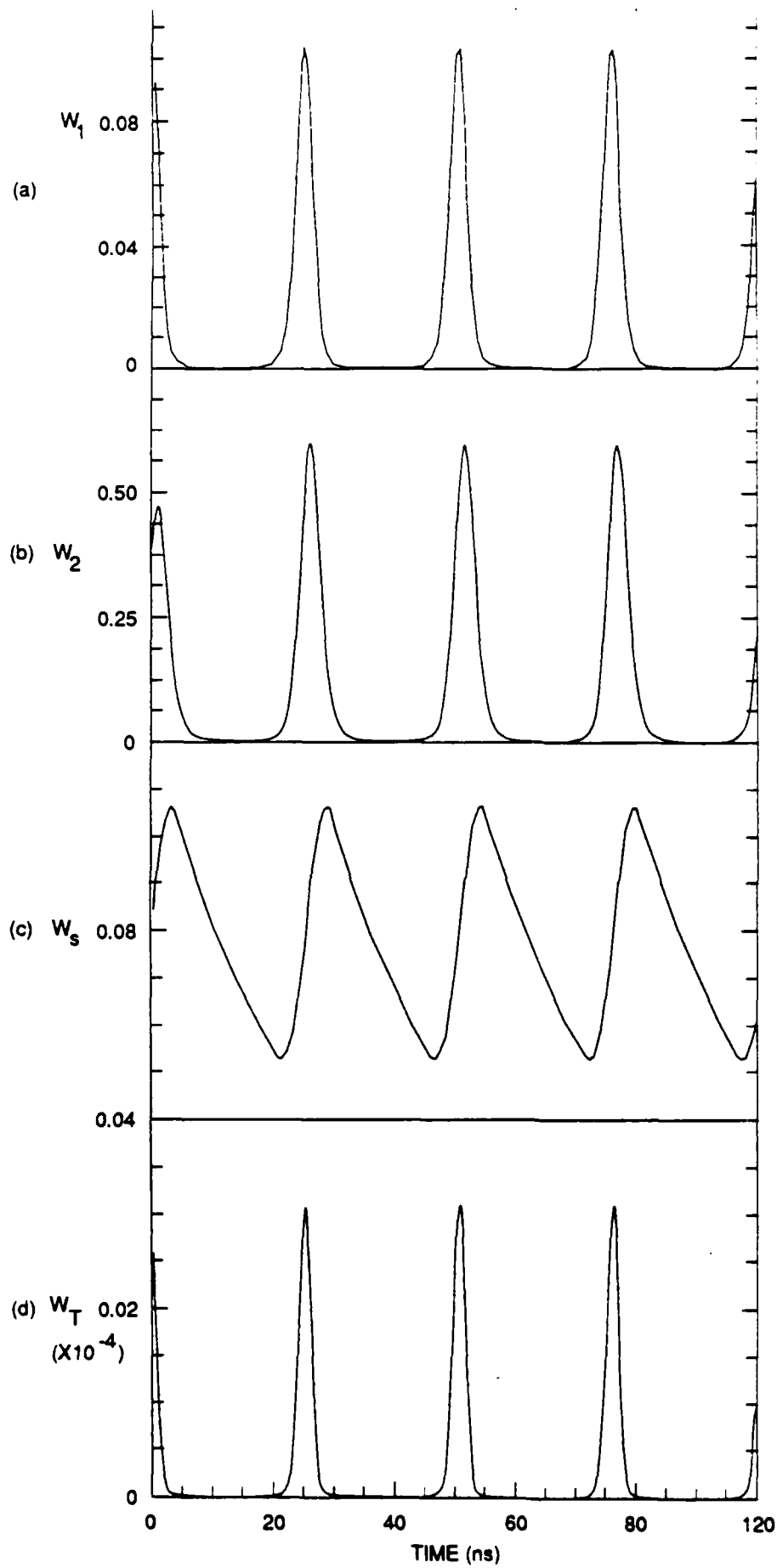


Figure 27

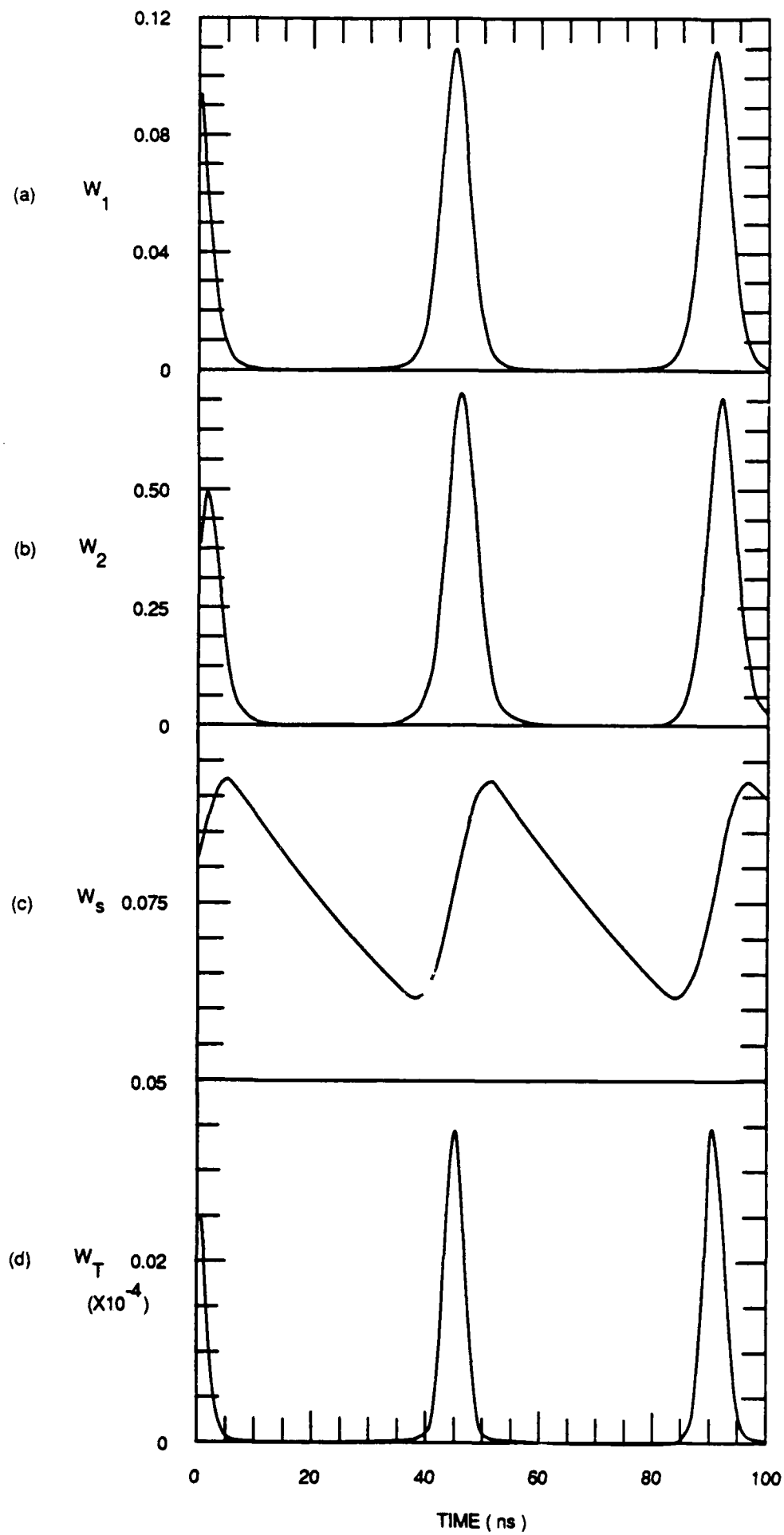


Figure 28

APPENDIX C
PLASMA-ANODE ELECTRON GUN

This paper will be submitted to Journal of Applied Physics.

PLASMA-ANODE ELECTRON GUN

R.W. Schumacher, J. Santoru, R.J. Harvey and A.J. Palmer

Hughes Research Laboratories

3011 Malibu Canyon Road

Malibu, California 90265

ABSTRACT

The plasma-anode electron gun (PAG) is a new cold-cathode electron source that is instant starting and provides long-pulse operation without gap closure. The PAG requires no cathode heater and only a minimal vacuum environment. The beam current is modulated at near ground potential obviating the need for a high-voltage modulator system. The PAG demonstrated square-wave, 17- μ s-long beam pulses at 100 kV and 10 A. The E-gun has operated stably at 70 kV and 2.5 A for 210- μ s pulse lengths without gap closure. The beam profile is consistent with beam transport via ion focusing by the background plasma and the Bennett pinch. A perpendicular beam temperature of 15 eV is inferred by comparing the measured 7-mm-diameter beam with a Bennett profile fit. Scaling of the beam current with ion flux within the gun indicates that the beam current is ultimately limited by ion space charge at the anode. The measured secondary electron yield from the molybdenum cathode is 13 at 100 kV.

INTRODUCTION

Efficient, rugged, high-voltage, high-current electron guns are the key, enabling technology for many advanced systems. These include free-electron lasers, high-power excimer lasers, and electron-beam weapons. The PAG is an original Hughes concept¹ that maintains many novel features, including instant starting, no cathode heater, nonpoisoning cathode, minimal vacuum requirements, long-pulse operation without gap closure, high brightness, beam modulation with low power at ground potential, and constant beam energy.

I. PAG OPERATING PRINCIPLES

Figure 1 illustrates the PAG concept, which involves a collective interaction between counterpropagating streams of electrons and ions in a high-voltage diode gap. A Pierce electron-gun² configuration is employed, but the thermionic cathode is replaced with a cold, secondary-electron-emitting electrode. Electron emission is stimulated by bombarding the cathode with high-energy ions. The ions are injected into the high-voltage gap through a gridded structure from a plasma source, which is embedded inside the anode electrode. The gridded structure serves as both a cathode for the plasma discharge and as an anode for the PAG. The plasma can be generated by various means, but the preferred approach is to use a wire-anode glow discharge^{3,4} at low gas pressure (<50 mTorr). As high-voltage ions impact the cathode surface, secondary electrons are emitted and accelerated back through the diode gap. If the proper electrode configuration is chosen (which accounts for electron and ion space-charge in a self-consistent manner) then electrostatic fields can be generated that focus the electrons through the on-axis aperture in the anode to form a laminar beam with a uniform circular cross section.

Since gas from the plasma source in the anode may pass into the high-voltage gap, the operating point of the gap must be chosen so as to standoff high voltage against both vacuum- and Paschen-breakdown mechanisms. This selected operating point limits the voltage per gap to typically 200 kV. Beam acceleration to higher voltages can be accomplished with multiple gaps.

Because the pressure limit is imposed by Paschen breakdown, helium gas is usually employed since it provides the highest voltage holdoff against Paschen breakdown relative to any other gas. Published data,⁵ and data reported in this paper indicate that a secondary-electron yield of 13 to 15 is obtained for 100-keV helium-ion impact upon molybdenum surfaces in the presence of a background helium gas.

The E-beam current in the PAG is controlled at low voltage by modulating the ~1 kV wire-anode discharge at the ground-potential environment of the anode electrode. Since the plasma is confined within the gridded anode structure (the electrons cannot penetrate into the anode-cathode gap because of the high electron-repelling E-gun potential), plasma closure of the high-voltage gap cannot occur and long-pulse ($\gg 1 \mu\text{s}$) operation is achieved. Modulation of the plasma source modulates the ion flux incident upon the cathode which, in turn, controls the beam current. A monoenergetic beam is obtained throughout the beam pulse because the E-beam is switched on and off by the plasma source and not by the high-voltage supply for the cathode. Low-energy electrons, which result from the rise and fall of the cathode voltage in conventional pulsed beams, are not present. All of this is accomplished without heater power and without high-vacuum-environment requirements because the ordinary-metal cathode used in the PAG cannot be poisoned.

II. PAG COMPUTER-CODE APPLICATION

We developed new computer programs that are capable of computing the trajectories of electrons and ions through the PAG in the self-consistent space-charge field of both species. Realistic boundary and electrode potentials are used as input data. Dr. W. Herrmannsfeldt of Stanford University revised an earlier version of his electron trajectories code⁶ to self-consistently compute the trajectories and space-charge fields of more than one charged species in an E-gun, with each species having an arbitrarily specified charge-to-mass ratio. The code was adapted for the VAX 11/785 and 8650 computers at Hughes Research Laboratories. The new Herrmannsfeldt code maintains the versatility of the original code. For example, the number of iterations on the space-

charge computation can be reduced to one to simulate space-charge neutralization (i.e., remove the self-consistent space-charge field) by plasma in specified regions of some PAG designs. An electron-generation code that supports the new Herrmannsfeldt program was also constructed. This code iteratively generates the initial conditions for the electrons at the cathode surface by multiplying the local ion flux at the cathode by the appropriate secondary-emission coefficient.

New physical processes were revealed using this code that were not observed using an earlier single-species code. One new feature was a reduction in the electron emittance which was made possible by the presence of the ion space charge. This effect is illustrated dramatically by the runs shown in Figure 2 for the PAG operating at 80 kV and 10 A. The two trajectory plots show the transport of electrons with identical initial conditions, but with [Figure 2(a)] and without [Figure 2(b)] the presence of positive helium ions. Electron-beam focusing and collimation are greatly assisted by the presence of the ion space charge. Perturbation analyses of these trajectories reveal that the greatest influence of the ion space charge is near the cathode where the electron velocities are small.

III. EXPERIMENTAL APPARATUS

The 120-kV PAG scaling experiment is shown schematically in Figure 3 and in a photograph in Figure 4. The experiment was designed to compare actual PAG data with code predictions and to investigate E-beam quality at voltages and currents up to 120 kV and 18 A, respectively. The detailed geometry of the high-voltage gap was determined using the modified Herrmannsfeldt code described earlier. Figure 2(a) shows the diode configuration used, together with equipotential contours and ion and electron trajectories for an 80-kV 10-A E-beam. The optimum cathode radius of curvature was found to be 5.0 cm for these parameters. The anode-grid electrode was chosen to be planar to facilitate Langmuir-probe access to the low-voltage portion of the gap. A photograph of the completed molybdenum cathode and field-shaping electrodes mounted on the high-voltage dielectric bushing is shown in Figure 5. The bushing is terminated on a 6-in. conflat flange that

allows the cathode to be precisely positioned inside the 4-in.-diameter stainless-steel vacuum chamber. An RG-220/U high-voltage coax cable (shown to the right in Figure 4) feeds the cathode through an oil-filled high-voltage connector at the rear of the bushing.

Electrical diagnostics consist of voltage dividers to measure the cathode and ion-source voltages, and current transformers to measure the cathode, E-beam, and ion-source currents. A three-dimensional probe array was used to measure the beam profiles and divergence angle, and a Faraday cup was used to measure the total beam current. As shown in Figure 3, the Faraday cup can be positioned just downstream of the anode assembly to intercept the entire beam envelope. The cup is moved further downstream when probe measurements are made. A "beam-slit shadowgraph" was used with the probe array to measure the parallel beam temperature.

The E-beam diagnostics discussed above are mounted on the two, four-way conflat-flange crosses shown in Figure 4. This arrangement offers optimum flexibility and diagnostic access to the E-beam. The experiment is evacuated by a turbomolecular pump to avoid the surface-contamination problems associated with diffusion pumps. The helium gas pressure is regulated in the range of 10 to 50 mTorr by flowing gas into the system through a leak valve.

IV. PAG OPERATION

The PAG has demonstrated well-collimated, high-quality beams in good agreement with the predictions of the modified Herrmannsfeldt code. The E-beam was focused electrostatically by the diode geometry to form a 7-mm-diameter collimated beam, which was transported over the 1-m length of the experiment without the aid of magnetic-focusing fields.

Figure 6 shows oscilloscope waveforms for a 17- μ s-wide pulse with a beam voltage of 100 kV. The ion-source discharge current was modulated at up to 100 A using the CROSSATRON^R switch as shown in Figure 3. The discharge generated 10 A of cathode current, which is the sum of the E-beam and incident-ion currents. In this case the Faraday cup collected 8 A of beam current. We have also demonstrated stable PAG operation with ultrawide beam pulses

without high-voltage-gap closure. Figure 7 shows operation with a pulse width of 210 μ s at 2.5 A of Faraday-cup current at 70-kV beam voltage. The droop in the current waveforms in Figure 7 is caused by the voltage droop in the capacitor bank supplying the ion-source discharge current and is not a feature of the PAG.

We measured the scaling of Faraday-cup and cathode currents with ion-source discharge current and the beam voltage. We found that the E-beam current is ultimately limited by ion space charge at the anode. Figure 8 shows the scaling of cathode and Faraday-cup currents with ion-source discharge current over the 9 to 100 A range at a constant beam voltage of 90 kV. Both the cathode and Faraday-cup currents increase linearly until the discharge current reaches 30 A. Beyond this point the currents increase at much slower rates. This behavior is also shown in Figure 9, which is the same scaling, but recorded for a lower beam voltage of 50 kV. As the discharge current is increased beyond 20 A, the Faraday-cup current reaches a saturated value of 2 A, while the cathode current continues to increase.

The change in slope of the Faraday-cup and cathode currents is caused by the limitation of ion current incident on the cathode. For normal operation, the ion current is restricted to its space-charge-limited value at the anode grid where ions are extracted into the gap. We can estimate the ion-space-charge-limited cathode current using a planar diode approximation for the PAG gap. The expression for Child-Langmuir space-charge-limited current in a planar diode is

$$I_{sc1} = \frac{4}{9} \epsilon_0 \left(\frac{2e}{m} \right)^{1/2} \frac{V^{3/2} A}{d^2} , \quad (1)$$

where V is the gap voltage, d is the gap spacing, A is the emitting surface area, e/m is the charge-to-mass ratio of the charged species, and ϵ_0 is the permittivity of free space. Since the space-charge-limited current scales as $m^{-1/2}$, ion emission at the anode will become space-charge limited well before electron emission at the cathode. For singly charged helium ions, the space-charge-limited ion current is

$$I_i = 2.72 \times 10^{-8} \frac{V^{3/2} A}{d^2} \quad (2)$$

The total cathode current is the sum of the ion and E-beam currents, or

$$I_c = I_i + I_b \quad (3)$$

But the electron-beam current can be expressed in terms of the incident ion current and the secondary yield, γ , as

$$I_b = \gamma I_i \quad (4)$$

Combining Eqs. (2), (3) and (4), the saturated cathode current is

$$I_{c,sat} = 2.72 \times 10^{-8} \frac{(\gamma + 1) V^{3/2} A}{d^2} \quad (5)$$

Using the PAG experiment parameters $A = 3.8 \text{ cm}^2$, $d = 3.3 \text{ cm}$, $V_b = 90 \text{ kV}$, and $\gamma = 13$, Eq. (5) predicts a saturated cathode current of 3.6 A.

The observed linear scaling of cathode current with ion-source discharge current in Figure 8 shows the saturation begins at the slightly higher value of 4.7 A. This correspondence is sufficiently close considering the E-gun model does not include the geometrical enhancement of ion perveance resulting from the nonplanar gap configuration. As shown in Figure 9, the cathode current begins to saturate at 1.9 A when the beam voltage is reduce to 50 kV; this is consistent with the ion-space-charge-limited voltage scaling predicted by Eq. (5).

As the discharge current is increased beyond $I_{c,sat}$ in Figures 8 and 9, the cathode current continues to increase. This is due to penetration of the ion-space-charge cloud at the anode into the high-voltage gap. This phenomena reduces the effective cathode-to-anode spacing (i.e., $d < 3.3$ cm), increases the ion-emitting area, and thereby increases $I_{c,sat}$. Although the cathode current continues to increase, the Faraday-cup current approaches a constant value in Figures 8 and 9. The Faraday cup, therefore, does not collect all the beam current which is generated in this regime; an observation which suggests that the beam becomes defocused when the gap is operated beyond the ion-space-charge limit. Beam profiles presented in the next section verify that this is indeed the case. The beam defocusing is caused by the release of ions from the extended ion space charge cloud at the anode. Ions from the edge of expanded cloud are released on trajectories which map onto the cathode surface at large radii from the PAG axis. These ions stimulate the emission of secondary electrons at large radii on the cathode which are over focused and cross the gun axis thus creating broad wings on the beam profile.

By comparing the cathode and Faraday-cup currents at each beam voltage we can deduce the secondary electron yield using

$$\gamma = \frac{I_b}{I_b + I_c} \quad , \quad (6)$$

which is derived by combining Eqs. (3) and (4). Figure 10 shows the computed electron yield per ion to scales up a value of 13 at voltages up to 100 kV. This plot was prepared by assuming that all the beam current is collected by the Faraday cup. However, since the discharge current was 21 A for this experiment, the PAG was operating in the ion-space-charge current-limited mode for voltages less than 50 kV (as shown in Figure 9). Below 50 kV, therefore, the measured yields are smaller than those actually obtained since some portion of the beam falls outside the Faraday-cup entrance aperture in this regime.

V. ELECTRON-BEAM PROFILE

Radial beam profiles were measured using the array of disk probes shown in Figure 3. The probe current was measured at each radial position using the $\theta = 0^\circ$ and 90° probe orientations shown in Figure 11. At 90° the probe current is largely background-plasma electron current. By subtracting the current measured at 90° from the current measured at 0° , we eliminate the background plasma contribution to the beam-probe current. A beam profile measured by slowly scanning the probe across the beam channel is shown in Figure 12. A rather narrow well-collimated, 7-mm-diameter (FWHM) beam was found at 67 kV and 3 A of cathode current.

The beam profile was found to be consistent with beam collimation via ion focusing and the Bennett-pinch effect. As the E-beam propagates through the background helium gas, a tenuous plasma is generated by electron-neutral collisions. Ions in this plasma neutralize the space-charge in the beam and allow it to propagate free of space-charge blow-up effects. However, rather than simply drifting in a ballistic manner, the beam is also subject to the magnetic "pinch" force from the poloidal magnetic field produced by the beam current. This force will constrict the beam channel if the magnetic-field pressure exceeds the transverse thermal beam pressure as shown schematically in Figure 13. This phenomena is known as the Bennett-pinch effect.⁷ Quantitatively, the pinch condition may be expressed as

$$\frac{B_p^2}{8\pi} \geq n_b T_{b\perp} \quad , \quad (7)$$

where B_p is the poloidal magnetic field, n_b is the beam density, and $T_{b\perp}$ is the transverse beam temperature. The beam current at which the pinch occurs can be expressed as

$$I_b^2 \geq 3.2 \times 10^{-10} n_b A_b T_{b\perp} \quad , \quad (8)$$

where A_b is the cross-sectional beam area in square cm, n_b has units of electrons per cubic cm, and $T_{b\perp}$ is expressed in eV, and the beam current has units of amperes. Under equilibrium conditions when the magnetic-pinch force balances the transverse thermal pressure, theory predicts the beam will have a Bennett profile, given analytically by the equation,

$$I_b(r) = \frac{I_{b0}}{\left[1 + \left(\frac{r}{a}\right)^2\right]^2}, \quad (9)$$

where r is the radial position relative to the center of the beam, I_{b0} is the maximum beam current at the center of the beam profile, and a is the Bennett radius given by

$$a = \frac{2\sqrt{2}\lambda_D}{b} \left(\frac{T_{b\perp}}{T_{b\perp} - T_e} \right)^{1/2}. \quad (10)$$

In this expression, T_e is the background plasma electron temperature, λ_D is the Debye length of the beam plasma, and $\beta = v/c$.

Figure 14 shows a fit comparison of the measured profile with a beam current of 2.1 A with a curve which corresponds to the Bennett-profile theory. The data points correspond quite well to the Bennett-pinch prediction for a Bennett radius of $a = 0.5$ cm. Using beam parameters of $V_b = 67$ kV, $I_b = 2.1$ A, $n_b = 1.1 \times 10^9$ cm⁻³ and $A_b = 0.8$ cm², and the Bennett radius from the curve fit in Figure 14, we calculate a transverse beam temperature of $T_{b\perp} = 15$ eV using Eq. (10). This transverse beam temperature is in rough agreement with the result from the "beam-slit shadowgraph" diagnostic discussed in the next section.

When the ion-source discharge current is increased to values where the ion current becomes space-charge limited, the beam profile broadens significantly. Figure 15 shows such a profile where the discharge current was set to 102 A at a beam voltage of 63 kV. The 7-mm-diameter on-

axis beam is still observed, but now broad wings extend several centimeters around the central peak. These wings are generated by the defocusing of the beam by the high ion-space-charge levels near the anode as described earlier.

VI. BEAM-TEMPERATURE MEASUREMENTS

Cold, high-brightness, low-divergence beams are required for advanced systems such as free-electron lasers, E-beam weapons, and excimer lasers. One parameter which quantifies the quality of an electron beam is the transverse temperature. To accurately determine this beam parameter in the PAG, we used a "beam-slit shadowgraph". As shown schematically in Figure 16, the E-beam impinges on the front plate of the shadowgraph, which has a narrow slit with dimensions $2L_x$ and $2L_y$ in the x and y dimensions, respectively). A small portion of the total beam current passes through the slit, drifts through the length of the analyzer, and is collected by a probe. By measuring the spatial beam profile at the back plate, we obtain an estimate of the transverse beam temperature.

To estimate the transverse beam temperature from the full width of the beam image on the back plate in the x direction, W_x , we use the equation

$$W_x = 2L_x + 2L_z \tan[(T_x/E_b)^{1/2}] , \quad (11)$$

where L_z is the distance between the front plate and the current-collecting probe, T_x is the beam temperature in electron volts in the x direction, and E_b is the beam energy in electron volts. For example, if we use $2L_x = 1$ mm, $L_z = 10$ cm, $T_x = 20$ eV, and $E_b = 100$ keV, we find that $W_x = 3.8$ mm. The temperature in the y-direction T_y can be measured by rotating the analyzer 90° in the x-y plane and repeating the measurement.

We tested this diagnostic technique using the setup shown in Figure 17. An aluminum plate with a variable-width molybdenum slit was mounted to a probe shaft. The other probes downstream of the plate were used to measure the current distribution at different distances from the plate. The

measured current distribution using a 2-mm-wide slit and a 70-kV, 2.5-A beam is shown in Figure 18. Using the simplified analysis represented by Eq. (11) to estimate the transverse beam temperature we obtain a value of $T_{b\perp} = 14$ eV which is consistent with the result that was obtained from the Bennett-profile fit.

SUMMARY

We have developed the Plasma-Anode Electron Gun, which is a new cold-cathode electron source. Stable operation has been achieved for pulse widths of up to 210 μ s at 70 kV and 2.5 A. The transverse beam temperature, calculated using two different techniques, is estimated to be about 15 eV. Scaling of the beam current with ion flux incident on the cold cathode indicates that the beam current is ultimately limited by ion space charge at the anode.

ACKNOWLEDGEMENTS

We wish to thank D. Gregoire for writing and integrating the electron-generation routines with the Herrmannsfeldt code. D. Gregoire also performed the initial analysis of the beam-slit shadowgraph. We wish to acknowledge technical discussions with N.A. Krall and M. Rosenberg. We also wish to thank R. Watkins for his expert technical assistance in fabricating and assembling the PAG. This research was funded by Air Force Office of Scientific Research Contract Number F49620-86-C-0105.

REFERENCES

1. R.J. Harvey, "Plasma-Anode Electron Gun," Hughes Aircraft Company patent disclosure No. 84050, U.S. patent pending.
2. J.R. Pierce, Theory and Design of Electron Beams, 2nd Ed., Van Nostrand, New York, 1954.
3. G.W. McClure, "Low-Pressure Glow Discharge," Appl. Phys. Lett. **2**, No. 12, 233 (1963).
4. J.R. Bayless and R.J. Harvey, "Continuous Ionization Injector for Low-Pressure Gas-Discharge Device," U.S. Pat. No. 3, 949, 260 (1976) [Assigned to Hughes Aircraft Company].
5. P.F. Little, "Secondary Effects," Band XXI, Vol. XXI, Handbook der Physics (1956). Also see A.G. Hill et al., Phys. Rev. **55**, 463-470, March 1939.
6. W.B. Herrmannsfeldt, SLAC Report No. 226, November 1979.
7. W.H. Bennett, Phys. Rev. **45**, 890 (1934); also see N.A. Krall and A.W. Trivelpiece, "Principles of Plasma Physics," McGraw Hill, New York (1973).

FIGURE CAPTIONS

1. Plasma-anode E-gun (PAG) concept.
2. Modified Hermannsfeldt-code runs at 80 kV and 10 A showing electron trajectories with (a) and without (b) ions in the gap.
3. 120-kV PAG scaling experiment.
4. Photograph of the 120-kV PAG scaling experiment.
5. Photograph of the PAG cathode and high-voltage bushing assembly.
6. PAG operation demonstrating 10 A of cathode current at 100 kV.
7. PAG operation with 210- μ s pulse length at 2.5 A of Faraday-cup current at 70-kV beam voltage.
8. Cathode and Faraday-cup current scaling with ion-source discharge current at $V_b = 90$ kV.
9. Cathode and Faraday-cup current scaling with ion-source discharge current at $V_b = 50$ kV.
10. Electron yield per ion as a function of beam voltage.
11. Beam current measured by a 1-mm-diameter disk probe.
12. Radial beam profile.
13. Bennett-pinch effect.
14. Electron-beam profile is consistent with Bennett-pinch theory.
15. Beam profile with PAG operating in the ion-space-charge current-limited regime.
16. Schematic of the "beam-slit shadowgraph" .
17. Schematic of the 120-kV PAG scaling experiment with a beam-slit shadowgraph. The beam slit is located just upstream of the Langmuir-probe array.
18. Current distribution measured 7.9 cm downstream of the beam slit.

14272-5R1

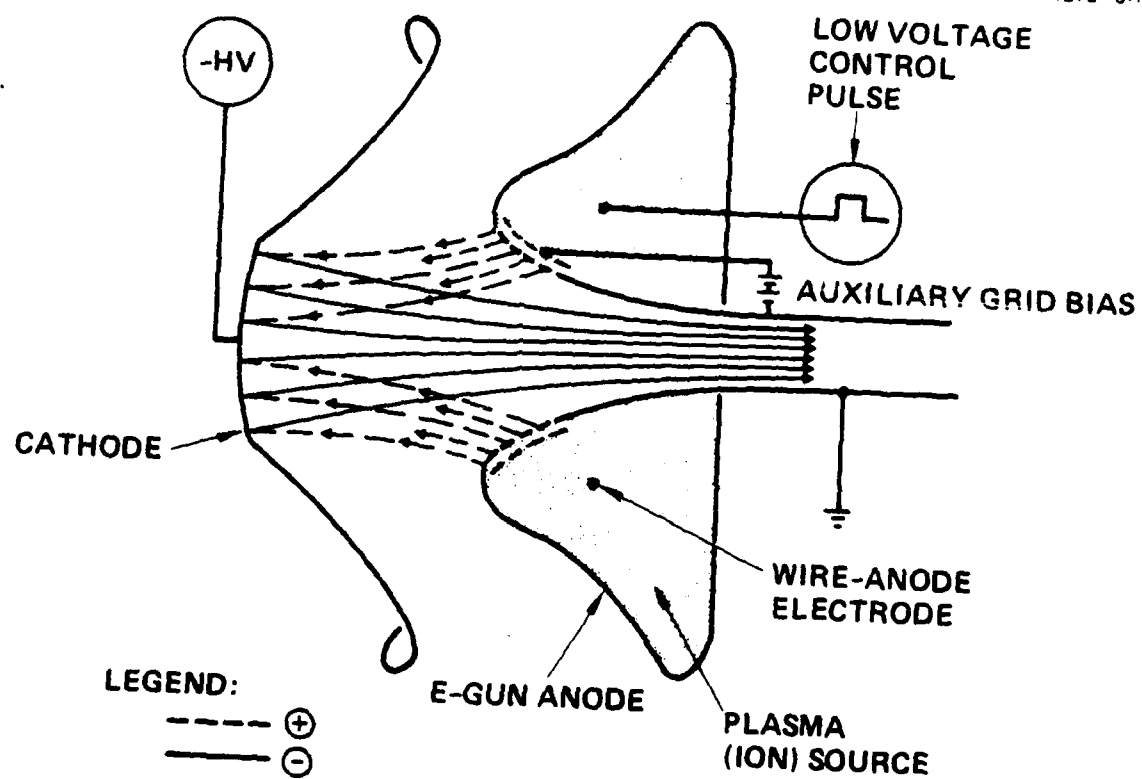
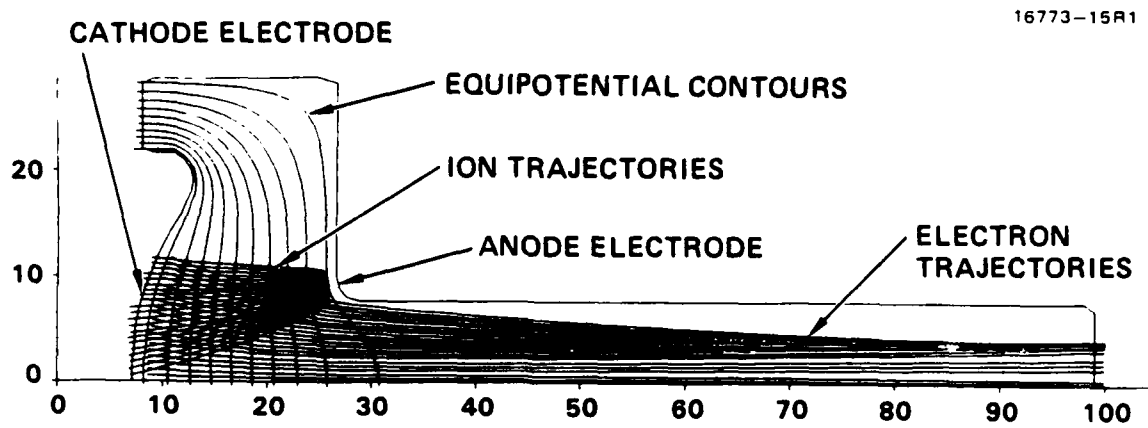
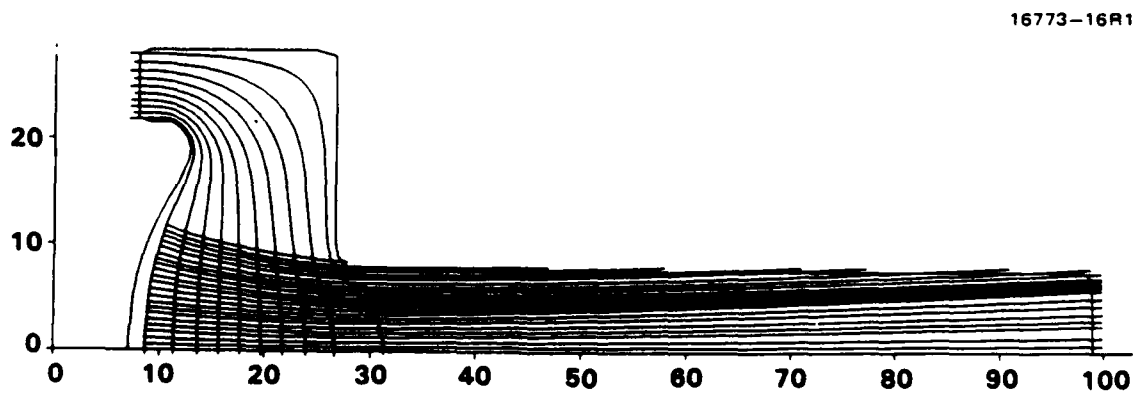


Figure 1



(a)



(b)

Figure 2

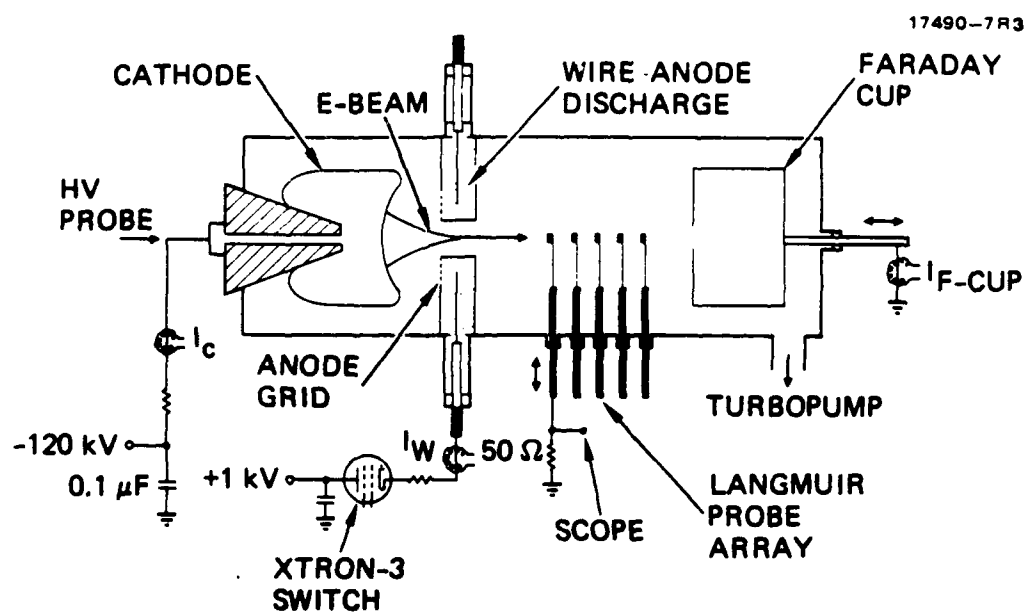


Figure 3

MC 17241



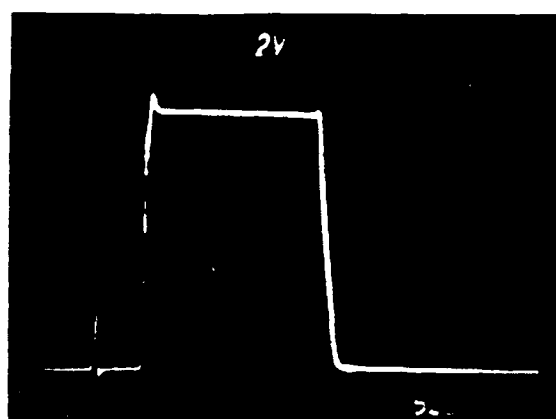
Figure 4

MC 17240

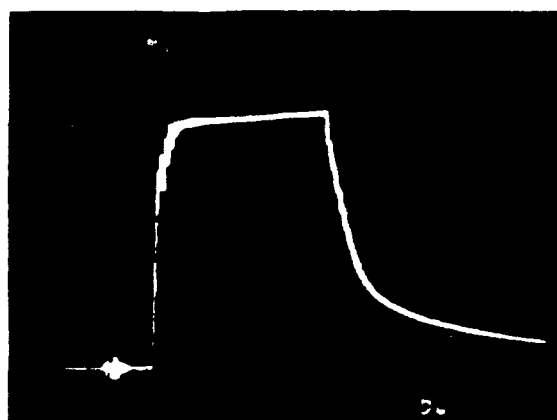


Figure 5

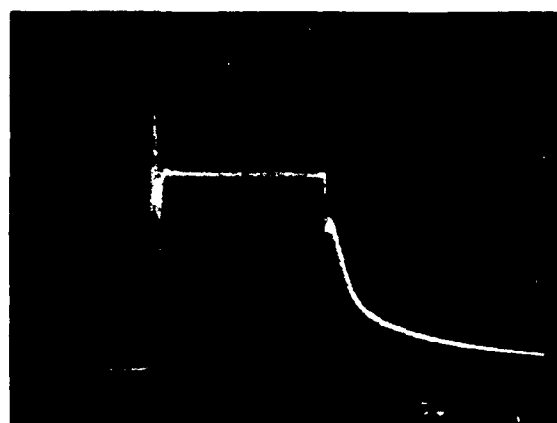
C-21



ION-SOURCE
DISCHARGE CURRENT
20 A/DIV



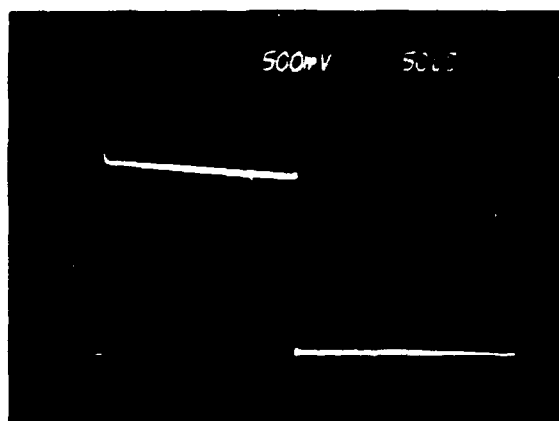
CATHODE CURRENT
2 A/DIV



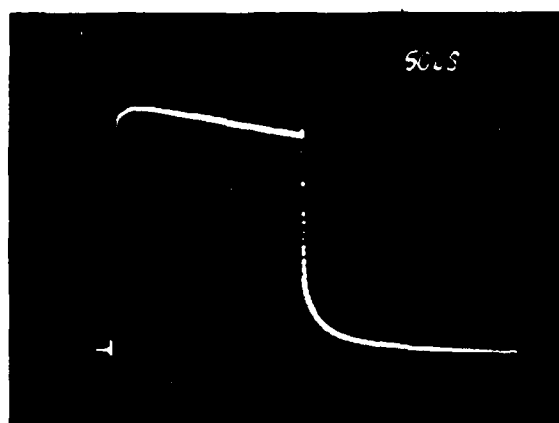
FARADAY-CUP
CURRENT
2 A/DIV

TIME, 5 μ s/DIV

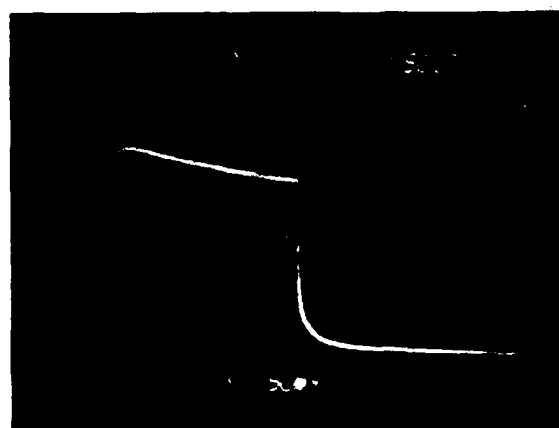
Figure 6



ION-SOURCE
DISCHARGE CURRENT
5 A/div



CATHODE CURRENT
0.5 A/div



FARADAY-CUP
CURRENT
0.5 A/div

TIME, 50 μ s/div

Figure 7

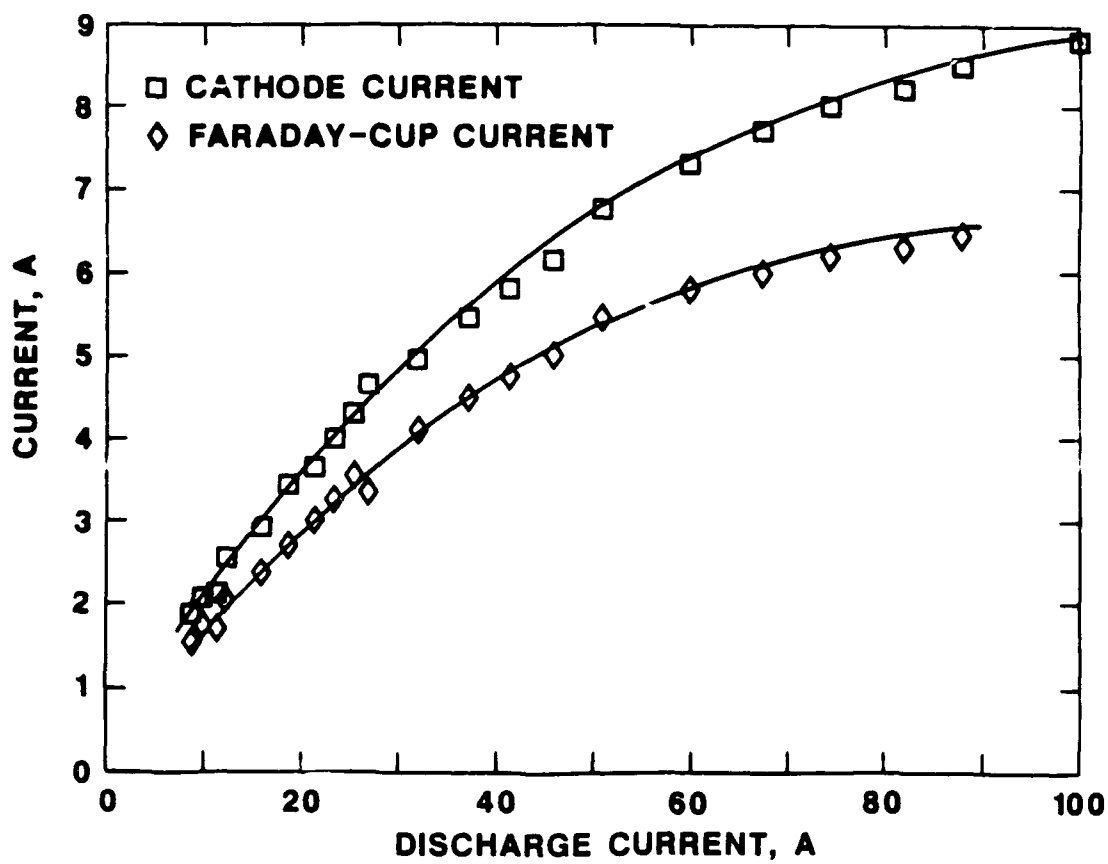


Figure 8

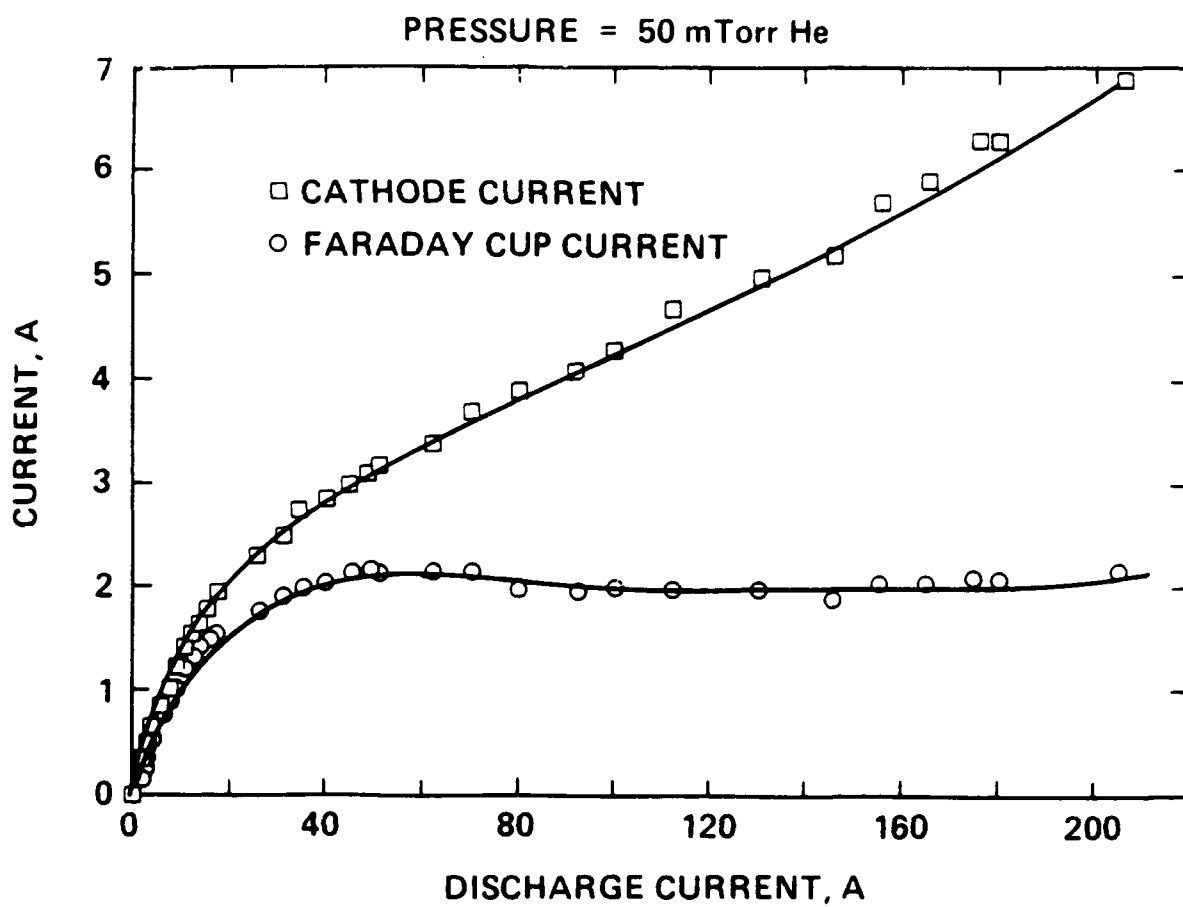


Figure 9

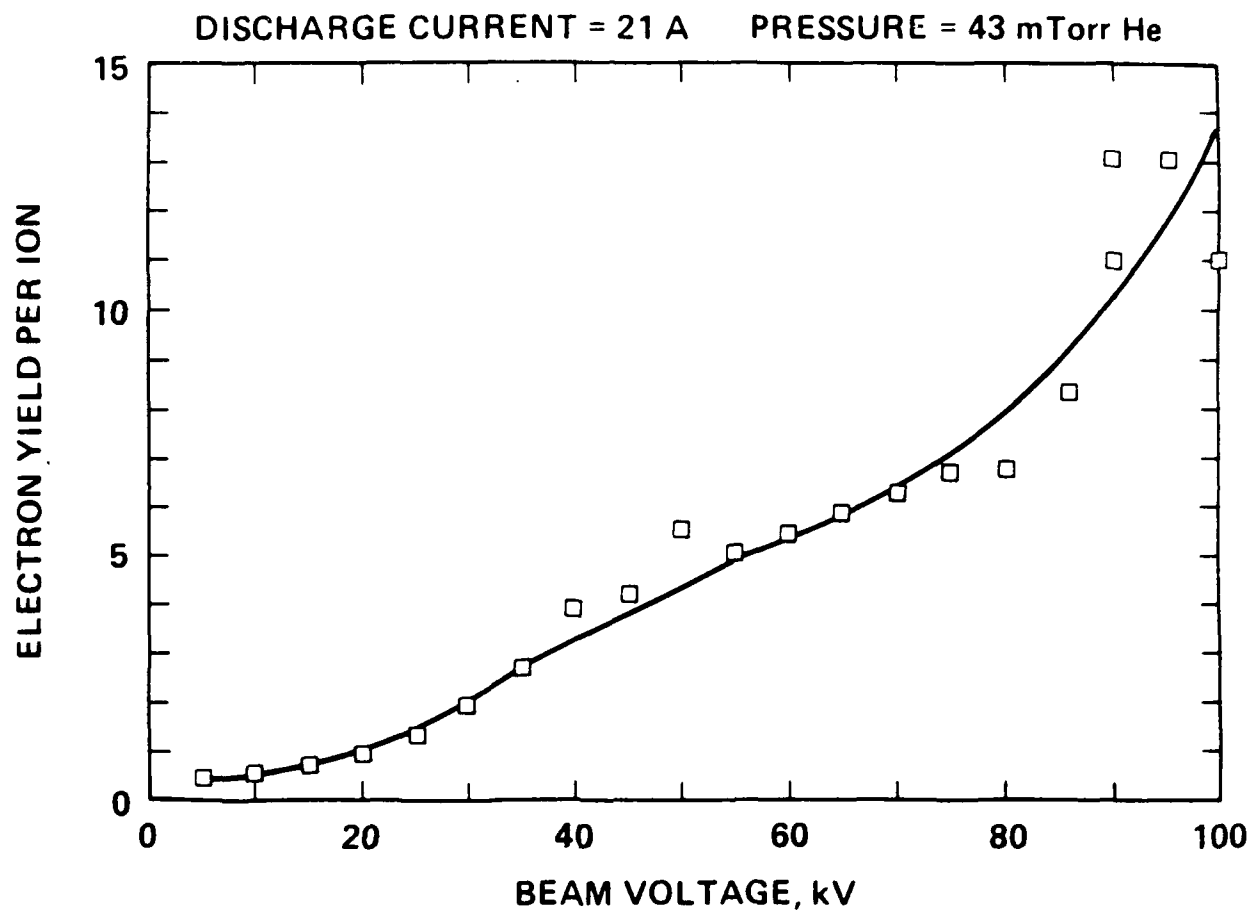
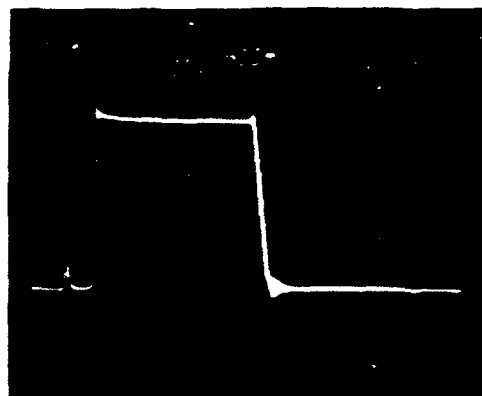


Figure 10

ION SOURCE DISCHARGE CURRENT



5 A/div

5 μ s/div

PROBE CURRENT

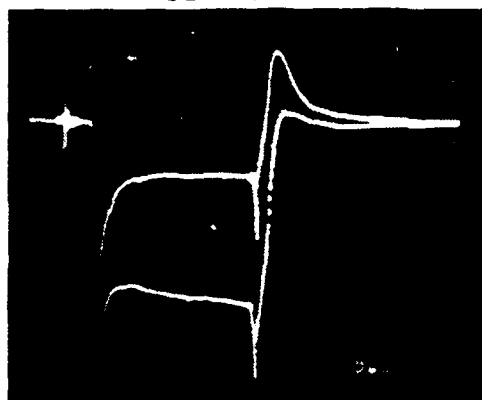
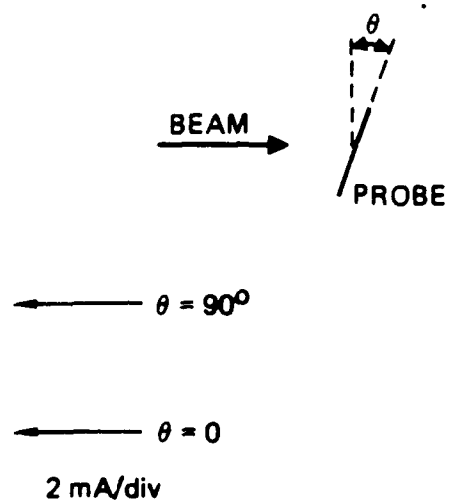
5 μ s/div

Figure 11

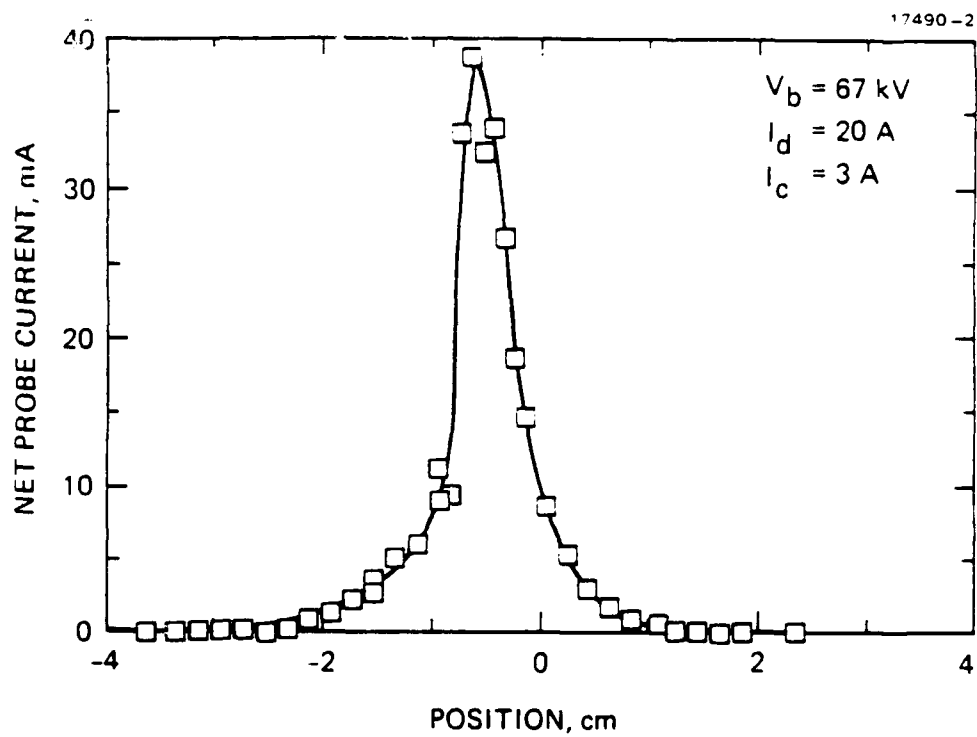


Figure 12

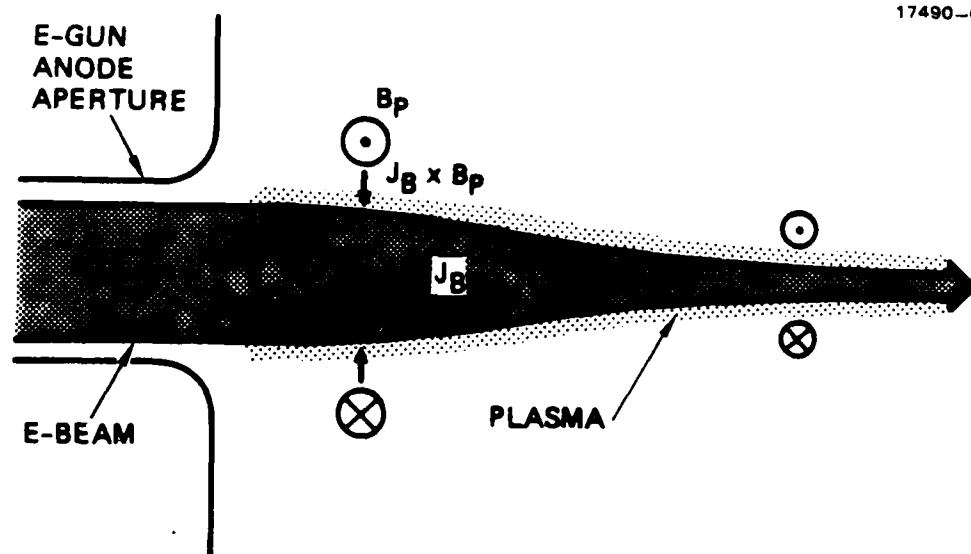


Figure 13

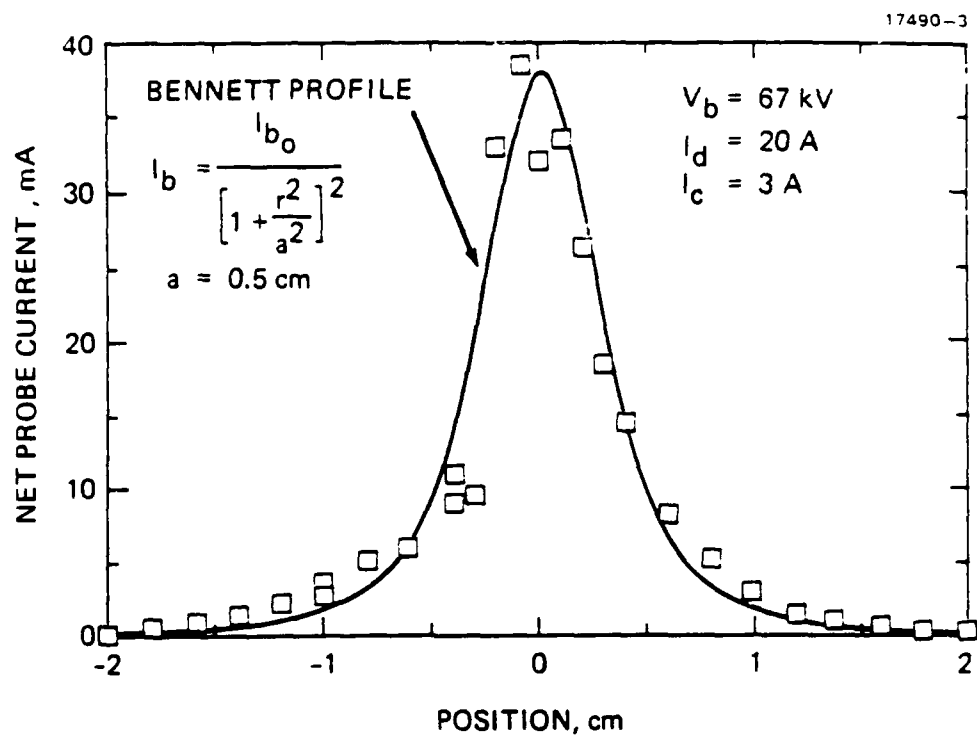


Figure 14

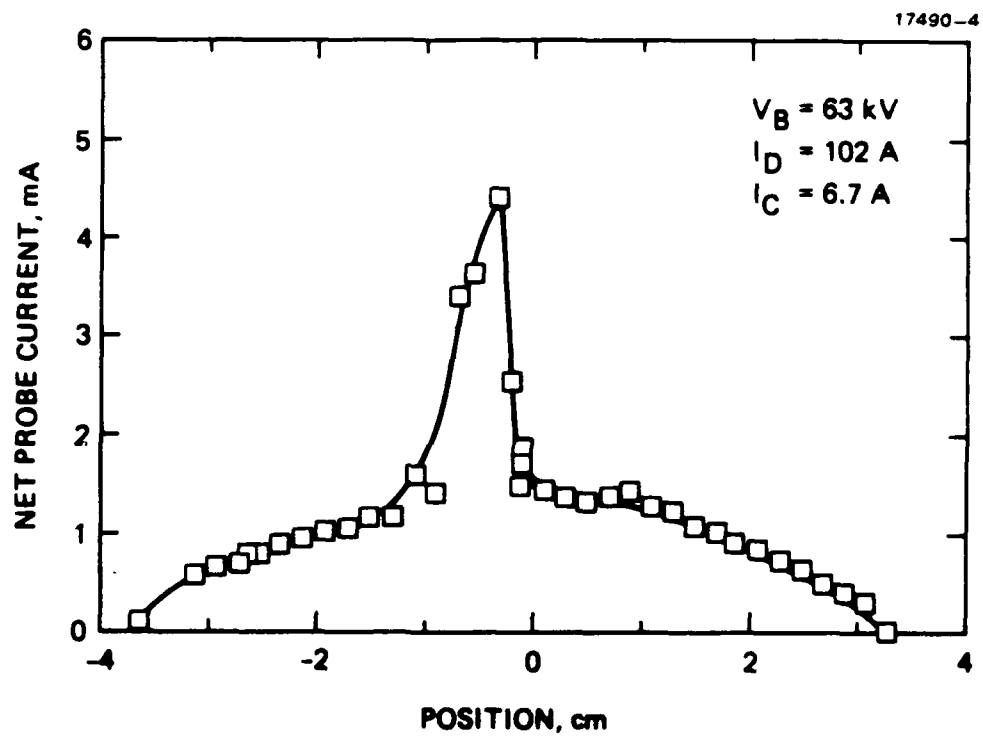


Figure 15

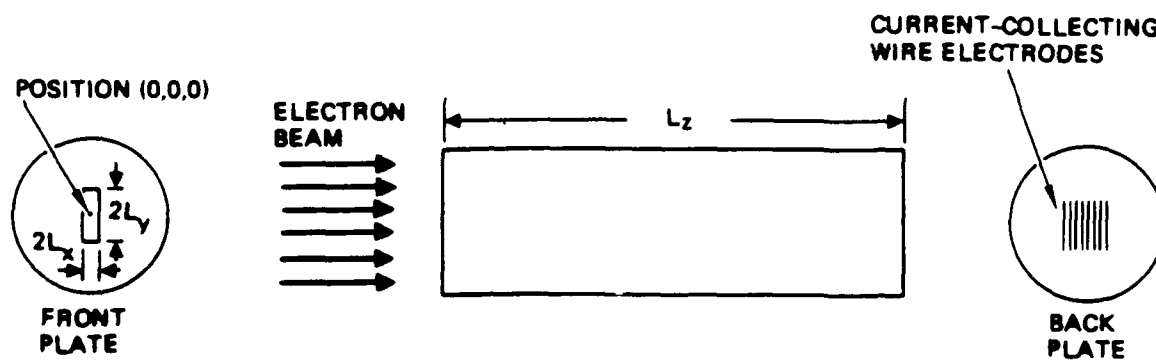


Figure 16

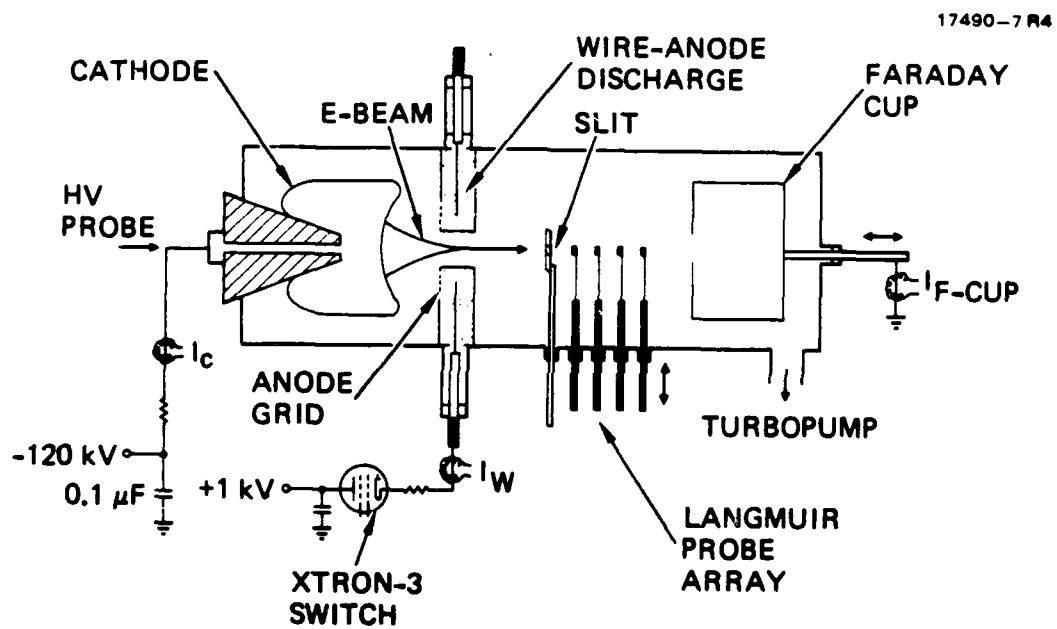


Figure 17

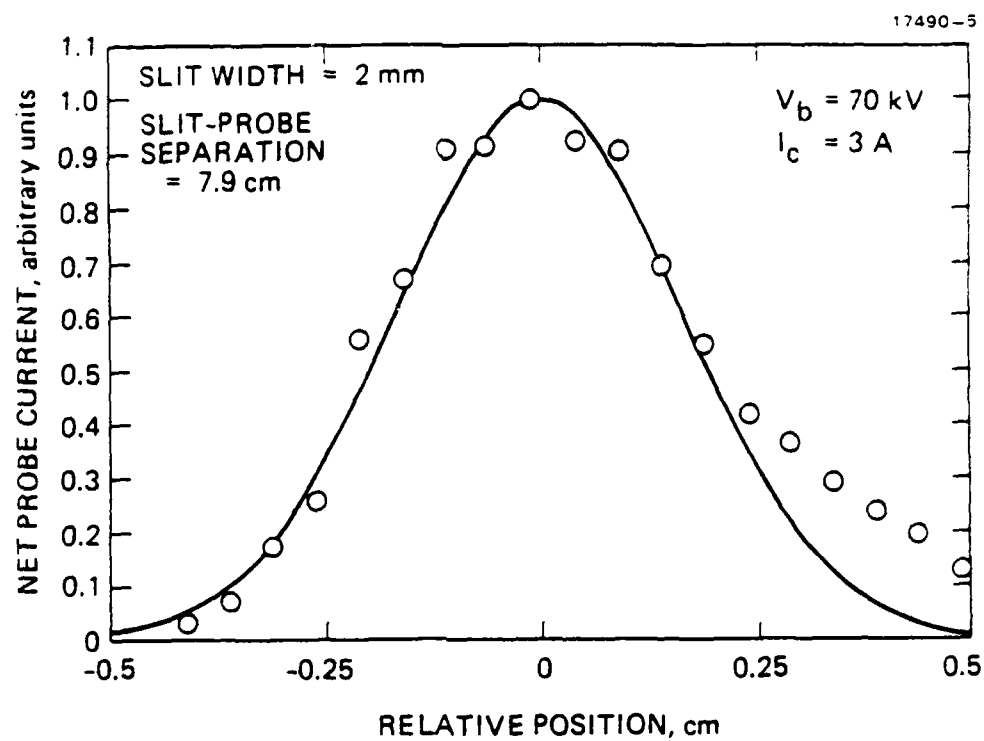


Figure 18